THE·UNIVERSITY·OF

WARWICK

Biophysical studies on novel metallo-systems and their interactions with DNA and small molecules

Kirti Kantilal Patel

Submitted for the degree of Doctor of Philosophy

University of Warwick, Department of Chemistry
October 2001

To My Family

Contents

Declaration

The observations and recommendations in this thesis are those of the author except where acknowledgement has been made to results and ideas previously published. The work was undertaken at the Department of Chemistry, University of Warwick between November 1997 and October 2000 and has not been previously submitted for a degree at any institution.

Abstract

The DNA binding interactions of five novel bis(2,2′:6′2″-terpyridine)ruthenium(II) complexes functionalised with an aryl tail group (i) biphenylene (biphen), (ii) β-napthyl (napth), (iii) phenanthrene (phen), (iv) anthracene (anth) and (v) pyrene (pyr) in the *4′* position on each terpyridine ligand were investigated with calf thymus DNA (ct-DNA), poly $[d(A–T)]_2$ and poly $[d(G–C)]_2$ DNA using the spectroscopic techniques of absorbance, circular dichroism (*CD*) and linear dichroism (*LD*). All five complexes bind non-covalently to DNA. At low complex concentrations, the anth, phen and pyr complexes were found to intercalate their aryl tail groups between DNA bases. The napth complex exhibits both an intercalative and a non-intercalative mode. The biphen complex exhibits groove binding with no significant tail intercalation. At high metal complex concentrations, aggregation of the complexes on the DNA is observed, resonance light scattering indicate aggregates of low nuclearity along the groove.

The DNA binding interactions of a novel series of structurally similar eighteen platinum(II) square planar complexes with subtle ligand variations of the formula [Pt(L)Cl(DMSO)] where L denotes an acylthiourea ligand system were investigated with ct-DNA, poly $[d(A–T)]_2$ and poly $[d(G–C)]_2$ DNA, 5′-mononucleotides and 9-methylguanine. Absorbance, *CD* and *LD* studies indicate ligand variation affects DNA binding interaction. Mass spectrometric studies suggest these complexes bind covalently to DNA via the loss of the chloride or possibly the DMSO groups on the platinum.

Supramolecular copper(I) and silver(I) metallo-cyclophanes and their interactions with the isomers of di- and tri-methoxybenzenes and chiral anionic compounds were investigated. The metallo-cyclophanes can adopt two conformations, a helical and a bridging non-helical structure. *CD*, NMR and X-ray crystallography show the dianion sodium antimonyl-L-tartrate can resolve this mixture. Absorbance and fluorescence studies suggest the metallo-cyclophanes bind methoxybenzenes. The design and synthesis of novel longer asymmetric ligands capable of assembly into a larger supramolecular metallo-cyclophanes is included.

Abbreviations

λ	wavelength
λ_{max}	wavelength of an absorption maximum
λex	excitation wavelength
λem	emission wavelength
ε_{max}	molar absorbitivity at wavelength maximum
T	transmittance
α	angle between a transition polarisation and the orientation axis
θ	angle between macroscopic and molecular orientation axis
ϕ	fluorescence quantum yield
Δ	right-handed enantiomer
Λ	left-handed enantiomer
m	muliplet
s	singlet
d	doublet
t	triplet
dd	doublet of doublet
td	triplet of doublet
(s)	strong
(m)	medium
(w)	weak
n	non-bonding
CT	Charge transfer
MLCT	Metal-Ligand Charge transfer
IL	In-ligand/ligand centred
MC	metal centred
12dmb	1, 2-dimethyoxybenzene
13dmb	1, 3-dimethyoxybenzene
14dmb	1, 4-dimethyoxybenzene
123tmb	1, 2, 3-trimethyoxybenzene
135tmb	1, 3, 5-trimethoxybenzene
AgOAc	CH_3COOAg, silver acetate
A	adenine
G	guanine
T	thymine
C	cytosine
AT	adenine and thymine DNA base pair
GC	guanine and cytosine DNA base pair
AT DNA	poly $[d(A–T)]_2$ DNA
GC DNA	poly $[d(G–C)]_2$ DNA
GMP	5′-guanosine monophosphate
AMP	5′-adenosine monophosphate
TMP	5′-thymidine monophosphate
CMP	5′-cytosine monophosphate

Ar	aryl
Bipy	bipyridine
CD	circular dichroism
ct-DNA	calf thymus DNA
chrysi	5,6-chrysenequinone dimine
DNA	deoxyribonucleic acid
DMF	N,N-dimethylformamide
DMSO	dimethylsulfoxide
dppz	dipyrido(3,2-a:2′,3′-c)phenazine ligand
dpq	dipyrido(3,2-d:2′,3′-f)quinoxaline ligand
dmphen	2,9-dimethyl-1,10-phenanthroline
ex	excitation
em	emission
h	hour
ICD	induced circular dichroism
J	coupling constant
K	Binding constant
LD	linear dichroism
LD^r	reduced linear dichroism
MB	methylene blue
MG	9-methylguanine
MS	mass spectrometry
NMR	nuclear magnetic resonance
NaSbtat	sodium antimonyl tartrate
phi	9,10-phenanthrenequinone
1,10-phen	1,10-phenanthroline
phen	phenanthrene
ppm	parts per million
PVA	polyvinyl alcohol
R	mixing ratio
RNA	ribonucleic acid
S	orientation parameter
SM	starting material
terpy	2,2′:6′,2″-terpyridine
UV	ultra violet

Part of this thesis has been accepted for publication in the *Journal of Inorganic Biochemistry.*

K. K. Patel, E. A. Plummer, M. Darwish, A. Rodger and M. J. Hannon: Aryl substituted ruthenium bisterpyridine complexes: Intercalation and groove binding.

1 Introduction and spectroscopic techniques

1.1 Background

The work presented in this thesis describes novel inorganic metal complexes and their interactions with bio-molecules. The main aim has been to develop methods to study metallo-complexes spectroscopically. A variety of systems have been studied, the common features of which are the spectral techniques used and the need to solubilise the systems in organic solvents. In chapter 2, the interaction of a series of octahedral ruthenium(II) bis-terpyridine complexes with DNA is described and discussed. Similar studies on some smaller platinum(II) square planar complexes form the subject matter for chapter 3 with mass spectroscopic data contributing to the overall picture of the interactions. Chapter 4 reports the investigation of the molecular sensor potential of the simplest class of system studied, that of novel self-assembling copper(I) supramolecular metallo-cyclophanes,[1] with small aromatic compounds and concludes with the description of the synthesis of a novel larger ligand capable of self-assembly into a box structure. Chapter 5 contains the overall conclusions of this thesis.

1.2 Introduction

In this introductory chapter, the background to each aspect of the work is discussed. In Section 1.3 the spectroscopic techniques used to the conduct bio-physical studies are explained. Section 1.4 contains a basic explanation of the use of inorganic metal complexes in biology. Section 1.5 covers the different ways in which molecules interact. Section 1.6 provides an overview of DNA and its binding modes. Finally

Section 1.7 reports on the preliminary studies conducted on the potential use of organic solvents with DNA for the work in chapters 2, 3 and 4.

1.3 Spectroscopic techniques

1.3.1 Introduction

The sun is a burning mass of energy that emits electromagnetic radiation, more commonly known as light. Visible light, which is the electromagnetic radiation our eyes detect, represents only a very small portion of the electromagnetic spectrum. Electromagnetic radiation waves of different frequencies and wavelengths can also be produced by different sources. For example, light is emitted by very hot objects such as the filament of a light bulb.

The characteristics of the electromagnetic radiation depend on its wavelength and can be grouped accordingly: from the long wavelength, low frequency radiowaves to microwaves, infrared waves, light waves (sub-divided into the visible and invisible (the ultra-violet (UV))), x-rays and cosmic rays (short wavelength, high frequency). Electromagnetic radiation is described as having dual wave and particle properties. It is the energy resulting from the acceleration of electric charge and the associated electric fields and magnetic fields (found everywhere in the universe). It can be considered as made up of two components, electric and magnetic waves that both oscillate at right angles to each other and to the direction of motion, with wavelength, λ, and frequency, ν. It can also be described in terms of a photon (a particle of light with no mass) of a particular wavelength with an energy ΔE. [2-6]

$$\Delta E = \frac{hc}{\lambda} = h\nu \qquad (1.1)$$

where h = Planck's constant (6.626×10^{-34} J s), ν = frequency of the radiation, λ = wavelength of the radiation and c = speed of light (3.0×10^{8} m s^{-1}). No two wavelengths have the same photon energy. [2,5]

Spectroscopy is the study of the interactions between radiation and matter — specifically in this instance the interaction between light and matter. Different molecular processes occur when light in each region is absorbed by matter. The internal energy of a molecule can be due to energy associated with electrons (electronic), energy associated with vibrations between atoms (vibrational), and energy associated with rotation of various groups of atoms within the molecule relative to other groups (rotational). Microwave radiation stimulates the rotational motion of molecules when is is absorbed, infrared (IR) stimulates vibrations of molecules, ultra violet radiation and visible light cause electrons to be promoted to higher energy electronic levels and X-rays and short wavelength UV break chemical bonds and ionize molecules (bond breaking and ionisation).[2,5]

The emphasis of the work in this thesis is on the interpretation of optical (electronic) spectra in terms of the macroscopic electronic properties of molecules and the changes in these properties that occur upon interaction with other molecules *e.g.* DNA.

The spectroscopic techniques used to probe interactions, *i.e.* the changes in the electronic properties of molecules, are described in the following sections.

1.3.2 Normal absorption spectroscopy

The interaction of radiation with matter involves the transfer of energy [5] from the light beam to the molecule. The simplest form of spectroscopy is that of absorption. Normal absorption spectroscopy, more commonly termed UV-Visible absorbance

spectroscopy, probes the electronic transitions of a molecule when it absorbs the energy (ΔE) of one photon at certain wavelengths. If the energy of the incident photon corresponds to the energy required to move (promote) an electron in a molecule from its ground state (low energy) to an excited state (higher energy) the photon may be absorbed and a redistribution of electron density between those states induced. The movement of the electron is termed an *electronic transition*. [4]

The rearrangement of electron density during an electronic transition can be characterised in terms of a *net linear displacement of charge*. The magnitude and direction of a given transition is described by the (electric dipole) *transition moment*, μ, a vector of defined length and direction within the framework of the molecule.[4] The length of the vector squared is proportional to the intensity of the transition, whereas its direction is the *transition polarisation*. The probability that absorption will occur depends on the relative alignment of the transition moment and the electric field of the incident light. The probability is maximised when the transition moment and electric field are aligned in parallel.

In the visible region of the spectrum, when white light is shone onto coloured material, it is either absorbed or reflected. What is actually seen by the eyes are the colours that are not absorbed, the complementary colours. These therefore form the flat part of the spectra with no signal, as they are not absorbed. The absorbance bands correspond to the wavelengths at which the complex absorbs energy. The smaller the difference in energy between the ground and excited states, the longer the wavelength. Absorption also depends on the environment (see Section 1.7). Absorption spectroscopy can be used to probe the interactions of a molecule if the interaction perturbs the transitions.

The transmittance, T, of a sample of molecules is related to the absorbance by

$$\log_{10}\left(\frac{1}{T}\right) = \log_{10}\left(\frac{I_0}{I}\right) = A \qquad (1.2)$$

where A is the sample absorbance at each wavelength, I_0 is the intensity of light incident on the sample and I is the intensity of light emergent from the sample. The *Beer Lambert law* [2-4] states that absorbance is linearly related to the concentration of the absorbing species c (mol dm^{-3}) and the path length l (cm) of the cell in which the solution is placed,

$$A = \varepsilon c l \qquad (1.3)$$

where ε is the molar absorptivity also known as the extinction coefficient (mol^{-1} dm^3 cm^{-1}) of the species. There are limitations to this linear relationship. ε is characteristic of the sample, its environment and the wavelength.[2] If a solution is too concentrated then the absorbance is no longer linear with concentration. This may be due to very few photons being transmitted or to chemical features (usually intermolecular interactions) of the system.

1.3.2.1 Spectroscopic transitions [3, 5-8]

Molecules can undergo a number of different electronic transitions (see Figure 1.1). Intense absorbance bands are produced by σ–σ^* and π–π^* transitions, (typically conjugated molecules can exhibit $\varepsilon_{max} > 10{,}000$) and weak bands by n–σ^* and n–π^* transitions (these require less energy and can exhibit $\varepsilon_{max} < 100$). The strongest σ–σ^* transitions can be found below 200 nm in the UV region of the spectrum.

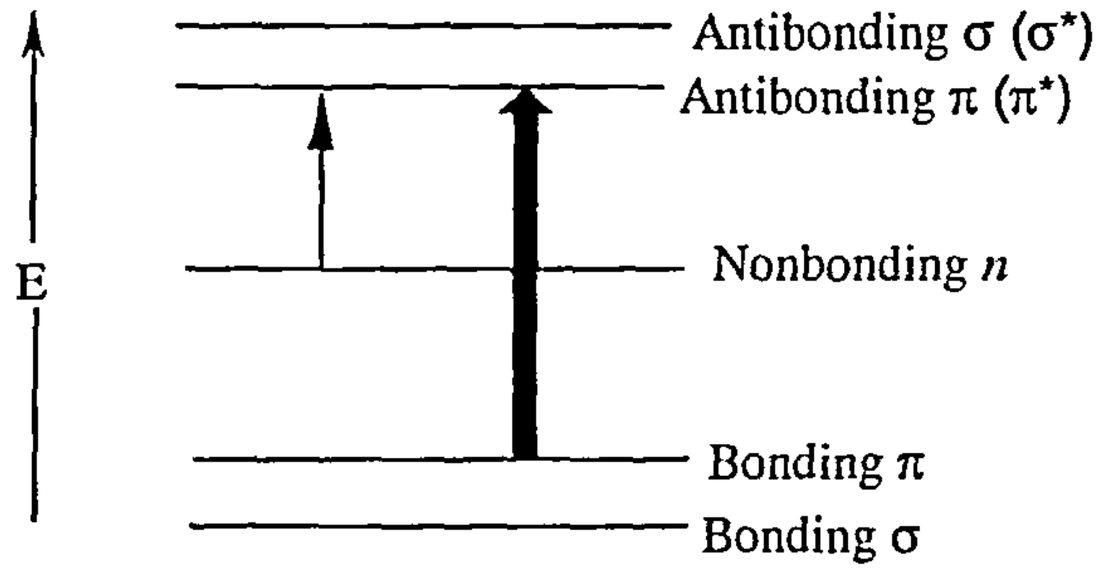

Figure 1.1 Summary of electronic energy levels. The n–π^* and π–π^* (heavy arrow) transitions are indicated.[3]

All ligands possess a number of molecular orbitals which may be σ, σ*, π, π* or *n* (non bonding) in character. Those ligands containing π bonds *e.g.* conjugated aromatic π system molecules or unsaturated groups (chromophores) can exhibit electronic spectra of n–π^*, π–π^* transitions (promotion of electrons from non-bonding levels (*n*) or filled molecular orbitals (π) to anti-bonding (π*) orbitals). In the context of this thesis, the promotion of an electron from a π ligand to antibonding π* orbital *i.e.* π_L–π_L^* is referred to as a ligand centred/in ligand (IL) transition.

Transition metal complexes can also exhibit small metal-metal or *d*–*d* transitions (due to the re-distribution of electrons in the partially filled *d*-orbitals), metal centred (MC) transitions, (*i.e.* π_M–σ_M^* through the promotion of an electron from a π metal orbital to an antibonding σ* metal orbital) and metal-to-ligand charge transfer (MLCT) transitions (*i.e.* π_M–π_L^* where an electron is promoted from metal centred π bonding (π_M) orbital to an unfilled ligand centred antibonding (π_L^*) orbital). Charge transfer (CT) bands are due to a change in electron distribution *e.g.* between delocalised orbitals as in aromatic groups of the ligand or conversely empty orbitals of the metal.

1.3.2.2 DNA transitions

DNA is composed of planar aromatic bases attached to a sugar phosphate backbone. Its spectroscopy, that can be readily measured in a laboratory, is due to transitions from π bonding orbitals to π antibonding (π^*) orbitals of these bases. Duplex DNA concentrations can be determined spectroscopically using established ε values and utilising the Beer-Lambert law. At known wavelengths for ct-DNA (calf thymus) ε_{258} = 6600 $mol^{-1}dm^3cm^{-1}$; for poly[d(G-C)]$_2$ referred to as GC DNA, ε_{254} = 8400 mol^{-1} dm^3cm^{-1}; for poly[d(A-T)]$_2$ referred to as AT DNA ε_{262} = 6600 mol^{-1} dm^3cm^{-1}.

The absorption spectrum of DNA is sensitive to changes in structure (heating, for example, produces a hyperchromic effect — an increase in absorbance) or interactions with other molecules. The changes can aide characterisation of the type of binding. A decrease in absorbance intensity (hypochromic effect) is thought to be attributable to π-π^* stacking interactions, with wavelength shifts to longer wavelengths (red shifts) being characteristic of intercalation of a planar molecule between DNA base pairs. The effect on the absorption spectroscopy of groove binders is usually less dramatic upon binding to DNA. Figure 1.2(a) illustrates the spectroscopy of ct-DNA. Ct-DNA is colourless in water, and therefore transparent above 300 nm, its transitions are below 300 nm in the UV region of the spectra. These π-π^* transitions are due to the planar purine and pyrimidine bases (see Section 1.6).

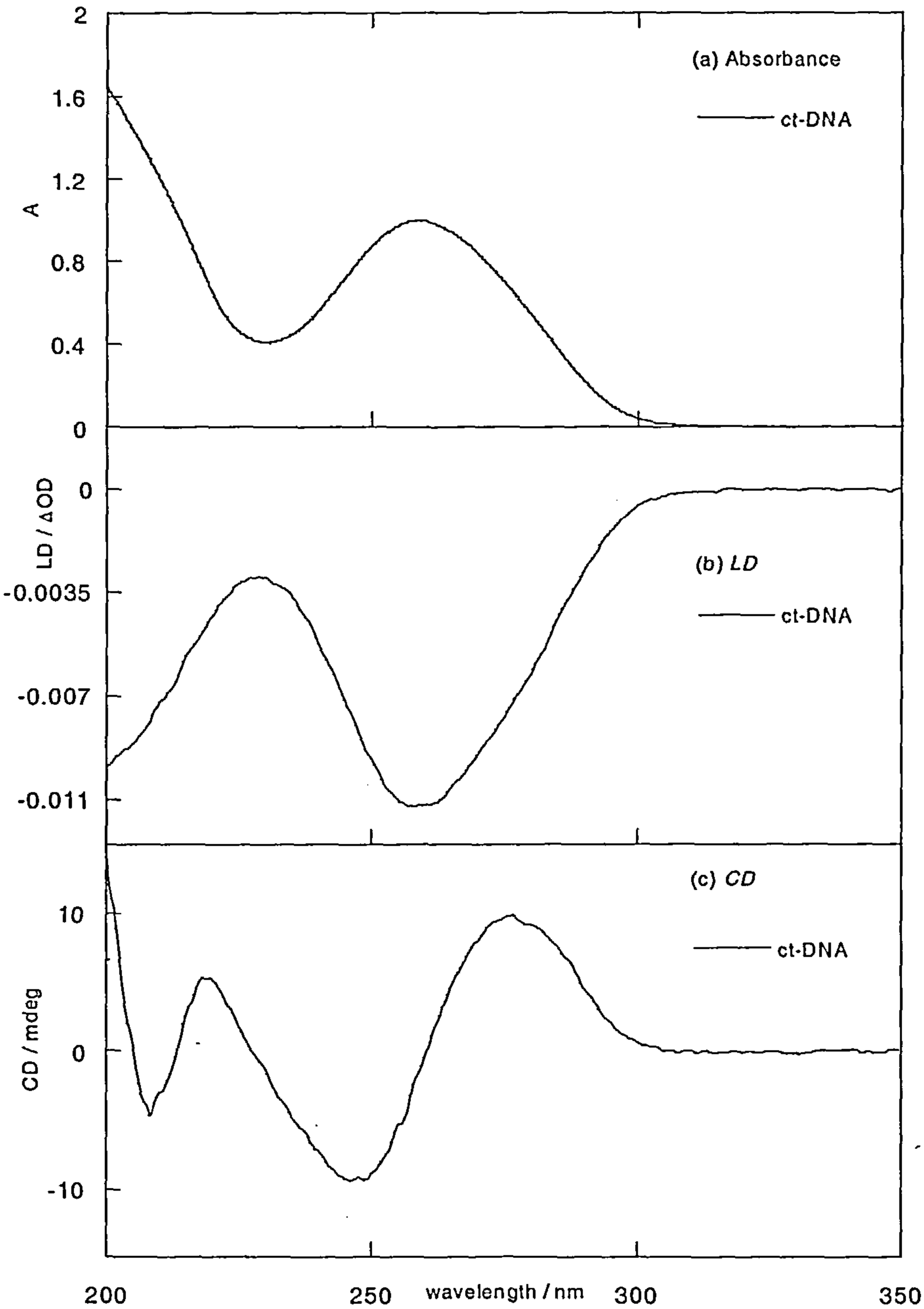

Figure 1.2[4] The spectroscopy of ct-DNA (125 μM) in water, (a) the ***absorbance spectrum*** of ct-DNA, (b) the ***LD spectrum,*** the negative *LD* signal is due to the transitions of the bases perpendicular (⊥) to the long axis of DNA and (c) ***CD spectrum*** of ct-DNA, the positive and negative signals seen are due to transitions of the planar achiral bases that are attached to the chiral sugar phosphate backbone of the DNA.

1.3.3 Linear dichroism spectroscopy

Linear dichroism (*LD*) is defined as the difference in anisotropic absorption of light linearly polarized parallel $(A_{||})$ and perpendicular $(A_{\perp})$ to the direction of orientation.[4]

$$LD = A_{\parallel} - A_{\perp} \tag{1.4}$$

An isotropic collection of molecules will have no *LD*, whilst a group of molecules whose transition moments are macroscopically oriented will absorb differing amounts of parallel and perpendicular plane polarised light, producing a non-zero *LD* spectrum. For a perfectly oriented molecule when uniaxially oriented *i.e.* for a transition polarised exactly parallel to the orientation direction, the measured *LD* would equal $A_{||}$ (> 0) or for a transition polarised exactly perpendicular to the orientation direction, the measured *LD* would equal $\frac{-A_{\perp}}{2}$ (< 0) (the factor of 2 being due to cylindrical symmetry of the orientation system). Thus qualitative information about the orientation of molecules in space can be extracted from the sign of the *LD*. A more quantitative picture of molecular alignment can be obtained from the reduced *LD* (LD^r).[4]

$$LD^r = \frac{LD}{A} = \frac{A_{\parallel} - A_{\perp}}{A} \tag{1.5}$$

where A is the normal isotropic absorption and constitutes an average over all possible orientations.

Molecules can be macroscopically oriented in a number of ways. Small molecules can be oriented in stretched polymer films, whereas longer molecules like DNA may be oriented by viscous drag (flow orientation) or an electric field.[4] In this

thesis, stretched polymer films and flow orientation are used to orient and determine geometry of complexes using *LD*.

1.3.3.1 Stretched film linear dichroism

Stretched film *LD* can provide information about the polarisation directions of transition moments of a particular molecule. The symmetry of the molecule is often helpful is assigning the orientation of the molecules within the film. In addition, it governs the polarisations of transition moments. Once polarisations for complexes have been assigned, they can be used to determine binding orientations of the complexes on a flow-oriented macromolecule (DNA).

Stretched film preparation[4]

Blank and complex saturated films were prepared using Polyvinyl alcohol (PVA Type III low molecular weight) purchased from Sigma Chemical Co. Low molecular weight PVA was dissolved in water (10 % w/v). The solution was then heated with stirring to near boiling until a clear viscous solution was formed. To half of this PVA solution, a saturated solution of the complex to be oriented (200 μL) was added with slow mixing. The mixture was cast onto a glass plate, covered and allowed to dry over 3 days. A second film containing no complex, the blank film, was also prepared using the remaining half of the solution. Film UV and *LD* spectra of both films were collected both before and after each film was mechanically stretched (in a mechanical stretching device using heat) to twice its length in order to determine complex transition polarisations. The blank spectra were then subtracted from those of the complex.

The LD^r spectra of unstretched and stretched film were calculated by dividing the *LD* by the Absorbance, *A*

$$LD^r = \frac{LD}{A} \tag{1.6}$$

The LD^r is an absorbance independent measure of LD, the magnitude of which reflects the average orientation of an electronic transition relative to the axis of orientation.

The long and short axis of a molecule can usually be intuitively assigned. The long and short axes of the molecule (and the one perpendicular to them) are usually coincident with its spectroscopic axes if these are defined by symmetry. When the molecule is inserted into a stretched film, the long axis of the molecule will preferentially orient/lie along direction of orientation (stretch) whilst the short axis would resist the stretch and therefore lie at right angles to the stretch direction.

Molecular orientation can be achieved by stretching the film, however, the degree of orientation attained is imperfect and an orientation distribution results. The distribution can be discussed in terms of an axis framework which relates the macroscopic (laboratory) axis, such as the stretch of the film, to the molecular axes of the system (Figure 1.3).[4]

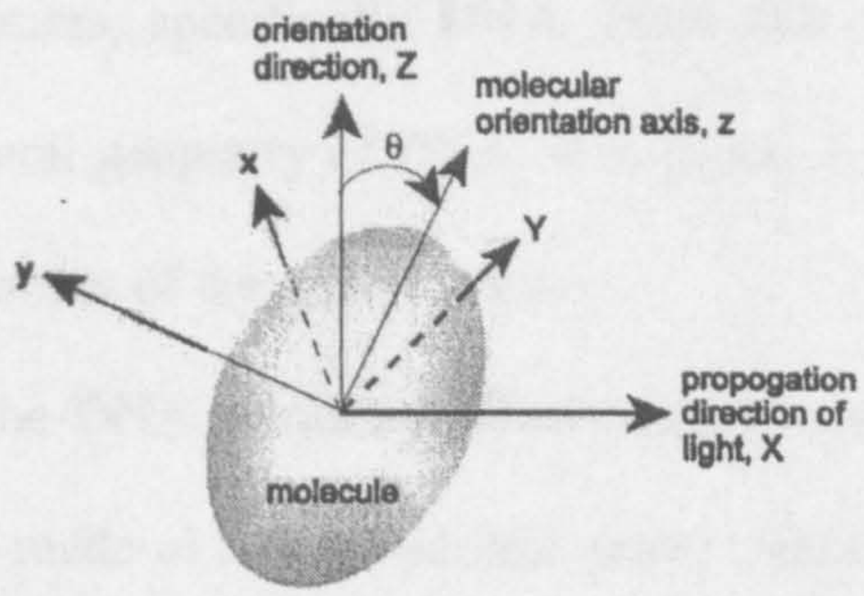

Figure 1.3 Macroscopic {X, Y, Z} and molecular {x, y, z} axis systems, where θ is the angle between Z and z

In order to analyse film LD data, we make the assumption that the molecule behaves as an uniaxial rod[4] in the stretched film. The degree of orientation can be described in terms of the average orientation parameter, S, for a uniaxially oriented rod within a stretched film. To determine S from the LD^r in ideal situations, one identifies a long axis polarized transition and assumes that the angle between its transition moment,

μ, and the orientation axis, α, is 0. The reduced linear dichroism for that whole absorption band is then: $LD^r(z) = +3S$, where S is the orientation parameter defining the efficiency of the macroscopic orientation ($S = 1$ perfect orientation, $S = 0$ for no orientation). Alternatively, short axis polarisation transitions (that would be perpendicular to z) therefore here $\alpha = 90°$ and $LD^r(x,y) = -1.5S$. If the molecular axes do not coincide with molecular long and short axes, the situation is more complicated. Thus transition polarizations can be assigned according to the signs of the stretched film LD^r. Generally, positive LD^r features are assumed to correspond to long axis polarised transitions and negative LD^r signals to short axis polarisation transitions, though if the degree of orientation is too low, the short axis polarised transitions may appear as less positive rather than negative.[4]

1.3.3.2 Flow linear dichroism

Flow *LD* can be applied to systems that are intrinsically orientable in solution or become oriented on interaction with a molecule that has intrinsic orientability *e.g.* long molecules such as polymers, specifically DNA. Flow *LD* can be used to probe the conformation and structural geometry of DNA or to probe the orientation of molecules bound to DNA relative to that of the nucleobases.

Experimentally the DNA solution is flow oriented using a quartz couette flow cell.[4] The couette cell is made of two concentric quartz cylinders, the inner of which is solid and rotates (Figure 1.4). The sample (1.8 – 3 mL volume) can be contained in a narrow gap between the two cylinders with a 1 mm (0.5 mm on each side) path length. Rotation of the inner cell at constant speed exposes the solution to a hydrodynamic shear force that macroscopically orients the solution by the resulting viscous drag, thus providing a constant flow of solution. The flow must be laminar to avoid light scattering and loss of orientation.

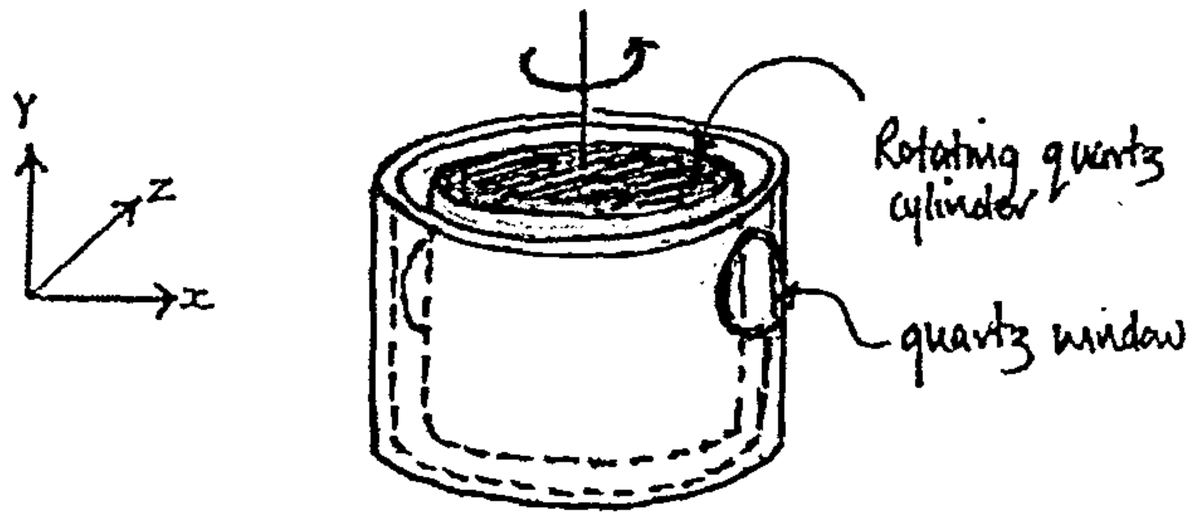

Figure 1.4 A schematic of a Couette flow *LD* cell.[4] Light is propagated in the X direction (perpendicular to the flow direction). $A_{\parallel}$ is the absorbance of Z polarised light and $A_{\perp}$ is the absorbance of Y polarised light

Long strands of DNA will orientate in the direction of flow of the solution (DNA of at least 500 base pairs is necessary in order to facilitate orientation)[4] and exhibit a *LD* signal at their absorption wavelengths. The flow oriented *LD* spectrum, (Figure 1.2(b)) of B-DNA above 190 nm exhibits a negative signal due to the plane π–π^* transitions of the bases attached at ~90° to the DNA long helix axis. Linearly polarised light is passed through the cell, if a molecule binds to DNA, an induced *LD* in the bound molecules' transitions or a change in magnitude of the DNA *LD* signal may be noted. A non-zero *LD* signal outside the DNA region when DNA is present is generally indicative of interaction between a metal complex and DNA. An increase in negative *LD* magnitude may be indicative of DNA stiffening or lengthening, conversely a decrease in *LD* magnitude may suggest that the DNA is shortening or bending.

Flow *LD* of effectively rod-like DNA, *e.g.* B-form ct-DNA duplexes, is assumed to exhibit uniaxial orientation about the helix axis for which the LD^r may be expressed as[7, 9]

$$LD^r = S\frac{3}{2}\left(3\left\langle\cos^2\alpha\right\rangle - 1\right) \qquad (1.7)$$

where α refers to the angle between a transition moment and the DNA helix axis and $\langle\ \rangle$ denotes an ensemble average over the orientation distribution function. In flow orientation, S for DNA is usually determined by assuming that the DNA bases are all

polarised at $\alpha \sim 86°$ from the helix axis. A value for α of 86° has been calculated for the predominantly π–π^* in-plane polarised transitions of the DNA bases found perpendicular to the DNA helix.[4] Using this value, a value of S for the in plane $\pi - \pi^*$ transitions of the DNA bases can be determined from the magnitude of its LD^r at 260 nm using equation 1.7. Once S for DNA has been determined, α may be computed for the transition moments of DNA bound complexes with known polarisations. The value of α for a bound complex can then be used to help identify the mode of binding. The in-plane transitions of a bound intercalator, for example, would be expected to have negative LD^r of similar magnitude to that of the DNA bases since the complex and bases would be co-planar. In practice, intercalators locally stiffen the DNA and so usually have LD^r values slightly higher than the average DNA base. A bound complex in the minor groove of B-DNA, by way of contrast, would have positive *LD* and $\alpha \approx 45°$ for a long axis polarised transition that followed the pitch of the groove.

If the DNA absorbance and flow *LD* at 260 nm is overlaid by transitions of bound molecules, then *S*, for the orientation of the DNA bases, will not be able to be determined. An independent check of the DNA orientation can be made at varying ligand concentrations by measuring the *LD* of a probe, such as methylene blue (MB), a known intercalater.[10] Methylene blue can be added to solutions when ligand transitions overlap the DNA transitions, as it exhibits a long axis polarised transition at 675 nm outside the spectroscopic range of most DNA binding ligands.[10] It has a strong binding constant and large extinction coefficient so only low concentrations of it (~1 μM) are required (see Chapter 2) and the DNA signal remains relatively unperturbed.

When working with organic solvents in flow *LD* studies, the concentration of DNA, evaporation, viscosity and turbulence effects all need to be taken into account and the experimental set up adjusted accordingly (see Section 1.7).

1.3.4 Circular dichroism spectroscopy[4]

Circular Dichroism (*CD*) is defined as the difference in absorption *A* of left (A_l) and right (A_r) circularly polarised light. [4] *CD* probes the spectroscopy and structure of chiral or asymmetric molecules.

$$CD = A_l - A_r \qquad (1.8)$$

In technical terms, *CD* measures the difference in helical redistribution of electron density that occurs in chiral chromophores upon excitation with left or right circularly polarised light. The origin of the helical electron motion lies in the non-perpendicular and non-coplanar polarisations of μ, the electric transition moment and m, the magnetic dipole transition moment that is unique to chiral chromophores. Helical transitions are then a consequence of the linear charge displacement induced by the electric field vector of the exciting light, combined with the circular displacement of charge induced by the magnetic field vector of the exciting light.[4]

In simple terms, left and right circularly polarised light is passed through a solution, if the molecules are achiral there is no difference between the interaction with the two polarisations and there will be no signal on the spectra. If the molecule is chiral, a difference in the absorbance of the left and right light is seen and a *CD* signal results.

CD has been used to prove a chiral molecule has been synthesised, or resolved into pure enantiomers, or to probe the structures of biological marcromolecules *e.g.* protein conformational changes and the interaction of ligands with biomolecules. *CD* provides information about the spectroscopically active chiral species in solution. Thus achiral compounds will give a zero signal unless they are bound to a chiral molecule *e.g.* DNA, in this case an induced *CD* (*ICD*) signal is observed.

The *CD* spectrum of B-form ct-DNA (Figure 1.2(c)) above 190 nm is due almost exclusively to the π–π^* transitions of the nucleobases. The bases themselves are

achiral in isolation, however, due to a combination of their helical arrangement in space in duplex DNA (permitting electronic coupling between the transitions of adjacent bases) and their attachment to the intrinsically chiral deoxyribose sugar they produce a *CD* spectrum that is due to the convolution of all the transitions of the bases.[4] The form of the spectrum is dependent on both the base composition and conformation of the DNA being probed. Other DNA conformations also have characteristic *CD* signatures as variations in the precise relative orientations of the bases between the different polymorphs are reflected in the *CD* spectrum[4] (see Section 1.6 and Chapters 2 and 3).

Although in principle *CD* can be used to give geometric information about the observed species through a knowledge of transition moments,[4] in practice this is often very difficult and DNA-ligand spectra are normally interpreted empirically. *CD* is, however, usually the most sensitive spectroscopic technique for probing changes in binding mode as a function of concentrations and/or mixing ratios.[4] Any change in the behaviour of the system is reflected in the *CD* spectrum. A change in the intensity of the ligand *ICD* usually mirrors a change in the amount of bound ligand, whereas a variation in shape of the ligand *ICD* reflects a change in binding mode.

Although many DNA binding ligands are achiral, investigation of DNA-ligand interactions is still possible by *CD*. The bound ligand may perturb the structure of the host DNA resulting in a change in the *CD* signature of that DNA, and the ligand itself will acquire *ICD* enabling its transitions to be probed directly. The *ICD* originates from the coupling of the ligand transitions with those of the DNA bases or the imposition of a chiral conformation on the ligand by the DNA binding site.[4] The presence of *ICD* at the wavelength of an achiral ligand transition therefore implies DNA binding.

Stacking interactions between DNA bound ligands can also be detected in the *CD* spectrum. The occurrence of stacking interactions results in electronic coupling

between the ligand transition moments.[4] This coupling is apparent in the CD spectrum as anomalously large signals usually changing between positive and negative with the zero point at the absorption wavelength of the ligand transitions. This is commonly referred to as exciton *CD*. The strength of the coupling depends on the individual oscillator strengths of the coupled transition moments and their relative orientation and energies.

1.3.5 Fluorescence spectroscopy[11]

The emission (fluorescence or luminescence) of a compound results from the re-emission of radiation that was absorbed by a molecule. Atoms and molecules are excited by the absorption of electromagentic radiation. The excited species then relax to the ground state, giving up their excess energy as photons. The lifetime of an excited species is brief because there are several ways in which an excited molecule or atom can give up its excess energy and relax to its ground state, *e.g.* by non-radiative relaxation[12] (vibrational relaxation and internal conversion) and fluorescent relaxation (radiationless decay and fluorescence).

Fluorescence is one of several mechanisms by which a molecule returns to the ground state after it has been excited by the absorption of radiation. Thus all absorbing molecules have the potential to fluoresce, but most do not because their structure or environment provides radiationless pathways by which relaxation can occur at a greater rate than fluorescent emission. If an excited molecule can find no other way to lose energy it will fluoresce to its ground state. The extent to which a molecule is fluorescent is also determined by the environment to which the molecule is exposed. Fluorescence spectroscopy is useful as an interaction can lead to a change in the fluorescence properties of a ligand, *e.g.* octahedral $[Ru^{(II)}(bipy)_2(dppz)]^{2+}$ (where bipy is 2,2′-

bipyridine and dppz is dipyridophenazine) is termed a 'molecular light switch': the complex shows no luminescence in aqueous solution, but when bound to DNA it luminesces strongly. It is thought that this is because the hydrophobic environment of the intercalation site of dppz prevents fluorescence quenching by the solvent.[13, Chapter 2] Wavelengths shifts and quenching may also be observed in the ligand fluorescence spectrum if ligand–ligand interactions are occurring.

At low concentrations the fluorescence intensity is linearly proportional to the concentration of the fluorescent solute according to:

$$F = 2.3 I_0 \phi \varepsilon c l \qquad (1.9)$$

where F is the fluorescence intensity, I_0 is the intensity of the excitation source, ε is its molar absorptivity at the excitation wavelength ($mol^{-1}cm^{-1}dm^3$), l is the path length (cm), c its concentration (mol dm^{-3}) and ϕ is fluorescence quantum yield, (the number of molecules that fluoresce divided by the total number of excited molecules or equivalently, the ratio of photons emitted to photons absorbed; for highly fluorescent molecule, ϕ tends toward unity). The fluorescence signal is directly proportional to the concentration of the fluorophore so K, a binding constant can be determined. Because of this direct proportionality, the quantitative treatment of fluorescent binding data can be carried out in the same manner as that for absorption spectroscopy. However, the direct proportionality between F and c is lost when the latter becomes high enough that more than a few percent of the incident radiation is absorbed. This is the result of self-quenching in which the analyte molecules absorb the fluorescence produces by other analyte molecules.

1.3.6 Mass spectrometry

Mass spectrometry is a powerful tool for the rapid identification and quantification of small amounts of unknown compounds.[5] Mass spectrometry requires that the complex of interest is charged. This can be achieved by a number of methods.[14,15] It can provide information about the molecular mass of a compound. A range of mass spectrometric (MS) techniques have been used in this work. It is usual under the conditions of many MS experiments for fragmentation of the molecule to occur, resulting in the formation of fragment ions. Thus it is possible to determine which ligands or groups of atoms are bonded together from the way the compound breaks up or fragments.

Mass spectrometry (MS) has recently extended to the analysis of large molecules, *e.g.* proteins, enlarging its application in the biochemical field with the development of soft ionisation techniques[5,14] including electrospray ionisation.[15] Electrospray ionisation (ESI) is not a real ionisation process (*i.e.* conversion of neutral molecules to ions). It is the transfer of species, ionised in the condensed phase into the gas phase as isolated entities.[15] This method does not destroy compounds and can often retain non-covalently bound complexes[15] as the principle function of the electrospray interface is the disruption of the non-covalent interactions between compound and solvent molecules. Ions attributable to non-covalently bound species have been observed in electrospray mass spectra suggesting the presence of associations much stronger than between compound and solvent.[15]

The few ESI-MS experiments reported in this thesis were run on a Bruker BioTOF mass spectrometer. The di-sodium salts of the 5′-nucleotides and methyl guanine were used and investigated in positive mode.

1.4 Inorganic metal complexes

1.4.1 Inorganic chemistry in biological systems [16-18]

There are approximately thirty essential elements that are indispensable to some form of life. Carbon, hydrogen, nitrogen and oxygen make up 99% of the human body. Other essential elements play a vital role in the human body, *e.g.* calcium, fluorine and phosphorus are important in the construction of healthy teeth and bones, iron is necessary for the transport and storage of oxygen, respiration and cell division. An imbalance of elements can lead to numerous illnesses and diseases, *e.g.* an excess of manganese can lead to psychiatric disorders, a deficiency of magnesium can lead to convulsions.

Other non-essential elements have been found to be important and are used in medicine. 'Metallodrugs'[17] containing gold have been used for years to treat arthritis, copper is used in the treatment of rheumatism and as an anti-inflammatory agent and lithium is used in psychotropic drugs as an anti-depressive.[18] Newer drugs containing elements such as bismuth and antimony have been found to have anti-ulcer and anti-parasitic properties respectively. Perhaps the most well known coordination complex used in therapeutic applications is cisplatin, an anticancer agent. Metal complexes made up of manganese(II) and barium and also some lanthanides especially gadolinium(III) are also being used as diagnostic agents in MRI (magnetic resonance imaging) in the detection of diseases. [16-18]

Undeniably, inorganic chemistry plays a large role in biological and bio-medical processes, with applications in medicine in the treatment, management and diagnosis of disease. Advances in and understanding coordination chemistry can and are leading to the design of new complexes with potential applications in the treatment of a variety of illnesses and diseases.

1.4.2 Coordination chemistry as a tool for supramolecular chemistry

Nature uses self-assembly processes in a variety of ingenious ways to construct large and ordered molecular arrays such as proteins and other biomolecular structures which exhibit an exquisite specificity in their molecular recognition properties. Most self-assembly processes in nature use the many weak, non-covalent interactions found between pre-formed sub-units or well defined assemblies to guide the formation of a structure. The assembly of the tobacco mosaic virus (TMV) is an excellent example of molecular recognition and self assembly in nature (Figure 1.5).[19]

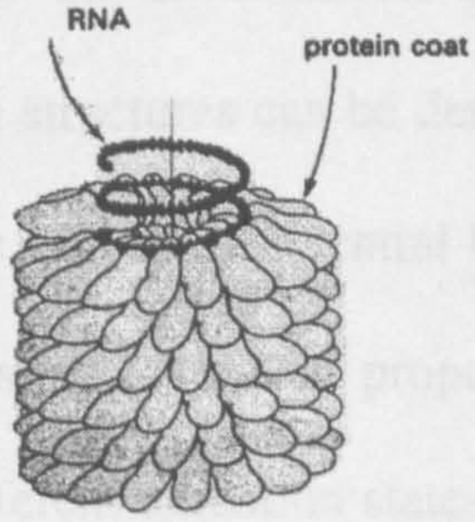

Figure. 1.5 A schematic diagram of a tobacco mosaic virus particle. It is 300 nm in length, 18 nm in diameter and is composed of approximately 2130 identical subunits that self assemble to form a helical sheath around a single strand of RNA, 6390 base pairs in length, through non-covalent interactions. (Diagram taken from reference 19)

The last few years have seen the emergence of self-assembly as a promising approach to the generation of *synthetic* compounds with large, rigid, molecular-sized cavities.[19–22] This approach, combined with an understanding of the coordination chemistry of metal ions and their structural role in the spatial arrangement of a wide range of ligand complexes have been incorporated into a new type of chemistry — supramolecular inorganic chemistry.

Supramolecular chemistry [23–25] can be defined as a highly interdisciplinary field of science covering the chemical, physical, and biological features of self-assembling chemical species held together by organised non-covalent binding interactions. Supramolecular (intermolecular) interactions are at the foundation of highly specific

biological processes, and together with molecular recognition processes play roles of vital importance. Examples of this include the fact that resistance to disease relies on the presence of antibody molecules which recognize and combine with specific molecules on the surface of an invading organism; the substrate binding by enzymes or receptors; the intercalation complexes of nucleic acids; and cellular recognition (immunology).[26] Coordinate metal-ligand bonds possess partial covalent character, but like many supramolecular interactions are frequently labile (especially first row transition metals) and are distinct in nature from traditional covalent bonds (e.g. C–C or C–H).

An increase in awareness of the coordination chemistry of specific metals, together with (i) the ease with which structures can be designed and synthesised to self assemble (*i.e.* the number of ligands added, or potential binding sites can be carefully controlled), (ii) the fact that cavity size, shape and properties can be altered by using different ligands and metals with different oxidation states, and (iii) the development of new innovative, inexpensive approaches[1] has led to metals now being a key feature in the formation of supramolecular structures. Chapter 4 reports the investigation of the molecular sensor potential of novel self-assembling copper(I) supramolecular cyclophanes with small aromatic compounds, and includes the synthesis of a new ligand capable of self assembling into a box structure. Chapter 2 reports on the DNA binding properties of novel octahedral bis-terpyridine ruthenium(II) complexes with potential intercalating functionalities. Chapter 3 investigates the DNA binding properties of a number of novel square planar platinum(II) complexes with subtly different electron withdrawing/donating functionalities with possible anti-cancer therapeutic potential.

1.5 Molecular interactions

Molecules can interact covalently (bond forming) or non-covalently.[27–30] Covalent interactions are short range chemical interactions arising from electron sharing. Non-covalent interactions are generally weaker. An understanding of the nature of non-covalent interactions is useful, especially since these interactions are fundamental to many of the biomolecular processes involving recognition, binding and self-assembly found in nature.[28, 31] Examples of non-covalent interactions are the formation of duplex DNA and the assembly of supramolecular systems. The five main types of non-covalent interactions are: electrostatic interactions, hydrogen bonding, π-π interactions, hydrophobic/hydrophillic and van der Waals forces. Electrostatic interactions can be defined to include charge-charge, dipole-dipole, dipole-induced dipole *etc.* The strongest of these is charge-charge. It dominates the binding when cationic molecules bind to DNA though the other kinds of interactions may be more important for determining the binding mode and the relative binding strengths within classes of molecules.

Hydrogen bonding is an example of predominantly electrostatic interaction between molecules. A hydrogen bond involves the sharing of a hydrogen atom between one atom that has a H atom (donor) and another atom that has a lone pair of electrons (acceptor). The hydrogen can be bonded formally (covalently) to one atom (the donor, D) and still interact favourably with another (the acceptor, A) due to strong dipole-dipole attraction caused by the electron withdrawing properties of the more electronegative atom (e.g. F, N, O) attracting electrons from the hydrogen. Schematically it may be illustrated as:

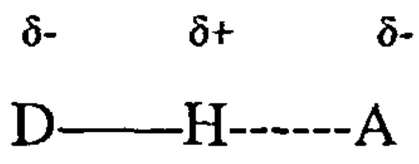

H-bonding interactions are directional, in other words they are strongest when linear, and the distance between acceptor and donor atoms is typically ~ 2.8 Å.[28] A hydrogen bond has approximately a tenth of the strength of the covalent bond, with the strongest (and shortest) hydrogen bonds produced from electronegative or charged acceptors or donors. Hydrogen bonds in DNA-ligand systems typically occur between a hydrogen that is covalently attached to a N or O (hydrogen donor) and a N or O donor with a partial negative charge (H acceptor).

Aromatic rings can interact favourably in either face-to-face or face-to-edge orientations (Figure 1.6). This is because the π electrons of an aromatic system are localised above and below the plane of the ring giving the aromatic ring face a small net negative charge (electron rich region) and the ring hydrogens a small positive charge (electron deficient region). In the face-to-face interaction (Figure 1.6(a)), referred to as π stacking, the rings sit on top of each other but due to the electrostatic interaction, in a slightly offset arrangement. The face-to-edge interaction (Figure 1.6(b)) is also sometimes described as a C–H---π interaction. Electron rich atoms (high electron density) interact with the ring edges whereas electron deficient groups (*e.g.* protonated amino groups) interact favourably with the ring face.[28,30]

(a) (b)

Figure 1.6 (a) Offset face-to-face stacking and (b) face-to-edge stacking, taken from reference 30.

London dispersion interactions, or van der Waals interactions, are long range interactions that occur between atoms. Weak attractive London dispersive forces arise as a result of induced charge separation, polarization of the electron clouds as two

molecules approach each other, leading to temporary dipole-induced dipole interactions. This weak attractive force increases as the distance between atoms is decreased up to a particular point, the van der Waals contact distance (~ 3.75 – 2.5 Å). Closer contact between atoms results in repulsion (electrostatic charge-charge repulsions between the adjacent electron clouds) between the two atoms becoming dominant. This force is important as it can be considered as the force that stops matter collapsing in on itself.[28]

As with all non-covalent interactions the medium (solvent, solutes *etc.*) exerts a considerable influence on interactions.

Hydrophobic interactions are due to the very low solubility of non polar molecules in polar media *e.g.* water. A polar compound is able to organise favourable H bonding interactions with the polar water molecules but non-polar molecules are unable to this — disrupting the hydrogen-bonding network resulting in an unfavourable re-ordering of the hydrogen bonding network. This interaction between water and a non-polar molecule/fragment is termed a hydrophobic interaction. In general, polar molecules (*e.g.* water) interact poorly with hydrophobic (*i.e.* non polar) molecules or molecular regions. Hydrophobic molecules therefore tend to aggregate and 'squeeze out' water from the interacting faces of the hydrophobic molecules, so that overall less surface is exposed to aqueous solution. This minimal surface requires less reordering of hydrogen bonding interactions in water and is more favourable, thus the hydrophobic interactions describe the tendency of non-polar groups to associate when in polar environments. Hydrophobic guests are thus more likely to interact with hydrophobic hosts, thus this hydrophobic interaction may be major driving force for molecular association. This is an important non-covalent interaction in biological terms.[32]

Non-covalent interactions can occur over the whole structure unlike limited covalent localised bonds. A large number of these interactions are necessary for

stability. Many weak interactions are needed to provide the strength of one covalent bond — therefore any recognition events will be highly specific and any biomolecular interactions are readily disrupted by changes in environment, such as pH, temperature and concentration.[28]

1.6 DNA

DNA— deoxyribonucleic acid — is present in all living things, large and small. It is arguably the most complex structure and we are only just beginning to understand it. An indication of the complexity of the molecule is the fact that the DNA in the human haploid genome (the total genetic message) is made up of 3×10^9 base pairs.[33]

DNA is responsible for the maintenance of the species, it passes from one generation to the next in germ cells. It also carries the information to enable all proteins required for the operation of biological systems to be synthesised. The genetic message is encoded by the sequence of purine and pyrimidine bases in the nucleotide chains. Three nucleotides specify a single amino acid in the ultimate protein product. The text of the message is the order in which the amino acids are lined up in the proteins manufactured by the cell.

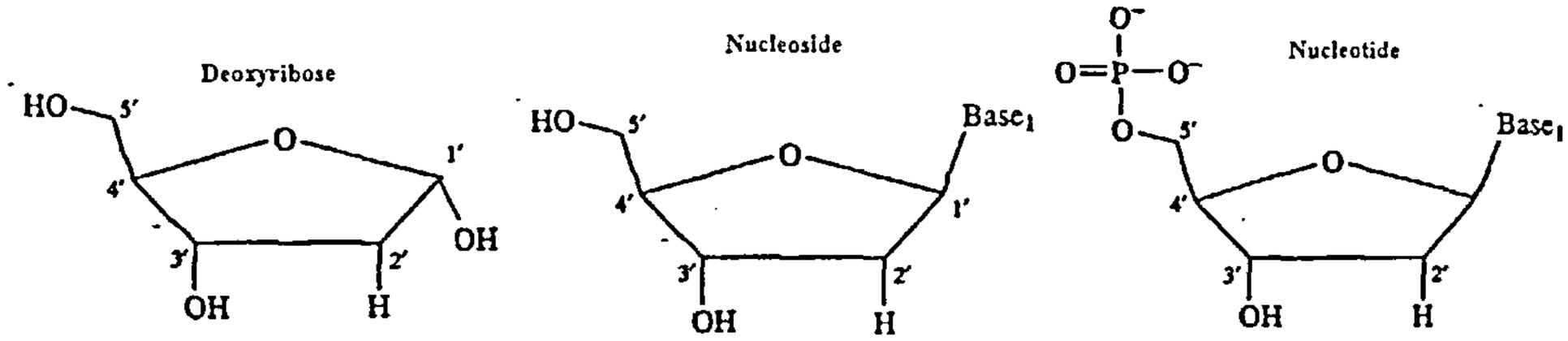

Figure 1.7 The general structure of deoxyribose, a nucleoside and a nucleotide

DNA consists of two complementary polymer strands that intertwine to give a double helix running in anti-parallel directions.[31,34–36] Each strand is made up of a series

of units called nucleotides. A nucleotide is made up of a sugar (deoxyribose for DNA), a phosphate and base (Figure 1.7). There are four different types of nucleotides in DNA, these share the same sugars and phosphates but have different bases attached to them. These bases are planar aromatic nitrogen-containing heterocyclic molecules. They are the purines, adenine (A) and guanine (G), and the pyrimidines, thymine (T) and cytosine (C) (Figure 1.8).

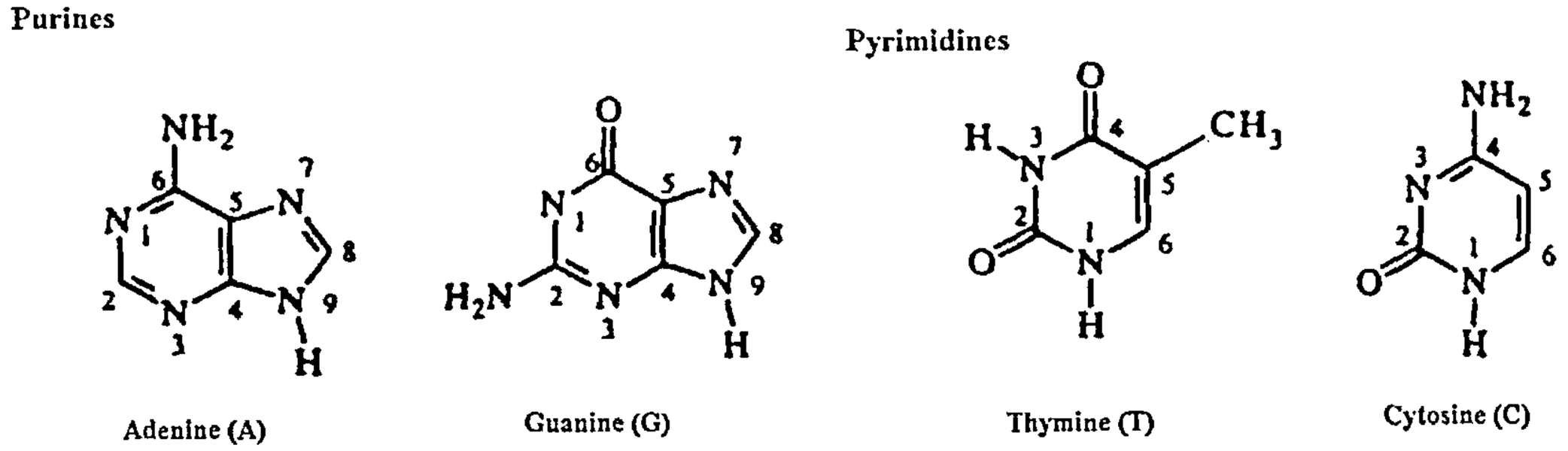

Figure 1.8 The purines adenine(A) and guanine (G) and pyrimidines thymine (T) and cytosine (C)

A base attached to a sugar (a nucleoside) is formed by connecting the N9 of the purine or the N1 of the pyrimidine bases to the C1′ position of the deoxyribose. These nucleosides are linked to one another with a certain directionality *i.e.* through phosphate groups attached to the 5′ hydroxyl group and the 3′ hydroxy group of adjacent sugars [34] to form nucleotides as shown in Figure 1.9.

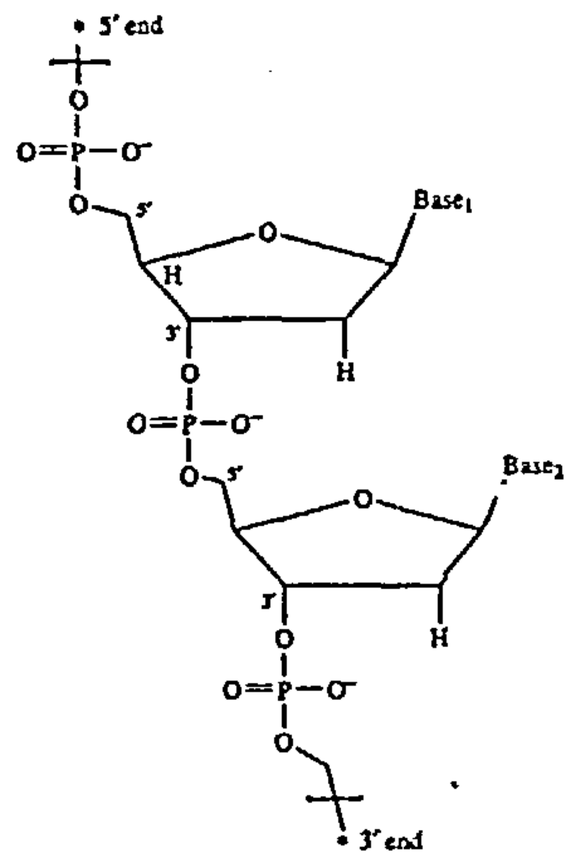

Figure 1.9 Directionality of the nucleotides 5′ to 3′ on a flexible phosphate chain

Using the Watson Crick rules for base pairing,[34–36] the four different bases form specific pairwise interactions: A with T forming two hydrogen bonds and G with C forming three hydrogen bonds (see Figure 1.10). The bases are attached to a flexible sugar phosphate chain. The DNA strands associate by the hydrogen bonding between these planar base pairs. The base pairs are not necessarily planar: they can twist and roll, or in a base pair they can propeller twist or buckle.[4,34, 35]

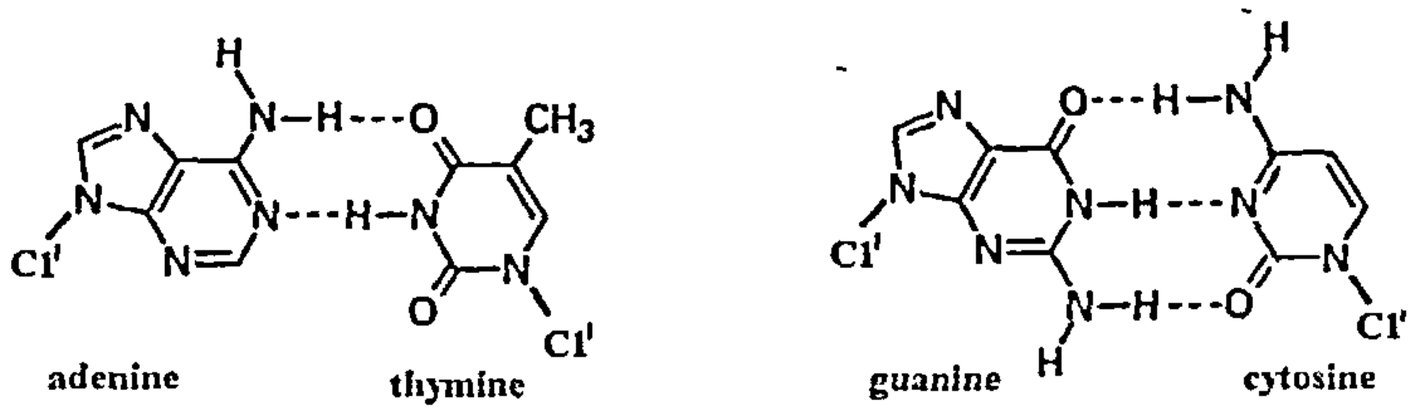

Figure 1.10 The four different bases of DNA showing Watson-Crick hydrogen bonding between the pairs that join the two strands of DNA together. C1' denotes connection to the sugar

As the base pairs are hydrophobic they tend to tuck themselves away from water by stacking on top of each other creating a non-polar interior in the double helix. This leads to the DNA forming a helix with a given number of bases per turn. The DNA double helix is therefore stabilised by this hydrophobic action.

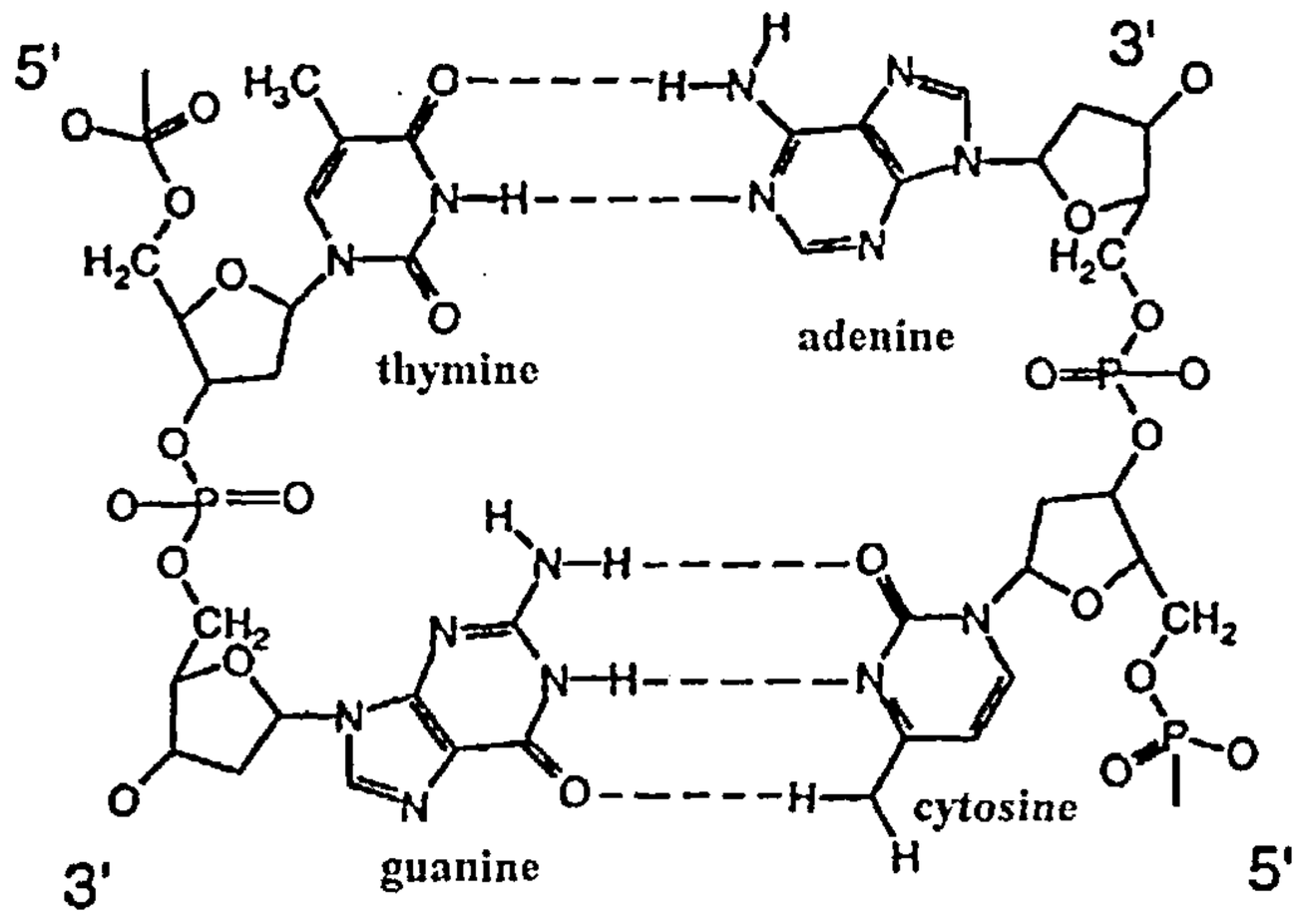

Figure 1.11 A portion of the structure of double stranded DNA showing the hydrogen bonding interactions. Diagram reproduced from *reference 4*

The hydrogen bonds also contribute to the overall stability of the double helix but their main function is the specificity for forming the correct base pairs.[35] The phosphate backbone is negatively charged, and as such the phosphates tend to repel each other. This repulsion can destabilise the DNA double helix. High ionic strength (high salt concentration) shields the negatively charged phosphates from each other, thus decreasing the repulsion and stabilising the double helix, similarly, cationic molecules can stabilise DNA.

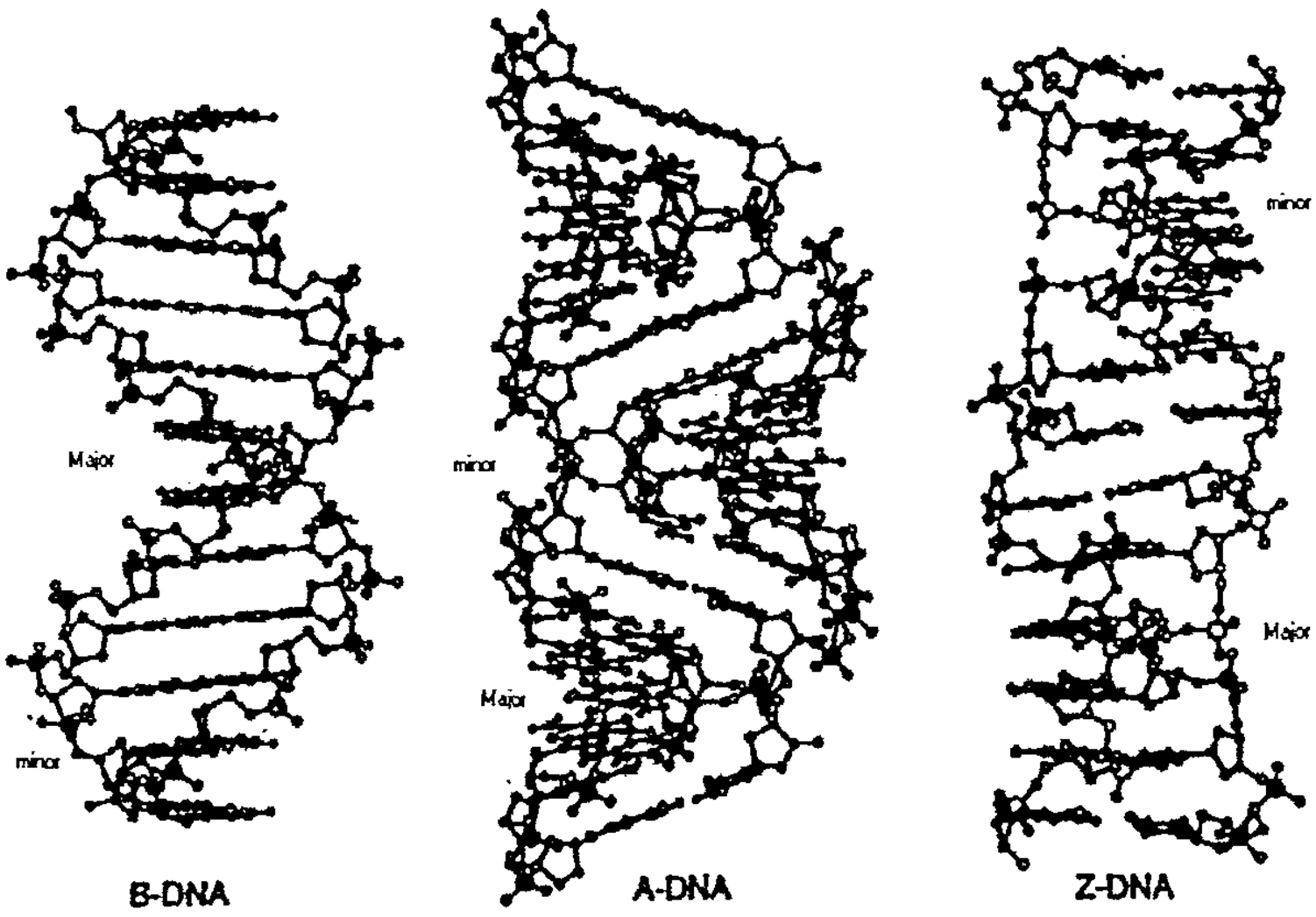

Figure 1.12 Double helical structures of B, A and Z DNA. Note the major and minor grooves are indicated. Picture *reproduced from reference 4.* See Tables 1.1 and 1.2

A number of different conformations of double helical DNA can be formed by rotating various bonds.[34,35] The structures of A-DNA, B-DNA and Z-DNA are shown in Figure 1.12. DNA under physiological conditions is generally assumed to be in a B-type conformation.[34] The B-form ct-DNA used in this work is made up of 42% AT and 58% GC.

B-DNA and A-DNA are right handed with 10 and 11 bases per turn respectively, Z-DNA is left handed with 12 bases per turn. A and B conformations differ in pitch (how much the helix rises per turn). Z-DNA is a left handed helical form of DNA in which the phosphate backbones of the two antiparallel DNA strands are still

arranged in a helix but with a more irregular appearance (see Table 1.1). The conformation of DNA (A, B and Z) depends on temperature, salt concentration, as well as base composition of the DNA. Structural changes from A to B forms in mixed sequence DNA are induced by changes in the relative humidity of the surroundings.[31, 34, 35]

Table 1.1 Groove dimensions in DNA double helices [4,34]

Parameters	B-DNA	A-DNA	Z-DNA
Bases / turn of helix	10	11	12
Major groove	wide and deep	narrow, deep	flat
Minor groove	narrow, deep	broad, shallow	narrow, deep

Table 1.2 Groove dimensions in DNA double helices [4,34]

	Major groove		Minor groove	
DNA	Width (Å)	Depth(Å)	Width (Å)	Depth(Å)
A	2.2	13.0	11.1	2.6
B	11.6	8.5	6.0	8.2
Z	8.8	3.7	2.0	13.8

The arrangement of the double helix is such that there are two distinguishable grooves running the length of the DNA: the major and the minor groove. For B-DNA, the major groove has a width of ~12Å and a depth of ~8 Å; the minor groove 6 Å and 8 Å respectively (see Table 1.2).[34] This means that only thin molecules, that can twist can interact with the minor groove whereas much larger molecules can interact with the major groove. The grooves are of different sizes because the two strands come together through the bases that attach to the phosphate backbone at an angle that is not 180° apart around the axis of the helix. Many sequence specific interactions of the proteins with DNA normally occur along the major groove, because the bases (which contain the sequence information) are more exposed along this groove.

1.6.1 Duplex formation determined using melting curve experiments

When duplex DNA is heated, it can lose its helical structure as the two strands separate, this action is termed denaturation and is shown by an increase in absorbance at 260 nm as the bases unstack — termed a hyperchromic shift. When the same DNA is slowly cooled, the two strands should come together again — reanneal — to form the duplex through hydrogen bonding and hydrophobic interactions. The decrease in absorbance at 260 nm is termed a hypochromic shift. In practice ct-DNA is too complicated to reanneal correctly. A typical melting curve takes the form of an S - shaped absorbance plot (this is characteristic of the double to single stranded transition). If the DNA is not duplex, and does not either denature on heating nor reanneal on cooling, its absorbance will change very little with temperature. Melting curve experiments can be used to determine whether a given type of DNA is duplex under a given set of conditions. They can also be used as an estimate of ligand binding strength, since stronger binders stabilise duplex DNA more effectively.

1.6.2 Binding modes with DNA ligands

There are a number of ways in which metal complexes, which are usually cationic can interact with the polyanionic duplex DNA. [31,34] These include (i) major or minor groove binding, (ii) intercalation — where a planar molecule slips between the base pairs (into a hydrophobic environment) and leads to unwinding of the DNA, (iii) external binding to the phosphate backbone (this is usually non-specific, electrostatic binding), (iv) covalent binding inter / intra strand binding i.e. *inter* between two strands, *intra* on same strand — usually to the guanine N7.

Molecules bind to DNA by recognising structural features of the DNA. The difference between binding in the major and minor groove binding is due to hydrogen

bonding characteristics, electrostatic potential, solvation and steric effects.[34] Hydrogen bonding is fundamental in the recognition of target binding sites.[34] The edges of the bases have hydrogen bonding potential for ligand binding. Both the major and minor grooves of B-DNA and the different bases present numerous H-bonding donor and acceptor sites at which specific interactions may occur.[31,34,35] Figure 1.13 indicates the directionality of the hydrogen bonds. The minor groove contains hydrogen bond acceptors at N3 on adenine and guanine, O2 on thymine and cytosine, with the amino group of guanine at C2 acting as a hydrogen bond donor. In the major groove, N7 on guanine and adenine, O6 on guanine and O4 on thymine can act as H bond acceptors and the amino groups at C6 on adenine and C4 on cytosine as potential H bond donors.

Hydrogen bonding can be accepted to the N3 of adenine but the C2 amino group of guanine presents a steric block to hydrogen bond formation at N3 of guanine and at C2 carbonyl of cytosine (Figure 1.13). This is because the hydrogen bond between the amino group of guanine and the carbonyl oxygen of cytosine in GC pairs lies in the minor groove and sterically inhibits penetration of molecules into this groove in GC rich regions.

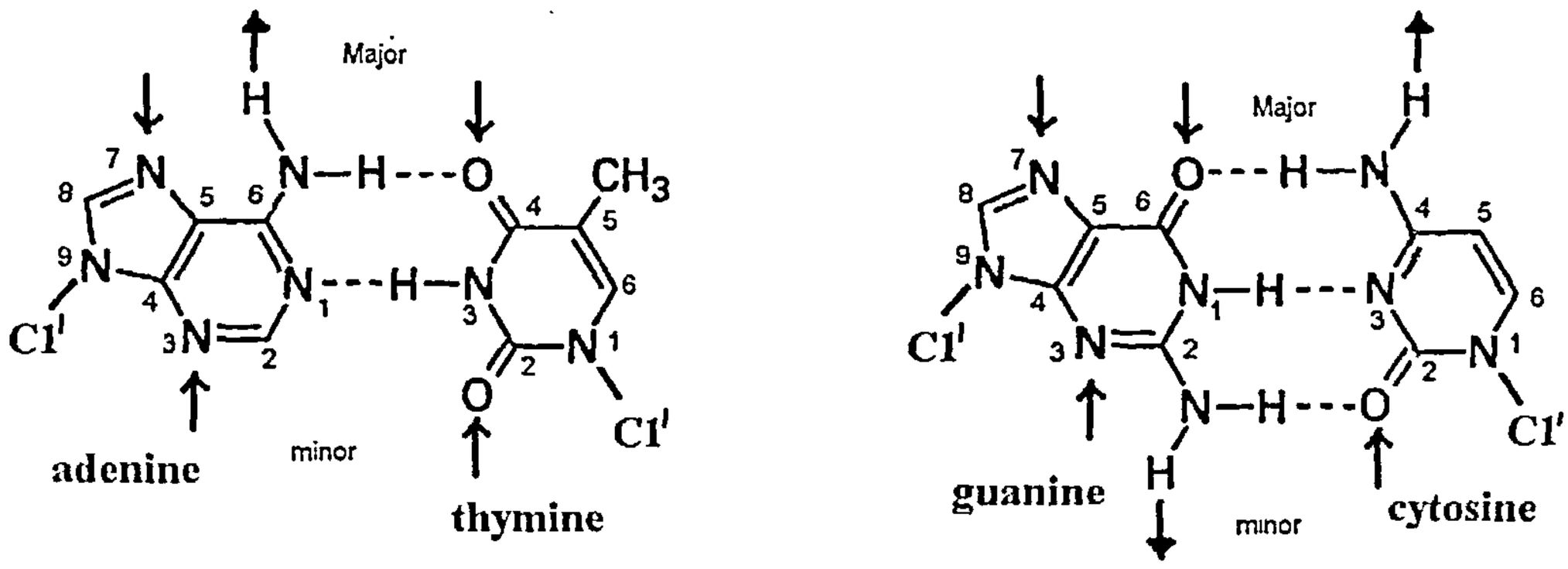

Figure 1.13 The arrows indicate the directionality of the hydrogen bond donors and acceptors in A-T and G-C base pairs; *major and minor indicate respective grooves.* [34]

Metal complexes can interact with DNA[31,34] by (i) covalent or (ii) non-covalent binding interactions. Most covalent interactions take place with non-specific binding to the phosphodiester backbone or sugar residues, *e.g.* DNA strand scission.[34] The recent main emphasis for covalent binding has been on the recognition of particular sites on DNA by nucleophilic reactions. Purines are most susceptible to covalent attack, with guanine preferred over adenine. This is because the pyrimidine bases are less aromatic than the purines, the latter are more electron rich. Guanine N7 is the most electron rich site on DNA and is the most easily oxidised. It is also mainly the N7 on the G and N7 on A in the major groove that are exposed to the solvent, and are considered to be general binding sites, they are electron rich and are surrounded by negative charge of the phosphate groups. Particular sites for covalent binding are N7, N6 and O6 in the major groove and N2 in the minor groove. Metal complexes, can bind to either one or two sites at once forming a crosslink. This crosslinking binding mode can be *intra- or interstrand* (on the same strand, or between two strands) depending on the distance between the two functional groups on the drug and on the affected DNA sequence. The best known example of this is cisplatin, which binds covalently to guanine, and is known to bind intra and interstrand depending on the positions of the guanines.

1.7 Studies on organic solvents with DNA

In the work reported in this thesis, it has been necessary to use organic solvents to get some of the metal complexes into solution. It is essential that the solvent chosen provide a good spectroscopic window, does not interact with the complex in an unfavourable fashion (spectroscopy is dependent on solvent environment) and most importantly does not change the structure of the DNA. The use of non-aqueous solvents may also be advantageous in drug delivery terms (see Chapter 3). Organic solvents are

not commonly used with DNA, as the presence of organic solvents can lead to a change in the conformation of DNA and/or the break up of the DNA duplex. It was therefore crucial to determine the extent to which DNA can tolerate organic solvents.

1.7.1 Organic solvent tolerance of DNA

Absorbance and *CD* and melting curve studies were conducted to determine the solvent tolerance limits of ct-DNA with acetonitrile (MeCN), N,N-dimethylformamide (DMF) and dimethylsulfoxide $(Me)_2SO$ (DMSO). Ct-DNA is made up of 42 % AT and 58 % GC. It is a long DNA that is fairly robust. Therefore, it was expected to be more stable than the shorter synthetic DNAs: poly[d(A-T)]$_2$ and poly[d(G-C)]$_2$ referred to as AT and GC DNA respectively.

Experiments on ct-DNA with and without sodium cacodylate buffer (NaCac) were primarily investigated. The absorbance and *CD* spectra can be found in Appendix 1. From this study, maximum organic solvent limits of 70% acetonitrile and 10% DMF or DMSO were set when working with ct-DNA (see Table 1.3). At or below these stated percentages, the *CD* spectrum of the DNA was found unchanged indicating its structure was standard B-form The absorbance spectra of ct-DNA with MeCN remained approximately constant up to a 80% MeCN v/v, whereas the spectra of ct-DNA with DMSO and DMF did not, showing an immediate increase in absorbance on solvent addition. This increase indicates an unwinding of the DNA helix.

Table 1.3 The percentage organic solvent that can be used with ct-DNA without any significant spectroscopic structural change in the DNA

	Without buffer / % solvent		With buffer / % solvent	
	CD	Absorbance	*CD*	Absorbance
MECN	70%	80%	70%	70%
DMF	10 – 20%	-	20 – 30%	10 – 20%
DMSO	10 – 20%	-	20 – 30%	10 – 20%

AT and GC DNA were also investigated with acetonitrile, the solvent of choice for Chapter 3, without salt or buffer. Melting curve experiments showed that the DNA was not remaining duplex. An inconsistent change in absorbance as temperature was increased and little or no decrease in absorbance on cooling (not shown) was thought to be due to the acetonitrile disrupting the hydrophobic and hydrogen bonding interactions between the base pairs leading to an increase in the ability of the bases to tilt and slide around or the loosening or breaking of base pair hydrogen bonding interactions in favour of other hydrogen bonding interactions (*e.g.* with solvent). This resulted in both AT and GC DNA being unable to reanneal.

Therefore when using MeCN, salt (NaCl) and buffer (a constant 1 mM sodium cacodylate buffer) were required to ensure AT and GC DNA duplex conformation. The amount of salt and sodium cacodylate buffer required was found to be dependent on the percentage organic solvent present and are summarised in Table 1.4. This was confirmed under experimental conditions.

Table 1.4 Salt (NaCl) requirements determined for AT and GC DNA using a 1 mM NaCac buffer

	Minimum requirements	≤ 40% MeCN	≥ 40% MeCN
AT-DNA	30 mM NaCl	30 – 40mM	30 mM, > 60% 40 mM
GC DNA	10mM NaCl	10 mM	20 mM

GC DNA shows more stability with acetonitrile than AT DNA hence the need for less salt and buffer. This is attributable to its stronger hydrogen bonding interactions (three hydrogen bonds) compared to those for AT DNA (two hydrogen bonds).

1.7.2 Organic solvents in film *LD*.

Film *LD* of organic soluble complexes proved difficult to measure due to the different solvent requirements of the complexes and polyvinyl alcohol (PVA). See Section 1.3.3.1. The possibility of using a 50:50 v/v water:organic solvent to make up a

film for *LD* experiments proved impossible as the PVA immediately precipitated out of solution.

The alternative and ultimately the method used involved the preparation of a water based film and limiting the organic solvent addition to complex sample introduction. That is, addition of sample (in this case of a volume of 200 μL of complex) in organic solvent mix ratios of up to 50:50 water:DMSO; 50:50 water:MeCN and 90:10 water:DMF to a water based PVA solution could be tolerated. The blank film was also prepared using an equal volume of organic solvent.

1.7.3 Flow LD with organic solvents.

When working with organic solvents in flow *LD* studies, the concentration of DNA, evaporation, viscosity, turbulence effects all need to be taken into account and adjusted accordingly. The use of organic solvents in flow *LD* studies of DNA can cause a reduction in viscosity, an increase in turbulence and DNA signal-scattering, and leads to evaporation. The use of MeCN, in this case in combination with water, was found to be more prone to evaporation than when working with water alone, leading to signal errors. The use of a cell covering (in this case parafilm) to limit evaporation with a higher minimum cell volume of 2000 μL was found to be sufficient in order to avoid baseline errors, as was a slower couette rotating speed. Additionally, the use of an organic solvent (MeCN) leads to a decrease in the overall viscosity of a solution, but using too high a rotating speed can lead to turbulence and spillage or evaporation. Therefore a lower speed than used for aqueous samples was found necessary. However, too low a speed can lead to problems as reduction in speed reduces the *LD* signal especially of shorter DNA sequences (see Table 1.5). Each time the rotating speed was changed a baseline *LD* of solvent mix was measured to avoid baseline errors.

The number of scans taken for each titration step (*LD* measures the average signal of bases) also affects the signal quality. Furthermore, shorter DNA are prone to having larger noise/scattering effects. A minimum of 8 scans was found to be ideal, a larger number of scans led to noticeable solvent evaporation and signal deterioration. It was necessary to experiment and compromise on signal size, quality and noise. An option would be to work at higher DNA concentrations, but limited sample availability precluded this course of action.

The flow *LD* signal of ct-DNA is large enough to compensate for the effects of using MeCN. The DNA signal of the shorter synthetic GC duplex (~750 base pairs) and AT DNA is on average much smaller and here the effects were found to be much more noticeable. GC DNA was found to be much less viscous than ct-DNA at similar concentrations. This led to greater difficulty in achieving a reasonable signal, as well as a decrease in signal-to-noise ratio relative to ct-DNA. More scans or the use of higher concentrations were necessary. *LD* studies of AT DNA were not undertaken, the AT DNA does orientate, but the flow *LD* signal was considered too small even before the addition of potential ligand binding agent which may cause an increase or decrease in signal size.

Table 1.5 Flow *LD* signal size of duplex DNAs ct-, GC and AT DNA

duplex DNA/ (concentration)		Flow *LD* signal size at 260 nm/ ΔOD
Ct-DNA	(100 μM)	~ -0.01
GC DNA [a]	(200 μM)	~ -0.003 30 mM NaCl + 1 mM NaCac buffer
AT DNA [b]	(200 μM)	~ -0.0005 30 mM NaCl + 1 mM NaCac buffer

a = The *LD* signal of GC-DNA (at the same concentration and conditions) is itself small when compared to the signal size of ~0.01 for a lower concentration solution of ct-DNA (100 μM)

b = AT DNA does orientate but its *LD* signal at 260 nm has a distinct negative maxima of ~0.0005 for a ~200μM (30mM salt + 1mM buffer) solution, this is before the addition of any metallo complex which may increase or decrease the size.

1.8 References

1. M. J. Hannon, C. L. Painting, A. Jackson, J. Hamblin and W. Errington, *Chem Commun.*, 1997, 1807.

2. D. C. Harris, *Quantitative chemical analysis*, 4th Ed., New York: W. H. Freeman, 1995, p124

3. R. M. Silverstein, G. C. Bassler and T. C. Morrill, *Spectrometric Identification of Organic Compounds*, John Wiley & Sons Inc., 1991, 5th Ed.

4. A. Rodger and B. Nordén, *Circular Dichroism and Linear Dichroism*, Oxford University Press, 1997 and references therein.

5. D. J. Holme and H. Peck, *Analytical biochemistry*, Longman, 1998, 3rd Ed., p 36

6. D. H. Williams and I. Fleming, *Spectroscopic methods in Organic chemistry*, McGraw Hill, 1995, 5th Ed.

7. A. K. Brisdon, *Inorganic spectroscopic Methods*, Oxford University Press, 1998

8. D. F. Shriver, P.W. Atkins and C. H. Langford, *Inorganic Chemistry*, Oxford University Press, 1990

9. B. Nordén, M. Kubista and T. Kurucsev, *Q. Rev. Biophys.*, 1992, **25**, 51

10. C. Hiort, B. Norden and A. Rodger, *J. Am. Chem. Soc.*, 1990, **112**, 1971

11. G. G. Guilbault, *Practical Fluorescence. Theory, Methods, and Techniques*, New York and Basel, 1973.

12. D. A. Skoog, D. M. West and F. J. Holler, *Analytical Chemistry*, Saunders College Publishing, 1994, 6th Ed.

13. C. Hiort, P. Lincoln, B. Nordén, *J. Am. Chem. Soc.*, 1993, **115**, 3448

14. J. R. Chapman, *Practical Organic Mass spectrometry: A guide for Chemical and Biochemical Analysis*, Wiley, 2nd Ed.

15. S. J. Gaskell, *Journal of Mass Spectrometry*, 1997, **32**, 667

16. Z. Guo and P. J. Sadler, *Adv. Inorg. Chem.*, 2000, **49**, 183

17. Z. Guo and P. J. Sadler, *Angew. Chem. Int. Ed.*, 1999, **38**, 1512

18. P. C. Wilkins and R. G. Wilkins, *Inorganic Chemistry in Biology*, Oxford University Press, 1997.

19. D. Philp and J. F. Stoddart, *Angew. Chem. Int. Ed. Engl.*, 1996, **35**, 1154.

20. M. M. Conn and J. Rebek Jr, *Chem Rev.*, 1997, **97**, 1647.

21. C.A. Hunter, *Angew. Chem. Int.Engl.*, 1995, **34**, 1079.

22. B. Linton and A. D. Hamilton, *Chem. Rev.*, 1997, **97**, 1669.

23. J. -M. Lehn, *Angew. Chem. Int. Ed. Engl.*, 1990, **29**, 1304.

24. J. -M. Lehn, *Angew. Chem. Int. Ed. Engl.*, 1988, **27**, 89.

25. C. Seel and F. Vogtle, *Angew. Chem. Int. Ed. Engl.*, 1992, **31**, 528.

26. F. Vogtle, *Supramolecular Chemistry*, Wiley, Chichester, New York, 1993

27. P. W. Atkins, *Physical Chemistry*, Oxford University Press, 1990, 4th Ed.

28. L. Buckberry and P. Teesdale, *Essentials of Biological Chemistry*, John Wiley and Sons Ltd, 2001

29. J. W. Steed and J. L. Atwood, *Supramolecular Chemistry*, Wiley, 2000

30. C. Hunter, *Chem. Soc. Rev.*, 1994, **23**, 101

31. G. M. Blackburn and M. J. Gait, *Nucleic acids in Chemistry and Biology*, Oxford University Press, 1997, 2nd Ed.

32. K. A. Connors, *Binding Constants: The measurement of molecular complex stability*, John Wiley and Sons, 1987

33. W. F. Ganong, *Review of Medical Physiology*, Appleton and Lange, Prentice Hall International Inc., 1993, 16th Ed.

34. S. Neidle, *DNA structure and recognition*, ed. D. Rickwood, Oxford University Press, 1994

35. C. R. Calladine and H. R. Drew, *Understanding DNA: The molecule and how it works,* Academic Press: Cambridge, 1997, 2nd Ed.

36. J. D. Watson and F. H. C. Crick, *Nature*, 1953, 737

2 DNA binding of aryl substituted ruthenium bis-terpyridine complexes

2.1 Introduction

There is an extensive literature on ruthenium(II) transition metal complexes and their binding to DNA. In particular there has been a drive to design intercalating metal complexes. Sometimes the complexes are designed for their own properties, but often it is because the ruthenium analogue of complexes of other metals (such as rhodium) binds in the same geometry to DNA but is chemically stable so can be used to identify DNA binding modes of more reactive species. In this project, five novel ruthenium(II) *bis*-terpyridine chloride complexes with potentially intercalating aryl tails were investigated for their DNA binding interaction. Figure 2.1 shows the general structure of the parent complex $[Ru(terpyAr)_2]^{2+}$ and the aryl tail group (Ar) substituted in the 4′ position on each tridentate 2,2′;6′2″-terpyridine (terpy) ligand. Each complex is hereafter referenced by its aryl tail group abbreviation.

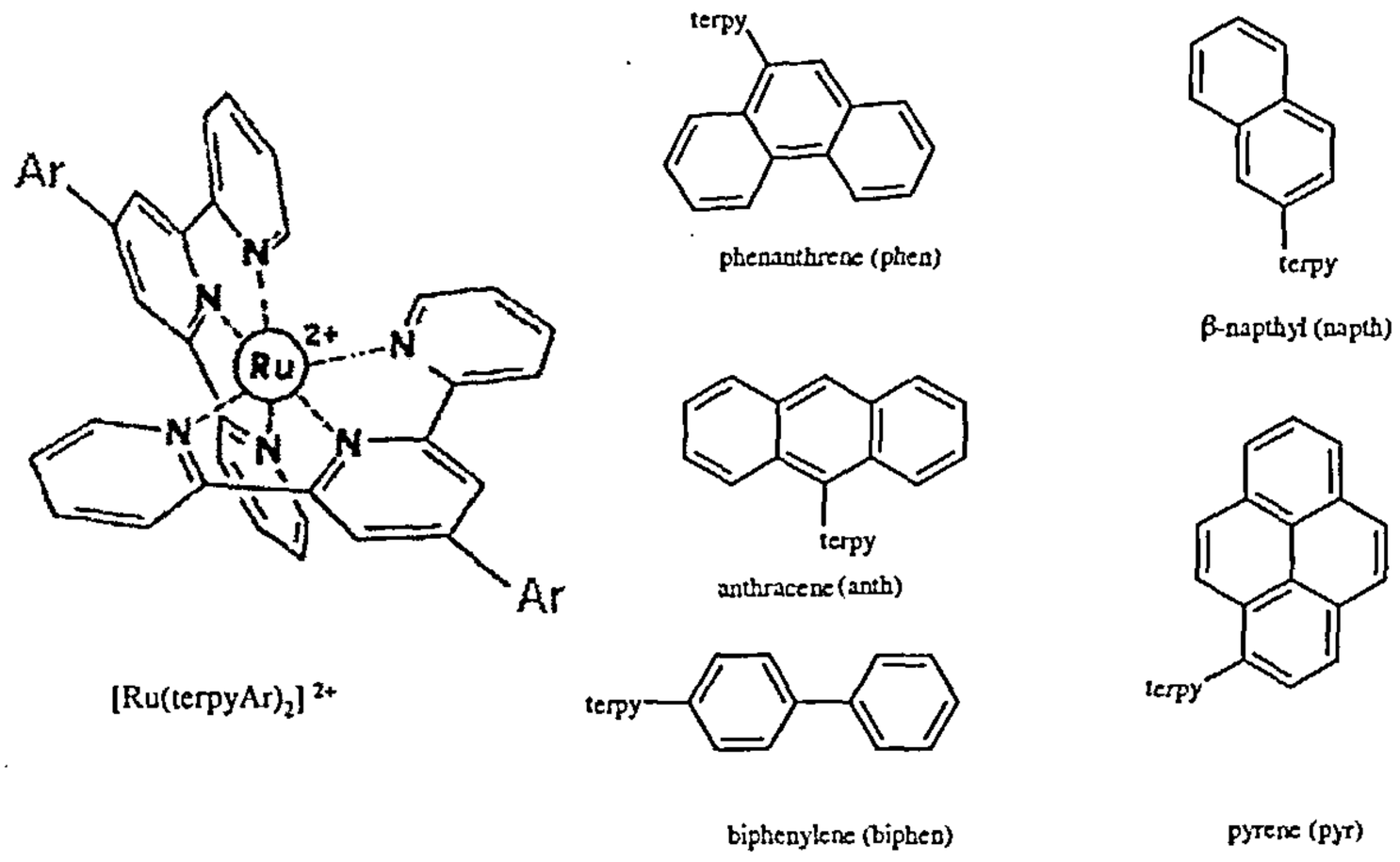

Figure 2.1. *The general structure of the* $Ru(terpyAr)_2Cl_2$ complexes and the aryl tail group of each of the complexes investigated where Ar = aryl tail group (i) biphenylene (biphen), (ii) β-napthyl (napth), (iii) phenanthrene (phen), (iv) anthracene (anth) and (v) pyrene (pyr); terpy indicates point of attachment of tail group to 4′ position on the terpyridine (terpy).

Bidentate polypyridyl ligands such 2,2′-bipyridine, (bipy) or 1,10-phenanthroline (1,10-phen) (Figure 2.2) complex to six coordinate ruthenium(II) to form tris chelate complexes which are well known as effective non-covalent DNA binders.[1–10] Their binding interactions are complicated by the chirality of the metal complex resulting in different enantiomeric effects, these are covered in section 2.1.1.

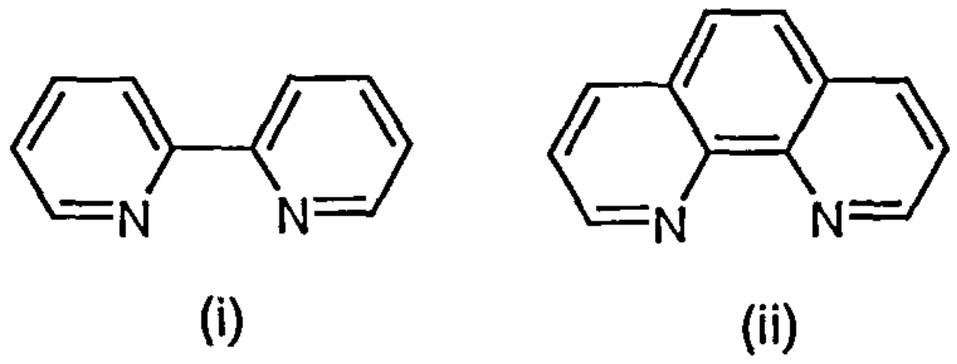

(i) (ii)

Figure 2.2 Bi-dentate ligand structures investigated include (i) 2,2′ bipyridine = bipy (ii) 1,10-phenanthroline = 1,10-phen

Complexes formed when two terpy ligands are attached to six coordinate ruthenium(II) have a distinct advantage over their bidentate (tris chelate) counterparts in that the ruthenium(II) metal forms achiral $[Ru(terpy)_2]^{2+}$ complexes where no stereoisomerism is possible. The terpy ligand also introduces a significant element of planarity into the geometry of the complex that might provide steric advantages. In addition, controlled substitution in any position on the terpy is possible thus increasing the options for metal complex geometry (though asymmetric substitution leads back to the complication of stereoisomerism which we wished to avoid).[11,12]

Sauvage and co-workers have provided a comprehensive review of the spectroscopic properties of $[Ru(terpy)_2]^{2+}$ complexes.[12,13] Many $[Ru(terpy)_2]^{2+}$ complexes and other heavy transition metal bis-terpy complexes (e.g. osmium(II)) have also been described.[14–16] Research into the spectroscopic properties of these bis-terpy complexes has mainly concentrated on symmetrical aromatic ligands[11,13,17] and recently branched out to include asymmetric ligand ruthenium(II) terpy complexes,[18]extended conjugated systems[19] and bis-ruthenium(II) complexes.[20,21] There is a literature precedent for terpy metal complexes binding to DNA. Terpy substitued platinum

complexes have been shown to bind in a range of intercalative and groove binding modes.[22-28] Reports on the interactions of ruthenium(II) bis-terpy complexes with DNA are, however, limited. Perhaps the reason why not as much work has been carried out on the DNA interaction of terpy complexes as has been done with the bidentate ligands is that $[Ru(terpy)_2]^{2+}$ exhibits less favourable photophysical properties at room temperature than its tris-chelate counterparts.[14] The $[Ru(terpy)_2]^{2+}$ complex, in fact is essentially non-emissive in water at room temperature (see section 2.3.4).[29,30]

2.1.1 Tris(chelate)ruthenium(II) complexes

Chiral tris-chelate complexes of the structural formula $[Ru(L)_3]^{2+}$ are formed when a six coordinate ruthenium(II) metal is bonded to three bidentate ligands (L) where L typically equals bipy or 1,10-phen.[31,32] This is simply due to the bidentate nature of the ligands and the geometry of the metal. The structure formed is a three-winged propeller in shape. Its stereoisomers, *i.e.* two enantiomers, are usually annotated as Δ for the right-handed enantiomer and Λ for left-handed, these are illustrated in Figure 2.3.

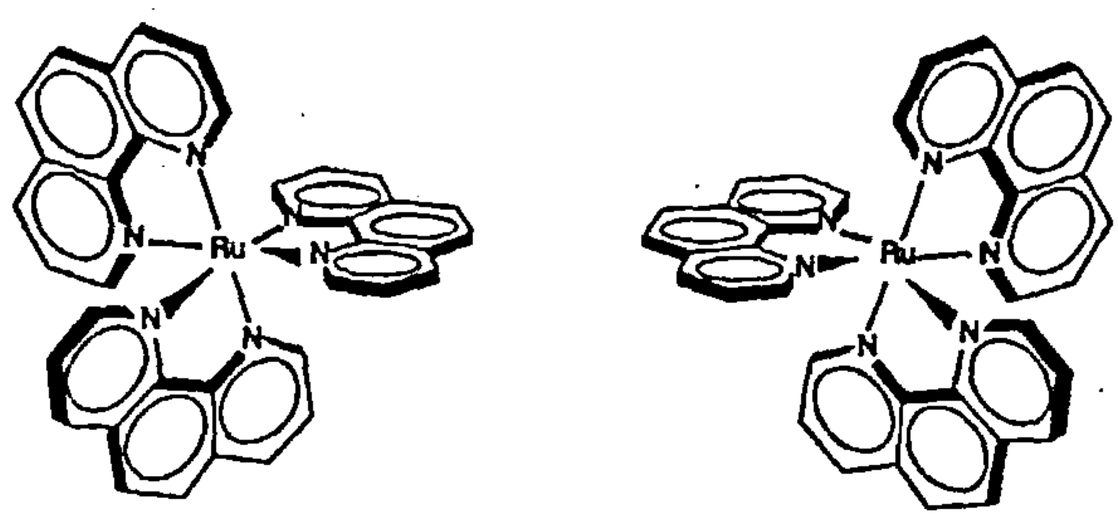

Figure 2.3 The Δ and Λ enantiomers of ruthenium(II) tris 1,10-phenanthroline. *Taken from reference 4*

Ruthenium(II) complexes of structural analogues and mixed ligand analogues have been extensively investigated mainly because of their potential for enantioselective

recognition of DNA as well as their photophysical properties (*i.e.* excited state lifetimes, luminescence intensities, chemical stability and redox properties. [2,5,31–33]

The most widely studied member of this group of tris-chelate compounds is $[Ru(1,10\text{-phen})_3]^{2+}$ tris(1,10-phenanthroline)ruthenium(II) [3,34] (Figure 2.3). Its binding modes to DNA are still not clear — most likely because there are a range of binding modes that all occur. The methods used to determine mode of binding include UV-Visible absorbance, circular dichrosim and linear dichroism experiments, viscosity studies, NMR, molecular modelling and energy calculations.

Satyanaryan *et al.* provide a comprehensive review of the work on the tris(1,10-phenanthroline)ruthenium(II) complex.[4] In summary, Barton *et al.* conducted unwinding studies with closed circular DNA, absorbance and fluorescence spectroscopy and concluded that both enantiomers bind to DNA through two different modes of binding one intercalative and the other surface binding.[5,6] Further investigations using ^{1}H NMR suggested that Δ-$[Ru(1,10\text{-phen})_3]^{2+}$ preferred intercalation, while the Λ-$[Ru(1,10\text{-phen})_3]^{2+}$ preferred surface binding, possibly in the minor groove.[7] Satynaryan and co-workers, in the absence of definitive X-ray crystallography data however, concluded that their linear dichroism and viscosity experiments on the enantiomers (when compared with those of classical intercalators *e.g.* ethidium and actinomycin) suggested that there was one mode of binding for each enantiomer which is non-intercalative in nature.[3,8] This was also proposed by Haworth *et al.* who on the basis of molecular modelling studies concluded that partial insertion of one phenanthroline ring was feasible between the base pairs but not full insertion, due to steric hindrance from the other two external phenanthroline rings.[9] Later, using 2D NMR, Eriksoon *et al.* proposed that both enantiomers bound only in a non-intercalative fashion in the minor groove and displayed an AT binding preference.[10] The non-intercalative nature of the

binding was re-confirmed by Coury *et al.* using scanning force microscopy, which revealed that neither enantiomer caused changes in the length of DNA.[35]

Coggan *et al.* have suggested that the conflicting data on the binding modes of ruthenium(II) tris-phenanthroline complex could be due to a number of factors: the different techniques used and therefore timescales, different DNA sequences being used, and different behaviours of the enantiomers.[1] They showed that the binding modes adopted are concentration and mixing ratio dependent. They also investigated methyl substituents of the parent phenanthroline tris-chelate. Both the Λ and Δ enantiomers of the metal complex and its [4,7]-dimethyl derivative showed at least two binding regimes. They concluded from *CD*, *LD*, and molecular modelling studies that for the Λ enantiomer the partially inserted mode is favoured at all mixing ratios whereas the Δ complex, at excess DNA, prefers a minor groove binding mode with the chelates spanning the groove. At close packed metal complex loading a slotted minor groove mode becomes more favourable for Δ and some major groove partial insertion also occurs.[36]

Research in this area has focussed on octahedral ruthenium, rhodium or osmium complexes containing mixed ligands of 1,10-phen and bipy derivatives, such as the dipyrido(3,2-a:2′,3′-c)phenazine (dppz) ligand (Figure 2.4(i)).

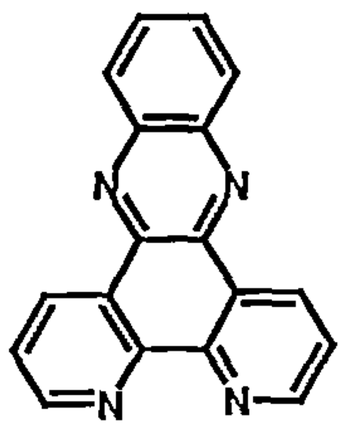

(i) dppz

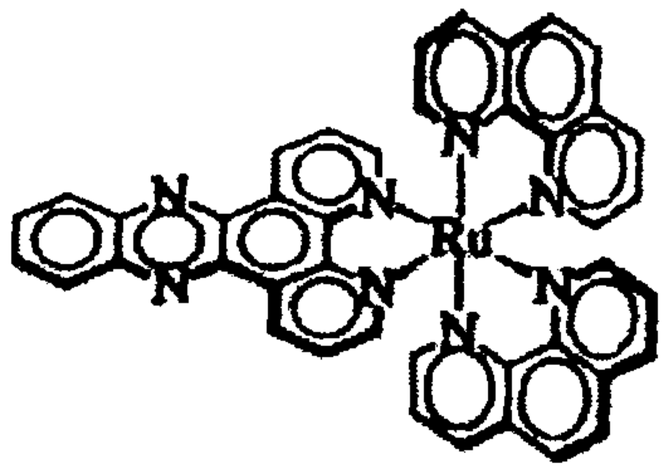

(ii)

Figure 2.4 (i)The dipyrido(3,2-a:2′,3′-c)phenazine (dppz) ligand (ii) Δ–[Ru(1,10-phen)$_2$(dppz)]$^{2+}$ complex, reproduced *from reference* 37

Complexes containing the dppz ligand have been shown to bind strongly to DNA by intercalation of the dppz ligand.[37–39] Osmium(II) and ruthenium(II) complexes containing one dppz ligand and two ancillary ligands (bipy or 1,10-phen) *e.g.* $[Ru(bipy)_2(dppz)]^{2+}$ or $[Ru(1,10\text{-phen})_2(dppz)]^{2+}$ (the latter is illustrated in Figure 2.4(ii)) have been found to function as 'molecular light switches for double helical DNA'. These complexes show no luminescence in aqueous buffer but when bound to DNA by intercalation of the dppz ligand they luminesce strongly.[37–40] However, the specifics of the binding geometry (including the apparent lack of DNA sequence specificity) has not been firmly established and has been subject to some debate with the following different NMR studies implicating both major and minor groove.

Using proton NMR and a duplex DNA hexamer $d(GTCGAC)_2$, Dupureur and Barton proposed that $[Ru(1,10\text{-phen})_2(dppz)]^{2+}$ intercalates from the major groove.[41,42] Further investigations using known major and minor groove DNA binding agents in competition with the complex for DNA binding sites on double stranded AT-DNA, GC-DNA and ct-DNA also resulted in support for the original proposal of intercalation of the ruthenium(II) complex from the major groove. The study additionally indicated an AT site preference for intercalation of the dppz ligand.[43] By way of contrast, Lincoln *et al.* have proposed that both isomers of the same complex, $[Ru(1,10\text{-phen})_2(dppz)]^{2+}$ intercalate from the minor groove of the DNA helix, on the basis of photophysical studies and the similarities between the DNA binding geometry of the metal complex with that of the intercalator actinomyin D.[36,44,45]

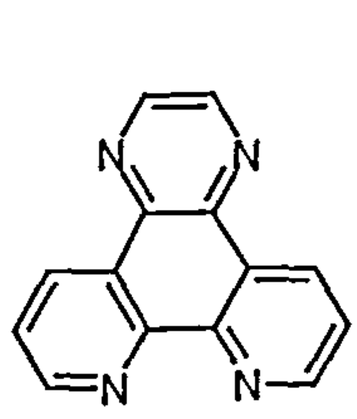

(i) dpq

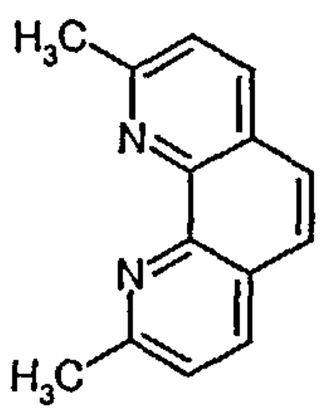

(ii) dmphen

Figure 2.5 (i) dpq = dipyrido[2,2-d:2',3'-f]quinoxaline, (ii) dmphen = 2,9-dimethyl-1,10-phenanthroline

Aldrich-Wright and colleagues conducted a proton NMR study of the binding of the DNA hexamer $d(GTCGAC)_2$ with Δ-$[Ru(1,10\text{-phen})_2dpq]^{2+}$ where dpq denotes dipyrido[2,2-d:2′, 3′-f] quinoxaline ligand (Figure 2.5(i)) which is closely related to Δ-$[Ru(1,10\text{-phen})_2(dppz)]^{2+}$.[46,47] The complex was found to intercalate from the minor groove. Further studies of binding of the Δ enantiomer of $Ru(1,10\text{-phen})_2L)^{2+}$ where L= 1,10-phen or dpq showed that both complexes bound in the minor groove. NMR investigations into $[Ru(dmphen)_2dpq]^{2+}$ (where dmphen denotes 2,9-dimethyl-1,10-phenanthroline (Figure 2.5(ii)) binding to the DNA hexamer $d(GTCGAC)_2$ suggest that the dpq ligand of the Δ- enantiomer intercalates deeply into DNA hexamer base stack but the Λ enantiomer only partially intercalates, still from the minor groove.[48]

In contrast to the above *minor* groove intercalators, octahedral ruthenium(II), rhodium(III) complexes $[ML_2(phi)]^{n+}$, $[ML(phi)_2]^{n+}$,$[M(phi)_3]^{+}$, where phi = 9,10-phenanthrenequinone diimine (see Figure 2.6(i) and (ii)) and L = 1,10-phen or bipy have been prepared and found to bind to B-DNA via intercalation of the phi ligand from the *major* groove when M = rhodium(III).[49 – 53]

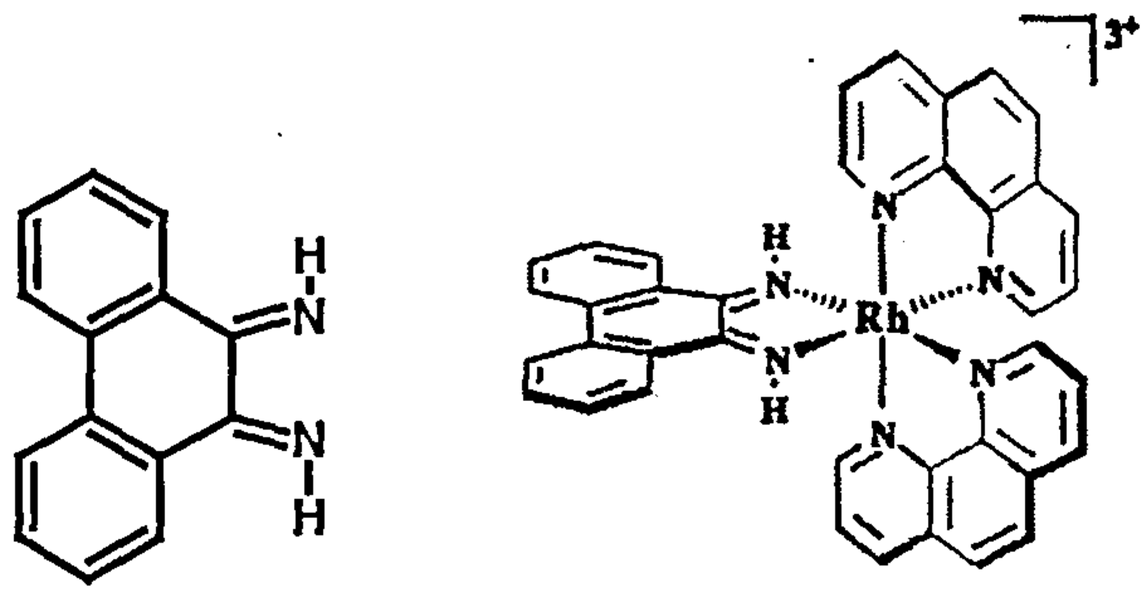

(i) (ii)

Figure 2.6 The structures of (i) phi = 9,10-phenanthrenequinone diimine, (ii) Δ-$[Rh(phen)_2phi]^{3+}$ complex taken from reference 53

The DNA binding location of these ruthenium(II) polypyridyl complexes is not yet firmly established. These complexes are known to promote direct strand scission via

hydrogen abstraction from the deoxyribose upon photoactivation.[50] The attraction of these major groove DNA binding agents is that a mechanism for DNA degradation involves the abstraction of a hydrogen atom from the sugar adjacent to the binding site, a major groove binder can then access C3′ and C2′ hydrogens which are accessible in the major groove of DNA. The phi complexes of rhodium(III) are major groove intercalators and their photo induced strand cleavage reactivity has thus been the subject of some study in an effort to probe the reaction and optimise it.

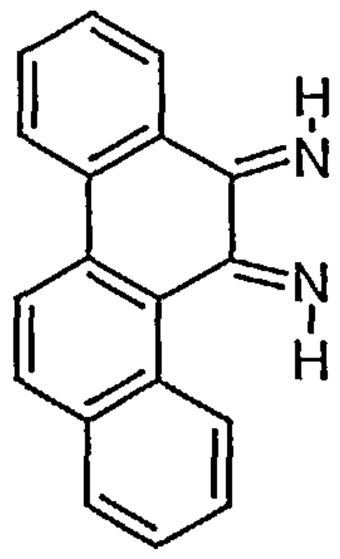

Figure 2.7 The 5,6-chrysenequinone diimine ligand denoted chrysi

A derivative of the phi ligand is the broader four ring 5,6-chrysenequinone diimine (chrysi) (Figure 2.7). Modelling has suggested that the chrysi ligand unlike the phi ligand is too bulky to intercalate between standard B-DNA base pairs but can do so near mismatched DNA base pairs which are destabilised as a result of the disruption of the regular B-DNA structure.[54] The chrysi complex is highly specific for such sites and has been shown to recognise and photocleave a single base mismatch in a 2725 base pair linearised plasmid heteroduplex.[52,55] Such sterically demanding intercalators have been suggested to have applications in mutation detection systems and as mismatch-specific chemotherapeutic agents.[52,56]

2.1.2 Octahedral terpy complexes

In the design of our ligands we began with the facts that terpy is known to lead to intercalation of square planar complexes.[22,24–26,28,57] Thorp *et al.* have investigated

octahedral terpy mixed ligand complexes that exhibit comparable DNA strand scission interactions [58,59] to those for the major groove intercalators $[Rh^{III}L_2(phi)]^{n+}$ (see section 2.1.1). The binding specificity of $[Ru^{II}(terpy)(L)OH_2]^{2+}$ where L = bipy or 1,10-phen with ct-DNA was initially investigated.[60] $[Ru^{II}(terpy)(bipy)OH_2]^{2+}$ was found not to cleave or lengthen DNA thus seeming to indicate that the intercalation of these and similar octahedral complexes containing terpy is not sterically feasible.[58]

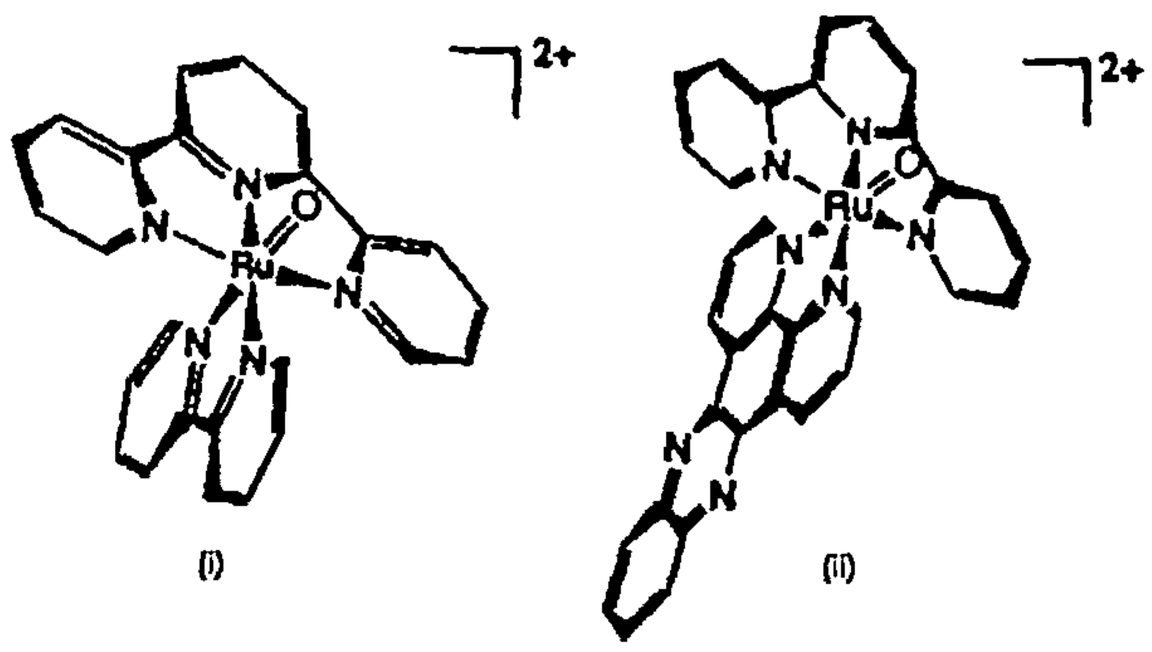

Figure 2.8 Structures of (i) $[Ru(terpy)(bipy)O]^{2+}$ (ii) $[Ru(terpy)(dppz)O]^{2+}$ structures taken from reference 58

However, the oxidised form, $[Ru^{(IV)}(terpy)(bipy)O]^{2+}$ (Figure 2.8(*i*)) combines a reactive oxoruthenium(IV) functionalitiy and has been found to cleave DNA by guanine oxidation and sugar oxidation of the C1′ hydrogen deoxyribose bond to cause strand scission.[61] The location of these C1′, C4′ and C5′ hydrogens of deoxyribose sugar in duplex DNA is deep within the minor groove. Complexes of this type exhibit *minor* groove binding compared to their major groove binding rhodium(III) counterparts. However, when the bipy ligand is replaced by dppz (see Figure 2.8(ii)), and binding specificity investigated, the complex is found to lengthen and unwind DNA indicative of classical intercalation. A study by Thorp *et al.* provides evidence that sugar oxidation by $[Ru(terpy)(dppz)O]^{2+}$ occurs from complexes bound in the minor groove, but as only 10 % of the complex was found to be consumed by sugar oxidation the study also states that there still remained 90 % of the complex (not undergoing the sugar reaction) which

may be bound in the major groove.[58] This is agreement with the NMR studies conducted by both Lincoln and Aldrich-Wright (see Section 2.1.1) although it must be noted that Thorp *et al.* worked with a dppz complex containing terpy and oxo groups whereas the NMR experiments were carried out using complexes containing dppz and either two ancillary bipy or 1,10-phen ligands.

Studies comparing the bipy complex, $[Ru(terpy)(bipy)O]^{2+}$ and its dppz equivalent, $[Ru(terpy)(dppz)O]^{2+}$ found that two of the interaction sites for dppz were not intercalative rather they were shape recognition specific to the dppz ligand.[58]

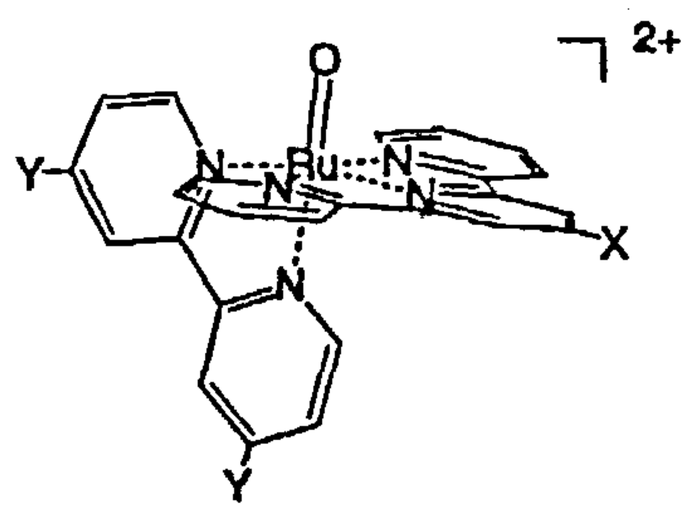

Figure 2.9 X and Y denote points of substitution on the terpy and bipy ligand respectively of the $[Ru(terpy)(bipy)O]^{2+}$ complex, reproduced from reference 59

When the $[Ru(terpy)(bipy)O]^{2+}$ complex was substituted with electron donating or withdrawing substituents at the 4′ position of the terpy or bipy (Figure 2.9), the electronic properties of the complex were found to change whereas the coordination environment of the reactive oxo ligand was not significantly affected. This suggested that the selective cleavage in duplex and single stranded DNA was not strongly reliant on the substituents on the metal complex.[59]

2.1.3 Planar aromatic DNA binding moieties

Another type of DNA binding of relevance to this work is the DNA binding modes of planar aromatic molecules such as anthracene and pyrene with cationically

substituted tails — specifically water soluble piperazinylcarbonyloxyethyl derivatives (see Figure 2.10).

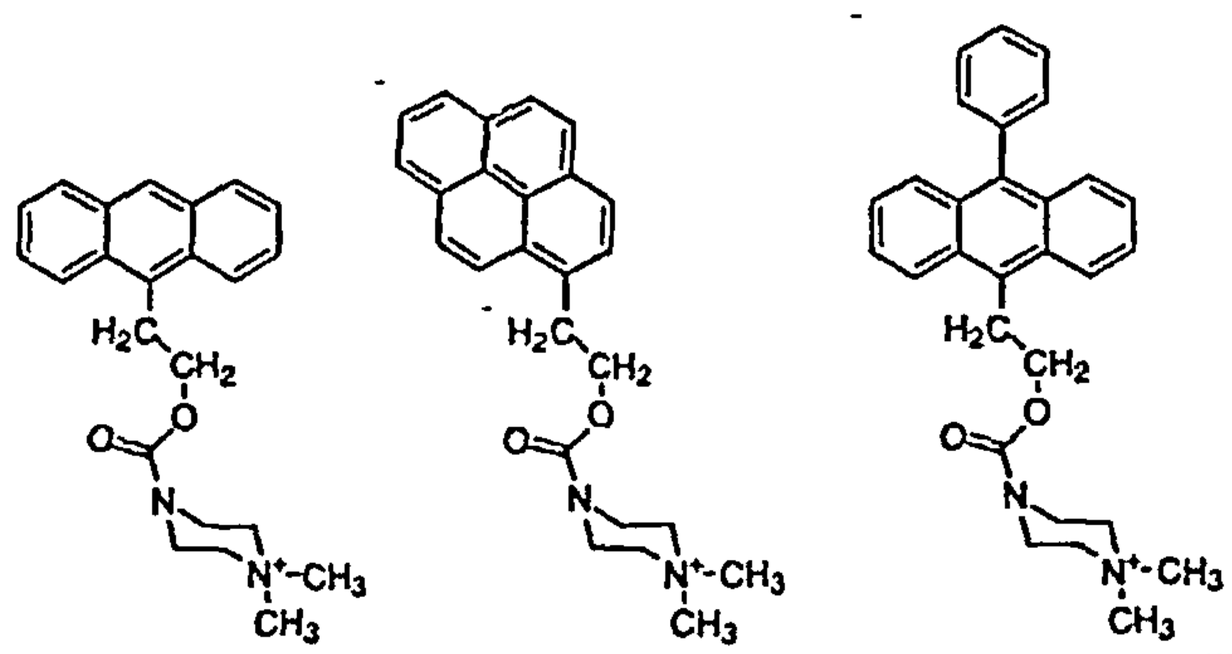

(i) (ii) (iii)

Figure 2.10 Piperazinyl carbonyloxyethyl derivatives denoted (i) anthracene (ii) pyrene and (iii) phenylanthracene (taken from reference 62)

Using *CD* and *LD*, Becker and Nordén found that the anthracene and pyrene aromatic portions were found to be capable of intercalation between base pairs in either the major or minor groove, but attached ancillary tail ligands were also found to have a role in determining the DNA binding mode, (*i.e.* location in the major or minor groove, strength of binding) and have a steric effect.[62,63] For example, substitution of anthracene (Figure 2.10(i)) with phenylanthracene (Figure 2.10(iii)) prevents intercalation and leads instead to the complex externally binding to both AT and GC.[62]

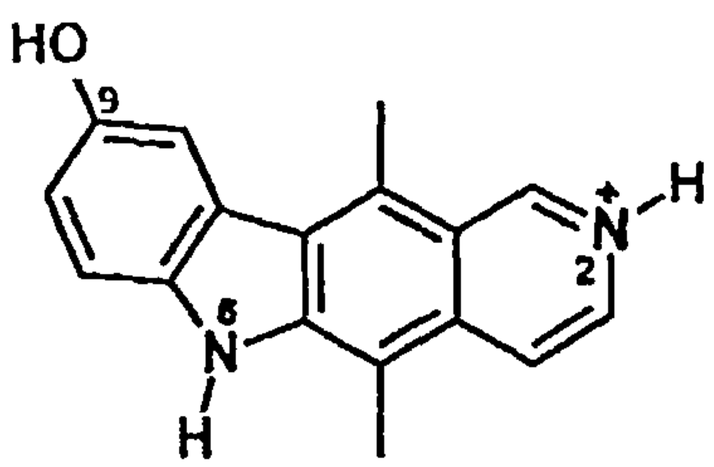

Figure 2.11 The structure of 9-hydroxyellipticine taken from reference 64

9-hydroxyellipticine (9-OHE), (Figure 2.11) and its derivatives exhibit anticancer activity in cell lines via interaction with DNA, and intercalation is thought to be the therapeutically active binding mode. Spectroscopic studies on the binding of 9-

OHE with ct-DNA, AT-DNA and GC-DNA conducted by Ismail *et al.*, have shown concentration dependent binding modes that change from intercalation to interaction in either major or minor grooves. [64] The complex has been shown to adopt two modes of binding, intercalative and the other a stacked binding mode involving the formation of drug oligomers in the DNA major groove dependent on the drug load.

9-OHE binds intercalatively to AT, GC and ct-DNA at very low drug load with the hydroxyl group projecting in the minor groove and the amino group is in the major groove. At higher concentrations, a non-intercalative binding mode with the drug oriented parallel to the DNA bases becomes operative probably in the major groove. The second mode was shown by resonance light scattering (RLS)[65] to be a stacked binding mode with small oligomer *i.e.* stacks rather than extended aggregates. Reduced *LD*, LD^r, studies suggested binding geometry that precluded a minor groove binding (where plane of drug is ~ 45 degree angle from the plane of bases) so it was concluded that the drug stacks in the major groove. Strong concentration dependence was observed for the two binding modes where intercalation is favoured at very low drug load with stacking interactions more prominent as concentration is increased.

2.2 The complexes of this study

The design of the molecules studied in this chapter benefits both from the extensive ruthenium metal complex DNA binding literature and the extended planar aromatic cationic binding. The interactions of these five complexes (Figure 2.1) with their bi-functional intercalating tail groups and shape sensitive [Ru(terpy)] core with DNA can be probed without danger of any photoactive strand scission taking place.

Ruthenium(II) usually adopts a six coordinate octahedral geometry. In our complexes, each terpy ligand has three nitrogen atom binding sites, the two terpys

attach either side of the inert ruthenium(II) in the sterically favourable octahedral arrangement. The tail groups in the complexes studied in this work (see Figure 2.12) are substituted on the 4′ position, para to the nitrogen of the terpy and lie opposite each other. The 4′ position on the terpy lies along its two-fold axis, and the aryl tail either lies or approximately lies with this two-fold axis along an axis of the aryl tail. The $[Ru(terpyAr)_2]^{2+}$ core thus has two reflection planes, an S_4 axis and three C_2 axes so it has D_{2d} symmetry.[12] The anthracene and biphenylene complexes have this symmetry when the tails are oriented coplanar with the terpy groups. The others have it on average if one assumes either free rotation about the link to the tail or no preference for either orientation of the planar tail.

The main techniques used in this chapter are spectroscopic and so the spectroscopy of the complexes is very important for the interpretation of the data collected. As discussed in Chapter 1, an absorption spectrum is made up of electronic transitions arising from molecules absorbing energy at certain wavelengths and their electrons are promoted from a ground to an excited state. Absorption spectroscopy can be used to probe the interactions of specific transitions of a molecule by changes in its environment *e.g.* by DNA binding perturbations. The individual spectroscopy of the tails [32, 66–69] is well established as is that of the $[Ru(terpy)_2]$ core of the molecule.[12–14,17,29,31,32,66] These are summarised in Figure 2.12 and in Tables 2.1 – 2.3 in section 2.3.

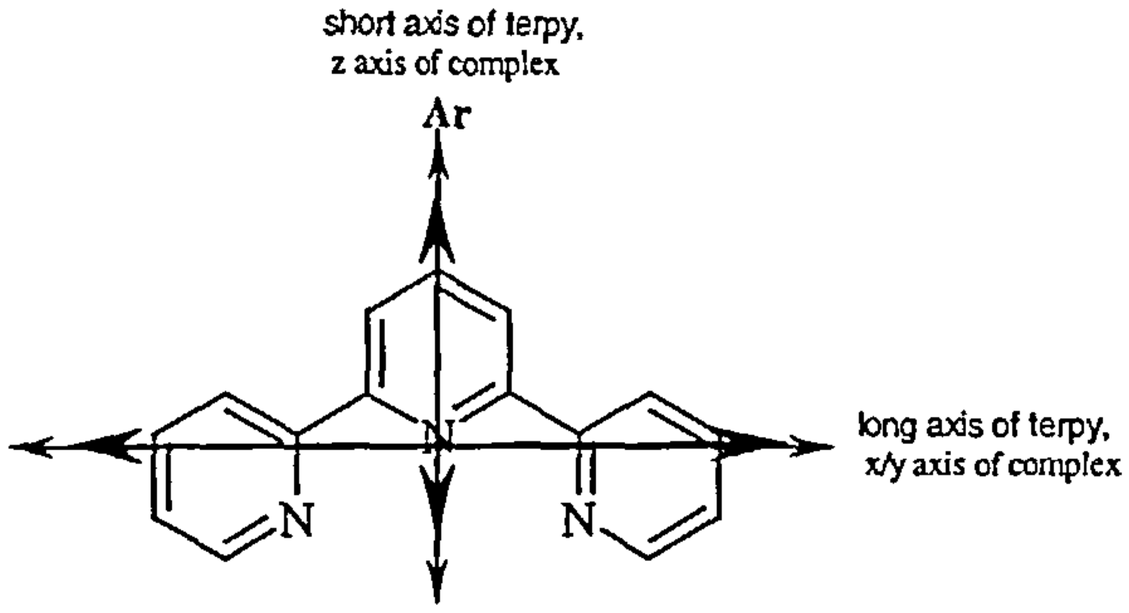

2,2';6',2'' terpyridine (terpy)

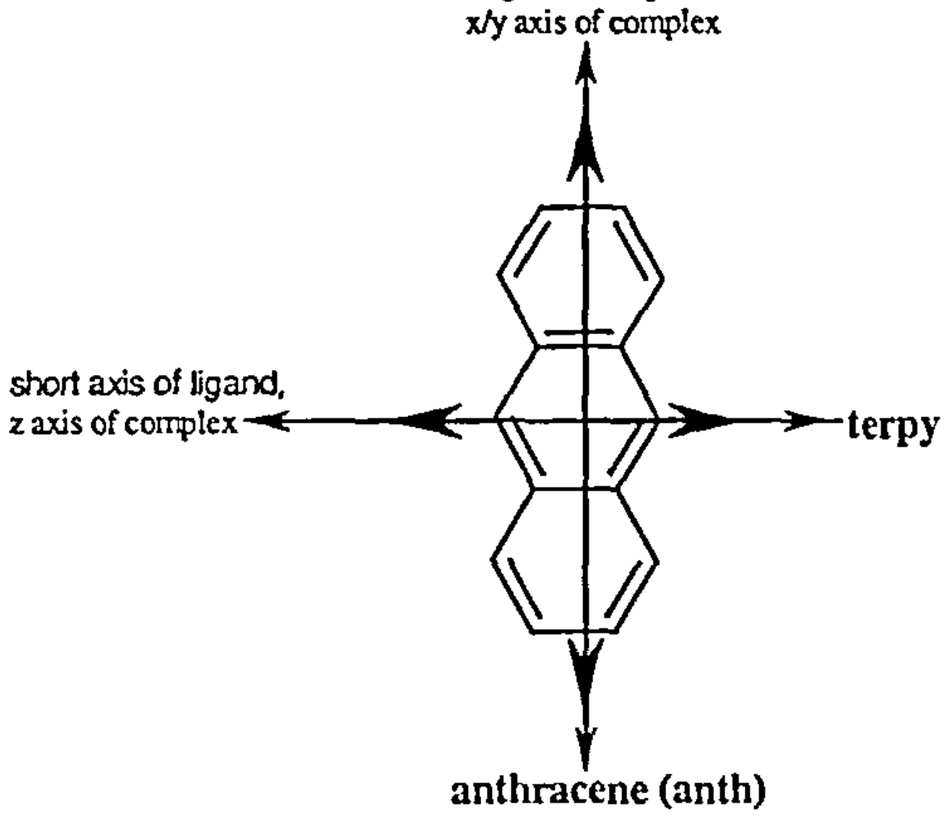

anthracene (anth)

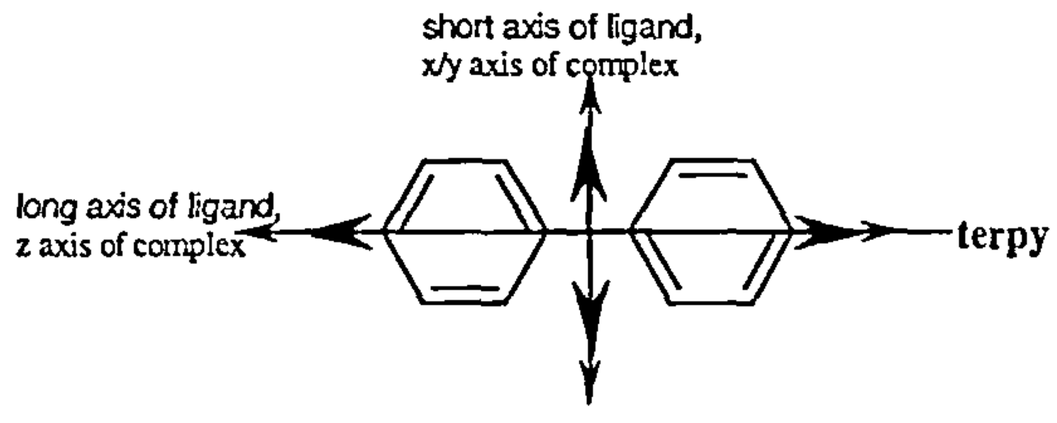

biphenylene (biphen)

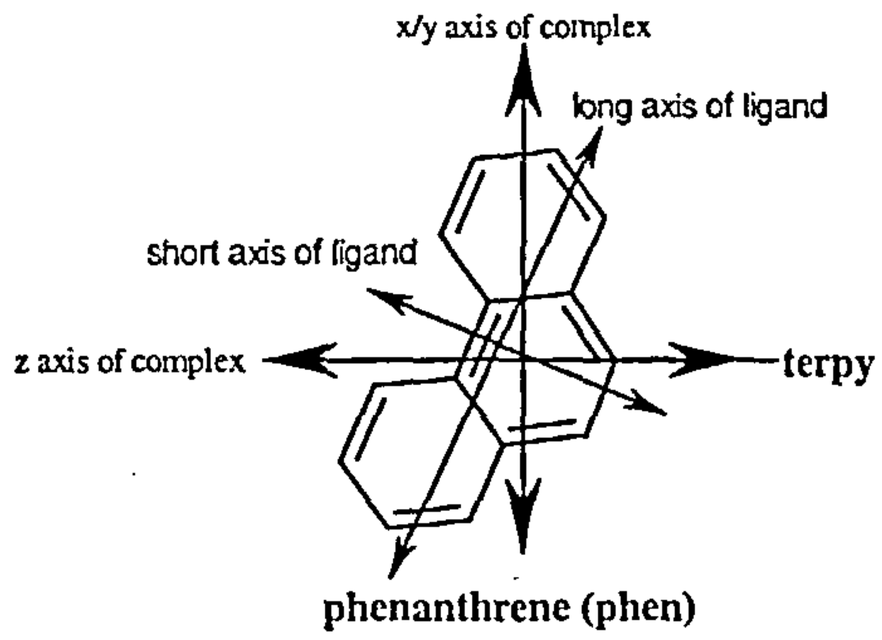

phenanthrene (phen)

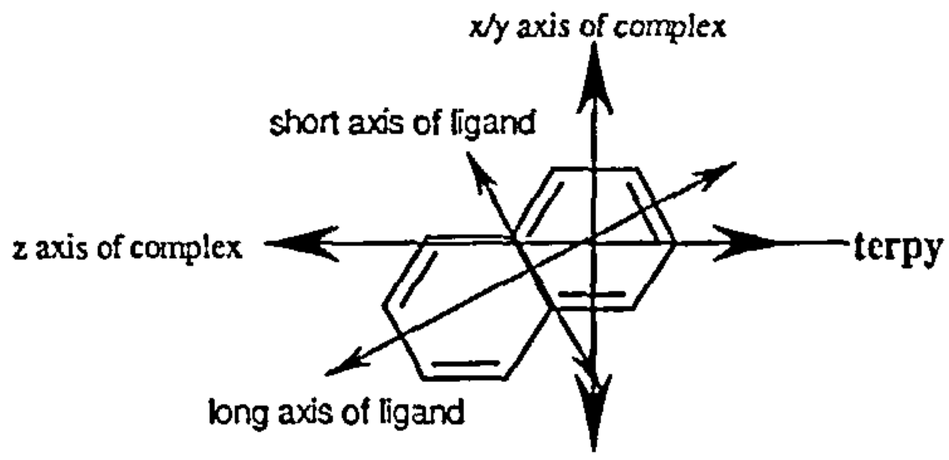

β-napthyl (napth)

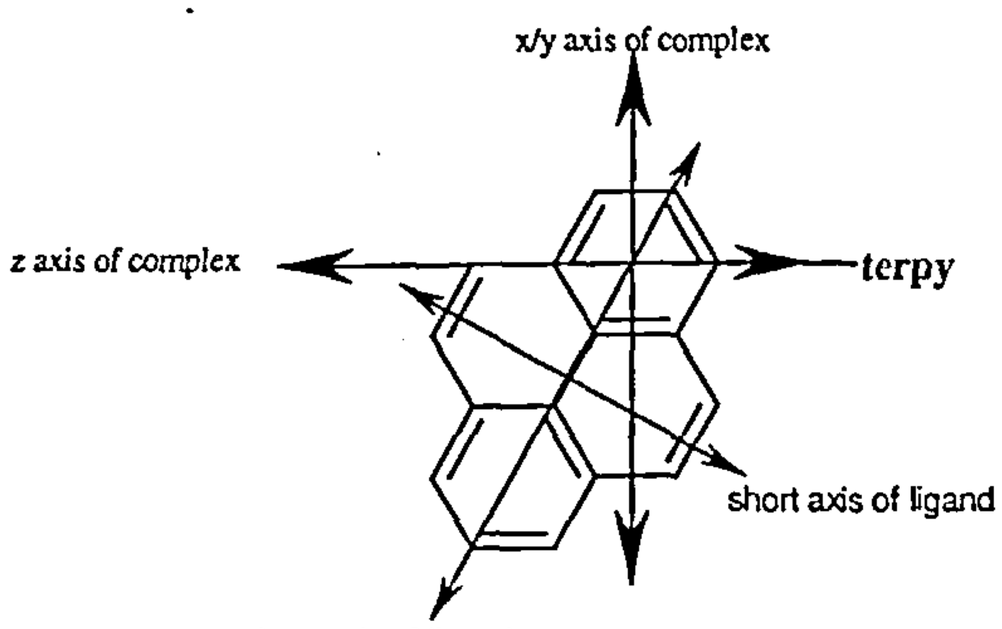

pyrene (pyr)

Figure 2.12 Molecular axis system for the metal complexes. In each case, the aryl tail groups (Ar = anth, pyr, biphen, phen, napth) are attached at the 4' position of the terpy (2,2';6,2''-*terpyridine*) *ligand*. The x, y, z axis system is the symmetry determined axis system of the $Ru(terpy)_2$ core of the molecule, as indicated by the large double arrows. The tail group long and short axes are indicated in the figure by small double arrows. The metal complex z axis aligns with the short axis of anth and terpy and the long axis of biphen. The short axis of phen and pyr and the long axis of napth lie close to the z axis. The long axis of the whole metal complex lies along its z axis.

2.2.1 Materials

Ruthenium complexes

The five novel ruthenium(II) bis-terpyridine chloride complexes[15] were provided by E. Plummer (University of Warwick). For each of the ligands, the solid state structure of either the ruthenium or iron complex cation has been determined by X-Ray crystallography.[15] In each case, the geometry at the metal is basically octahedral subject to the constraints of the terpy ligands. In solution free rotation about the terpy-aryl band is anticipated. These complexes were all water soluble, so the binding studies reported in this chapter were carried out in aqueous solution with the exception of the pyrene and phenanthrene complexes where a small amount of methanol was used to make up the metal complex stock solutions (5% and 1.5% respectively).

Polynucleotide samples

Duplex calf-thymus DNA, (deoxyribonucleic acid (DNA) Sodium salt, 'highly polymerised' Type I) purchased from Sigma (referred to as ct-DNA), poly $[d(A–T)]_2$ and poly $[d(G–C)]_2$ DNA both for *in vitro use only* from Amersham Pharmacia-Biotech (referred to as AT and GC DNA respectively), were all used without further purification. AT and GC DNA were made up in 30 mM NaCl, 1 mM sodium cacodylate buffer, pH 6.92 and 10 mM NaCl, 1 mM sodium cacodylate buffer, pH 6.92 respectively. Concentrated stock solutions of ct-DNA were made up in water. Duplex formation was confirmed under experimental conditions (*i.e.* melting curve experiments), concentrations were determined spectroscopically using extinction coefficients (see Chapter 1). Duplex DNAs of greater than 500 base pairs in length were necessary to facilitate orientation in solution for relevant *LD* (linear dichroism) flow experiments.

Other materials

Polyvinyl alcohol (PVA) (Type III) purchased from Sigma Chemical Co. was used to make the film for film *LD*. Methylene blue (MB) was purchased from BDH Chemicals Ltd. The solvents used were 18.2 MΩ water, and analytical grade methanol.

Instruments

Absorbance spectra were measured using a 1 cm pathlength quartz cuvette and either a Jasco V550 UV-Visible or Cary IE UV-Visible spectropolarimeter. *CD* and *LD* (film and flow) were measured on a Jasco J-715 spectropolarimeter adapted for *LD* measurements. The samples were flow oriented using a quartz couette flow cell.[70] Fluorescence spectra were measured using a 1 cm pathlength, four sided clear quartz cuvette on a Perkin Elmer LS 50b. Methylene blue (a known DNA intercalator)[1] was used as an internal reference to help determine binding geometries of the complexes under varying complex concentrations in relation to the orientation of DNA. For film *LD*, blank and complex saturated films were prepared using PVA as described in Chapter 1. *LD* spectra were collected both before and after each film was mechanically stretched to twice its length in order to determine complex transition polarisations.

2.2.2 Methods

Titration methods with ct-DNA

Metal complex-DNA binding interactions with each of the five ruthenium complexes was initially probed using UV-Visible absorbance, fluorescence and circular dichroism spectroscopies. For these preliminary studies, the metal complex concentration was kept constant as a known concentration of ct-DNA was added. In contrast, for the in depth spectral investigations, titration series were set up so that the

DNA concentration remained constant as the metal complex concentration was varied, this was achieved by adding aliquots of DNA with each addition of metal complex thus allowing for any variation in the interaction with DNA to be probed.

2.2.2.1 Film linear dichroism

Film *LD* can provide information about the polarisations of transition moments of a particular molecule. The symmetry of the molecule is often helpful in assigning the orientation of the molecules within the film. In addition, it governs the polarisations of transition moments. Once the transition polarisations for the ruthenium complexes have been assigned, they can be used to determine binding orientations of the complexes on a flow-oriented macromolecule (DNA) as outlined in Chapter 1.

The long and short axis of the molecules can usually be intuitively assigned. The long and short axes of the molecule (and the one perpendicular to them) are usually coincident with its spectroscopic axes if these are defined by symmetry. This is the case for the anth and biphen complexes studied in this chapter. In the case of the other complexes, the axes are not defined by symmetry, but the symmetry axes of the terpy core of the molecule are close to the long and short axes as illustrated in Figure 2.12. When the molecule is inserted into a stretched film, the long axis of the molecule will orient/lie along direction of orientation (stretch) whilst the short axis would resist the stretch and therefore lie at right angles to the stretch direction.

In order to analyse the film *LD* data, we make the assumption that the molecule behaves as uniaxial rods[70] in the stretched film and that the orientation axis is the S_4 axis of the [Ru(terpy)$_2$] core of the molecule (see Figure 2.1). Therefore, for a z-polarized transition, the angle between a transition moment and the orientation axis, α, is 0 and the reduced linear dichroism (LD^r)for the whole absorption band: $LD^r(z) = +3S$, where S

is the orientation parameter (see Chapter 1). For x/y polarisation transitions $\alpha = 90°$ and $LD^r(x,y) = -1.5S$.

Thus transition polarizations can be assigned according to the signs of the stretched film LD^r. Generally, positive LD^r features are assumed to correspond to long axis polarised transitions and negative LD^r signals to short axis polarisation transitions, though if the degree of orientation is too low, the short axis polarised transitions may appear as less positive rather than negative. Therefore the strongest positive LD^r indicates a transition of greatest long axis character, whereas a least positive or negative LD^r that of short axis character. Since the LD^r across an absorption band is constant, the absence of any flat LD^r features indicates that transitions of different polarisations overlap in all regions of the spectra. This is frequently the case for transition metal complexes of octahedral parentage. Therefore we begin our analysis of the film *LD* by making the assumptions that the most positive LD^r corresponds to a long axis (z) polarised transition and any negative (or positive minima at places of large absorbance intensity) LD^r correspond to short axis (x/y) polarised transitions.

2.2.2.2 Flow linear dichroism

Long strands of DNA will orientate in the direction of flow of the solution and exhibit a *LD* signal at their absorption wavelengths. If a molecule binds to DNA, an induced *LD* in the bound molecule's transitions or a change in magnitude of the DNA *LD* signal may be noted. As each ruthenium(II) complex is too small to be flow oriented, (confirmed experimentally by lack of signal complex on its own), a non-zero *LD* signal in the ruthenium complex transitions when DNA is present indicates interaction between the metal complex and DNA. Flow *LD* probes orientations of specific transitions relative to the DNA helix axis for transitions of known polarisation.

In flow orientation, *S* (the orientation parameter) is usually determined by assuming that the DNA bases are all polarised at ~86° from the helix axis. As ruthenium transitions overlay the DNA transitions, an independent probe, *i.e.* methylene blue (MB) was used to determine DNA orientations on mixing. See Chapter 1 for an explanation. The methylene blue/DNA absorbance, *LD* and LD^r and complex + DNA + MB experimental data are given in Appendix 2.1.

2.3 Results and discussion

2.3.1 Electronic absorption spectra of the ruthenium terpy complexes

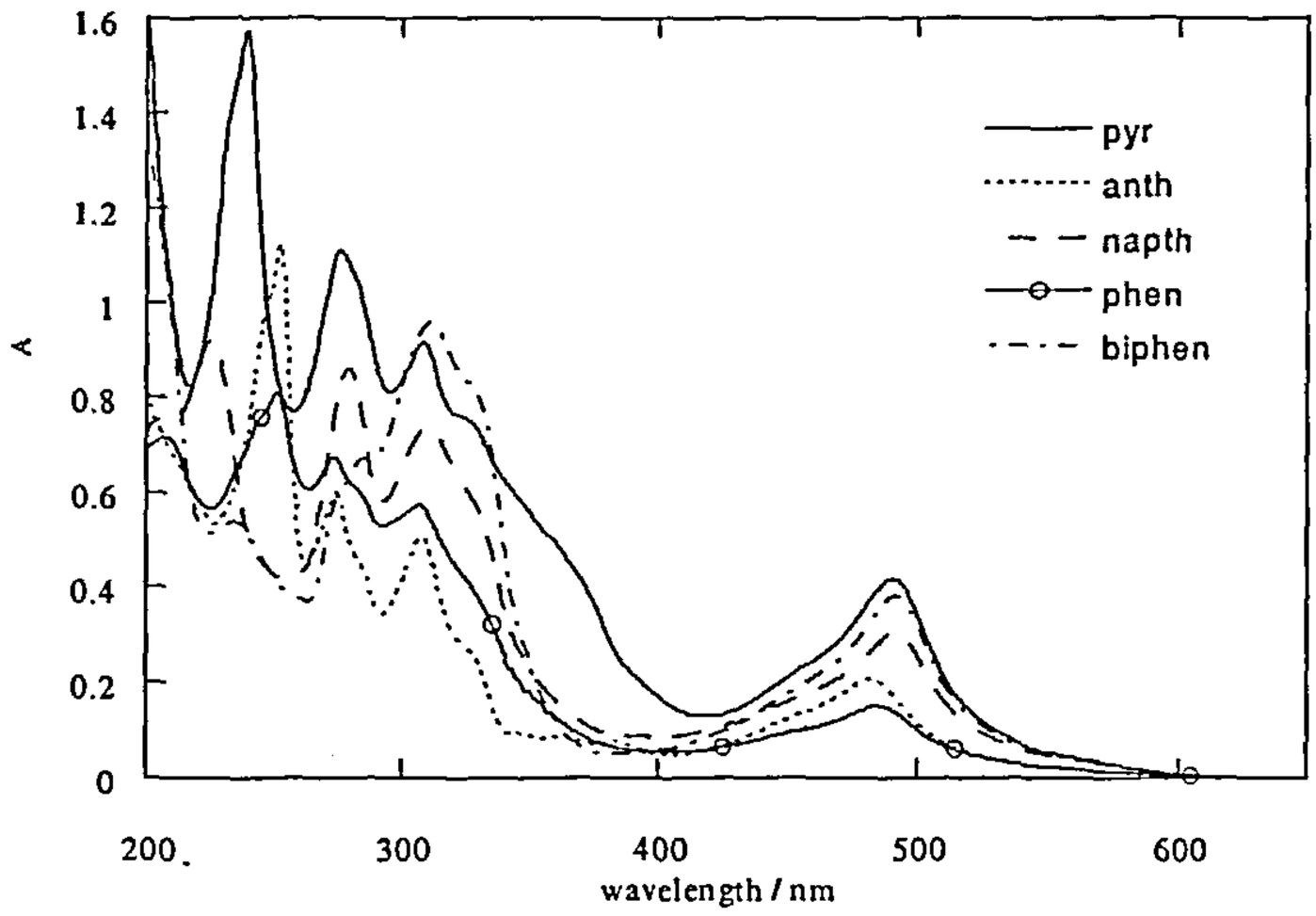

Figure 2.13 Absorbance spectra of the five ruthenium(II) complexes (10 μM) in water. Spectra are identified in the figure inset.

The complexes are a vivid orange-red colour in solution and absorb strongly in both the UV and visible regions of the spectrum. The absorption spectra of the five complexes in water are displayed in Figure 2.13. These spectra are in accord with expectations for ruthenium terpy complexes, which, as summarised in Table 2.1, are characterised by a variety of intense bands in the UV and visible region.[12–14,17,29,31,32,66–69]

Table 2.1 UV-Visible absorbance assignments for terpy and tail groups

		Ground state Absorption Maxima, λ_{max}/nm (ε = mol^{-1} dm^3 cm^{-1})
biphen [a]	assigned terpy	200 (130 000), 275^{sh} (60 000) and 280^{sh} (70 000), 310 (95 000), 330^{sh} (80 000)
	assigned biphen	230 (55 000), 330 – 400 ^{sh}, 400 (5 000)
	assigned MLCT	495 (40 000), 575^{t} (4 000)
napth[a]	assigned terpy	200 (75 000), 280 (85 000), 310 (70 000), 330^{sh} (55 000) – 340^{sh} (40 000)
	assigned napth	225 (95 000), 250 (42 000)minima, 400 (7 500)minima
	assigned MLCT	490 (30 000), 570^{t} (5 000)
phen [b]	assigned terpy	200 (70 000), 275 (65 000) and 280^{sh} (60 000), 310 (55 000), 330^{sh} (40 000)
	assigned phen	210 (72 000), 240^{sh} (73 000), 250 (80 000) and 400 (5 000) – 500 constant
	assigned MLCT	490 (15 000), 575^{t} (250)
anth[a]	assigned terpy	200 (80 000), 270 (60 000), 280^{sh} (45 000), 310 (50 000), 335^{sh}(25 000)
	assigned anthryl	225^{sh} (60 000), 245^{sh} (100 000) 250 (110 000), 350-400 (10 000)
	assigned MLCT	450 (10 000), 490 (20000), 575^{t} (2 500)
pyr [c]	assigned terpy	280 (110000), 310 (95000), 320-330^{sh} (75 000),
	assigned pyr	200-220 (150 000), 240^{sh} (160 000), 340 – 400 (*i.e.* 360^{sh}(50 000) 375^{sh}(40 000))
	assigned MLCT	420 (10 000), 490 (40 000), 570^{t} (5 000)

a = water, b = 1.5% MeOH , c = 5% MeOH, sh = shoulder, t = tail. Assignments made using references 12–14,17,29,31,32,66–69

Particular bands of relevance to our metal complexes are:

(i) the shoulders at ~200 nm and ~330 nm and the bands centred about 280 nm and 310 nm which correspond to the terpy ligand π-π^* transitions so can be assigned as in-ligand or ligand centred (IL) bands

(ii) the relatively intense and broad absorption bands in the visible region of the spectrum corresponding to metal (π_M) to ligand (π_M^*) charge transfer transitions (MLCT),

(iii) the other bands, mainly in the UV region of the spectra, that may be attributed to the IL transitions of the tail group,[32] though there may also be some metal centred (MC) or MLCT bands in the UV region

(iv) the long absorption tail found at lower energies (greater than 500 nm) for each complex in the visible region of the spectra that has been assigned to spin forbidden MLCT transitions by Kalyanasundaram *et al.* [32]

2.3.2 Film linear dichroism of the ruthenium terpy complexes

Film *LD* and film absorbance spectra, of the five metal complexes in stretched PVA films were measured to enable transition moment polarisations to be qualitatively assigned thus facilitating the use of flow *LD* in determining DNA binding geometries.

A number of assumptions have been made using the general figure of the parent $[Ru(terpyAr)_2]^{2+}$ complexes from Figures 2.1 and 2.12 as outlined in the Figure 2.12 caption. In particular, it has been assumed that the long axis of the metal complex lies along its z-axis (through the terpy and the tail) so z is preferentially oriented along the stretch direction of the film. If this assumption is correct, then the terpy long axis will lie perpendicular and the terpy short axis will lie parallel to the z axis of each complex as illustrated in Figure 2.12. Thus the long axis terpy transitions centred at 310 and 330

nm *in solution* will be expected to have a negative film *LD* signal and a maximum LD^r value. Conversely the 200 nm and 270–290 nm (solution phase) transitions would have positive LD^r values.

Figure 2.14 shows the film absorbance, film *LD* and film LD^r spectra for each of the five complexes. The absorbance in the film before and after stretching, when overlaid (data not shown), shows a small change in the shape of the spectrum and a decrease in magnitude upon stretching (due to the decrease in pathlength of the sample). Comparison with the water spectra of Figure 2.13 shows the absorbance is better resolved in the PVA environment and in general is also slightly red shifted for each complex relative to the water spectra. The observed spectra are consistent with the above expectations for the terpy transitions in each case, confirming that the assumption about the metal complex orientation in the film is indeed correct. The long wavelength (550–600 nm) spin forbidden transition has a reasonably large positive LD^r signal for each complex, suggesting that it is polarised predominantly along the metal complex z-axis. The MLCT bands are dominated by z-polarised transitions, particularly at ~ 500 nm where each complex has a large positive LD^r signal. The tail transitions are all consistent with this interpretation with the transitions along (or close to) the z-axis having large positive LD^r signals (usually not of maximum values as they overlap with other transitions of x/y polarisation). The tail group long and short axis polarisation transitions are summarised in Table 2.2 and the qualitative polarisation assignments of each complex based on the film *LD* studies are summarised in Table 2.3.

Table 2.2 Summary of long and short axis polarisations of individual tail group transitions

Tail	long axis / nm	short axis / nm
Biphen	200–220, 330-400* (355)	230–250
Napth	225–230, 340–400*(350)	200–210
Phen	200–210	225,275,330–400*(375)
Anth	250	225,340–400*(390)
Pyr	200–220, 350-400*	240,340

* = 340–400 mix of terpy(*l*), metal centred (MC) and tail transitions

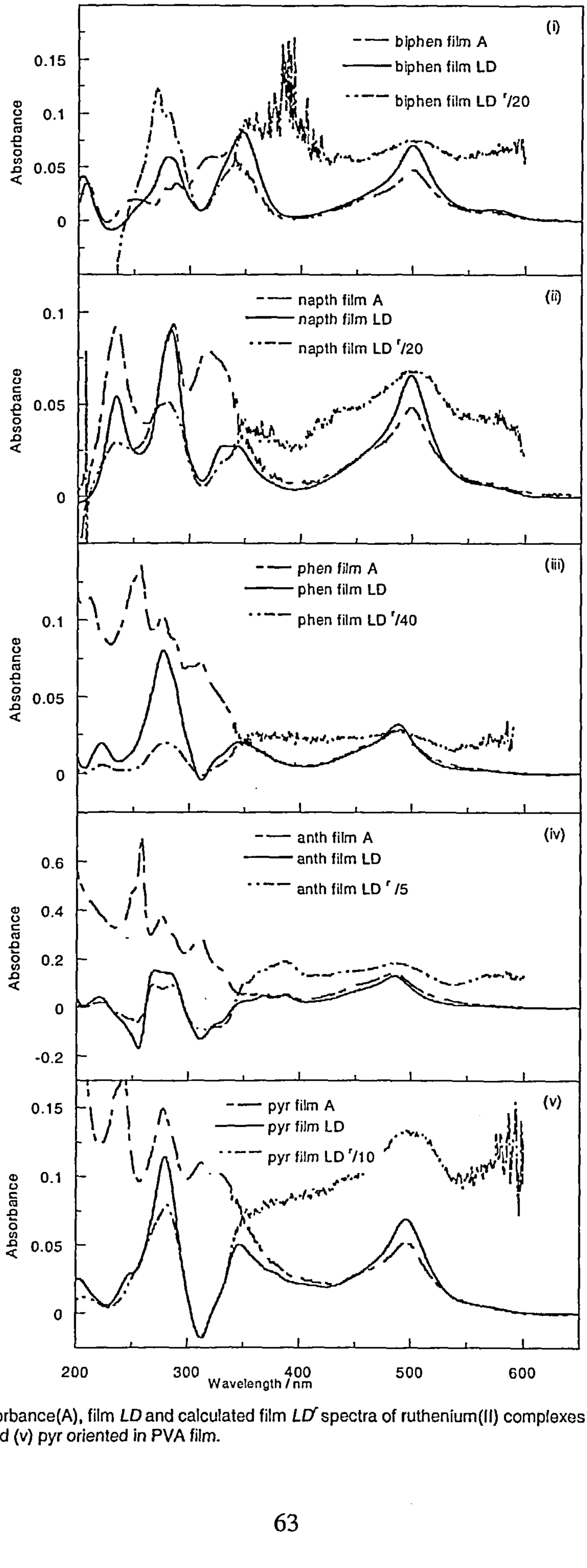

Figure 2.14 Film absorbance(A), film *LD* and calculated film *LD'* spectra of ruthenium(II) complexes (i) biphen, (ii) napth, (iii) phen, (iv) anth, and (v) pyr oriented in PVA film.

Table 2.3 Qualitative polarisation assignments of each complex based on the film *LD* studies

Complex		x/y polarisations / nm	z polarisations / nm
$[Ru(terpy)_2]^{2+}$core	assigned terpy	310 (*l*), 330^{sh} (*l*)	200 (*s*), 275 – 290 (*s*)
biphen	assigned terpy	310 (*l*), 330^{sh} (*l*)	270 – 280(*s*)
	assigned biphen	225 – 250 (*s*), 250(*s*)	200 – 220 (terpy(*s*) + biphen(*l*) mix), 330^{sh} – 400 (terpy (*l*) + MC + biphen LC(*l*))
	assigned MLCT		495, 575^{t}
napth	assigned terpy	310(*l*), 330^{sh} (*l*)	280(*s*)
	assigned napth	200 – 210 (terpy(*s*) + nap(*s*))	225 – 230(nap (*l*)), 340^{sh} – 400 (MC+ nap(*l*) mix)
	assigned MLCT		490, 570^{t}
phen	assigned terpy	310 (*l*), 330^{sh}(*l*)	280 (s)
	assigned phen	200 – 210 (terpy(*s*) + phen (*l*) mix)	225(s)(minima assumed z polarised), 275 (phen (*s*)), 330^{sh}-400(terpy (*l*) + MC + phen (*s*) mix)
		250 (*l*)	
	assigned MLCT		490, 575^{t}
anth	assigned terpy	310(*l*), 325^{sh} (l)	200(*s*), 275 (*s*), 290 (*s*)
	assigned anth	245 – 250 (*l*)	225 (*s*), 340-400 (anth IL(*s*) + tpy(*l*) + MC mix)
	assigned MLCT		450, 490, 575^{t}
pyr	assigned tepy	310(*l*), 330^{sh} (*l*)	280 (*s*)
	assigned pyr	200-220 (terpy (*s*) + pyr (*l*) *mix*),	240^{sh} (*s*) 340(*s*)
		350 – 400 (pyr IL (*l*)+ terpy(*l*) + MC(*s*))	
	assigned MLCT		420, 490, 570^{t}

l = long axis *s*= short axis, sh = shoulder, t=tail, IL = in ligand

It is not possible from the *LD* data to determine anything about the inter-aryl twist of the tail with respect to the terpy group since the non-z axis lies in the x/y plane of the uniaxial rod. Regions with significantly sloping LD^r signals are indicative of overlapping bands of different polarisations.

2.3.3 Preliminary studies of the interaction of ruthenium terpy complexes with ct-DNA

The visible absorption spectra of the complexes in the absence and presence of DNA in a 10:1 DNA base:complex ratio are illustrated in Figure 2.15. As both ct-DNA and the ruthenium complexes have overlapping transitions below 300 nm, metal complex spectral changes can be most easily seen above this wavelength where ct-DNA has no absorbance. A change in each of the five complexes' absorption spectra is observed on addition of ct-DNA. The change is least for the anth and phen complexes. The most notable changes are as follows:

(i) The wavelength shifts to longer wavelength (red shift) for all complexes. The effect is particularly noticeable for the biphen and napth complex where the solution changes from red-orange to pink. The other complex colour changes are more subtle as illustrated by the absorbance spectra.

(ii) The terpy transitions are in general not perturbed significantly upon binding to DNA. The 300–350 nm region of the spectrum shows very little change for anth, small changes for napth, phen and larger changes for biphen (wavelength shift) and pyr (intensity reduction). In the biphen case, some of the change may be due to changes in the biphen IL spectroscopy.

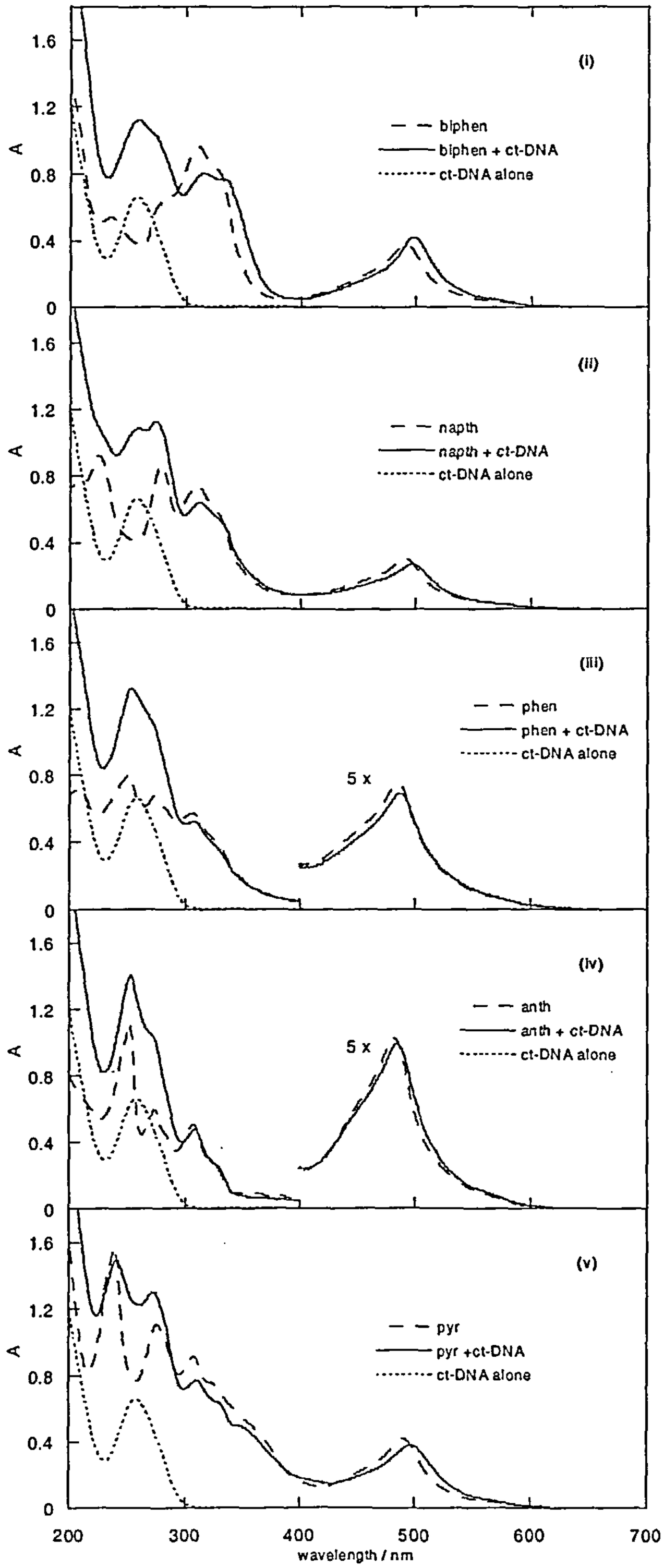

Figure 2.15 Absorption spectra of aqueous ruthenium(II) complexes (i) biphen, (ii) napth (iii) phen (iv) anth and (v) pyr in the presence and absence of ct-DNA in a [10 μM complex: 100μM ct-DNA] ratio. The dotted line represents the DNA alone in solution, the dashed line the metal complex alone in solution, the solid line is complex + ct-DNA.

(iii) The MLCT bands of phen and anth show a very small hypochromic effect and those of napth and pyr a larger one in addition to a red wavelength shift. Biphen by way of contrast shows a hyperchromic effect. This suggests that the biphen complex behaves in a different fashion to the other four complexes.

(iv) There is significant hypochromism in the DNA region of the spectrum for pyr and anth (where the magnitude of the absorbance is lower when the DNA is added at ~240 nm)

It is therefore clear that each complex binds to DNA in a binding mode that is close enough and strong enough to affects its absorption spectroscopy. An appreciable decrease in absorbance and a wavelength shift can be indicative of strong binding. A wavelength red-shift and hypochromic effect for π-π^* transitions on addition of DNA is often indicative of a π-π^* stacking interaction, usually due to intercalation between DNA base pairs or oligomerisation mediated by the DNA template.

The $[Ru(terpyAr)_2]^{2+}$complexes alone in solution are achiral and therefore do not exhibit a signal in *CD*. Addition of ct-DNA (~100 μM) to a constant complex concentration (10 μM) in a [10:1] DNA base:metal ratio, induces chirality in the complex transitions as illustrated in Figure 2.16.

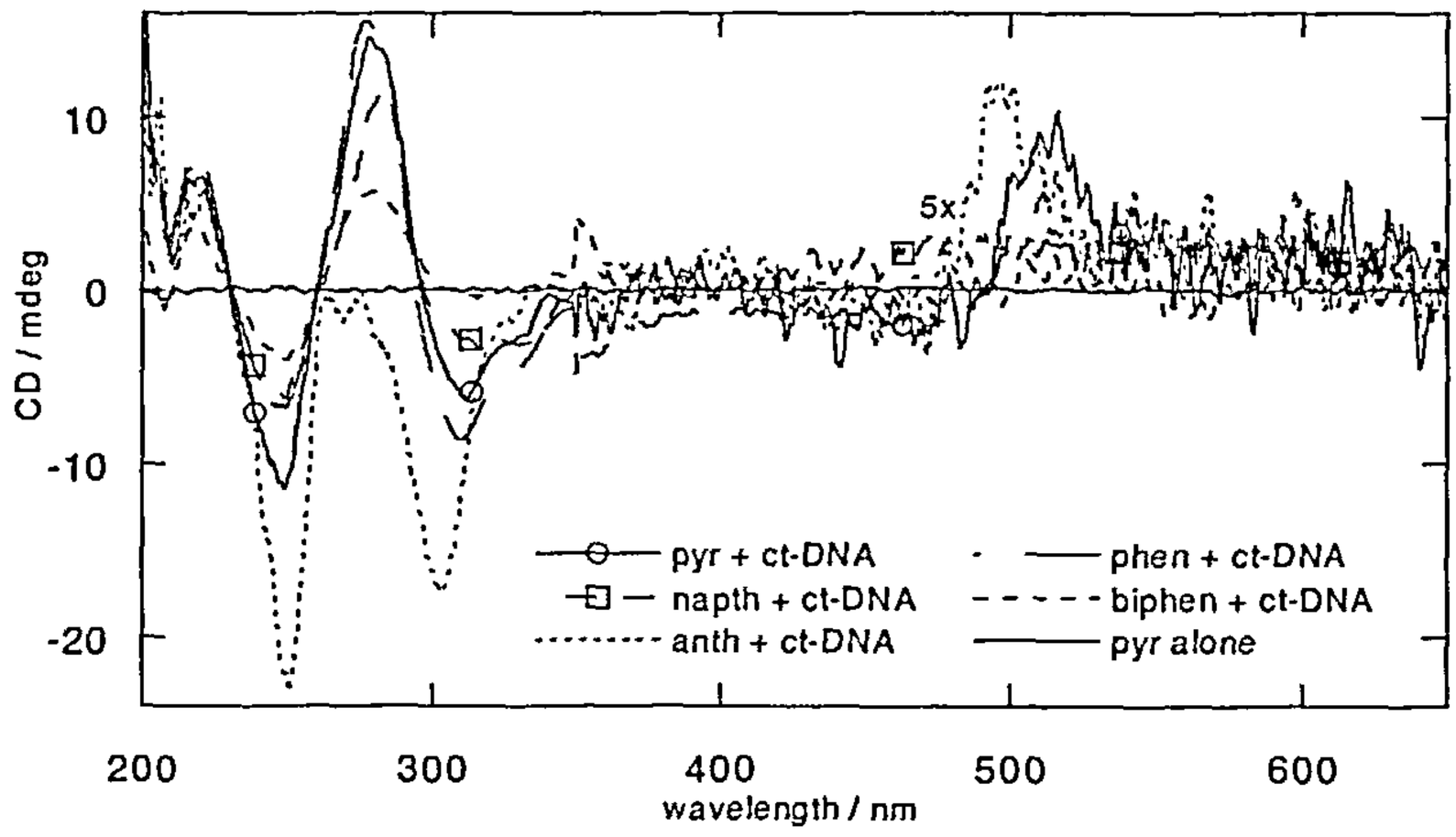

Figure 2.16 *CD* spectra of the ruthenium(II) complexes in the presence and absence of DNA (10:1 DNA base:metal complex ratio). The 350 nm – 650 nm region of the spectra has been magnified 5x

All five ruthenium(II) complexes exhibit a chiral signature on interaction with ct-DNA but not alone in solution as demonstrated by the flat unbroken line for the pyr complex on its own. The MLCT signal is positive above 500 nm and may be small positive or negative below this point. The terpy region from 300–350 nm gains a negative signal in each case. All the complexes except anth have a larger positive peak (which will include the DNA signal) at 275 nm. In the anth case, this positive component may be cancelled by the large negative 250 nm induced *CD* (*ICD*) of the anth itself.

Preliminary fluorescence studies

$[Ru(terpy)_2]^{2+}$ does not fluoresce in water at room temperature.[12,14,17,29–32] However, substitution in the 4′ position on the terpy ligand with electron withdrawing or donating groups,[11,13,14,17,19,29,31,67,68] has been shown to lead to a fluorescence signal.[17,71] All five tail groups of Figure 2.1 are aromatic and conjugated and some of them, including anthracene, pyrene, and phenanthrene, are themselves fluorophores.

Fluorescence studies on these ruthenium(II) complexes were therefore undertaken in aqueous solution at room temperature, in the presence and absence of ct-DNA. The complexes were excited at IL terpy, aryl tail and MLCT transitions. The excitation wavelengths (λ_{ex}) were as follows: for IL terpy (λ_{ex} = 270–280 nm, 310 nm), aryl tail transitions (λ_{ex} for pyr = 240 nm, anth = 250 nm, biphen = 235 nm, napth = 225 nm, phen = 250 nm) and MLCT (λ_{ex} ~ 490 nm).

Excitation of the MLCT band both before and after DNA addition resulted in no fluorescence or quenching. On excitation of the IL terpy and aryl tail bands, the complexes did exhibit a little fluorescence alone in aqueous solution (of less than 100

intensity units) in the 350 – 400 nm region assigned predominately to the aryl tails. On addition of ct-DNA (100 μM DNA to a 10 μM complex in a 10:1 ratio), the anth, biphen and pyr complexes exhibited a small enhancement in fluorescence whilst the napth and phen complexes exhibited fluorescence quenching.

As no significant fluorescence change was seen, we concluded that all complexes are generally non-luminescent in aqueous solution at room temperature despite the intrinsic fluorescence of the tail groups. Fluorescence studies were therefore not pursued further.

2.3.4 Titration series to investigate the interactions of the metal complexes with DNA

On the basis of the promising preliminary results, further investigations, using absorbance and *CD* and flow *LD* were undertaken over a wide range of DNA base:complex ratios to probe the interactions with ct-DNA and where appropriate with AT and GC DNA. Each complex-DNA interaction was investigated over a mixing ratio, R, of [20:1–1:1] DNA base:metal complex. At the 20:1 limit isolated binding may occur, whereas at 1:1 this is not possible.

2.3.4.1 UV-Visible absorbance titration spectra

The absorbance titrations of each complex with constant ct-DNA concentration (100 μM) are shown in Figure 2.17. The general trend of all five absorption spectra is, as expected, an increase in absorbance intensity as the complex concentration is increased with transitions of both the DNA and complex overlapping below 300 nm.

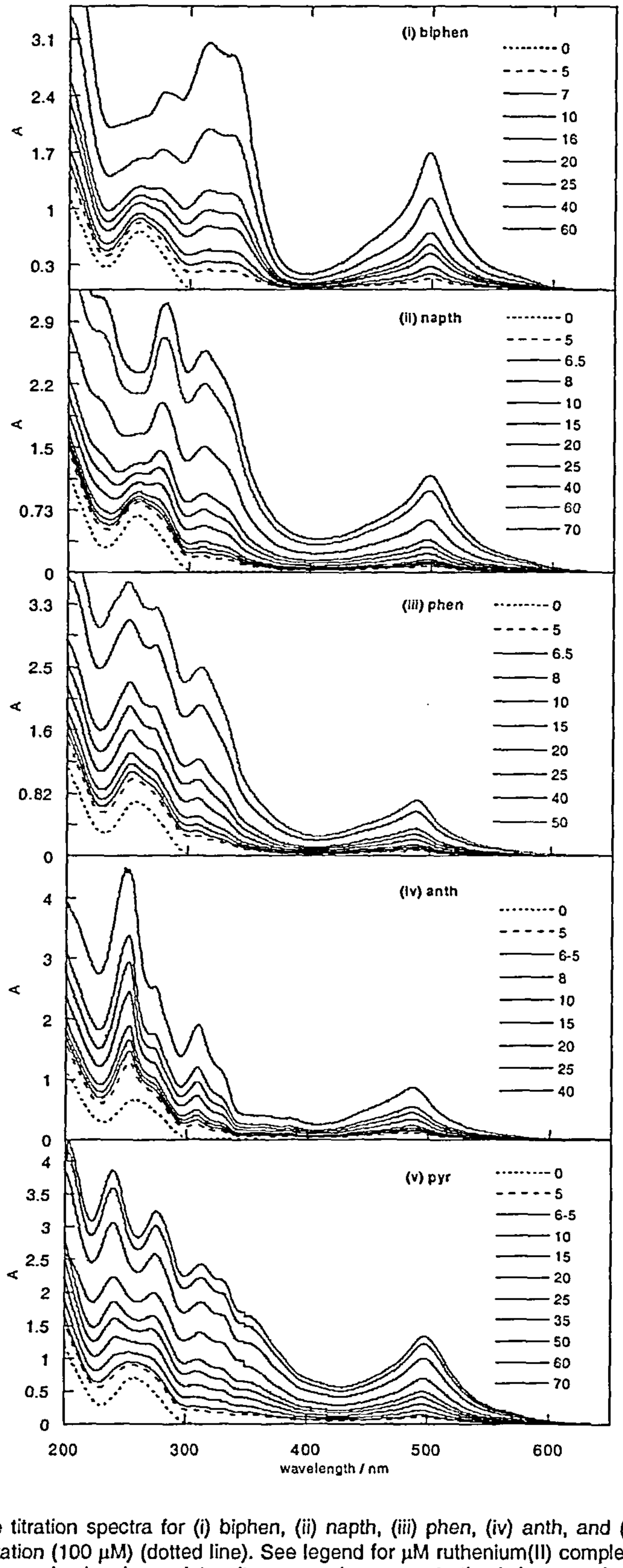

Figure 2.17 Absorbance titration spectra for (*i*) biphen, (*ii*) napth, (*iii*) phen, (*iv*) anth, and (*v*) pyr. Working with a constant ct-DNA concentration (100 μM) (dotted line). See legend for μM ruthenium(II) complex concentrations added. Each series shows an increase in absorbance intensity as complex concentration is increased.

2.3.4.2 Circular dichroism titration spectra

CD provides information about the spectroscopically active chiral species in solution. Thus the metal complexes will give a zero signal unless they are bound to the chiral DNA. Although in principle *CD* can be used to give geometric information about the observed species,[70] in practice this is often very difficult. *CD* is, however, usually the most sensitive spectroscopic technique for probing changes in binding mode as a function of concentrations and/or mixing ratios.[70] The *CD* titration series for each metal complex with ct-DNA is given in Figure 2.18

The anth, pyr and phen complexes (Figure 2.18(i) – (iii)) exhibit similar *CD* behaviour. They have positive MLCT signals at all ratios and small signals for the long wavelength tail transitions. At the low metal complex loads the 310 nm terpy regions of the spectra have negative *CD* bands and the DNA region is dominated by the DNA *CD* signal. At ~ 7:1 (DNA base:metal complex) for anth and ~ 4:1 for pyr and phen, the terpy region and the DNA region take on a very different form, indicating the switching on of a second binding mode. In each case there is an isosbestic point at the 310 nm absorbance maximum and the magnitude of the signals in this region and the DNA region increases significantly, though the increase is proportional to the metal complex added. The form and magnitude of the spectra suggest a degenerate exciton interaction between terpy groups and perhaps also between tail groups (there is *e.g.* an approximate isosbestic point at the anth maximum at ~250 nm).

The napth complex (Figure 2.18(iv)) by way of contrast has an isosbestic point throughout the whole series near the maximum of the 275 nm DNA band even though the 310 nm terpy region changes its spectral form gradually throughout the series, though remaining negative in sign. This is consistent with either a gradual occupation of a second mode (as opposed to two sequential modes) or a single binding mode which

demonstrates sequence selectivity. Its MLCT band is also significantly smaller than that of the other complexes. The signal (and presumably the specific binding) also saturates at about R = 2:1 (by 70 μM metal complex it is probably condensing).

The biphen complex (Figure 2.18(v)) also shows little change in the shape of its *CD* spectrum over the whole range of mixing ratios, though the very low metal complex load spectra are different in shape from the medium and high loadings. There is a small MLCT signal, the 330–400 nm biphen signal saturates at a comparatively small signal by R = 3.3:1, and the DNA region is largely unaffected by the addition of the metal complex. The data is consistent with a single binding mode, though weak signals may mask changes. The magnitude of these signals is typical for metal complexes binding to DNA.[1]

Figure 2.19 shows the *CD* spectra of the interactions of biphen with ct-DNA, GC DNA and AT DNA, the equivalent GC and AT DNA absorbance spectra are given in Appendix 2.2. The biphen complex behaves with GC in a manner similar to its ct-DNA behaviour except that the positive 350 nm band is not observed (Figure 2.19(i) – (ii)). With AT DNA (Figure 2.19(iii), the 310 nm terpy band is smaller than with ct-DNA and of opposite sign, while the 350 nm band is larger and also of opposite sign. The AT MLCT band is very small and negative in sign and the DNA region is perturbed by the metal complex. With AT DNA, at high metal complex loadings (above 5:1) there is a significant increase in signal magnitude in the 300 – 400 nm part of the spectrum, which corresponds to a negative exciton signal of the tail. At low loadings this mode is already dominating the spectra, suggesting a cooperative π-π self-stacking mode. The opposite *CD* signs for ct-DNA and AT DNA indicate that the twist of the biphen is opposite in each case. It is unusual to see such different behaviour with GC, AT and ct-DNA: the *CD* spectra suggest different binding modes with all of them.[10]

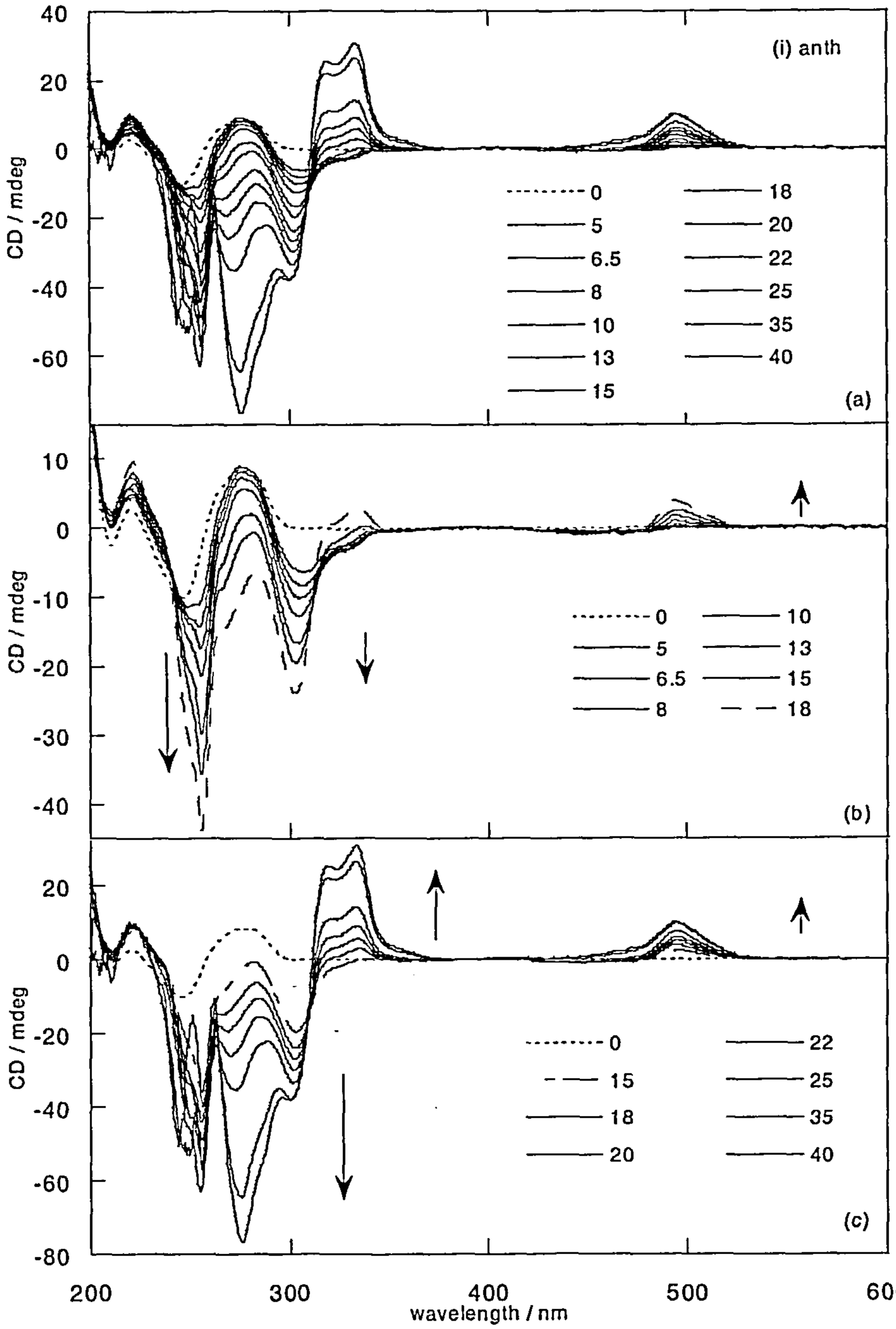

Figure 2.18 *CD* titration series for ruthenium(II) complexes (i) anth, (ii) phen, (iii) pyr, (iv) napth, and (v) biphen. Working with a constant ct-DNA concentration (100 μM)(dotted line) over (a) all mixing ratios, (b) at low complex concentrations and (c) at higher concentrations. Legend states μM ruthenium(II) complex concentration added.

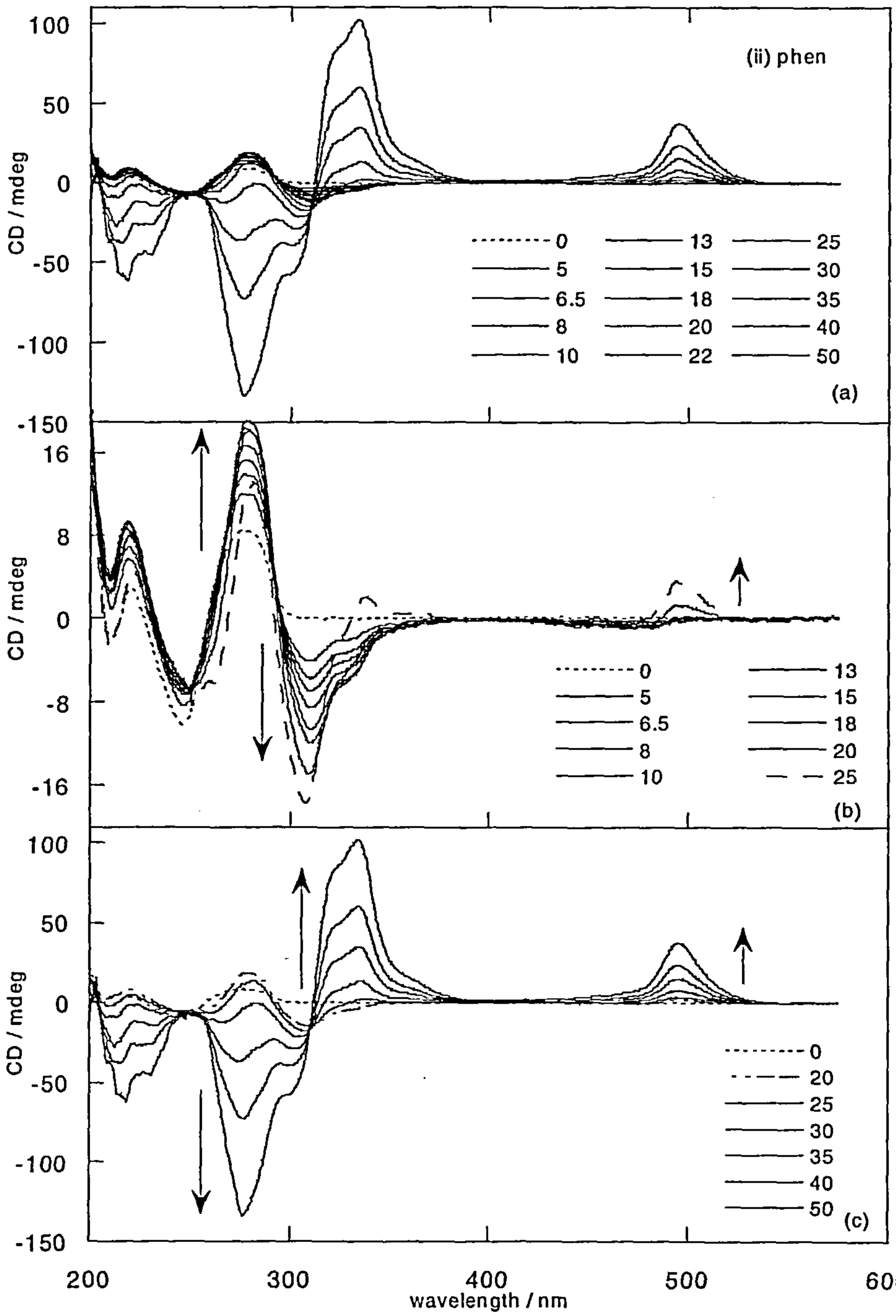

Figure 2.18 (ii) phen

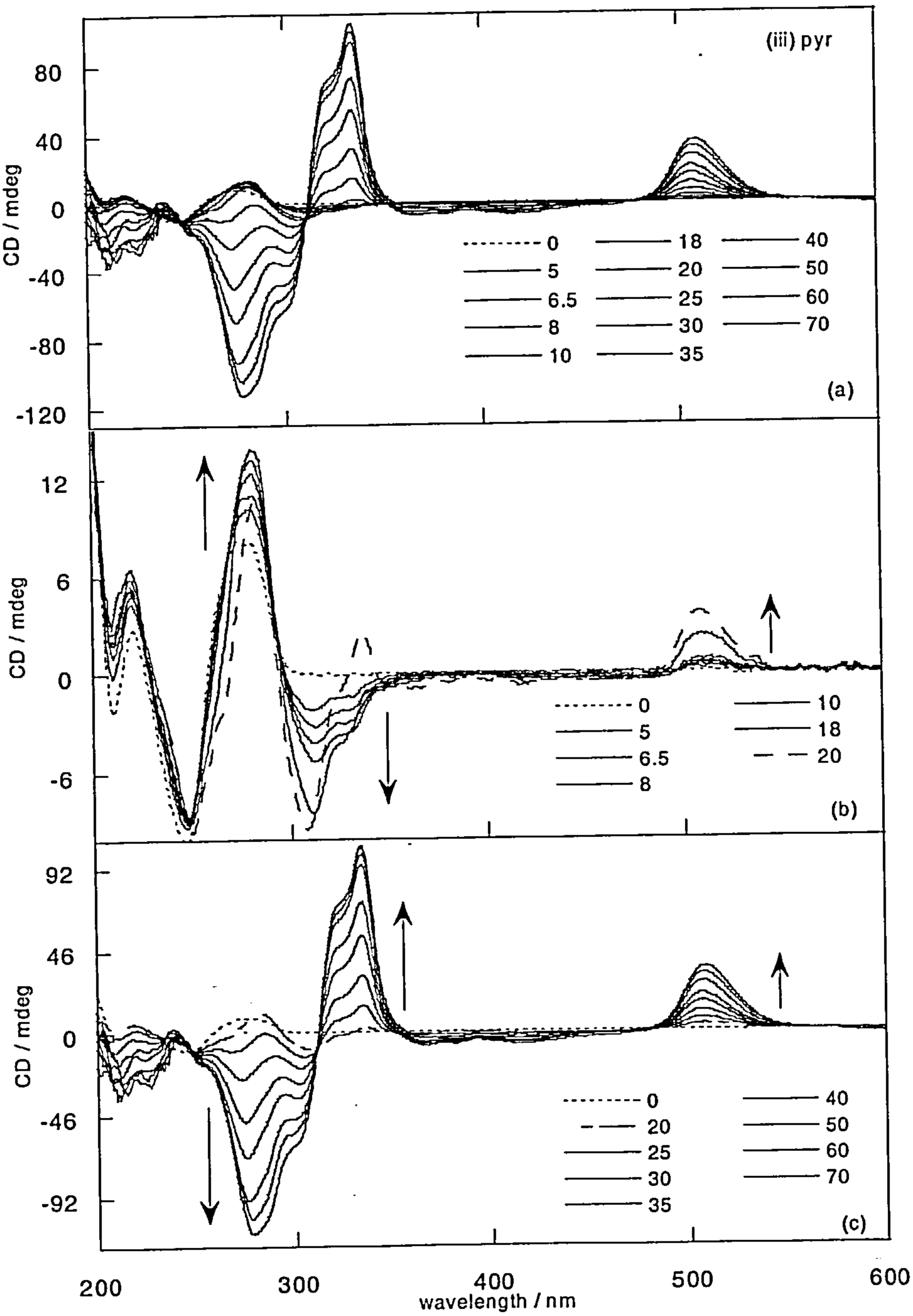

Figure 2.18 (iii) pyr

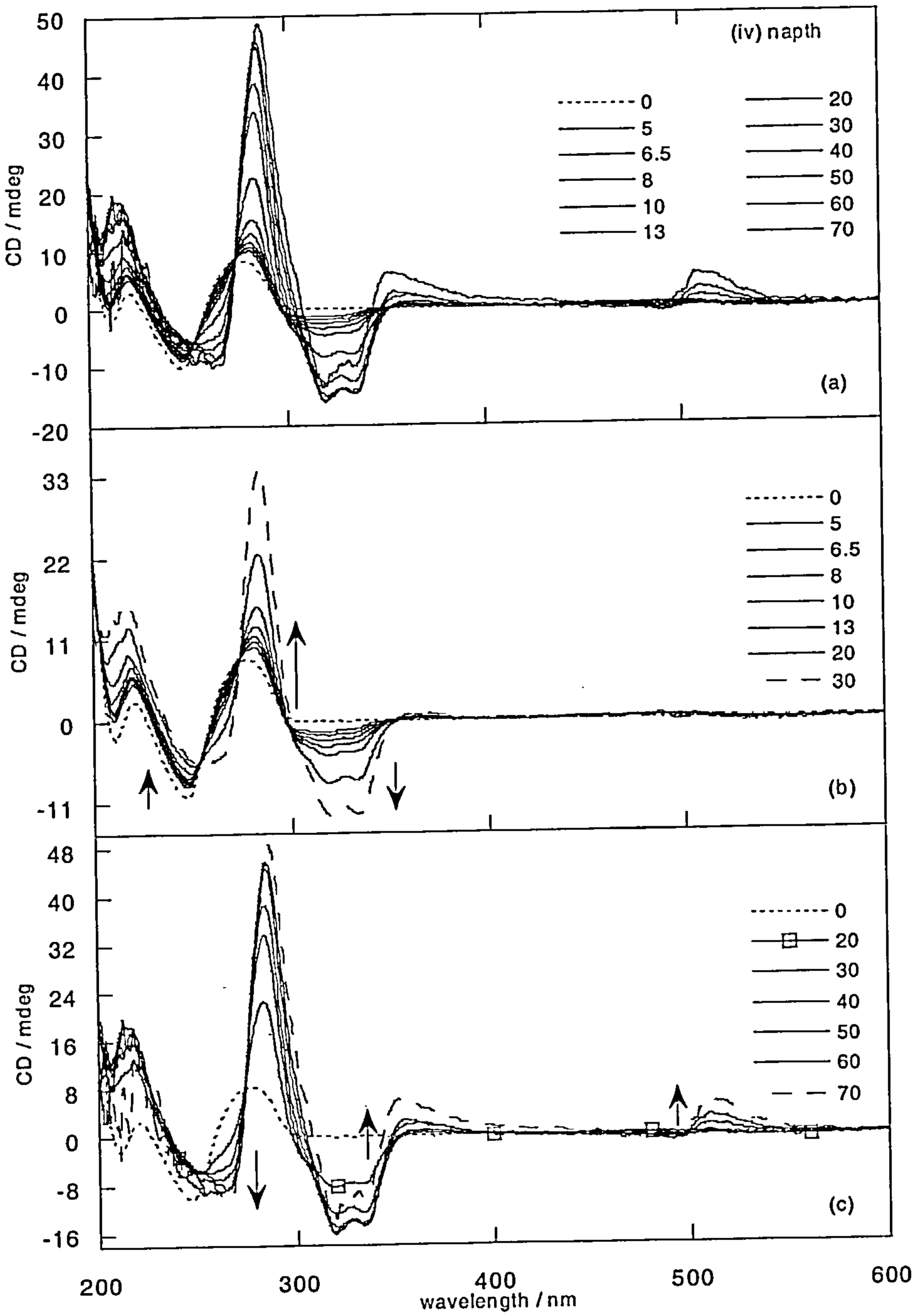

Figure 2.18 (iv) napth

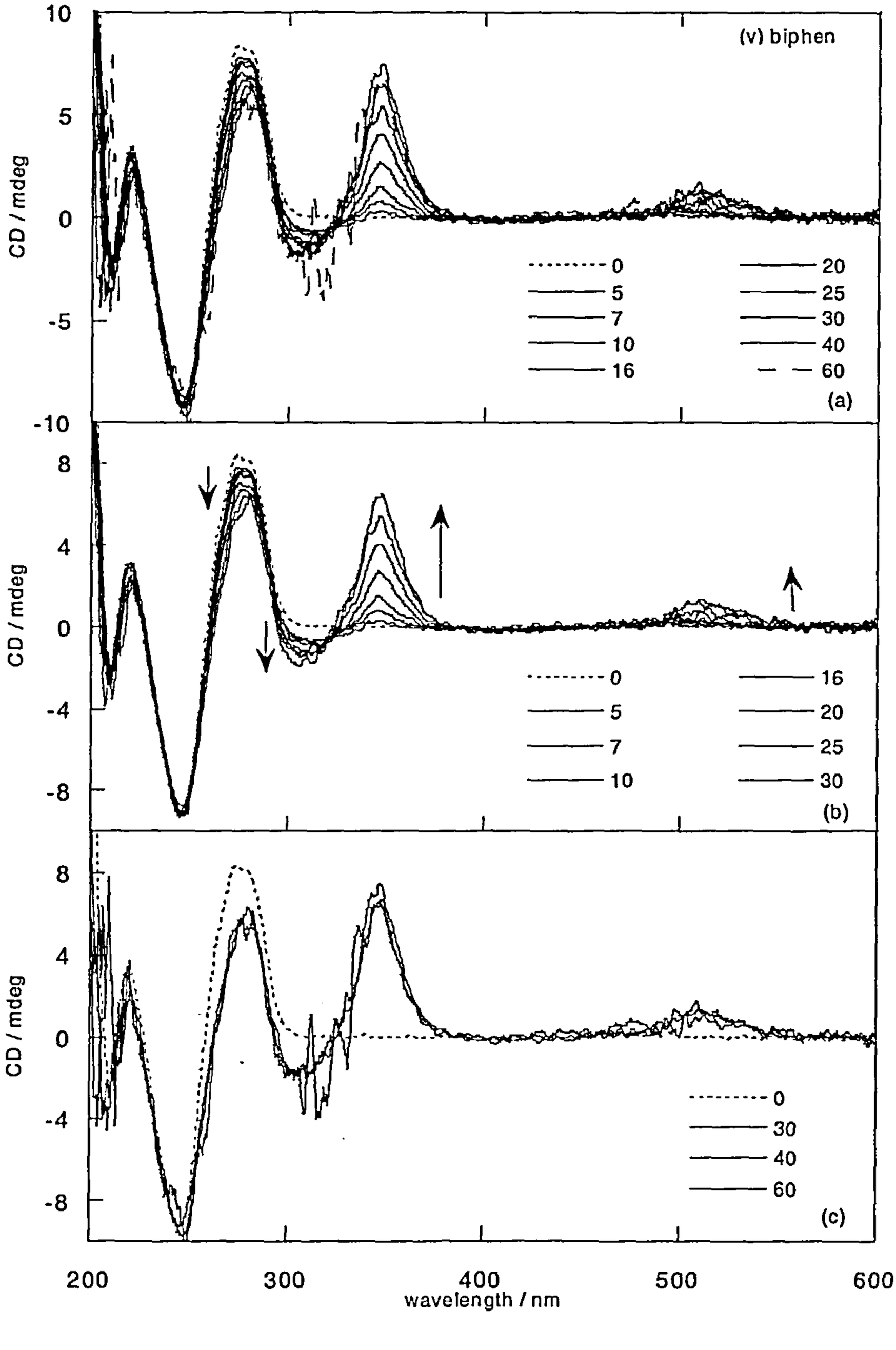

Figure 2.18 (v) biphen

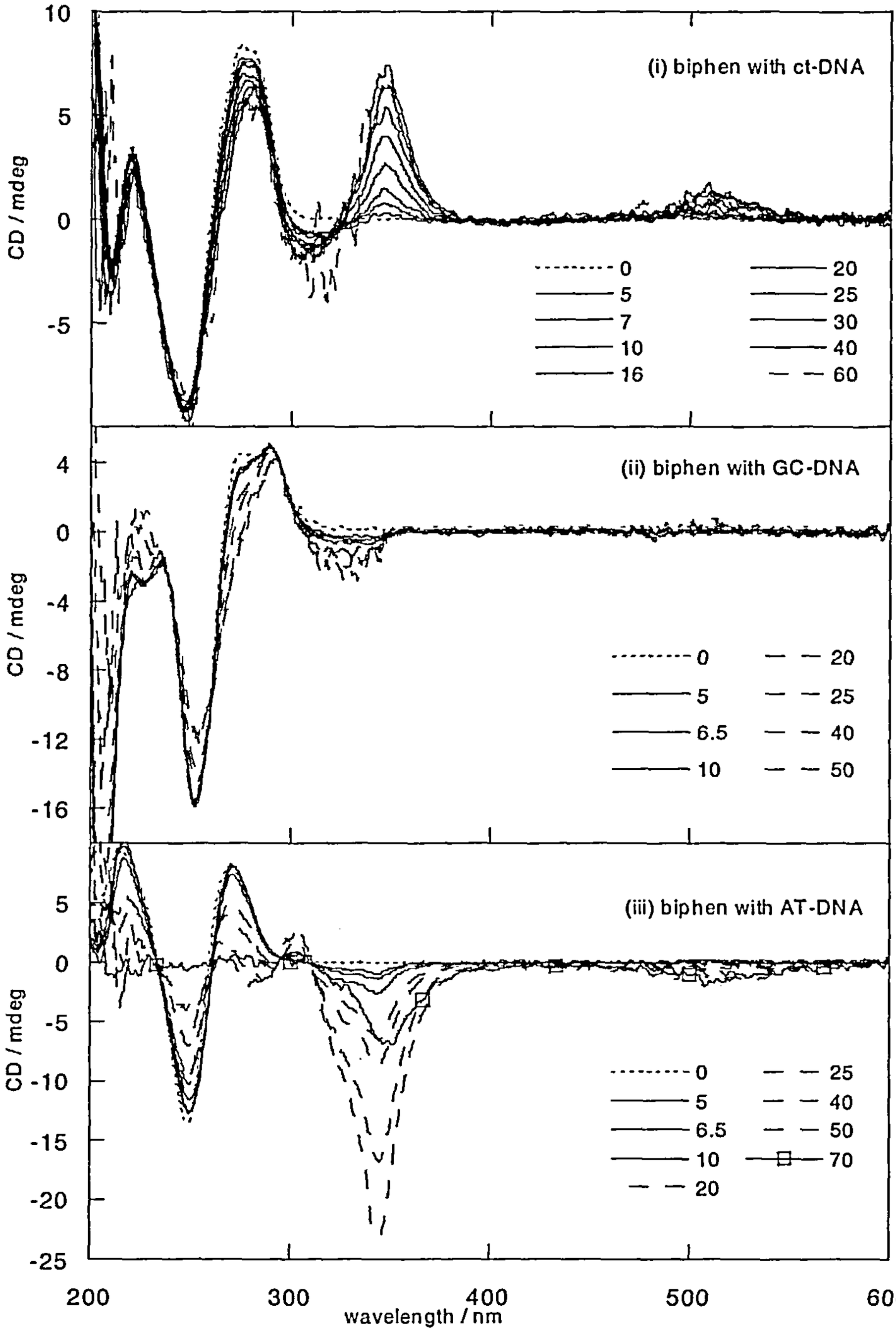

Figure 2.19 *CD* titration spectra of biphen with (i) ct-DNA, (ii) GC DNA and (iii) AT-DNA. Working with a constant DNA solution of 100 μM (*dotted line*). Legend indicates μM concentration biphen added. Titration spectra (i) has been reproduced from Figure 2.18 (v) for ease of comparison.

2.3.4.3 Flow linear dichroism titration spectra

DNA exhibits a negative flow *LD* signal between 200 – 300 nm, due to the transitions of its bases being approximately perpendicular to the long axis of DNA. All five complexes also give rise to *LD* signals above 300 nm upon addition to DNA. As the DNA absorbance is overlaid by metal complex transitions, the orientation of the DNA bases is not clearly distinguishable using LD^r in the presence of the metal complexes. An independent check of the DNA orientation was therefore made at varying metal concentrations by measuring the *LD* of a probe, methylene blue (MB), a known intercalater.[8] A small amount of MB was used such that the DNA signal remained relatively unperturbed. Appendix 2.1 contains the flow *LD* and LD^r spectra for the complexes with MB.

For each complex at R = 20:1, the MB + DNA + metal complex MB *LD* signal was found to be larger in magnitude than that of the MB + DNA alone with the ranking order being phen > pyr > napth > anth > biphen >metal complex free DNA (*i.e.* MB + DNA alone). However, as the metal complex concentration increased, the MB signal was found to decrease in magnitude with the exception of anth. This suggests that at R = 20:1 the DNA is either unwinding or lengthening or stiffening — all characteristic of intercalation. At higher R, bending or kinking of DNA or simply displacement of the MB by the metal complexes may be taking place.

Flow *LD* titrations were undertaken, in order to determine the orientation of the metal complexes on the DNA. Figure 2.20 shows the flow *LD* titration spectra of four of the five (anth, phen, pyr and napth) metal complexes on interaction with ct-DNA. Anth, phen and pyr exhibit similar flow *LD* titration spectra (Figure 2.20(i)–(iii)), with a negative MLCT region, negative tail region from 350–400 nm, and positive terpy region between 300 and 340 nm. Although the spectra are suggestive of only a single binding

orientation for each complex, there is a subtle change in the shapes of the spectra from ~4:1 anth and pyr and ~2:1 for phen. As the concentration of each complex is increased, from R = (20:1 – 4:1) for anth and pyr and (20:1 – 2.5:1) for phen, their *LD* spectra show an increase in the negative magnitude of the band centred at 260 nm attributed to DNA, with a progressive red shift leading to the sharpening of the transition to ~275 nm as the terpy transition gradually appears superimposed over the DNA signal. The anth spectra also show a sharp positive 250 nm band and phen and pyr have a shoulder in this region suggesting the presence of a positive band that is cancelled by the negative signal due to the DNA and perhaps other transitions. At higher metal complex concentrations, the prominent 275 nm terpy(s) band decreases in magnitude (less negative, more positive) for all three complexes, this suggests that the low and high loading binding modes are oriented in similar fashions.

The napth pattern (Figure 2.20(iv)) is similar to the anth, phen and pyr metal complexes at lower metal complex loadings except that the positive terpy 300–340 nm region is cancelled by the tail of the negative napth band. At higher metal complex concentrations the MLCT band first shows cancelling positive and negative signals and finally there appears to be a significant red shift of the band and a net small positive peak. The decrease of the negative signals is apparent from about 40 μM napth complex, though the positive signal is not dominant until 85 μM. This suggests that there are 2 modes in operation simultaneously with the second binding mode operative at higher metal complex loads ~2:1 mixing ratios, as opposed to one binding mode with some sequence selectivity. There is significant decrease in all the *LD* signals (though no corresponding decrease in absorbance signal) at these higher concentrations, which implies loss of orientation for both complex and DNA, which may be associated with DNA bending or coiling.

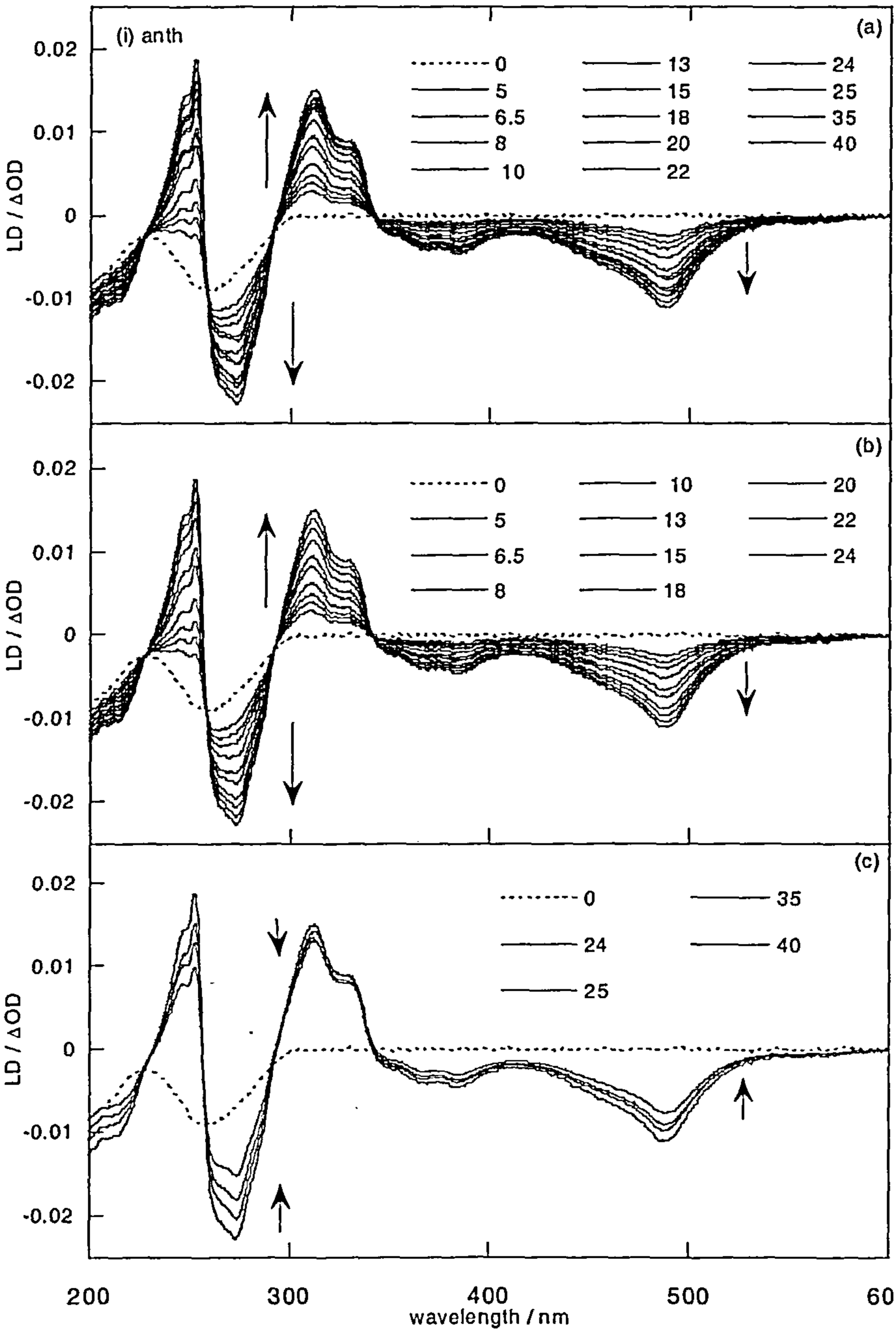

Figure 2.20 Flow *LD* titration spectra for (i) anth, (ii) phen, (iii) pyr, and (iv) napth. *Working with constant ct-DNA* (100μM) (dotted line) over (a) all mixing ratios, (b) at low complex concentrations, and (c) at higher concentrations. Legend indicates μM metal complex concentration added.

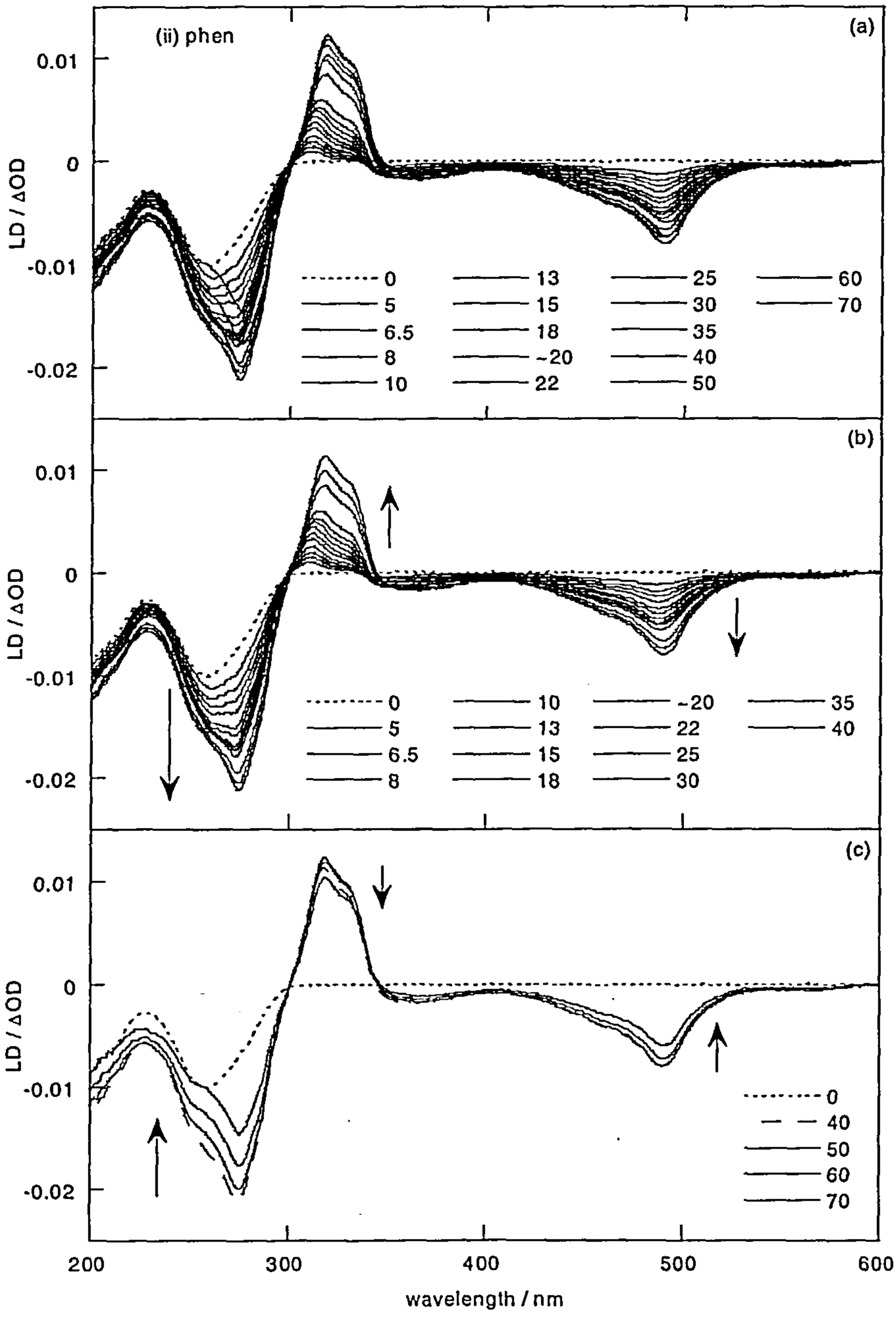

Figure 2.20 (ii) phen

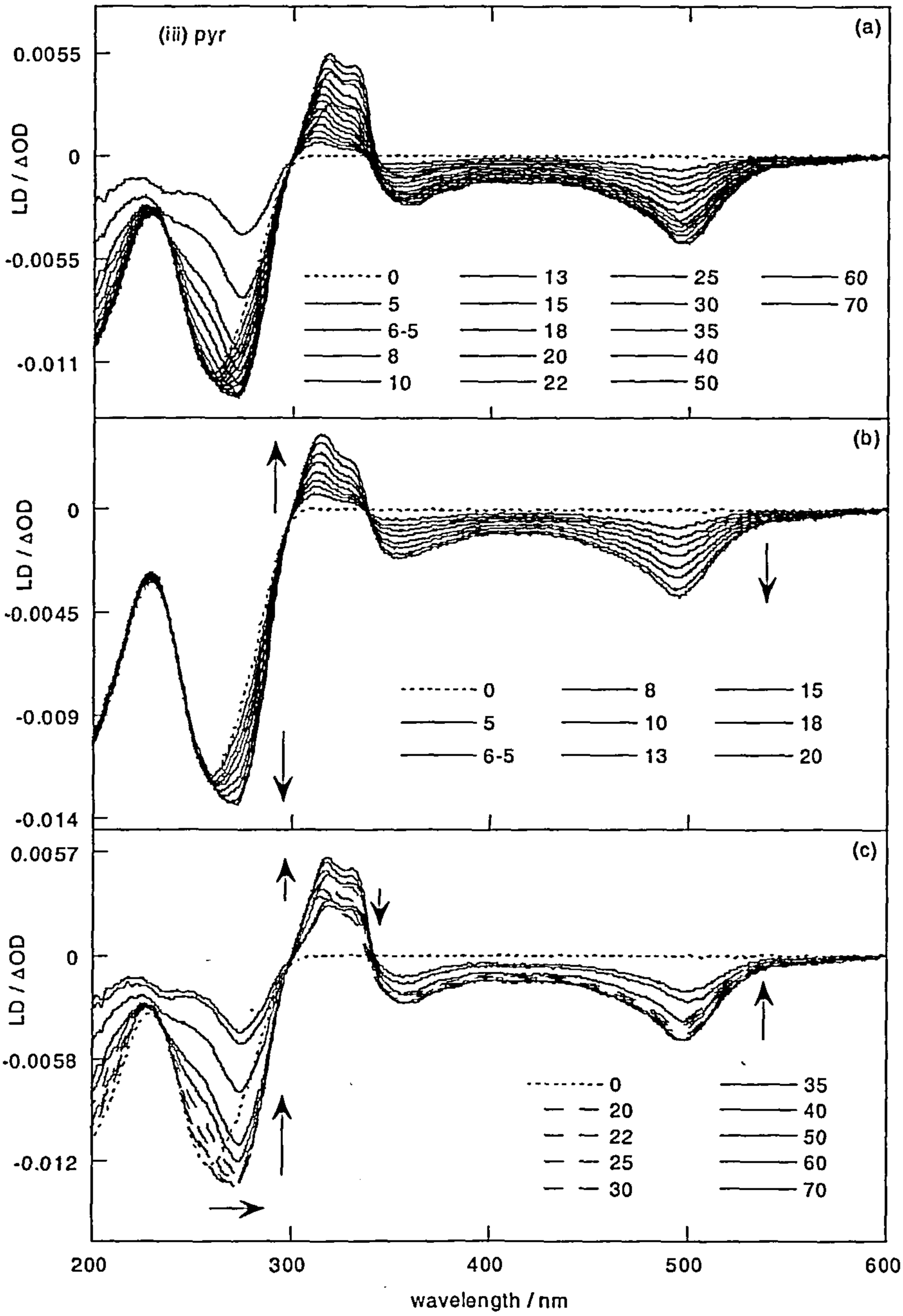

Figure 2.20 (iii) pyr

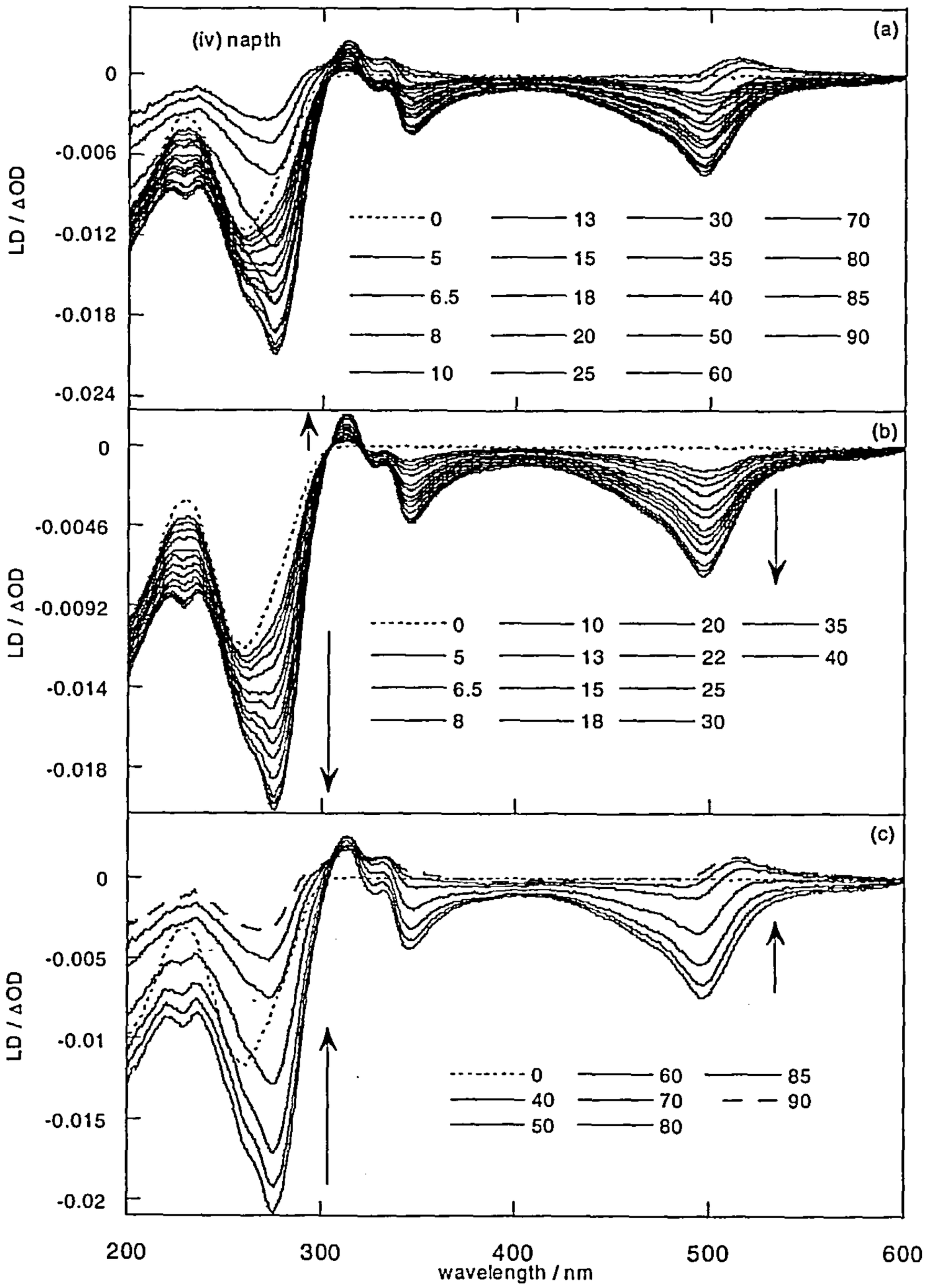

Figure 2.20 (iv) napth

To probe whether it was a sequence variation that gave rise to the high metal complex load differences, *LD* titration experiments with GC DNA were undertaken. For the anth, phen and pyr complexes, the *LD* spectra with GC DNA (Figure 2.21(i – iii)) are superficially similar to those with ct-DNA but show significantly greater signals in the aryl tail bands (350–400 nm) at medium metal complex loadings. The napth GC (Figure 2.21(iv)) results are similar to those of ct-DNA except that the positive 310 nm ct-DNA signal is a negative minimum with GC and the 275 nm band is smaller in magnitude than the 260 nm band for GC.

The biphen *LD* spectrum on interaction with ct-DNA (Figure 2.22(i)) is different to those for anth, phen and pyr and napth, with the MLCT region being positive at all mixing ratios and the spin forbidden transition having a clearly identifiable signal (rather than just being almost a shoulder under the MLCT band long wavelength tail as is the case for the other complexes). The terpy region of the biphen spectrum is positive, however the 310 nm region is a minimum rather than a maximum suggesting its *LD* is actually negative. The DNA region *LD* is negative, but of lower magnitude than the signal due to DNA alone, in contrast to the other metal complexes.

In order to determine whether there was any sequence dependence of the unusual behaviour of the biphen complex, the *LD* with AT and GC DNA were measured (Figure 2.22(ii) and (iii)). The three DNAs show almost identical spectra (except for the lower orientation parameter with the shorter synthetic DNAs). Importantly, the biphen transitions below 350 nm are all positive compared to the negative transitions exhibited by the anth, phen and pyr and to some extent napth complexes. This is another indication of a dissimilar binding interaction of biphen compared with the other complexes.

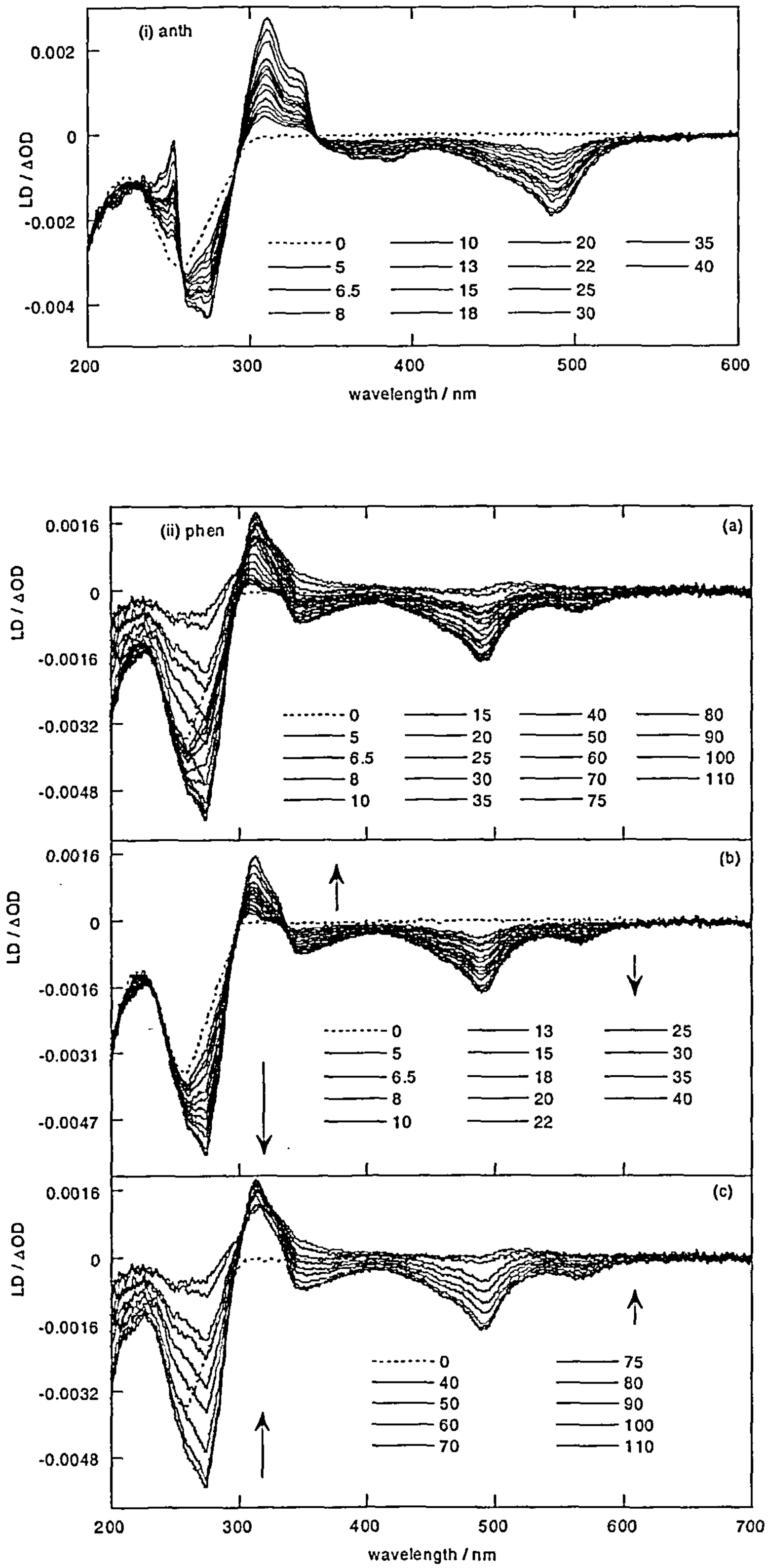

Figure 2.21 Flow *LD* titration series of (i) anth, (ii) phen, (iii) pyr, and (iv) napth with GC DNA. Working with constant GC DNA (100 μM) (dotted line) over (a) all mixing ratios, (b) at low complex concentrations, and (c) at higher concentrations. Legend states μM metal complex concentration added.

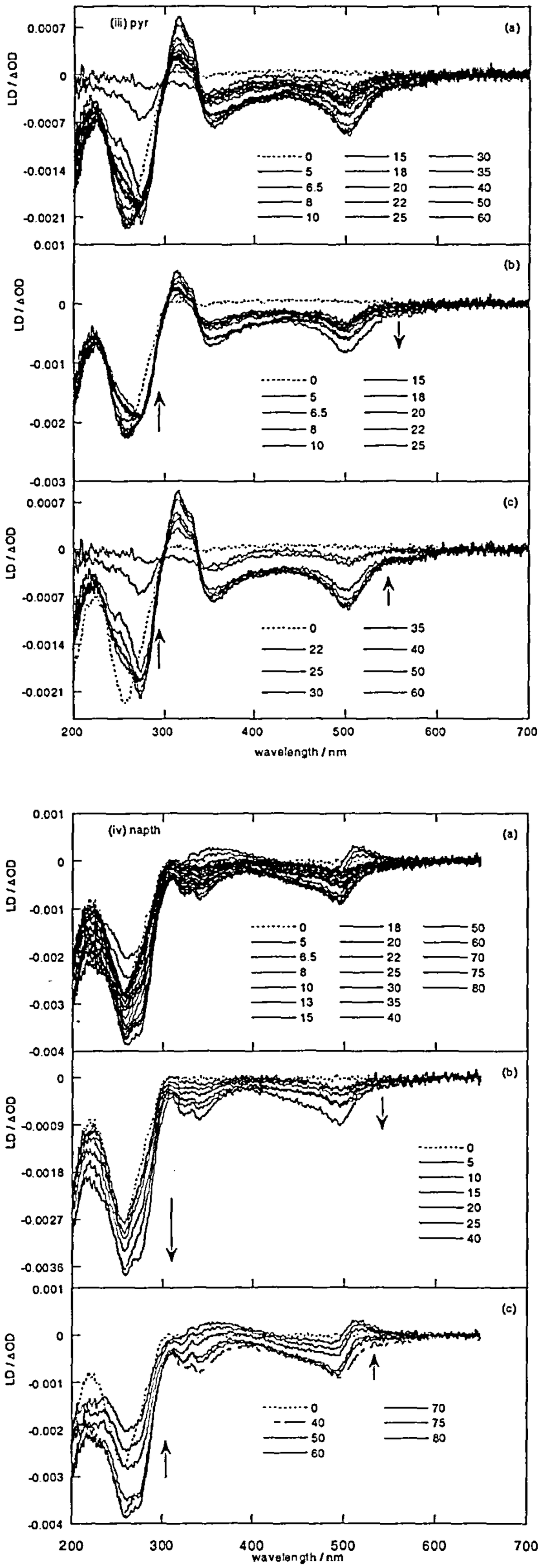

Figure 2.21 (iii) pyr and (iv) napth

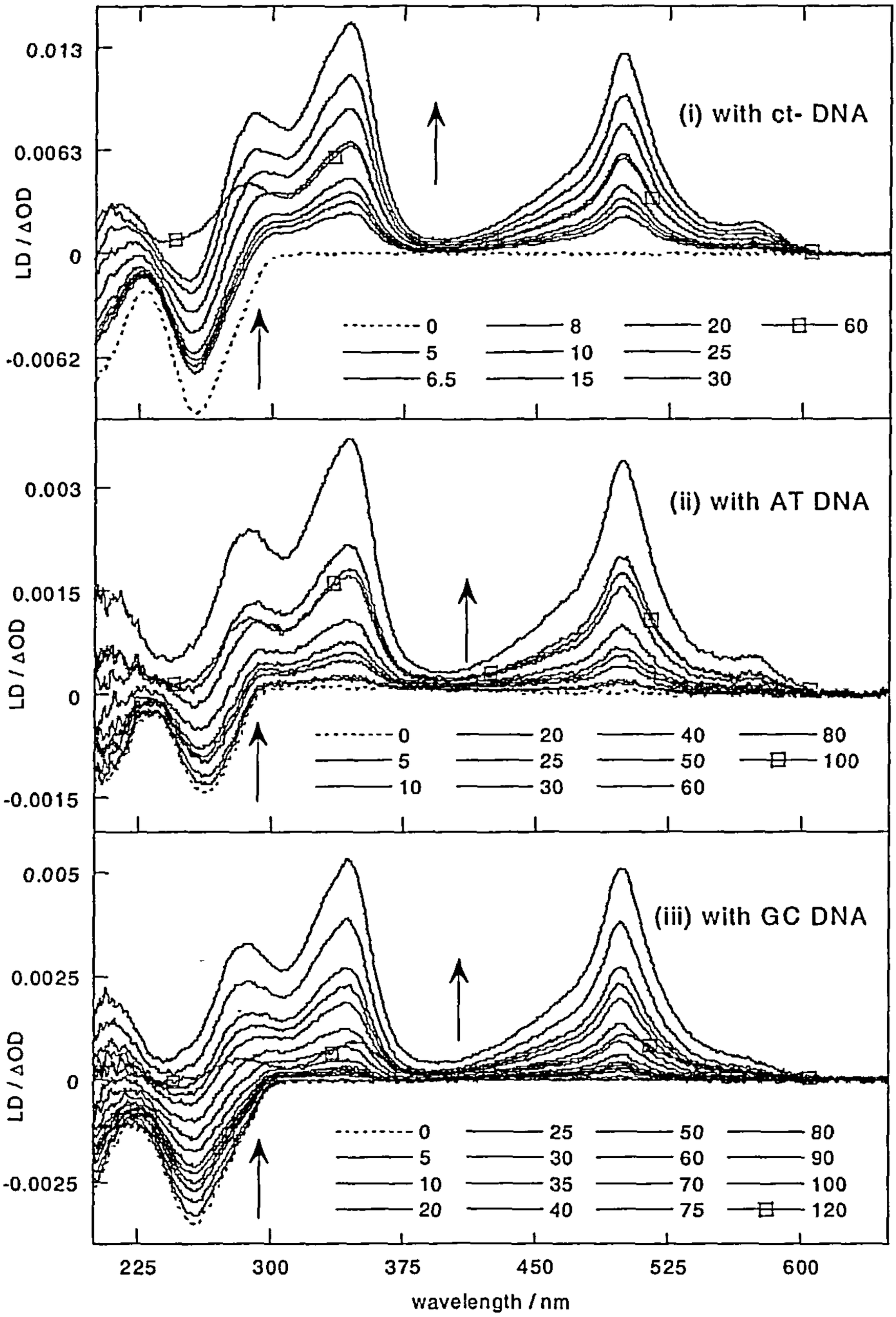

Figure 2.22 Flow *LD* titration spectra for biphen with (i) ct-DNA, (ii) AT-DNA and (iii) GC-DNA. Working with constant DNA concentration (100 μM) (dotted line). The legend states μM biphen complex concentration added. As the biphen complex concentration is increased, all three plots show increasingly positive *LD* signals with plot (a) for ct-DNA exhibiting the largest *LD* signals. At highest biphen concentrations for each plot, (a) ct-DNA, (b) AT-DNA and (c) GC-DNA, *i.e.* 60,100,120 μM respectively the *LD* signal shows a decrease in size, this is due to biphen precipitation.

The LD^r (the *LD* divided by the absorbance) can be used to determine the orientation of the complexes on the DNA. The LD^r spectra for the Flow *LD* titrations of anth, phen, pyr and napth with ct-DNA (Figure 2.20.) are shown in Figure 2.23 and those for biphen with ct-DNA, AT and GC (Figure 2.22) are shown in Figure 2.24. These are an aid to working out the orientation of the complexes on the DNA. Consider first the anth data. The largest magnitude (negative in this case) LD^r signal is in the MLCT region, which the film *LD* showed to be z-polarised. If we assume that this means these transitions are perpendicular to the DNA helix axis (in other words there is not significant local kinking of the DNA helix about the metal complex, which is supported by the MB data), then by comparison with the low metal complex loading DNA region then we must conclude that the z-axis of the metal complex is more perpendicular to the helix axis than the average DNA base. Consistent with this all the z-polarised transitions (*cf.* Table 2.3) have a negative *LD* signal. Thus the z-axis of the metal complexes lies approximately parallel to the DNA bases.

The two terpy groups of necessity lie perpendicular to one another in all complexes as well as perpendicular to the z-axis. Thus, regardless of their orientations in the x/y plane, the net *LD* signal from the two perpendicular terpy ligands will be positive if the z-axis lies perpendicular to the DNA helix.

The variations in the anth *LD* spectra as a function of loading are small so the orientation of the different chromophores is essentially independent of load. Unfortunately, due to the presence of the two terpy and anth groups, unless the anths are skewed there is no way intercalative or groove binding modes can be distinguished from the *LD*: if skewed, at least one would be non-intercalated. The retention of the structure of the anth spectroscopy at ~ 250 nm is also not a reliable guide since at least one anthracene per metal complex must be non-intercalated.[1]

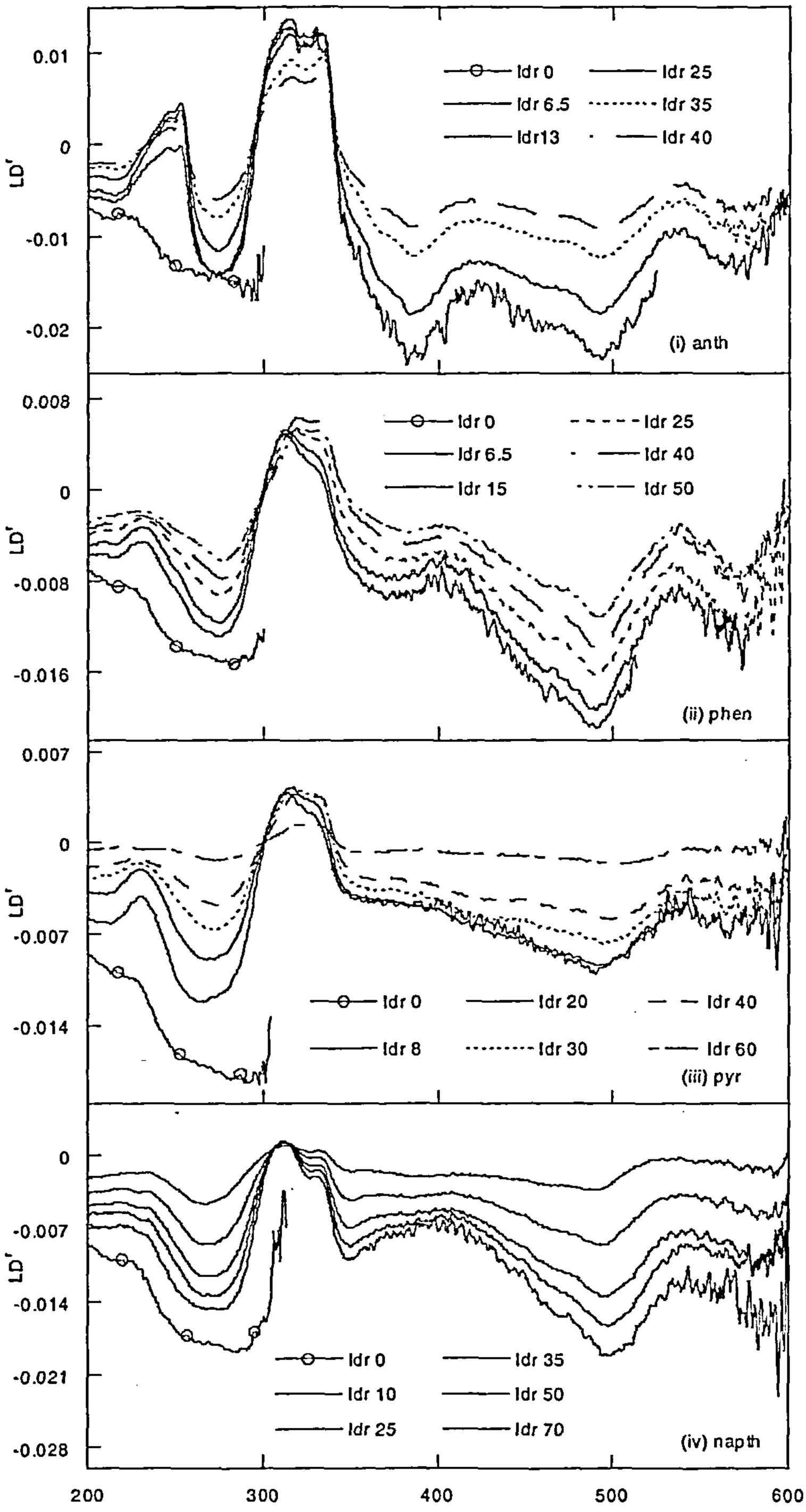

Figure 2.23 *LD′* plots for ruthenium(II) complexes (i) anth, (ii) phen, (iii) pyr and (iv) napth. Legend indicates *LD′* μM ruthenium(II) complex concentration equivalent, ldr 0 = *LD′* for ct-DNA alone in solution, its data above 300 nm has not been plotted due to excessive noise. *LD′* plots generated using **Figure 2.17 and Figure 2.20.** All four spectra show increasingly positive *LD′* signals as ruthenium(II) complex concentration is increased.

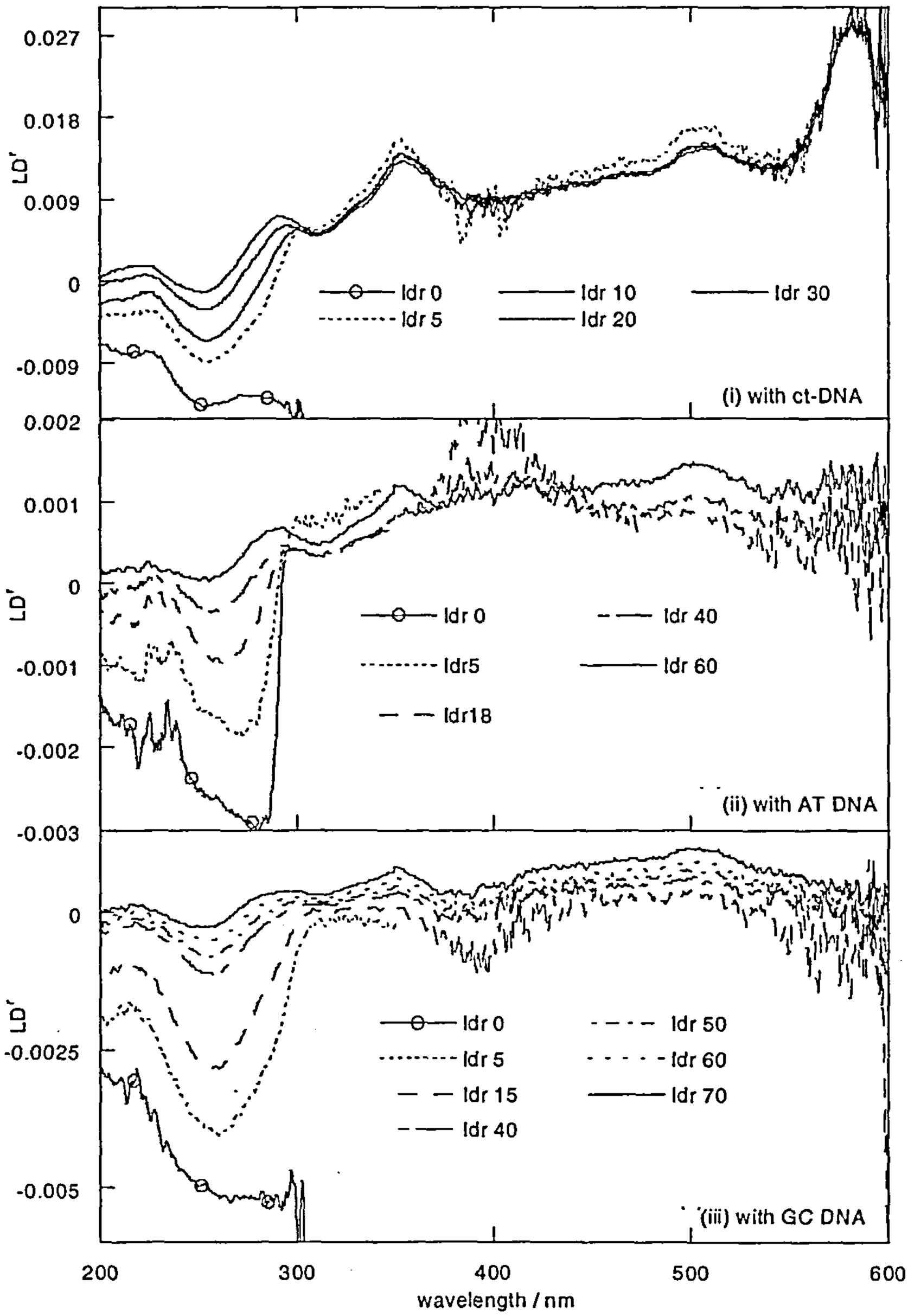

Figure 2.24. *LD' plots for biphen with* (i) ct-DNA, (ii) AT-DNA and (iii) GC-DNA Legend indicates *LD'* μM biphen complex concentration equivalent, ldr 0 = *LD'* of each respective DNA (100μM) alone in solution, data above 300 nm has not been plotted *due to excessive noise. LD' plots generated using* **Figure 2.17 and Figure 2.22.** As the biphen concentration is increased, all three plots show increasingly positive *LD'* signals, with plot (i) for ct-DNA exhibiting the largest positive *LD'* signals.

The 310 nm terpy band is pure x/y polarised (Figure 2.12), long axis polarised within the terpy, and its intensity is unaffected by the addition of DNA (Figure 2.20(i)). However, its LD^r signal is ~2/3 that of the MLCT band (Figure 2.23) which is 2/3 of what would be expected for two such terpy groups.[70] The most likely explanation for this is that the tail of the z-polarised band below 300 nm is cancelling some of the expected signal. The x/y polarised anth signal at ~250 nm is similarly overlaid by z-polarised transitions. The *LD* of anth with GC DNA is in fact very similar to that with ct-DNA except in the DNA region where the 250 nm positive band is missing. However, this is probably due simply to the DNA signal being larger in comparison than with ct-DNA.

The phen and pyr LD^r (Figure 2.23(ii) and (iii)) are similar to those of anth except for the fact that the 340 – 400 nm negative phen signal is smaller in magnitude compared with the MLCT signal than others.

For the anth, phen and pyr complexes, all transitions which the film *LD* showed to be z-polarised have negative LD^r of similar magnitude indicating they are polarised approximately perpendicular to the DNA helix axis. Thus these spectra are consistent with an intercalative orientation. For the biphen complex (Figure 2.24), the positive MLCT *LD* and LD^r signals mean that the z axis of complex is not parallel to the bases (and probably lies along a groove), suggesting that the binding mode is non-intercalative for all sequences.

2.4 Discussion

Using the polarisations determined for the transitions in the film *LD* experiments it is possible to interpret the absorbance, *CD* and *LD* data to give clues as to the binding modes of the five complexes on DNA. The clear geometric deductions to be made from the spectroscopic data are as follows:

(i) All the complexes bind to DNA.

(ii) Pyr and anth bind in a mode where the pyrene and anthracene tail spectroscopy is reduced in magnitude suggesting these groups are in a π-stacked mode even at low metal complex load on the DNA. The same may or may not be true of the other tails.

(iii) Anth, pyr and phen probably adopt the same binding mode that involves isolated binding to the DNA until the mixing ratio is ~4:1 DNA base:metal complex for pyr and phen and ~7:1 for anth. At higher mixing ratios, a new mode switches into play where the metal complexes stack close together but are oriented in the same way as in the isolated binding mode.

(iv) The napth complex exhibits a similar binding mode to anth, pyr and phen at low metal complex loading, but a second non-intercalative π-π self-stacking mode is favoured from slightly higher metal complex loadings. The orientation of this mode is different from the first, with the z-axis of the complex being closer to parallel to the helix axis than parallel to the bases, presumably lying along a groove.

(v) The complexes, except for the biphen complex, all have their z-axis approximately parallel to the DNA bases. This is necessary, though not sufficient, for intercalation of the tails. The similarity in flow *LD* shape of each of the complexes indicates similar binding modes.

(vi) The biphen z-polarised transitions are oriented in a manner consistent with the z-axis lying more perpendicular than parallel to the bases. This is consistent with a groove bound molecule and not intercalation. The orientation with ct-DNA, GC and AT is very similar. The biphen long axis transition at 350–400 nm has no induced *CD* signal with GC whereas this band dominates the AT spectra and to a

much lesser extent the ct-DNA spectra. The AT *CD* signals are opposite from those for GC and ct-DNA suggesting its binding mode is different (binding mode seems to have more effect on induced *CD* signs than does sequence). However, the *LD* suggests that the MLCT and terpy parts of the molecule are oriented in the same manner on ct-DNA, GC and AT.

(vii) At low metal complex load (20:1), methylene blue experiments (MB) indicate a lengthening/stiffening of ct-DNA with each complex.

The data is consistent with anth, phen, pyr and napth tails all intercalating as their most stable (low metal complex load) binding mode: their z-axis is perpendicular to the DNA helix, they stiffen the DNA helix, their transitions (where identifiable) are red shifted and hypochromic upon DNA binding. At higher metal complex loads, the metal complexes π-stack together. This involves terpy-terpy and presumably also tail-tail couplings (thus giving rise to the exciton *CD* signals). Since the orientations of the metal complexes in the new mode is the same as in the intercalated mode, we presume that the intercalators are being used as the starting point for a crystal structure type packing. This leads to the question of whether there is an extended stack or simply dimers.

The data suggests that napth occupies the two modes of anth, phenan and pyr simultaneously even at low metal complex concentrations. The inter-metal complex interactions are more prominent at higher metal complex concentrations.

The biphen complex by way of contrast does not occupy an intercalative binding mode at any stage nor does it show evidence of π-π self-stacking interactions with ct-DNA and GC DNA. The biphen does however exhibit a dominant π-π self-stacking mode with AT DNA at higher metal complex loads. The crystal structure of biphen is a

long stacked polymer that together makes a 'beads on a string' sort of structure. One can envisage this gaining a helical twist and fitting snugly up the major groove of the DNA. In this case, the z-axis of the metal complex would lie at ~45° to the DNA helix axis. The 310 nm terpy groups would also be expected to have a net positive *LD* (due to the factor of two from the rotational average about the DNA helix). There is no evidence for GC or ct-DNA facilitating such a structure, as there is no exciton *CD* signal in these cases. AT DNA, however, exhibits a biphen *CD* signal at 350 nm that increases rapidly in accord with ones' expectations for an exciton interaction. Biphen-terpy stacking, if it is reasonably cooperative, could be taking place even at quite low metal complex loadings.

The opposite signs for ct-DNA and AT DNA suggest that the twist of the biphen groups is opposite in each case. The fact that the AT coupling in largest suggests that it is running along the minor groove with one terpy propeller being slotted in and the biphen running along the groove. This would stiffen the DNA as with a spine of hydration. For GC this mode is not as attractive due to the steric effect of the G amino group in the minor groove, so the option for biphen-terpy coupling is lost. The *LD* and *CD* combined would be consistent with an isolated biphen molecule GC major groove binding mode with the z-axis lying along this groove.

The data suggests that with biphen, GC and ct-DNA individual molecules bind along the groove, probably in the major groove, whereas with AT (where the minor groove is less sterically hindered) the molecules are stacked along the groove.

2.5 Conclusion

Spectroscopically, all five ruthenium complexes have been shown to interact non-covalently with DNA. At low concentrations, three of the complexes, phen, anth

and pyr intercalate their aryl tail groups between DNA bases. The biphen complex predominately exhibits groove binding with no significant aryl tail intercalation. The napth complex exhibits intercalation of its aryl tail groups and a non-intercalative mode. At high metal concentrations, the complexes exhibit a non-intercalative binding mode, *i.e.* π-π self-stacking interactions on DNA.

Resonance light scattering (RLS) studies have since been conducted using ct-DNA in collaboration with M. Darwish of Dr Alison Rodger's group at the University of Warwick. RLS studies can be used to differentiate between extended stacks (long range π–π electronic couplings give large signals) or simple monomer/dimer formations (small π stacks give small signals)[65] at higher metal complex concentrations. At low complex loads, all five complexes were found to show a small decrease in the light scattering compared with ct-DNA free solutions. At higher loads, all complexes show some evidence of π stacking in solution, though the effect is small. In the case of anth, the DNA facilitates a π–π self-stacking of the tail that does not take place in free solution. With the other complexes, the DNA if anything reduces the stacking compared with free solution. So *CD* confirms a π stacking interaction compared with free solution, and the RLS studies indicate only short stacks are present.

2.6 References

1 D. Z. Coggan, I. S. Haworth, P. J. Bates, A. Robinson and A. Rodger, *Inorg. Chem.* 1999, **38**, 4486.

2 J. K. Barton, *Pure & Appl. Chem.*, 1989, **61**, 563.

3 S. Satyanarayana, J.C. Dabrowiak, J.B. Chaires, *Biochemistry*, 1992, **31**, 9319.

4 S. Satyanarayana, J.C. Dabrowiak, J.B. Chaires, *Biochemistry*, 1993, **32**, 2573.

5 J. K. Barton, *J. Biomol. Struct. Dyn.*, 1983, **1**, 621.

6 J. K. Barton, A. T. Danishefsky and J. M. Goldberg, *J. Am. Chem. Soc.*, 1984, **106**, 2172.

7 J. P. Rehman and J. K. Barton, *Biochemistry*, 1990, **29**, 1701.

8 C. Hiort, B. Nordén and A. Rodger, *J. Am. Chem. Soc.*, 1990, **112**, 1971.

9 I. S. Haworth, A. H. Elcock, J. Freeman, A. Rodger and W. G. Richards, *J. Biomol. Struct. Dyn.*, 1991, **9**, 23.

10 M. Eriksson, M. Leijon, C. Hiort, B. Nordén and A. Gräslund, *J. Am. Chem. Soc.*, 1992, **114**, 4933.

11 J.-P. Collin, S. Guillerez, and J.-P. Sauvage, *J. Chem. Soc., Chem. Commun.*, 1989, 776.

12 J.-P. Sauvage, J.-P. Collin, J.-C. Chambron, S. Guillerez, and C. Coudret, *Chem. Rev.*, 1994, **94**, 993.

13 J.-P. Collins, S. Guillerez, J-P. Sauvage, F. Barigelletti, L. De Cola, L. Flamigni and V. Balzani, *Inorg. Chem.*, 1991, **30**, 4230.

14 G. Albano, V. Balzani, E. C. Constable, M. Maestri and D. R. Smith, *Inorg. Chim. Acta,* 1998, **277**, 225.

15 N. W. Alcock, P. R. Barker, J. M. Haider, M. J. Hannon, C. L. Painting, Z. Pikramenou, E. A. Plummer, K. Rissanen and P. Saarenketo, *J. Chem. Soc., Dalton Trans.*, 2000, 1447.

16 J.-P. Collin, I. M. Dixon, J.-P. Sauvage, J. A. Williams, F. Barigelletti and L. Flamigni, *J. Am. Chem. Soc.*, 1999, **121**, 5009.

17 C. R. Hecker, A. K. I. Gushurst and D. McMillin, *Inorg. Chem.*, 1991, **30**, 538

18 X.-H. Zou, B.-H. Ye, H. Li, J.-G. Liu, Y. Xiong and L.-N. Ji, *J. Chem. Soc., Dalton Trans.*, 1999, 1423.

19 M. Maestri, N. Armaroli, V. Balzani, E. C. Constable and A. M. Cargill Thompson, *Inorg. Chem.*, 1995, **34**, 2759.

20 A. C. Benniston, V. Grosshenny, A. Harriman and R. Ziessel, *Angew. Chem. Int. Ed. Engl.*, 1994, **33**,1884.

21 L. Flamigni, S. Encinas, F. Barigelletti, F. M. MacDonnell, K-J Kim, F. Puntoriero and S. Campagna, *Chem. Commun.*, 2000, 1185.

22 M. Howe-Grant and S. J. Lippard, *Biochemistry,* 1979, **18**, 5762.

23 E. M. Ratilla, H. M. Brothers II and N. M. Kostić, *J. Am. Chem. Soc.*, 1987, **109**, 4592.

24 A. McCoubrey, H. C. Latham, P. R. Cook, A. Rodger, and G. Lowe, *FEBS Letters*, 1996, **380**, 73.

25 C. S. Peyratout, T. K. Aldridge, D. K. Crites and D. R. McMillin, *Inorg. Chem.*, 1995, **34**, 4484

26 K. W. Jennette, S. J. Lippard, G. A. Vassiliades and W. R. Bauer, *Proc. Nat. Acad. Sci. USA*, 1974, **71**, 3839.

27 K. W. Jennette, J. T. Gill, J. A. Sadownick and S. J. Lippard, *J. Am. Chem. Soc.*, 1976, 6159.

28 D. McFayden, L. P. Wakelin, I. A. Roos and B. L. Hillcoat, *Biochem J.*, 1987, **242**, 177.

29 M. L. Stone and G. A. Crosby, *Chem. Phys. Letters.*, 1981, **79**, 169.

30 J. R. Kirchoff, D. R. McMillin, P. A. Marnot and J-P. Sauvage, *J. Am. Chem. Soc.*, 1985, **107**,1138.

31 A. Juris, V. Balzani, F. Barigelletti, P. Belser and A. Von Zelewsky, *Coord. Chem. Rev.*, 1988, **84**, 85.

32 K. Kalyanasundaram, *Coord. Chem. Rev.*, 1982, **46**, 159.

33 A. Yamagishi, *J. Chem. Soc., Chem. Commun.,* 1983, 572.

34 J. K. Barton, J. M. Goldberg, C.V.Kumar and N. J. Turro, *J. Am. Chem. Soc.,* 1986, **108**, 2081.

35 J. E. Coury, J. R. Anderson, L. McFail-Isom, L. D. Williams and L. A. Bottomley, *J. Am. Chem. Soc.,* 1997, **119**, 3792.

36 P. Lincoln and B. Nordén. *J. Phys. Chem. B.*, 1998, **102**, 9583.

37 C. Hiort, P. Lincoln, B. Nordén, *J. Am. Chem. Soc.,* 1993, **115**, 3448.

38 Y. Jenkins, A. E. Friedman, N. J. Turro and J. K. Barton, *Biochem.,* 1992, 10809

39 A. E. Friedman, J-C. Chambron, J-P. Sauvage, N. J. Turro and J. K. Barton, *J. Am. Chem. Soc.,* 1990, **112**, 4960

40 R. E. Holmlin, J. A. Yao and J. K. Barton, *Inorg. Chem.,* 1999, **38**, 174.

41 C. M. Dupureur and J. K. Barton, *J. Am. Chem. Soc.* 1994, **116**, 10286.

42 C. M. Dupureur and J. K. Barton, *Inorg. Chem.,* 1997, **36**, 33.

43 R. E. Holmlin, E. D. Stemp and J. K. Barton, *Inorg. Chem.,* 1998, **37**, 29.

44 P. Lincoln, A. Broo and B. Nordén, *J. Am. Chem. Soc.,* 1996, **118**, 2644.

45 E. Tuite, P. Lincoln and B.Nordén, *J. Am. Chem. Soc.,* 1997, **119**, 239.

46 I. Greguric, J.R. Aldrich-Wright and J. Grant Collins, *J. Am. Chem. Soc.,* 1997, **119**, 3621

47 J. G. Collins, A-D. Sleeman, J. R. Aldrich-Wright, I. Greguric & T. W. Hambley. *Inorg Chem.* 1998, **37**, 3133.

48 J. G. Collins, J. R. Aldrich-Wright, I. D. Greguric & P. A. Pellegrini. *Inorg. Chem.* 1999, **38**, 5502

49 A. M. Pyle, M. Y. Chiang and J. K. Barton, *Inorg. Chem.*, 1990, **29**, 4487.

50 R. H. Terbrueggen, T.W.Johann and J.K.Barton, *Inorg. Chem.,* 1998, **37**, 6874.

51 J. G. Collins, T. P. Shields, J. K. Barton, *J. Am. Chem. Soc.,* 1994, **116**, 9840.

52 J. L. Kisko and J. K. Barton, *Inorg. Chem.*, 2000, **39**, 4942.

53 A. M. Pyle, E. C. Long and J. K. Barton, *J. Am. Chem. Soc.*,1989, **111**, 4520

54 B. A. Jackson and J. K. Barton, *J. Am. Chem. Soc.,* 1997, **119**, 12986.

55 B. A. Jackson, V.Y. Alekseyev and J. K. Barton, *Biochem.,* 1999, **38**, 4655

56 B. A. Jackson and J. K. Barton, *Biochem.*, 2000, **39**, 6179

57 A. H. Wang, J. Nathans, G. van der Mercel, J. H. van Boom, A. Rich, *Nature*, 1978, **276**, 471

58 P. J. Carter, C-C. Cheng and H. H. Thorp. *J. Am. Chem. Soc.,* 1998, **120**, 632.

59 B. T. Farrer and H. H. Thorp. *Inorg Chem*. 2000, **39**, 44.

60 N. Grover, N. Gupta, P. Singh and H. H. Thorp. *Inorg Chem*, 1992, **31**, 2014.

61 S. A. Ciftan, D. P Hondros and H. H. Thorp. *Inorg. Chem*, 1998, **37**, 1598.

62 H-C. Becker and B. Nordén. *J. Am. Chem. Soc.*, 1999, **121**, 11947.

63 H-C Becker and B. Nordén. *J. Am. Chem. Soc.*, 2000, **122**, 8344.

64 M. A. Ismail, K. J. Sanders, G. C. Fennell, H. C. Latham, P. Wormell and A. Rodger, *Biopolymers*, 1998, **46**, 127.

65 R. F. Pasternack and P. J. Collings, *Science*, 1995, 269, 935

66 T. K. Aldridge and E. M. Stacy and D. R. McMillin, *Inorg. Chem.,* 1994, **33**, 722.

67 J. F. Michalec, S. A. Bejune and D. R. McMillin, *Inorg. Chem.*, 2000, **39**, 2708.

68 E. Constable and A. M. Cargill Thompson, *Polyhedron*, 1992, **11**, 2707.

69 H.-H. Perkampus *'UV-VIS Atlas of Organic compounds' Part 1 Spectra and Part2*, VCH Publishers, New York

70 A. Rodger and B. Nordén, *Circular Dichroism and Linear Dichroism*, Oxford University Press, 1997.

71 F. Bargelletti, L. Flamigni, M. Guardigli, J.-P. Sauvage, J.-P. Collin and A. Sour, *Chem. Commun.*, 1996, 1329.

3 Novel platinum complexes and their interactions with DNA

3.1 Introduction

Metals and metal complexes have been used in medicines for years in the treatment of ailments and diseases.[1,2] Probably one of the best known metal complexes to have been used in the treatment against cancer is cisplatin (Figure 3.1).[3–6] The discovery of cisplatin and its variety of uses as an anticancer agent have led to an increase in interest in platinum coordination chemistry, and generally into interactions between metal ions and living matter. [1–3, 7–11]

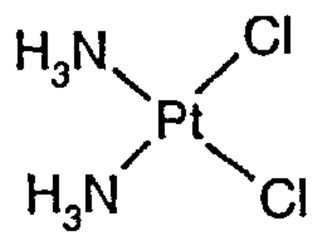

Figure 3.1 Cis-diamminedichloroplatinum(II) i.e. cis-$Pt(NH_3)_2Cl_2$ more commonly known as cisplatin

The work described in this chapter relates to novel acylthiourea platinum complexes that have been developed by Sacht *et al.*[12,13] with a view to their DNA binding chemotherapeutic activity. In the introduction this work is put in context by a brief historical review of platinum drugs.

Cisplatin was first synthesised in 1845.[3] Its profile however was raised unexpectedly in 1964 by Rosenberg. Whilst investigating the effect of electric current and electric fields on Escherichia coli (Æ-coli), Rosenberg found that although cell growth was not, cell division of the bacterium was inhibited. It eventually became apparent that this effect — the inhibition — was due to the formation of trace amounts (~10 ppm) of platinum complexes.[7] Studies of cell division conducted on these

complexes, specifically the *cis* isomers of cisplatin and platinum(IV) tetrachlorodiamine $Pt(NH_3)_2Cl_4$ found them to be effective against a number of animal tumours cell lines, hence their eventual use in combating cancer in humans.[4] These platinum complexes were ultimately found to be very effective against testicular and ovarian cancers, and active against a variety of cancers *e.g.* head, neck and cervical cancers and useful against melanomas.[3–5]

Some metal compounds *e.g.* those of gold, target proteins,[1] however, the target for cisplatin is DNA. Cisplatin has the ability to bind to DNA and block DNA replication *i.e.* it inhibits DNA synthesis. Cisplatin, and its analogues such as $Pt(en)Cl_2$ (en denotes ethylenediamine) (Figure 3.2), are more active than their trans counterparts.[8]

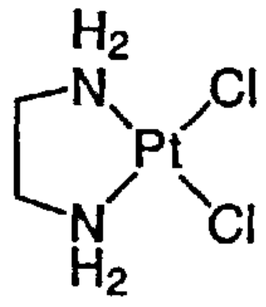

Figure 3.2 $Pt(en)Cl_2$ exhibits good anticancer activity

The activation process of cisplatin occurs via stepwise hydrolysis of the chloride ligands. The complex can then react in a number of different ways producing platinated DNA adducts. Cisplatin can apparently interact monofunctionally (*i.e.* forming one platinum-nucleotide bond), or bifunctionally either intrastrand, interstrand, or even intermolecularly with DNA (Figure 3.3).[4,6] There is a strong indication that the various species/adducts that can be formed and or possible condensation products display differing degrees of toxicity. For example, an aqueous solution of cisplatin becomes more toxic on ageing.[3–5] A certain number of these platinated adducts can trigger DNA degradation and apoptosis — programmed cell death; these are fundamentally responsible for the effectiveness of cisplatin as a drug.[4]

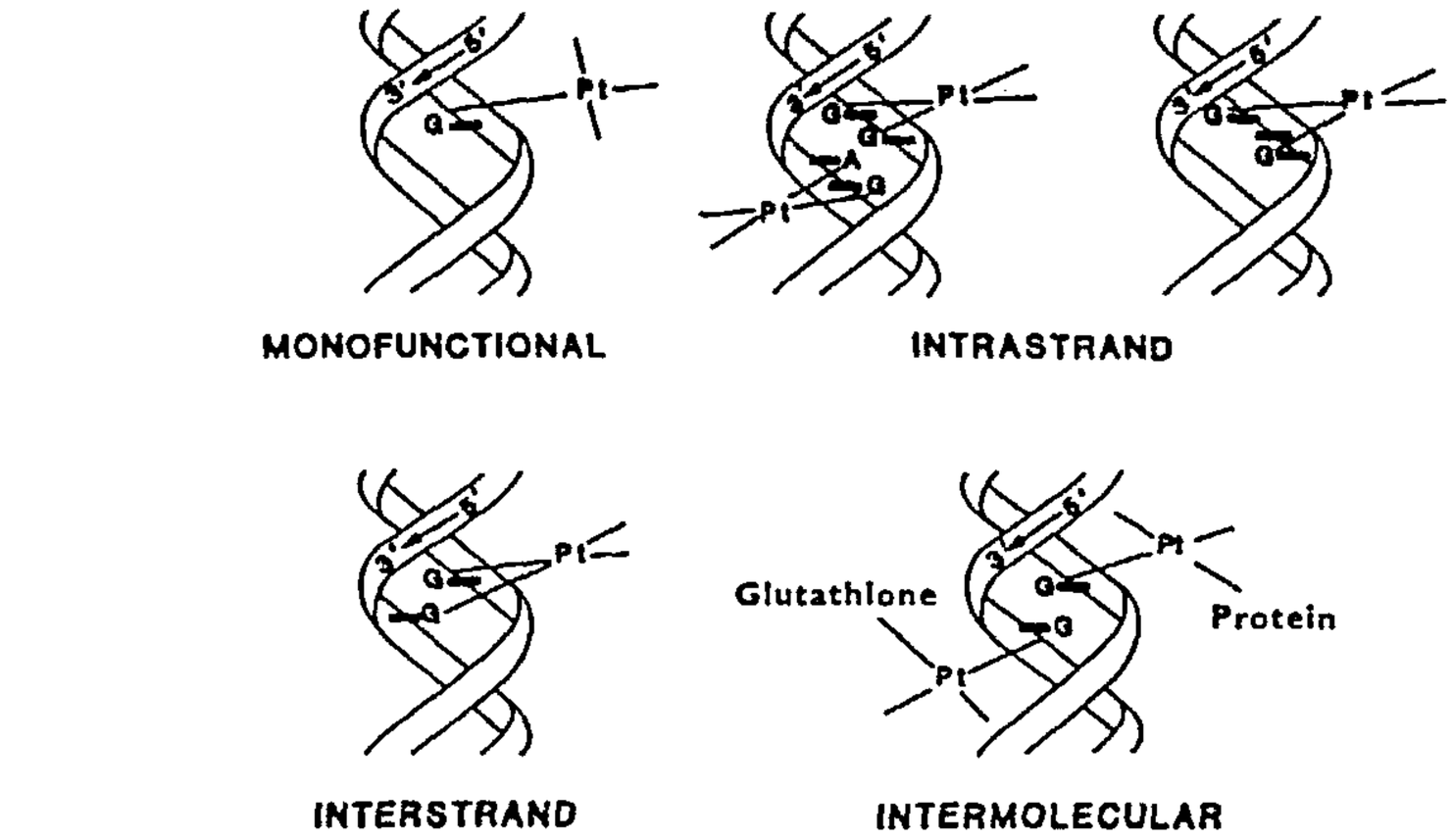

Figure 3.3 Structures of the various adducts produced in DNA by cisplatin. Diagram reproduced from reference 4.

To understand the differences in the biological activity of the different adducts formed by cisplatin, the mechanism of action of hydrolysis needs to be understood.[1–5] The labile chloride ion is not replaced by the water extracellularly, as high chloride concentration (104 mM)[3,4] in this region suppresses this action. The chloride concentration inside the cell (5 mM)[3,4] is, however, much less, therefore exchange of the chloride by water does occur intracellularly, and it is this aquated complex that is very active. Figure 3.4 shows the mechanism of action.

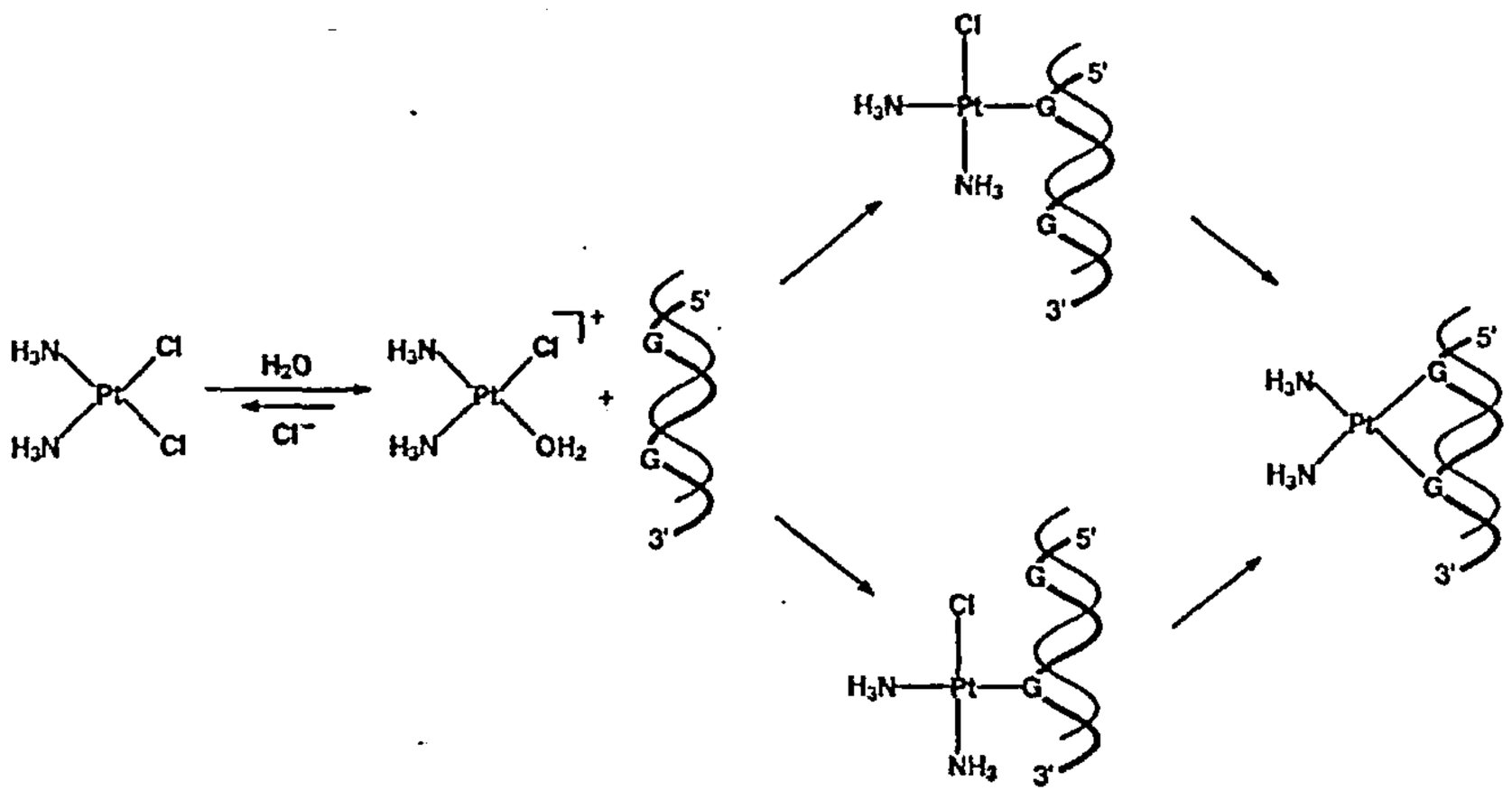

Figure 3.4 Mechanism of action of activation of cisplatin. Cisplatin is hydrolysed to give *mono aqua* and *diaqua* species which are much more reactive, for example towards substitution by G residues on DNA. Diagram taken from reference 1.

Products such as $[Pt(NH_3)_2(OH_2)_2]^{2+}$ and $[Pt(NH_3)_2(OH)_2]$ are generated. The Pt-OH_2 bond is very reactive, and is believed to be the active species towards DNA. This can interact with the nitrogen atoms, N7 of the guanine bases and to a lesser extent with the N atoms of the adenine bases to produce either inter- or intrastrand cis-$Pt(NH_3)^{2+}$ bridges.[3,5] The major adduct is formed by covalent intrastrand crosslinkage and occurs when the platinum complex uses two of its ligand binding sites to bind adjacent guanines on the same strand (intrastrand crosslink).[4] Transplatin, the trans-$[PtCl_2(NH_3)_2]$ complex cannot produce intrastrand bridging due to steric hinderance, hence its inactivity.[2,6,10]

Takahara and Lippard have determined binding sites of cisplatin using X-ray crystallography. Using a double stranded synthetic dodecamer d(CCTCTG*G*TCTCC/ d(GGAGACCAGAGG) they found that the *G bases are platinated at N7.[14,15]

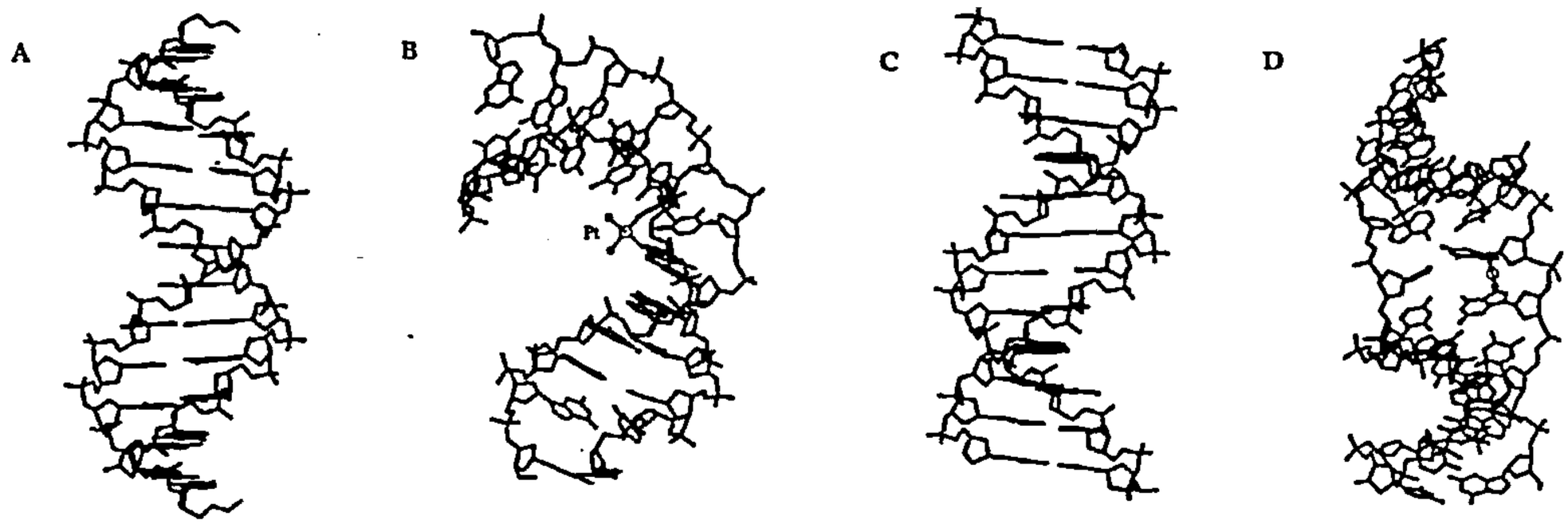

Figure 3.5 X-ray crystal structure of intrastrand binding interaction on DNA.[4,14,15] (A) shows the major groove of normal B-DNA and (B) DNA bend caused by cisplatin adduct. (C) shows the minor groove of normal B-DNA and (D) widening of minor groove by cisplatin adduct. Diagram taken from reference 4

Strong bonds are formed with DNA which disrupts base-base stacking interactions in the DNA helix and leads to a kink in the DNA. The degree of distortion of DNA depends on the sequence (Figure 3.5).[4,14] The separation of strands for replication cannot occur. The interaction of cisplatin with DNA interferes with these normal processes (*i.e.* DNA replication) and it is this perturbation of the DNA structure that

perhaps lies at the centre of its anticancer activity. In addition for activity, the normal cell repair mechanisms need to be confused.

Proteins known as HMG (high mobility group) proteins exist, whose function is to detect/repair or remove DNA which has been kinked or is distorted in any way such as G or A platination.[3,5] However, rather than being repaired by the HMG Proteins, the cisplatin adducts are wrapped up and protected.[5,16] These proteins ensure that the DNA is not repaired, thus this process leads to apoptosis. Apoptosis can be defined as a consequence of the mechanism of action of cisplatin and a failure of the mechanisms of cell resistance to foreign drugs.[3,4]

Although cisplatin exhibits activity against a number of tumour cell lines, it is also toxic towards some normal cells. It also has a limited spectrum of activity in that it is not active enough against several types of cancer, this and the unfortunate development of resistance towards it after continued treatment has led to further research being carried out. Perhaps its biggest problem is that the drug delivery is very inefficient as it can bind to biological molecules other than DNA *e.g.* proteins.[17] A wide range of analogues have been developed, some of which are illustrated in Figure 3.6.

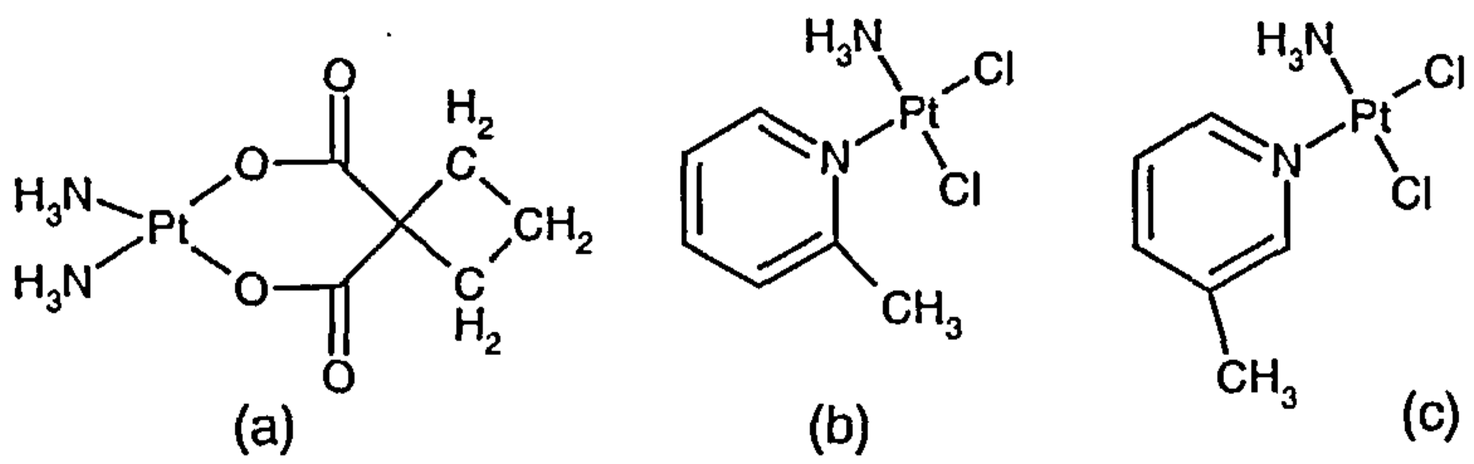

Figure 3.6 (a) carboplatin, (b) 2-picoline and (c) 3-picoline

The key structural features of effective cytostatic platinum drugs were found to be:[3] the complex must have a square planar disposition of the four ligands around platinum(II) with two cis-primary or secondary amine ligands and two (relatively easily

hydrolysed) chloride or carboxylate groups and good water solubility.[3] These criteria have been used as a guideline for further research on structurally similar first generation 'classical' compounds.

Hundreds of compounds have been tested for antitumour activity, eventually the lack of progress in overcoming any acquired resistance to cisplatin combined with the ever present need to increase the spectrum of activity of these platinum complexes towards a wider range of types of cancer, and the continuous emphasis on reducing the toxicity of platinum anticancer agents towards normal cells led to second generation compounds such as carboplatin (Figure 3.6(a)) being developed. Carboplatin is less toxic than cisplatin and is active against cisplatin resistant tumours, more or less the required characteristics of a new anticancer agent. Carboplatin's activity towards cisplatin resistant tumours could be related to the differences in their DNA binding characteristics since carboplatin binds preferentially in an interstrand crosslinking manner and does not bend DNA. Other compounds currently being investigated include 2-picoline and 3-picoline (Figure 3.6 (b) and (c)).

2-picoline platinum has been found to be active against cisplatin resistant tumour strains. The cellular half-life of cisplatin is ~ two hours whereas the picoline analogues last longer (2-picoline ~ ten hours, 3-picoline $\geq$ two hours). 2-picoline is less reactive than cisplatin, as it is sterically hindered by the 2-methyl group which lies over the top of the platinum centred square plane,[18] hence the hydrolysis rate is two to three times slower than cisplatin resulting in the linkage in cells and binding to plasma proteins to proceed more slowly,[1] so more survives to reach the ultimate target: DNA, though its DNA binding reactivity is similarly reduced.[18]

Research is now extending from 'classical' to 'non-classical' platinum complexes with structurally unique features that apparently contravene the structure-relationship

rules originally set up.[3,19] For cis-platin activity, Farrell *et al.*[20] have provided the first examples of cationic anticancer species containing sulphur leaving ligands. The general formula is $[PtCl(R'R''SO)(diamine)]NO_3$ where diamine denotes a bidentate amine such as 1,2-diaminocyclohexane (dach) and R'R''SO denotes substituted sulfoxides such as dimethyl (Me_2SO) and methyl phenyl (MePhSO) (Figure 3.7).

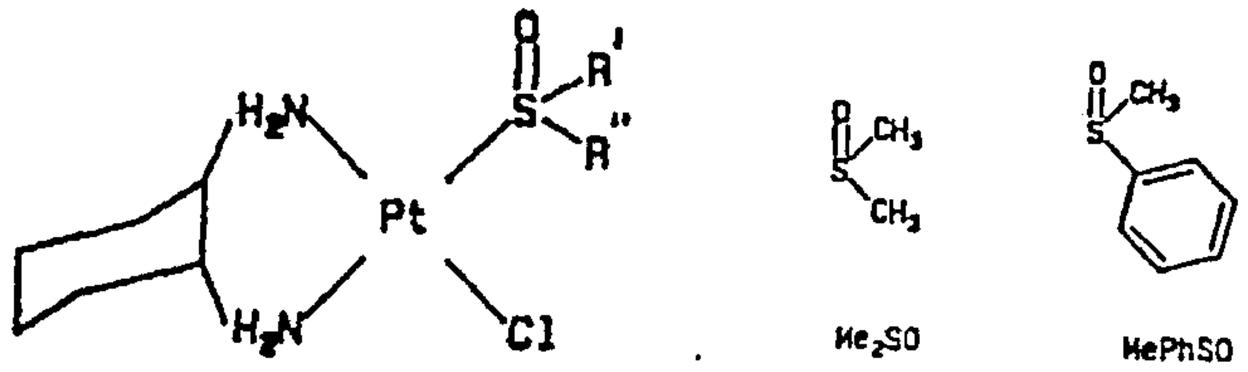

Figure 3.7 Structure of [PtCl(R' R'' SO)(dach)]$^+$ where dach is 1,2-diaminocyclohexane and *e.g.* R'R''SO = Me_2SO or MePhSO. *Structures taken from reference* 20.

These complexes have shown enhanced cytotoxicity in cisplatin resistant cell lines. The complexes act by binding covalently to DNA through the displacement and hydrolysis of the chloride ion followed by the subsequent loss of a sulfoxide ligand to complete the intrastrand link.[20, 21]

3.2 The complexes of this study

Novel platinum complexes (non-classical in design) containing acylthiourea ligand systems have been prepared by Sacht *et al.*[13] Their potential use as chemotheraputic agents are the focus of this chapter.[12,13] These acylthiourea ligand systems are extremely versatile in that small structural changes can be easily made that can lead to very different chemical and physical properties. Sacht has suggested that, by specifically changing the ligand structure, the biological activity of this novel series of complexes could be systematically modified to provide optimum antitumour response.[13]

The work in this chapter describes an investigation into the binding interaction of a series of these novel platinum(II) complexes with ct-DNA, AT and GC DNA. A preliminary screen of a series of eighteen platinum complexes with ct-DNA by UV-Visible absorbance and *CD* is followed by an in depth spectroscopic study on six complexes, structurally similar but with subtle ligand variations, with 5′- nucleotides, ct-DNA, AT and GC DNA. To provide a more comprehensive picture of any structure-activity relationship, a brief mass spectrometric study on three complexes of one particular subset with 9-methyl guanine (MG) and 5′-guanosine monophosphate (GMP) is also presented.

3.2.1 Platinum(II) complexes

Eighteen novel non-classical platinum complexes [12,13] were investigated with a view to their potential long-term use as anticancer agents. The general formula of these square planar platinum(II) complexes is [Pt(L)Cl(DMSO)] where L refers to an acylthiourea ligand system $R'C(O)NHC(S)NR_2$, R′ = aryl and R = amine, (O) and (S) denote points of attachment of the ligand to platinum(II), and DMSO denotes dimethylsulfoxide or a derivative of it. Figure 3.8 shows the general structure of the complexes.

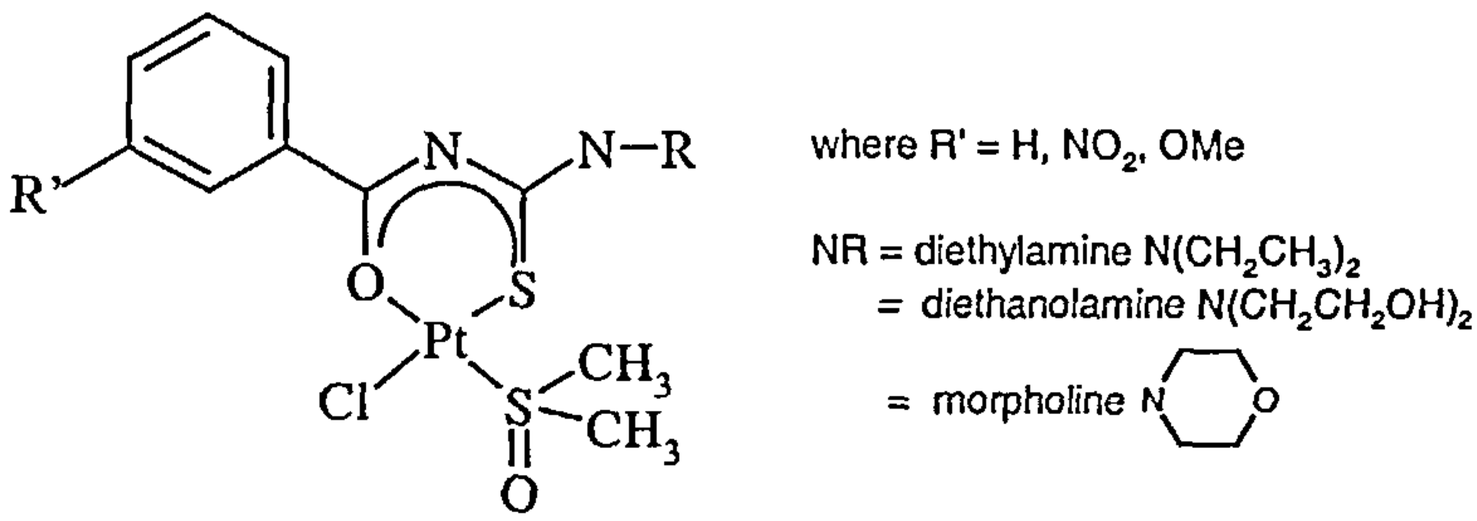

Figure 3.8 General structure of (PtX)

In the context of this thesis, each platinum complex is denoted (PtX) where X = 1 – 18. Their structures are shown in Figure 3.9. The purity of these complexes has been confirmed using NMR and CHN analysis.[12,13]

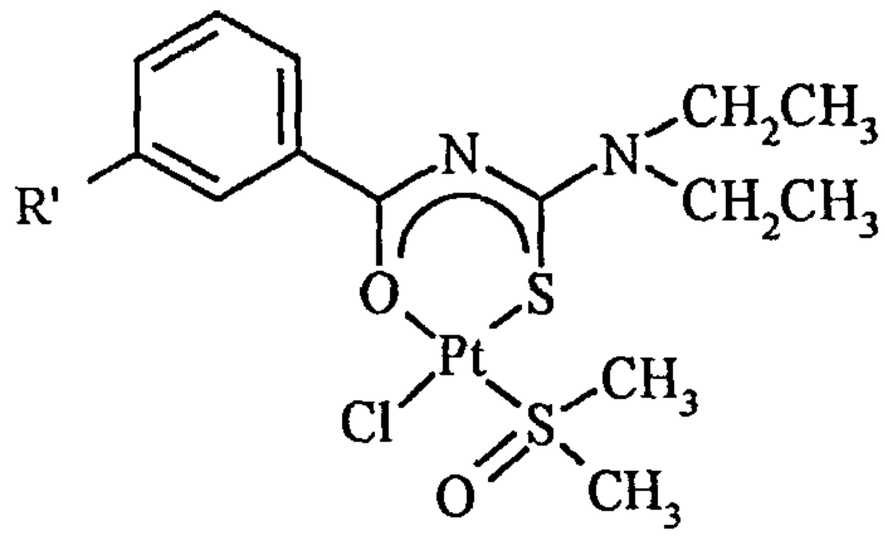

R' = H (Pt1)
R' = NO_2 (Pt4)
R' = OCH_3 (Pt8)

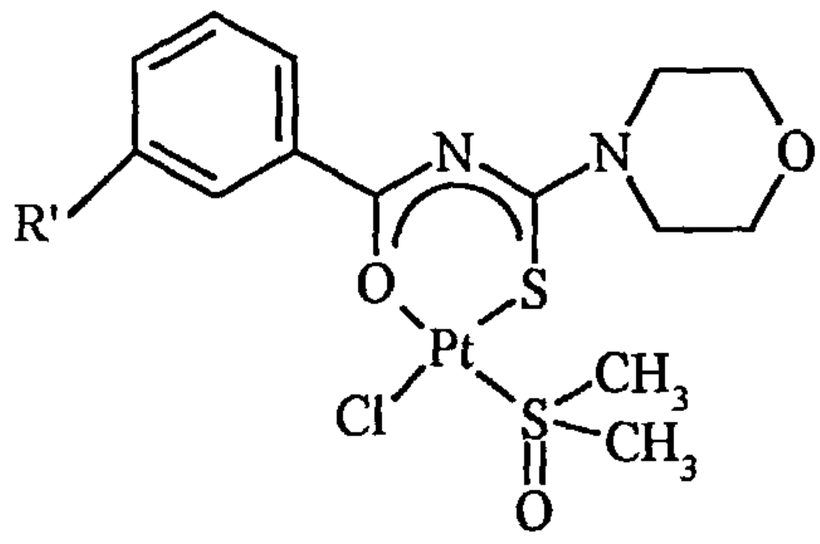

R' = H (Pt2)
R' = NO_2 (Pt5)
R' = OCH_3 (Pt7)

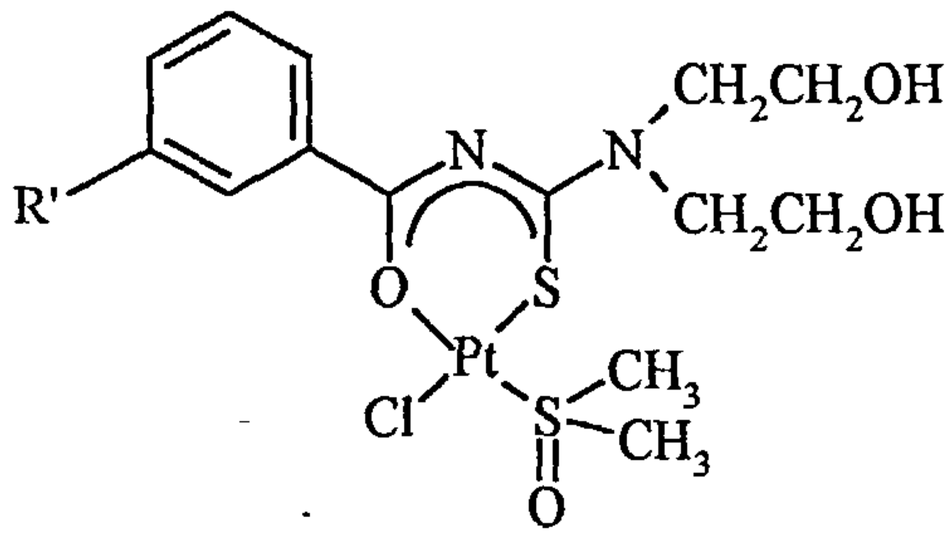

R' = H (Pt3)
R' = NO_2 (Pt6)
R' = OCH_3 (Pt9)

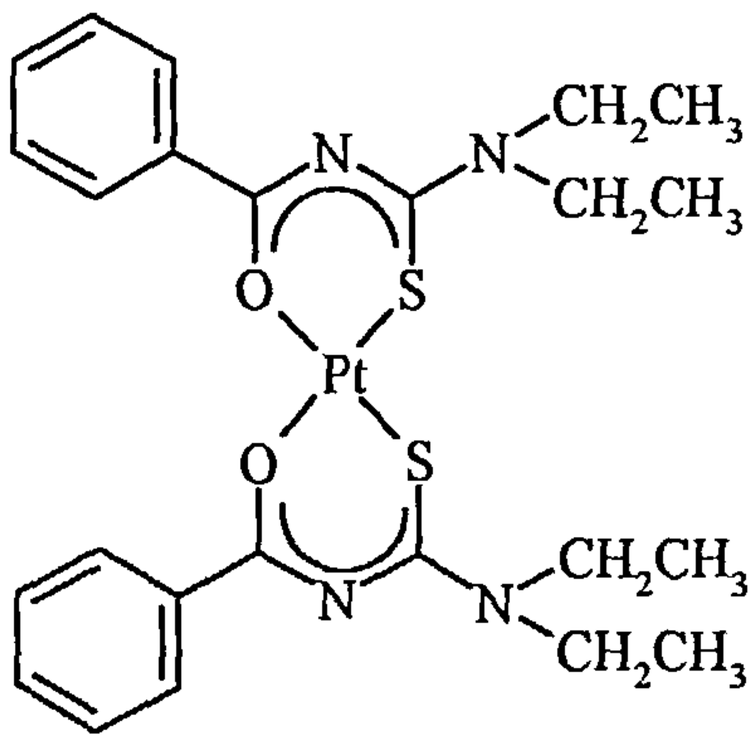

(Pt10)

Figure 3.9 Structures of platinum(II) complexes (Pt1 – Pt18). (Pt11 – 13) are chiral complexes, (Pt11) is the (-) isomer, no (+) isomer was provided. (Pt12)/(Pt13) are the (+/-) isomers respectively. (Pt14 – Pt18) are intercalators. (Pt14), Pt15), (Pt17) and (Pt18) are $(PF_6)^-$ salt complexes, (Pt16) is a bis-platinum $(PF_6)^{2-}$ salt complex.

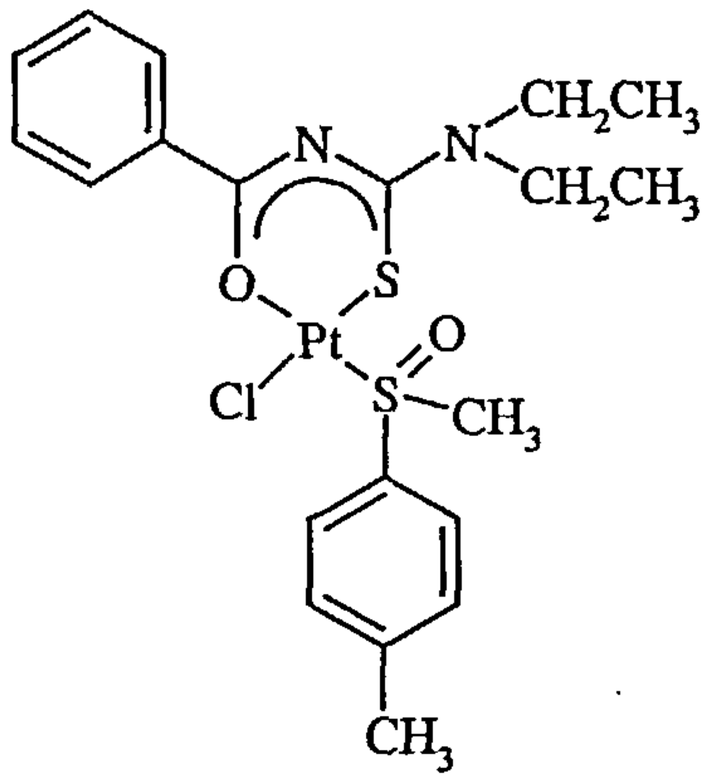

(Pt11,(-))

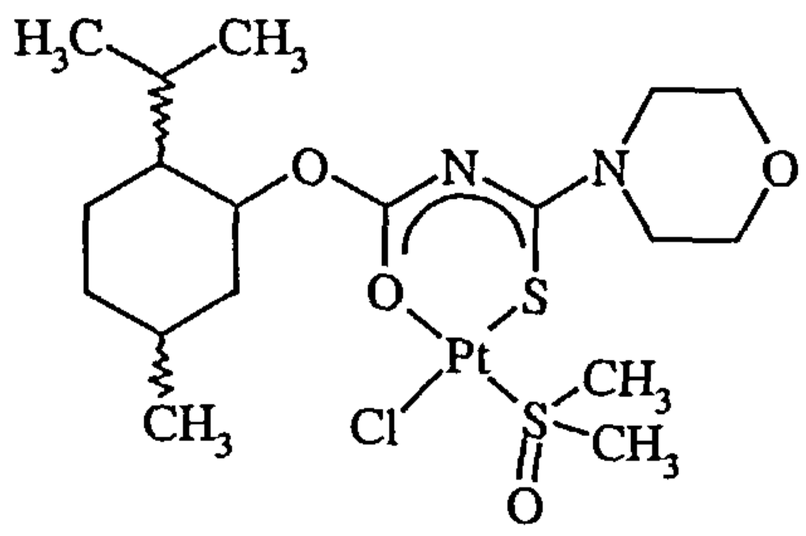

(Pt12,(+))/(Pt13,(-))

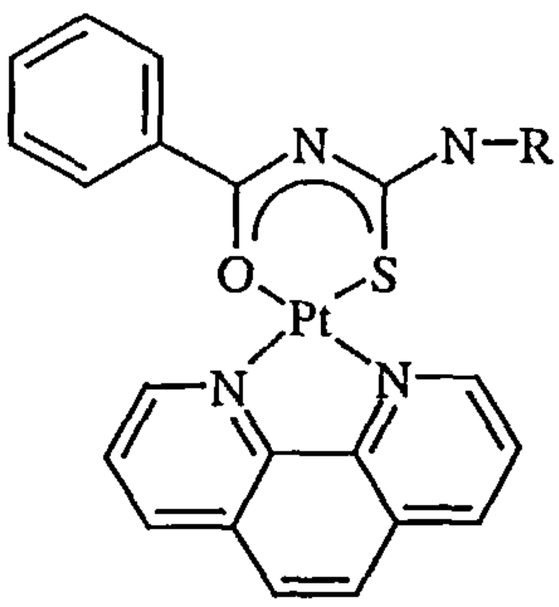

R = diethylamine (Pt14)

R = diethanolamine (Pt15)

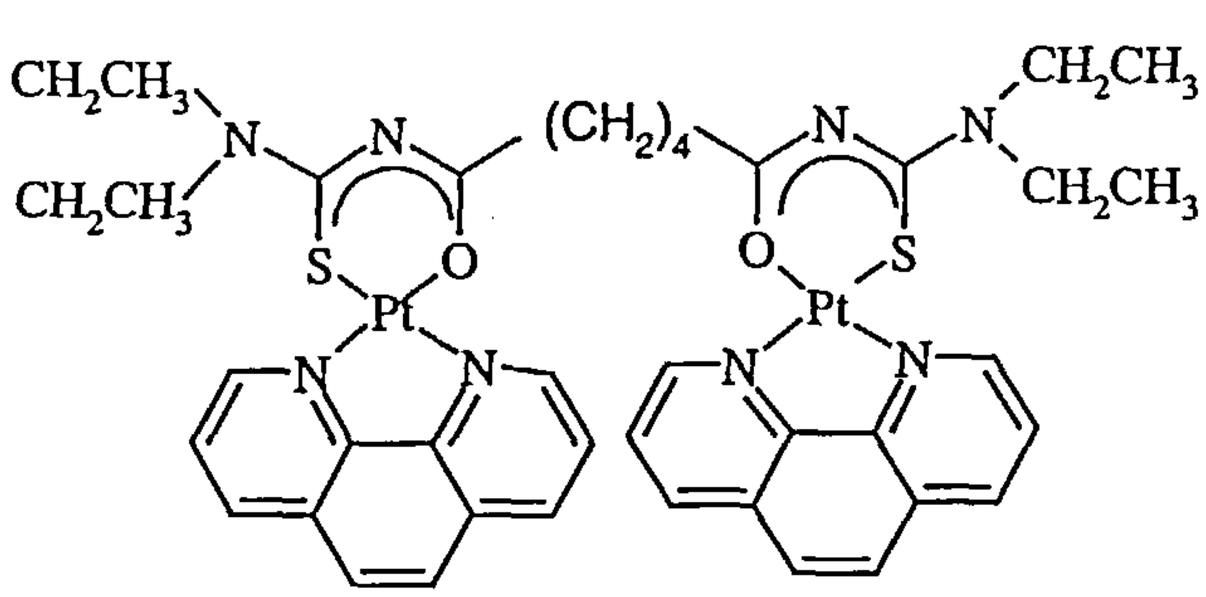

(Pt16)

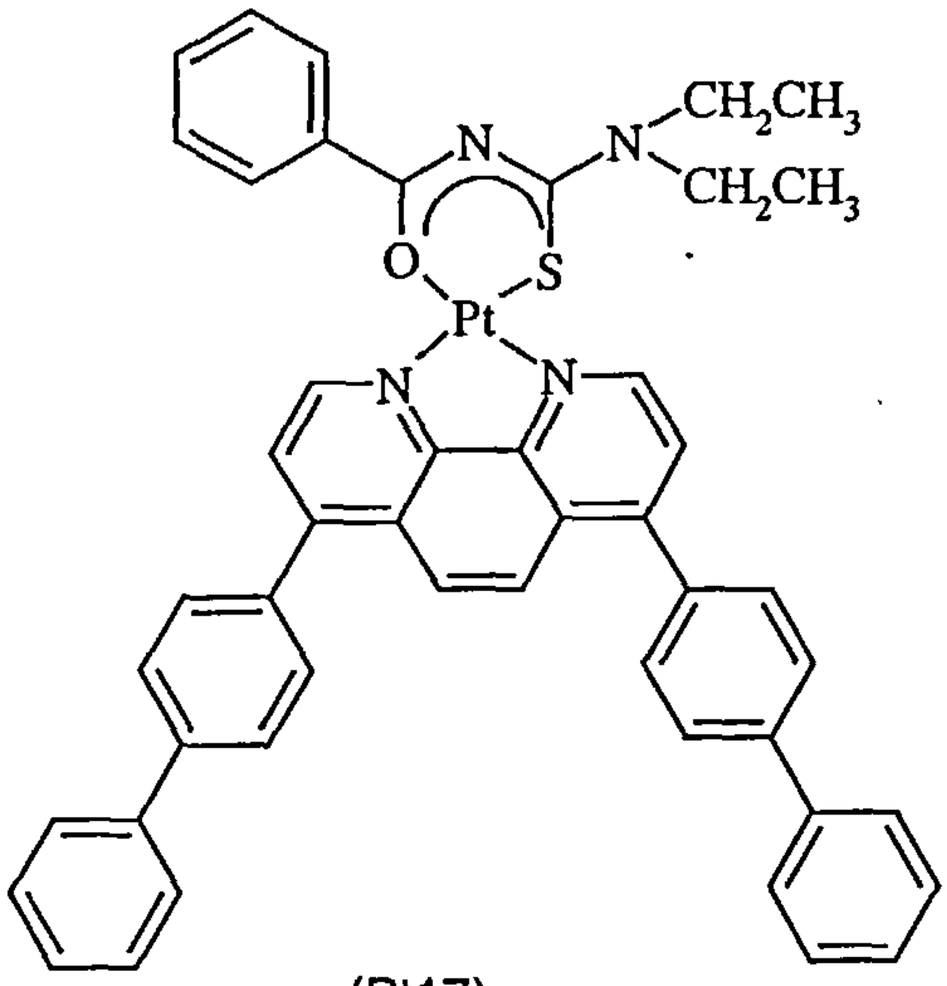

(Pt17)

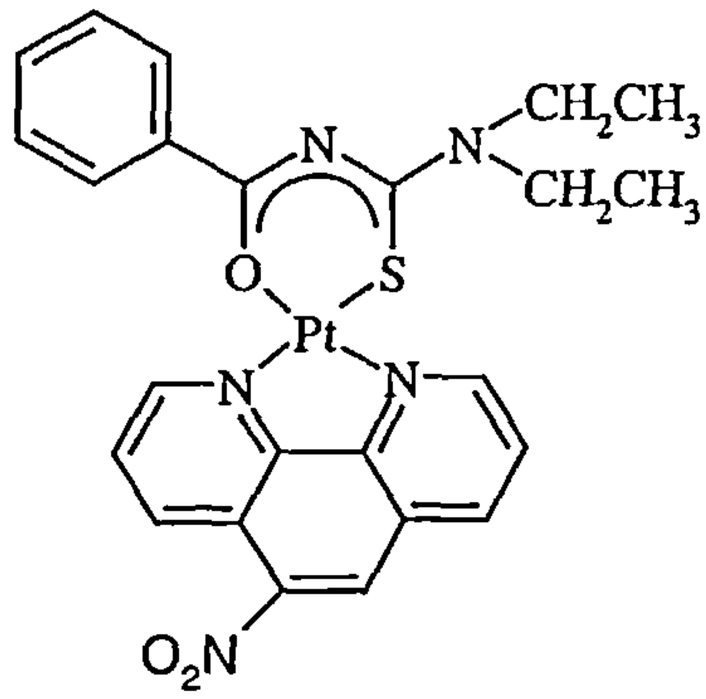

(Pt18)

Figure 3.9 continued

(Pt1 – Pt9) are similar in structure in that each complex contains a chloride and a DMSO group *cis* to one another other and only differ in substituents attached to the basic acylthiourea ligand. The variations of the amine attached to the thiocarbonyl functionality (R), are *diethylamine* $(CH_2CH_3)_2$; *diethanolamine* $(CH_2CH_2OH)_2$; or *morpholine* $(N(CH_2CH_2)_2O)$. The substituents on the aryl ring (R′) are denoted H for *hydrogen* (Pt1 – Pt3); NO_2 for *nitro* (Pt4 – Pt6); and CH_3O- for *methoxy* (Pt7 – Pt9). The two latter substituents have electron withdrawing or electron donating properties respectively. The (PtX) complexes are grouped in subsets according to the electron withdrawing or electron donating substituents on the aryl moiety.

(Pt10 – Pt18) differ slightly in substituent structure as can be seen in Figure 3.9 (Pt11 – Pt13) are chiral, and (Pt14 – Pt18) have been shown to unwind supercoiled DNA and so are thought to be DNA unwinders.[12,13] Sacht *et al.* have reported that (Pt4), (Pt5), (Pt7) and (Pt14) exhibit biologically activity against HeLa and MCF-7 cell lines.[13]

Of the eighteen complexes, (Pt10) is significant as it contains only the acylthiourea ligand system (L) (Figure 3.10), that is common to all the (PtX) complexes. (Pt10) can therefore be used as a model compound to see how the bulky acylthiourea ligand (L) itself can interact with DNA and act as a standard for comparison with other complexes of similar basic structure.

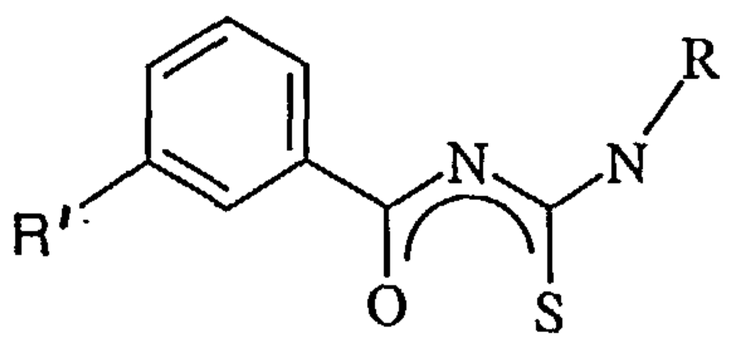

Figure 3.10 The structure of the basic acylthiourea ligand system $R'C(O)NHC(S)NR_2$, denoted L where R′ = H, NO_2, OMe and R = diethylamine, morpholine, diethanolamine

Variation of the substituent (nitro or methoxy group) on the aryl moiety has been found to influence the electronic properties of the molecule.[13] Sacht *et al.* noted the sensitivity of the ^{195}Pt NMR signal to changes in the aryl substituent, with NO_2 causing a downfield shift relative to H, Cl or OCH_3. The chloro-platinum ligand (Pt-Cl) bond (which is cis rather than trans to the aryl group) has the rate of substitution as a function of the aryl susbstituent being $NO_2 > Cl > OCH_3 \approx H \approx CH_3$ in accord with the ^{195}Pt NMR, though it is not obvious this effect is a through bond one.[13] Interestingly, Sacht and Datt found no evidence of DMSO substitution.

3.2.2 (PtX) spectroscopy

There is no spectroscopic literature for these novel complexes. The basic expected MLCT transitions for the (PtX) complexes are (i) the Pt-acylthiourea ligand system (made up of the Pt-benzoyl and Pt-thiocarbonyl amine portions of the ligand) denoted Pt-L, (ii) Pt-Cl band or (iii) Pt-DMSO bands. In a water:methanol mix, the methoxy and nitro substituted aryl rings are expected to exhibit transitions at 217 nm and 269 nm respectively.[22] These data suggest that these substituted aryl rings do not effect transitions outside the DNA region of the spectrum.

The lability of substituents on square planar platinum complexes have been extensively explored in terms of their DNA binding interactions, with for example, cisplatin and $[Pt(terpy)X]^+$ complexes where terpy is 2,2′:6′,2″-terpyridine and X = chloride (Cl), hydroxy (OH), or methoxy (OMe).[20,23–29] In the majority of the cases, these groups have been found to undergo partial solvolysis in water (*e.g.* Cl to OH or OH_2 and OMe to OH *etc.*) and in organic solvents.[26,27] For example, the platinum terpy complex, $[Pt(terpy)OH]^+$ has been found to be stable in aqueous solution for a number

of days but only exhibits limited stability in MeCN or DMSO for a few hours, after which a decrease in the long wavelength CT absorption band of the original complex is seen. It was suggested that this was due to the loss of the hydroxide ligand.[26] The spectra of the $[Pt(terpy)OH]^+$ complex in the different solvents are similar, but in the 300 – 310 nm region the complex exhibits a larger shoulder in DMSO, a distinct band is seen in MeCN and a much smaller absorbance shoulder is seen in aqueous solution.[26,27] On interaction with random sequence DNA, after a few hours the $[Pt(terpy)OH]^+$ spectrum was found to show a decrease in in-ligand (IL) absorbance at 332 nm (this was attributed to the loss of the OH bond), a corresponding increase in absorbance at 360 nm and a bathochromic shift of the centre of the charge transfer (CT) band from ~ 385 nm to 410 nm (attributed to the subsequent covalent binding of the complex to DNA).[26] Thus, the data suggests that the terpy Pt-OH band in aqueous solution exhibits transtion bands at ~ 332 nm. [26]

In general, charge transfer bands in the 300 – 350 nm region have been found to depend on the identity of the ligand, Pt-L in $[Pt(terpy)L]^{n+}$.[28] Using the literature on similarly assigned terpy Pt –Cl or OH, OMe transitions in aqueous and organic media [23 – 29] the expected wavelength assignments are summarised in Table 3.1.

Table 3.1 Summary of absorption literature assignments on selected platinum terpy complex transitions

Transition	Wavelength assignments / nm
terpy Pt – Cl [23,27,28]	(300 – 350);[28] (328);[23] (303, 317, 330, 347); *[27] (327, 343)[25], (342)[29]; (306, 318, 334,350)[24 #]
terpy Pt – OH[26,27]	(332);[26] (308, 325, 339)*[27]
terpy Pt – OCH_3	(310, 327, 339) *[27]

* = in MeCN # = 5:5:1 ethanol:methanol:DMF mix

3.2.3 Materials and Methods

(PtX) complexes

The synthesis and characterisation of the (PtX) complexes have been published by Sacht *et al.*[12,13] The (PtX) complexes have been provided by C. Sacht and confirmed to be pure by CHN analysis.

Polynucleotide samples

Duplex ct-DNA, sodium salt, 'highly polymerised' Type 1 was purchased from Sigma, synthetic DNAs, poly[d(A–T)]$_2$ and poly[d(G–C])$_2$ (AT and GC DNA respectively) for *in vitro use* were obtained from Pharmacia Biotech. DNA concentrations were determined spectroscopically using ε_{254} = 8400 mol^{-1} dm^{3}cm^{-1} for poly[d(G-C)]$_2$, ε_{262} = 6600 mol^{-1} dm^{3}cm^{-1} for poly[d(A-T)]$_2$ and ε_{258} = 6600 mol^{-1} dm^{3}cm^{-1} for ct-DNA. 9-methylguanine (MG) and the di-sodium salts of the 5′-monophosphates were purchased from Sigma and Aldrich and used without further purification.

For the reasons discussed in Section 1.7, ct-DNA was initially dissolved in water, rather than a buffer. Its double stranded behaviour in all solvent systems used was verified by performing melting curves and basic spectroscopic studies. Sodium chloride salt and a constant concentration of sodium cacodylate buffer (1 mM) were used to maintain AT and GC DNA structure. AT DNA was used with a minimum of 30 mM NaCl, 1 mM sodium cacodylate buffer, pH 6.92, GC-DNA was used with a minimum of 10 mM NaCl, 1 mM sodium cacodylate buffer, pH 6.92. These concentrations were shown to be sufficient to retain their duplex structures. The minimum salt concentration required to ensure AT and GC DNA duplex formation was

also dependent on the percentage organic solvent present. Therefore, for AT DNA, 30 mM NaCl was required for ≤ 40% MeCN and 40 mM NaCl was required at > 40% MeCN. For GC DNA, 10 mM NaCl was required for < 40% MeCN and 20 mM NaCl was required for ≥ 40% MeCN.

Other Materials

Polyvinyl alcohol (PVA) (Type III low molecular weight (hot water soluble)) was purchased from Sigma Chemical Co. to make the film for film *LD*. HPLC grade solvents acetonitrile, DMSO and DMF were used initially to dissolve the compounds, followed by addition of high purity water 18.2 MΩ.

Instrumentation and Methods

The spectroscopic techniques used to determine whether interactions are taking place in these (PtX):DNA systems were: UV-Visible absorbance spectroscopy, circular dichroism (*CD*), flow linear dichroism (*LD*) and film *LD*. These techniques are discussed in some detail in Chapter 1. UV-Visible absorbance spectra were run on either a Jasco V-550 or Cary IE spectrometer, the *CD* and *LD* spectra were run on a Jasco J-715 spectropolarimeter. *CD* and UV-Visible absorbance spectroscopy was performed in a 1 cm pathlength quartz cuvette. Flow *LD* measurements were made using a 1 mm pathlength quartz couette flow cell.[30] For film *LD*, both absorbance and film *LD* measurements were taken both before and after stretching to ×2 film length (using a mechanically stretching device and heat) on the Jasco V-550 and Jasco J-715 spectropolarimeter respectively.

Fresh samples of (PtX) complexes were prepared and used immediately unless otherwise stated. Titrations were set up where the DNA concentration was kept

constant as the (PtX) concentration was varied. Mixing ratios, R, are stated in order DNA base:(PtX).

3.3 Results

3.3.1 Preliminary spectroscopic study of the eighteen complexes

The platinum complexes exhibit poor water solubility, so the solutions were made as follows: the addition of a minimum amount of organic solvent required to dissolve the platinum complex followed by water, buffer, then DNA solution. Order and speed of addition was found to be important. Acetonitrile (MeCN) was the organic solvent of choice as it gives a nice spectroscopic window and allowed for sample recovery, however, not all the platinum complexes dissolved in it. DMF and DMSO were used in some cases. Although it was very difficult to achieve, in general, the platinum complexes (PtX) stayed in solution upon the addition of water and DNA. The percentage (%) organic solvent used is stated on the spectra.

All compounds were initially dissolved in the minimum amount of acetonitrile, if this was not successful then DMF or DMSO, or even a mix of DMF and DMSO was used. Structures of all the complexes are given in Figure 3.9.

In order to determine whether there was any interactions with ct-DNA, preliminary UV-Visible absorbance and *CD* studies were conducted on (Pt1) – (Pt18) using (PtX) solution concentrations of between 20 – 60 μM (PtX) complex and a constant 125 μM ct-DNA solution to give an approximate ct-DNA:(PtX) mixing ratio of between 6:1 and 2:1.

Preliminary absorbance studies

The platinum complexes examined are yellow in solution and exhibit transitions in both the UV and visible region of the spectra. If there is an interaction of some sort between (PtX) and ct-DNA a change in the absorbance signal should develop. With absorbance spectroscopy a difference between the (PtX)-DNA solution and the sum of (PtX) and DNA spectra indicates an interaction. In this case it may be difficult to distinguish between the induced signal and the sum of the two spectra as they may overlap or appear in the same region of the spectra and the change may be small.

In these preliminary studies, the addition of ct-DNA to a known concentration of (PtX) results in a slight dilution of (PtX) concentration, which has not been compensated for. Any induced interactions will therefore be more distinguishable in the *CD* spectra. The effect on the (PtX) absorbance spectroscopy when ct-DNA is added is illustrated for each of the eighteen (PtX) complexes in Figure 3.11. The spectra of (Pt13), (Pt14) in DMF and (Pt17) in DMSO denoted (Pt13ii), (Pt14ii) and (Pt17ii) respectively are also included. The (PtX) complex concentrations used are stated in the Figure 3.11 caption and the % organic solvent used to dissolve the (PtX) complexes is stated on each spectrum. Spectral recordings were taken immediately upon dissolution of the (PtX) complex in solvent and on mixing with DNA.

Where the mixture signal exceeds the (PtX) signal above 300 nm, we know there is an interaction (any dilution effect would cause a decrease). Further if there is an obvious change in the shape of the spectrum it is clear there is an interaction.

On addition of DNA, (Pt10), the complex with the two bulky acylthiourea ligands, L, shows no change in absorbance (except the small dilution effect). The chiral complexes (Pt11 – Pt13) and (Pt5) show small changes in absorbance. All the other complexes do exhibit a slight change in shape and intensity.

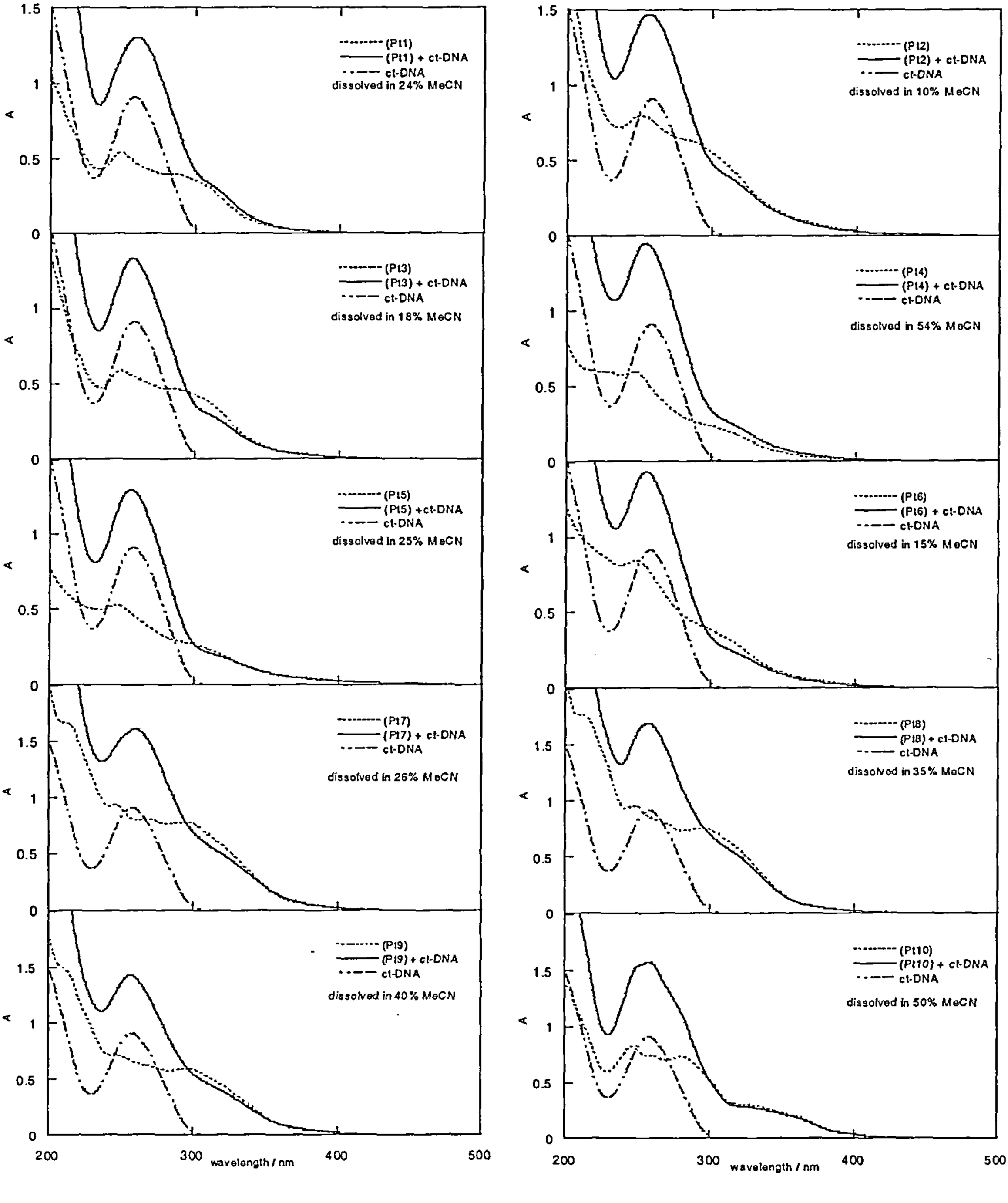

Figure 3.11 UV-Visible absorbance spectra of the eighteen (PtX) complexes (i) alone and (ii) with ct-DNA (125 μM). The (PtX) *concentrations are listed below. The spectra of* (Pt13), (Pt14) in DMF and (Pt17) in DMSO denoted (Pt13ii), (Pt14ii) and (Pt17ii) respectively are also included. The % organic solvent used to dissolve the (PtX) complexes is stated on each spectrum. The spectrum of ct-DNA alone in solution (125 μM) has been *included for reference.*

(PtX) complex concentrations used: (Pt1) 33 μM; (Pt2) 51 μM; (Pt3) 50 μM: (Pt4) 30 μM; (Pt5) 36 μM; (Pt6) 50 μM; (Pt7) 57 μM; (Pt8) 61 μM; (Pt9) 50 μM; (Pt10) 40 μM; (Pt11) 31 μM; (Pt12) 51 μM; (Pt13) 33 μM; (Pt13ii) 32 μM; (Pt14) 38 μM (Pt14ii) 32 μM; (Pt15) 40 μM; (Pt16) 30 μM; (Pt17) 18 μM; (Pt17ii) 25 μM; (Pt18) 34 μM.

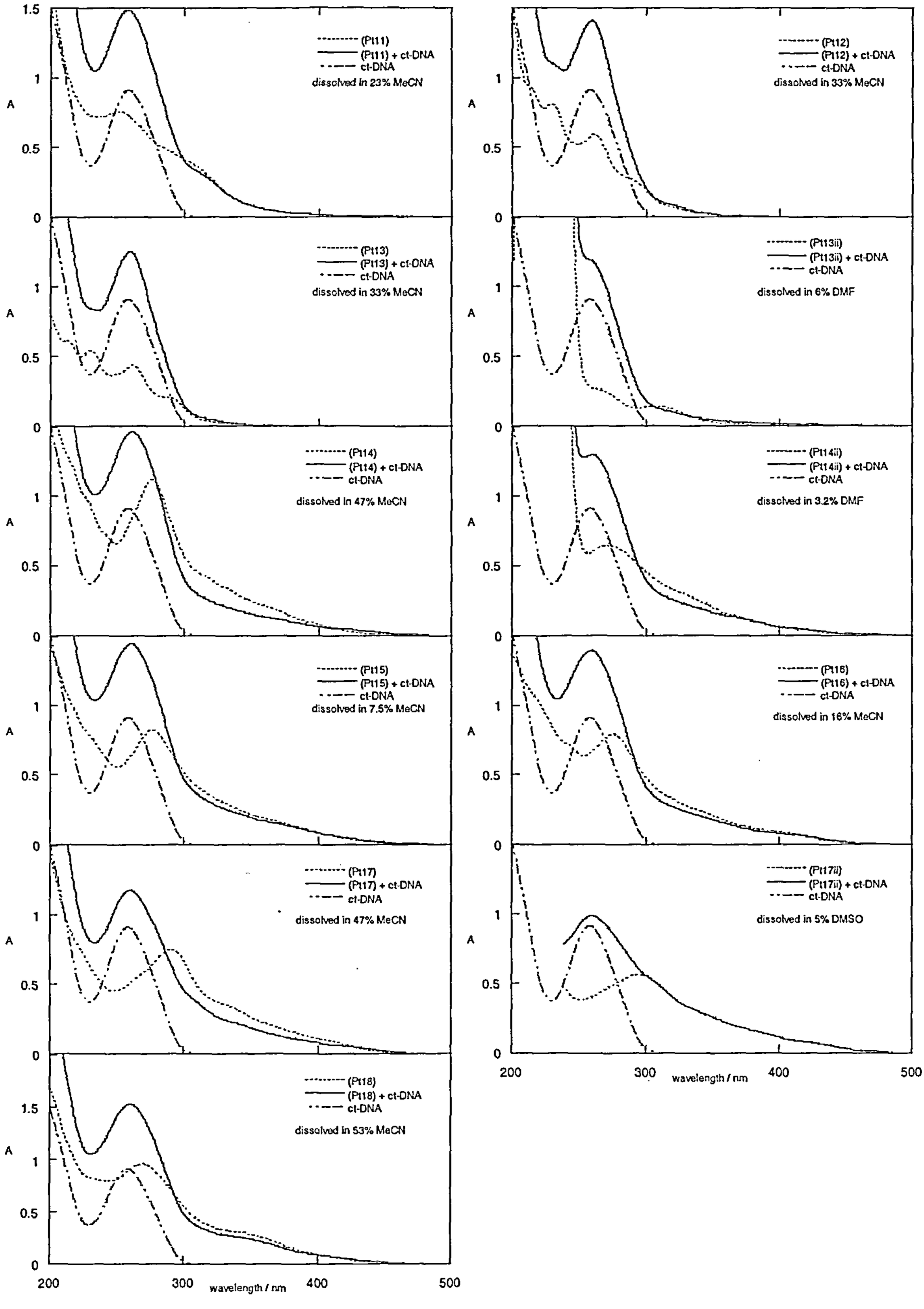

Figure 3.11 continued

On addition of ct-DNA, (Pt1) and (Pt4) show a small increase in absorbance intensity (hyperchromic effect) in 300 nm – 350 nm region, but no significant wavelength shift. (Pt2 – Pt3) and (Pt5 – Pt9) all show a decrease in absorbance intensity (hypochromic effect) between 300 – 350 nm, more significant than that due to the dilution effect. The potential intercalators (Pt14 – Pt18) also show a decrease in their transition intensities above 300 nm on addition of DNA, but all the spectra show no wavelength shift. Attempts to use DMF and DMSO as alternative solvents were not encouraging. (Pt17) almost certainly does not bind to DNA when dissolved in DMSO. The spectra of (Pt13) and (Pt14) when dissolved in DMF are so different from that in MeCN to suggest a different chemical species. These experiments were therefore not pursued.

Preliminary *CD* studies

CD was expected to be a better tool than absorbance for probing any interactions, as the isolated achiral platinum complexes (PtX) do not have a *CD* signal and ct-DNA only exhibits transitions below 300 nm. Thus the interaction of an individual (PtX) complex with ct-DNA would be clearly shown by an *ICD* signal above 300 nm. In the case of the chiral compounds (Pt11) – (Pt13), the intrinsic (PtX) spectroscopy must be subtracted to give the induced *CD* (*ICD*) signal due to the interaction. The effect on the (PtX) *CD* spectroscopy when DNA is added is illustrated for each complex in Figure 3.12. The (PtX) complex concentrations used are stated in the Figure 3.12 caption and the % organic solvent used to dissolve the (PtX) complexes is stated on each spectrum.

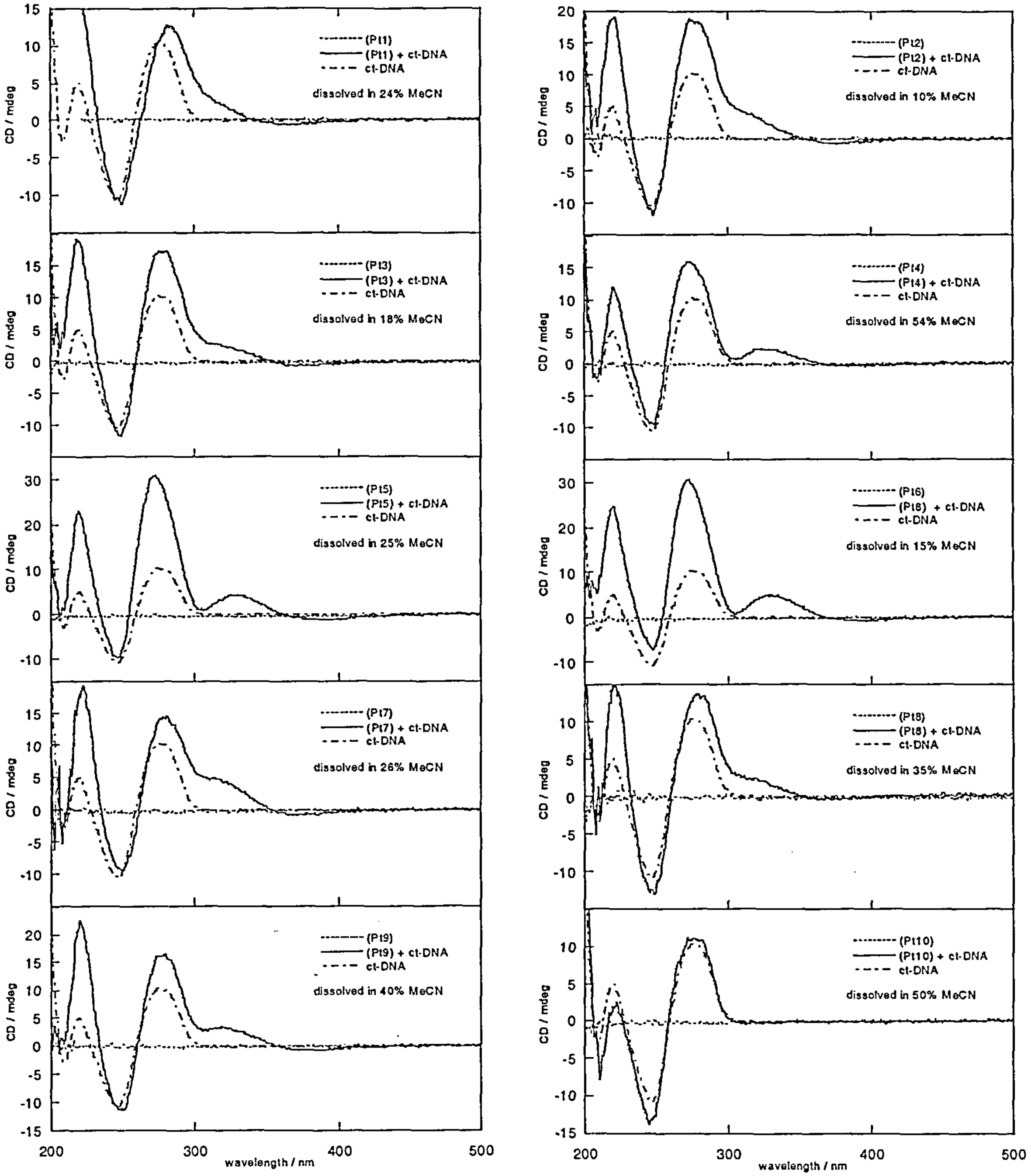

Figure 3.12 *CD* spectra of the eighteen (PtX) complexes (i) alone and (ii) with ct-DNA (125 μM). The (PtX) concentrations are listed below. The spectra of (Pt13), (Pt14) in DMF and (Pt17) in DMSO denoted (Pt13ii), (Pt14ii) and (Pt17ii) respectively are also included. In the case of the chiral compounds (Pt11) – (Pt13), the chiral (PtX) complex *CD* and DNA *CD* has been subtracted from the DNA + complex spectrum to give the *ICD* signal that has been plotted. The % organic solvent used to dissolve the (PtX) complexes is stated on each spectrum. The spectrum of ct-DNA alone in solution (125 μM) has been included for reference.

(PtX) complex concentrations used: (Pt1) 33 μM; (Pt2) 51 μM; (Pt3) 50 μM: (Pt4) 30 μM; (Pt5) 36 μM; (Pt6) 50 μM; (Pt7) 57 μM; (Pt8) 61 μM; (Pt9) 50 μM; (Pt10) 40 μM; (Pt11) 31 μM; (Pt12) 51 μM; (Pt13) 33 μM; (Pt13ii) 32 μM; (Pt14) 38 μM (Pt14ii) 32 μM; (Pt15) 40 μM; (Pt16) 30 μM; (Pt17) 18 μM; (Pt17ii) 25 μM; (Pt18) 34 μM.

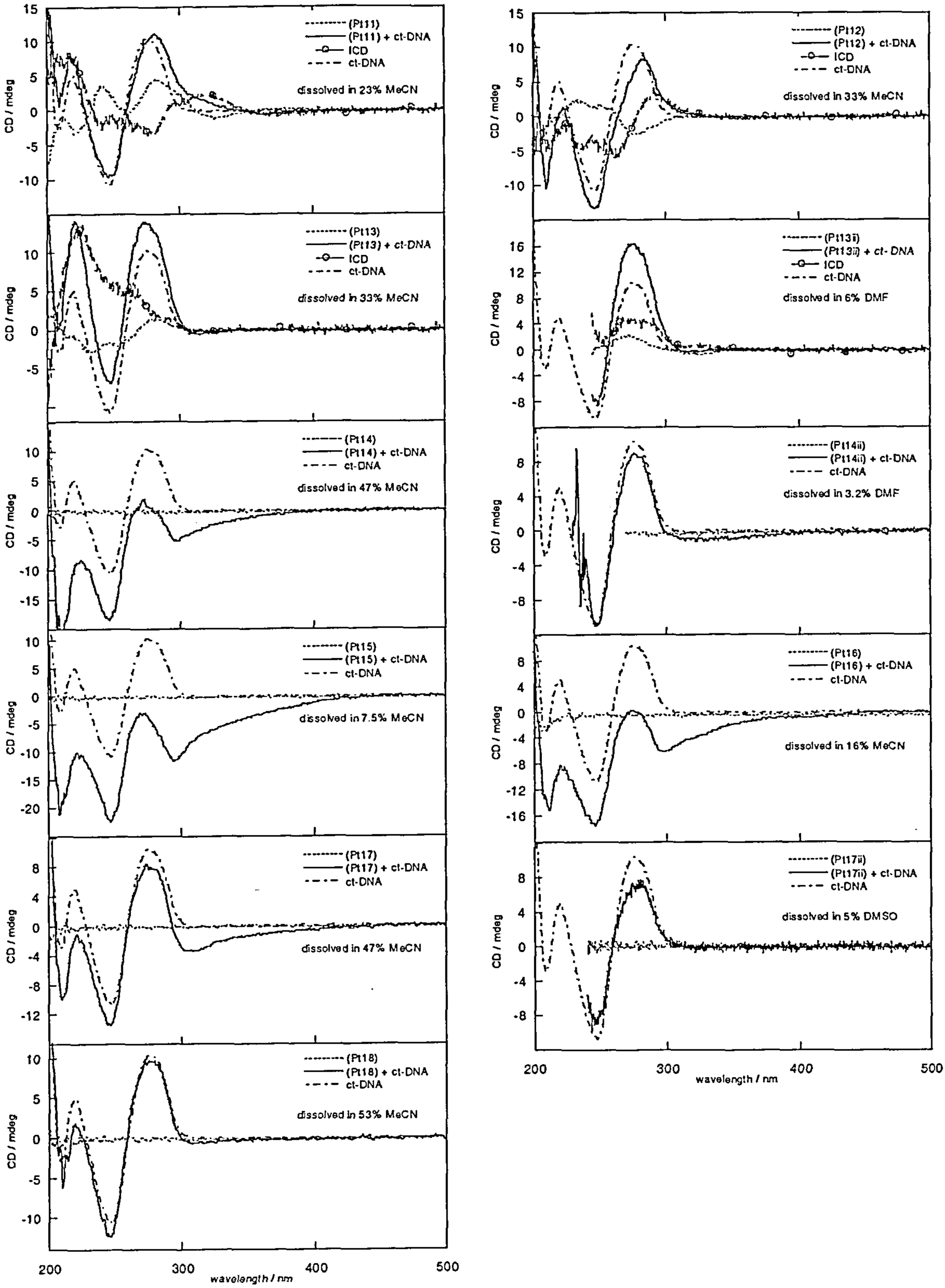

Figure 3.12 continued.

In summary, all the *CD* spectra of the DNA—(PtX) complexes except (Pt10) (and the DMSO spectrum of (Pt17)) show the (PtX) complexes interact with ct-DNA (see Figure 3.12). The developments of induced *CDs* (*ICDs*) at wavelengths/energies that correspond to platinum complex transitions (above 300 nm) confirm an interaction between the platinum complexes and DNA.

(Pt1 – P10), (Pt14 – Pt18) are achiral and therefore exhibit no intrinsic *CD* signal. Addition of ct-DNA to (Pt1– Pt9), (Pt14 – Pt18) induces chirality into the achiral (PtX) complexes. These (PtX) complexes may therefore be concluded to interact with DNA.

(Pt1– Pt3), (Pt7 – Pt9) (sets of complexes differing by addition of a methoxy group to the phenyl group) exhibit two similar *ICD* signals of varying magnitude above 300 nm (outside the DNA region): the first a positive shoulder (which becomes a more pronounced band for the methoxy groups) decreasing in magnitude from 300 nm to ~340 nm and a small negative signal centred at ~ 375 nm.

In contrast, complexes (Pt4 – Pt6) do not exhibit much *CD* intensity at 300 nm, rather a positive *CD* band centred at ~325 nm, is observed with an even smaller negative *CD* transition band of varying magnitude centred at 375 nm. These data immediately suggest that (Pt1 – Pt3) and (Pt7 – Pt9) have similar binding interactions whereas (Pt6 – Pt9) are similar to each other and somewhat different from the other sets.

In the case of the chiral compounds (Pt11 – Pt13), the chiral (PtX) complex *CD* and DNA *CD* has been subtracted from the DNA + complex spectrum to give the *ICD* signal that has been plotted. (Pt11) shows a small clear negative *ICD* signal below 300 nm, a positive *ICD* at 325 nm and a very small negative *ICD* at 375 nm were observed. The DNA region change may be due to a change in the DNA spectroscopy or (Pt11)

spectroscopy or both. (Pt12) shows an *ICD* signal below 300 nm, and a very small shoulder above 300 nm.

(Pt13) gave solubility problems in each of the organic solvents (MeCN, DMF and DMSO). The spectrum of (Pt13) in 33 % MeCN shows a minute positive *ICD* signal below 300 nm indicating a small (PtX):DNA interaction, the same complex in 6% DMF (denoted (Pt13ii)) shows a small positive *ICD* below 300 nm as well as a very small positive *ICD* at 325 nm. The *ICD* of (Pt13) is different in signal size from the *ICDs* of (Pt11) and (Pt12) in MeCN.

Of the hexafluorophosphate salt intercalator complexes, (Pt15 –16) were found to dissolve well in MeCN (very low % MeCN necessary). The remaining intercalators, in particular (Pt14) and (Pt18), exhibited poor acetonitrile solubility with high % MeCN required, as well as poor water solubility as shown by the large decrease in their absorbance signals. (Pt14 – Pt17) exhibit similar negative signals in *CD* with a negative shoulder extending from 300 – 440 nm, (Pt18) only exhibits a small band at 300 – 350 nm. The intercalators exhibit large changes in their DNA signature, in order of decreasing magnitude (Pt15) > (Pt16) > (Pt14) > (Pt17) > (Pt18), the latter showing only a small decrease in DNA signal. It should be noted that the long wavelength flat region of the spectra show that this is not due to scattering by undissolved compounds.

Interestingly, the spectrum of (Pt14) in DMF *i.e.* (Pt14ii) shows a much smaller negative *ICD* interactions between 300 – 400nm and no real deviation in the DNA chiral signature compared to its MeCN equivalent (see spectra (Pt14)); similarly the spectral interactions of (Pt17) in DMSO *i.e.* (Pt17ii) show no interaction above 300 nm in the (PtX) region, compared to its MeCN equivalent spectrum (Pt17). This suggests that the choice of solvent plays a *key role* in any interaction of (PtX) with DNA, perhaps by changing the identity of the compound as discussed above.

(Pt10)

Upon addition of ct-DNA to an acetonitrilic solution of (Pt10), the absorbance spectrum shows no change in the DNA *CD* signal or *ICD* signal. Figure 3.13 shows the absorbance spectra of (Pt10) on addition of DNA (data taken from Figure 3.11). Figure 3.13 includes the expected theoretical spectrum on addition of ct-DNA to (Pt10) (it has been modified to account for the dilution effect on the (Pt10) solution upon DNA addition).

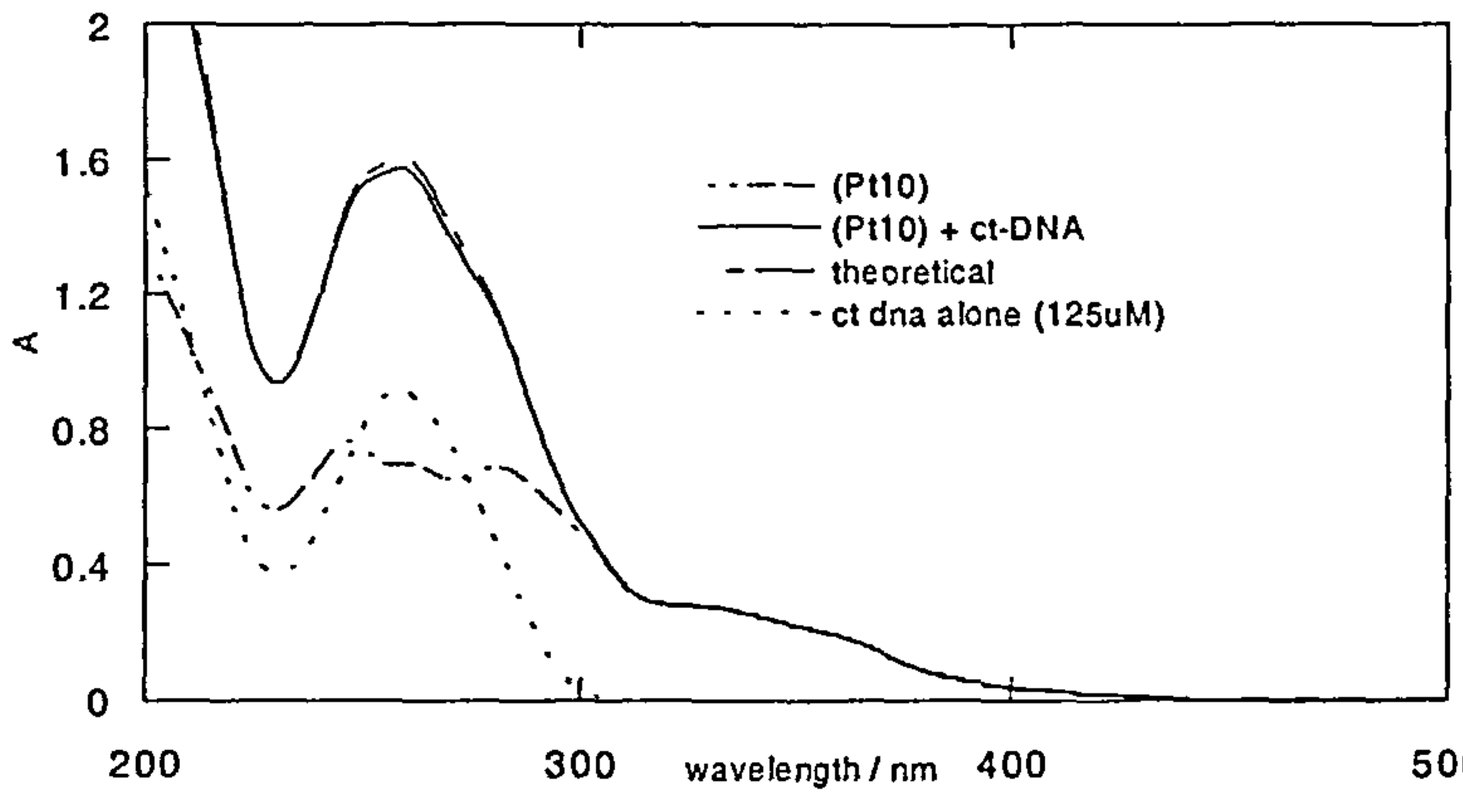

Figure 3.13 UV-Visible spectrum of (Pt10) with ct-DNA (the data has been modified to account for the dilution effect on (Pt10) (~40 μM) on addition of the ct-DNA (125μM) in a 3.1:1 DNA base:(Pt10) ratio

No significant wavelength shift, hypo- or hyperchromic effect is seen, importantly, the *CD* spectrum shows no interaction between (Pt10) and ct-DNA — the ct-DNA:(Pt10) spectrum is indistinguishable from that of ct-DNA alone. A further absorbance and *CD* titration of (Pt10) with a constant DNA concentration was undertaken over a range of mixing ratios, this also showed no interaction. Thus it can be concluded that (Pt10) does not interact with DNA. Flow oriented studies were therefore not pursued.

It is almost certainly the presence of two bulky acylthiourea ligands that is responsible for this lack of interaction with DNA. The other complexes only have one

acylthiourea ligand system. The (Pt10) results lead us to conclude that it is the less bulky side of the other complexes that interacts with DNA. Our investigations show that the basic acylthiourea ligand (L) system (specifically for (Pt10), the diethylamine system) has no interaction with DNA. This implies that the chloride and the DMSO groups (present on the majority of the other (PtX) complexes (Figure 3.9) investigated must play a pivotal role in any DNA interaction of this group of novel (PtX) complexes. This (Pt10) complex system can therefore be used as a standard for comparison with other complexes of similar basic structure.

The data provided by this preliminary study enabled the selection of a set of six complexes for closer analysis in this thesis. (Pt4 – Pt9) were chosen in part due to their clear large spectroscopic interactions on interaction with DNA, reasonable solubility in MeCN:water mixtures and ability to remain in solution on subsequent additions. (Pt4), (Pt5) and (Pt6) are similar in structure, each has a nitro (NO_2) substituent and differ only in the amine groups attached to the thiocarbonyl functionality, however Sacht *et al.* have suggested that of these only (Pt4) and (Pt5) are biologically active,[13] whereas (Pt6) is not. (Pt4), (Pt5) and (Pt6) (forming a subset denoted 'nitro') were therefore ideal to study in much greater detail.

The remaining three complexes (Pt7), (Pt9) and (Pt8), of which Sacht *et al.* suggest (Pt7) is biologically active,[13] have a methoxy (OCH_3) substituent in common, and again differ only in their amine groups and similarly to those of the 'nitro' subset (Pt4 – Pt6), make up a subset is denoted 'methoxy'. The main difference between the 'nitro' and 'methoxy' subsets is the nitro-electron withdrawing and the methoxy-electron donating groups respectively as well as different sizes and shapes. In terms of the electronic properties of the (PtX) complexes, these substituents may be important and affect DMSO or chloride group lability as well as steric aspects.

As the subsets differ in the group (methoxy- or nitro-) attached to the aryl ring, a direct comparison of the effect of these groups on interaction of (PtX) with DNA can be made. (Pt4) and (Pt8); (Pt5) and (Pt7); and (Pt6) and (Pt9) contain the same amine group *i.e.* each (PtX) complex within one subset has an amine equivalent (PtX) complex (denoted diethylamine, morpholine and diethanolamine) in the second subset. The effect of the variation of the amine ligands can be examined and compared between (inter) subsets as well as within (intra) each subset.

(Pt15), an intercalating complex, does not contain the DMSO and Cl ligands but has the most similar structure to those being studied. It was therefore also investigated in order to provide a spectroscopic comparison to (Pt4 – Pt9).

There was not enough material to initiate a thorough investigation into chiral (Pt11) and (Pt12); chiral (Pt13) had solubility problems. The intercalators (Pt14), (Pt17) and (Pt18) were not investigated because of their solubility issues. (Pt16) was excluded as it is structurally different from the subsets chosen but would be an ideal choice for a new study.[4,20] The hydrogen subset complexes (Pt1–Pt3) were not investigated since they showed similar spectroscopy in the preliminary studies to the methoxy subset of complexes.

3.3.2 (PtX) transition polarisation determination

In order to understand the effect DNA has on the spectroscopy of these platinum complexes, the assignments including transition polarisations need to be considered. Figure 3.14 shows the molecular axis system for the (PtX) complexes.

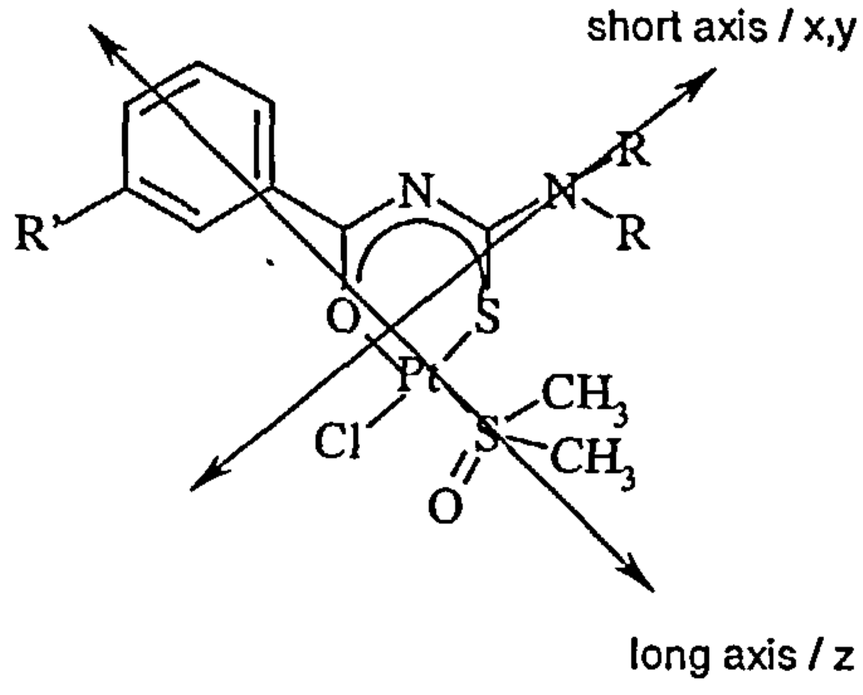

where R' = H, NO_2, OMe

NR = diethylamine, morpholine, diethanolamine

Figure 3.14 General structure and molecular axis system for the platinum complexes (PtX). The complex long and short axes and x,y and z axes are indicated in the figure.

When a molecule is absorbed into a stretched film, it is assumed that the long axis of the molecule will orient along the direction of orientation (stretch) (long axis) whilst the short axis would resist the stretch and lie at right angles to the stretch direction. We define the z axis of the molecule to lie along its long axis, and the x/y axis along the short axis. From Figure 3.14, one can deduce likely MLCT transition polarisations. MLCT bands into the sulfoxide π-system will be short axis polarised for example. However, given the overlap of different bands it was important for the flow *LD* experiments to have good assignments of dominant transitions. Table 3.2 contains a summary of the expected MLCT transitions.

Table 3.2 Summary of expected MLCT transitions

Short axis (x/y)	long axis (z)
Pt-Cl, Pt-DMSO	Pt-DMSO
Pt-L (Pt-thiocarbonyl amine)	Pt-L (Pt-benzoyl)

The use of organic solvents in the preparation of films for *LD* is not straight forward and is covered briefly in Section 1.7. (Pt4) was used as a model compound for the whole series since the basic platinum chromophore is the same for all complexes

(i.e. all (PtX) complexes will exhibit similar transition polarisations). The film absorbance (A) and film *LD* of (Pt4) were measured and film LD^r (*i.e. LD* divided by A) calculated and plotted to enable transition polarisation moments to be qualitatively assigned. Section 2.2.2.1 provides an explanation for film *LD*. Figure 3.15 shows the film absorbance (A), film *LD* and LD^r spectra of (Pt4) using MeCN as its solvent.

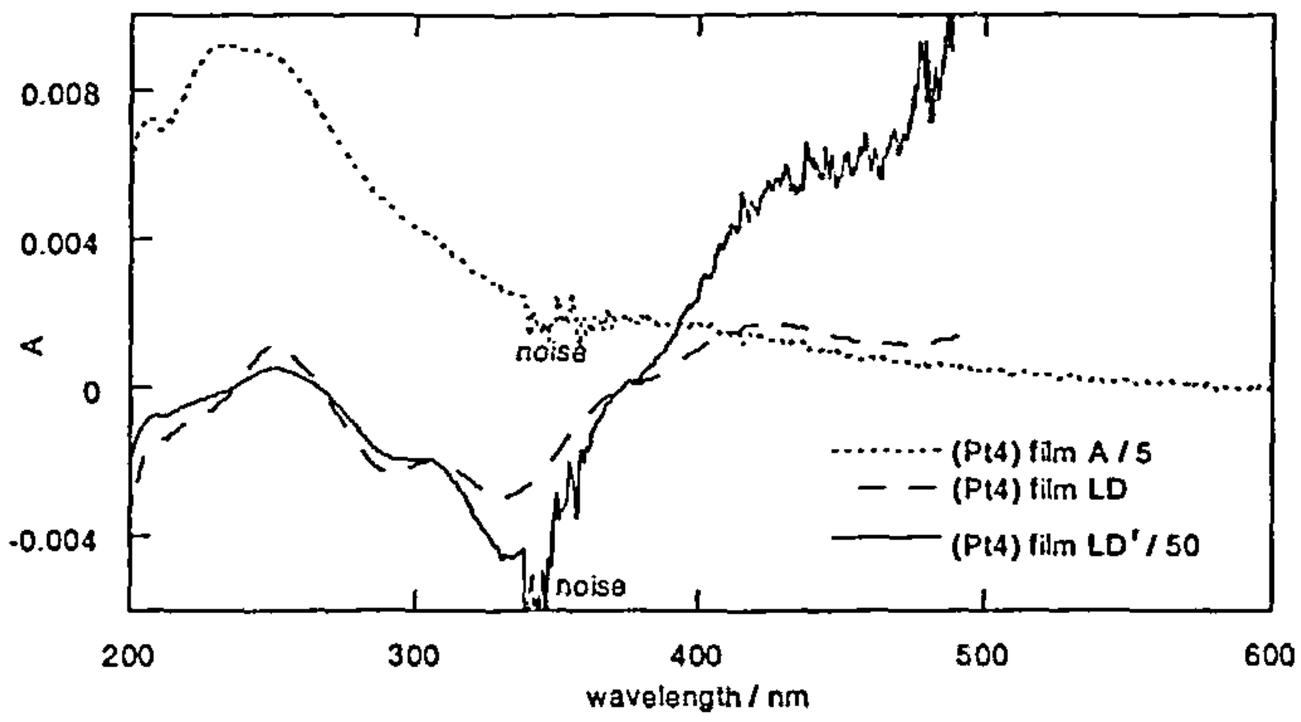

Figure 3.15 Film absorbance, *LD* and LD^r of (Pt4) oriented in PVA film. The noise (due to a hardware problem on the V-550) in the absorbance spectrum is translated into the calculated LD^r spectrum.

The film absorbance spectrum of (Pt4) consists of a large broad sloping band extending from the far UV to the visible region of the spectrum (200 nm – 550 nm). The long wavelength part of this is much larger than that seen for the absorbance spectra of Figure 3.11 is due to scattering. The LD^r spectrum consists of a positive LD^r maxima centred at 250 nm and positive LD^r signals above 400 nm in the MLCT region (suggesting predominately z-polarised transitions) with negative LD^r maxima bands at 210 nm, 290 (with a less negative signal at 310 nm) and ~330 – 340 nm and a sloping LD^r signal from 350 – 400 nm.

We assume that most positive LD^r belongs to a long axis (z) polarised transition and any negative (or positive minima at places of large absorbance intensity) correspond to short axis (x/y) polarised transitions. The negative maxima at 210 nm, ~ 290 nm, and ~330 – 340 nm may therefore be assigned as short axis polarised transitions. The positive bands at 250 nm, and less negative signal at 310 nm and transitions above 400

nm are assigned to long axis polarised transitions. The sloping LD^r signal from negative to positive 350 – 400 nm is assumed to be due to an overlap of short and long axis polarised transitions.

The transitions above 300 nm can be due to MLCT or in-ligand (IL) transition bands of either (i) the Pt—acythiourea ligand system (L) (made up of the Pt-benzoyl and Pt-thiocarbonyl amine), (ii) Pt—Cl band, or (iii) Pt—DMSO bands. In order to help with transition assignments, we look at the absorbance spectrum of (Pt10) (Figure 3.13). This complex is composed of two acythioureau ligand systems, and contains no chloride or DMSO groups unlike other complexes (Pt1 – Pt9). Its absorbance spectrum shows a larger absorbance band between 350 – 400 nm compared to other complex spectra. We therefore conclude that the 350 – 400 nm wavelength region is mainly composed of Pt-acylthiourea ligand (Pt-L) MLCT transitions. This same region in the film *LD* consisted of a sloping LD^r signal from negative to positive indicative of an overlap of short and long axis transitions.

The absorption band between 300 – 350 nm is not as significant for (Pt10) as for the other complexes, therefore is assumed to predominately be Pt-Cl[28] and Pt-DMSO transitions probably also with some underlying Pt-L transitions. This assumption correlates with the film *LD* finding of two short axis assigned transition bands at ~ 290 nm and at ~330 nm. Using a number of assumptions and the literature on similarly assigned Pt-Cl or OH, OMe transitions (from Table 3.1),[23–29] the following transition assignments have been made and are summarised in Table 3.3.

Table 3.3 Summary of MLCT transitions of (PtX) complexes using Table 3.1

Transition	short axis (x,y)/nm	long axis (z)/nm
Pt – L [22,28]	210 (s), 300 – 400 (s)	250 (l), 350 – 400 (mix), > 400 (l)
Pt – Cl[23,25, 27 – 29]	330 – 340 (s)	
Pt – DMSO[26,27]	290(s) – 310(s) (mix)	

(s) = short axis, (l) = long axis

3.3.3 Stability studies

The binding interactions of cisplatin are known to change over time.[3–5] Studies were undertaken in order to determine whether, like cisplatin the binding interactions of the (PtX) complexes change over time. Comparison of spectra of similar experiments using the same sample freshly prepared (day 1) then on day 3, day 14 or day 28 were found to show (slow) kinetic effects.

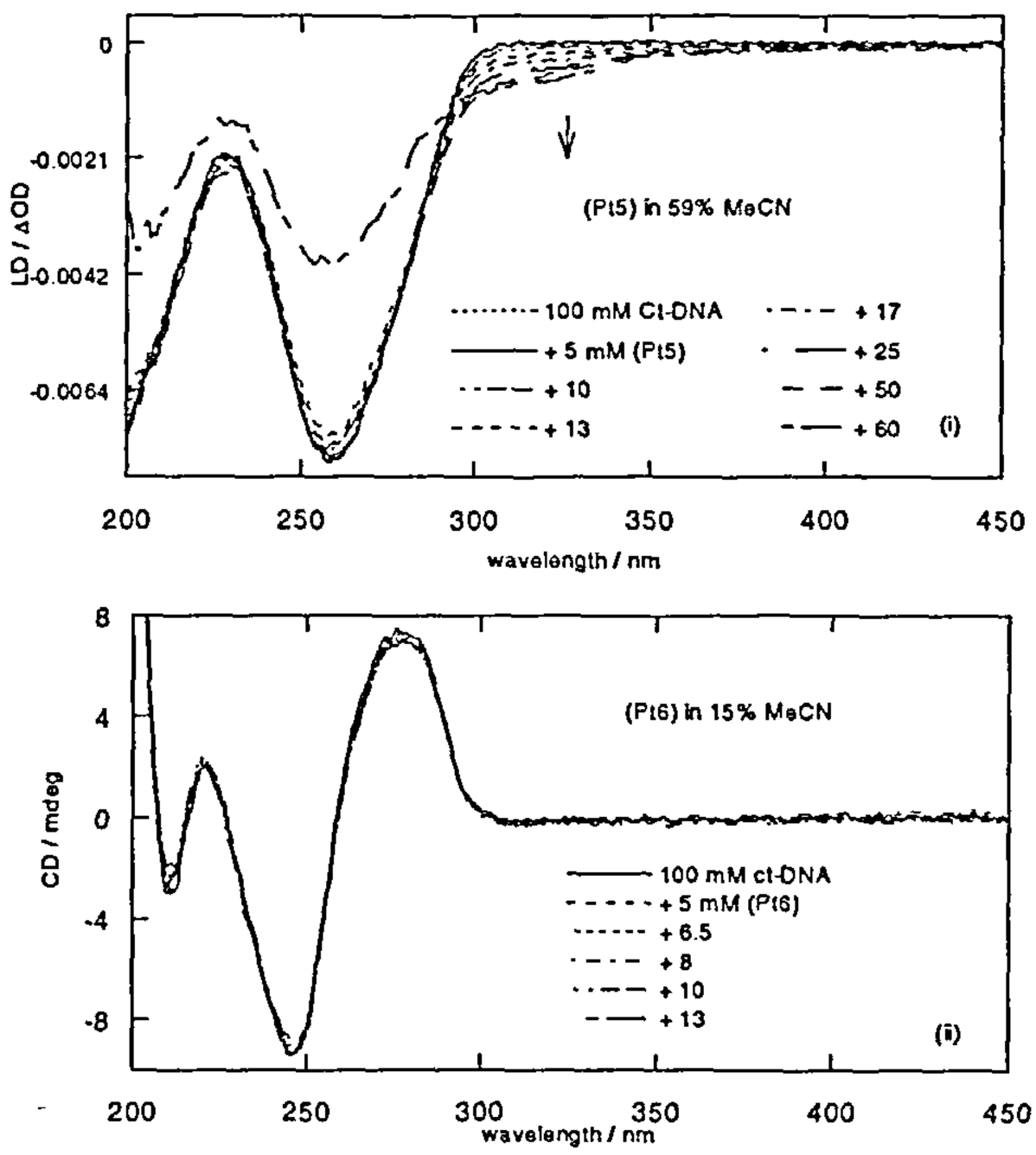

Figure 3.16 (i) *LD* spectrum of (Pt5)-ct-DNA interactions using a 14 day old solution, (ii) *CD* spectrum of (Pt6)-ct-DNA interactions using a 28 day old solution.

For example, Figure 3.16(i), shows the *LD* spectrum (see sections 3.2.3 and 3.3.5.3 for protocols used) of (Pt5) using a 14 day old sample of (Pt5). If this is compared to its equivalent from Figure 3.25, the spectra are different. Whereas the fresh (Pt5) spectrum shows a large decrease in signal at low mixing ratio, the spectrum using the 14 day old sample shows little change at the same and higher R. Figure 3.16(ii) shows the *CD* titration spectrum of a 28 day old sample of (Pt6) with ct DNA. In contrast to the preliminary studies (Figure 3.12), this suggests (Pt6) does not interact with DNA.

These studies show that (PtX) changes as a function of time and the 'product' interacts less effectively with DNA. Thus it is important to use fresh solutions.

3.3.4 Interactions with nucleotides

In order to clarify the preferential mode of action of the (PtX) complexes with DNA, the 5′-chiral di-sodium salts of the mono-nucleotides: guanosine 5′-monophosphate (GMP) (Figure 3.17), adenosine 5′-monophosphate (AMP), thymidine 5′-monophosphate (TMP) and cytidine 5′-monophosphate (CMP) were mixed individually with the (PtX) complexes of the nitro and methoxy subsets (Pt4 –Pt6) and (Pt7 – Pt9) and the products probed using *CD* and mass spectrometry. 5′-nucleotides were used as they represent a portion of DNA.

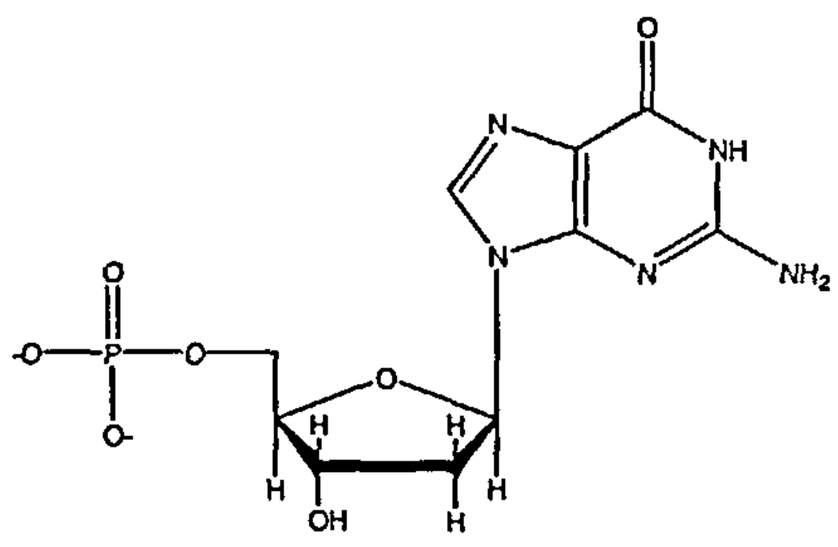

Figure 3.17 Structure of the disodium salt of 5' -guanosine monophosphate (GMP)

3.3.4.1 Circular dichroism studies

The UV-Visible absorbance and *CD* spectrum of each chiral nucleotide alone and with (PtX) working in a 1:5 (20:100 μM) (PtX): nucleotide ratio were recorded. Table 3.4 summarises the transition wavelengths associated with each mono-nucleotide.

Table 3.4 Transition bands associated with 5' mononucleotides below 300 nm

5′-nucleotide	Transition bands / nm
AMP	220 (-), 260 (-)
GMP	220 (+), 250 (-)
CMP	220 (-), 275 (+)
TMP	220 (-), 240 (-), 275 (+)

On addition of a nucleotide to (PtX) complex, minute induced signals are seen. Figure 3.18 shows the *CD* spectra of the nucleotides alone and on interaction with (Pt8).

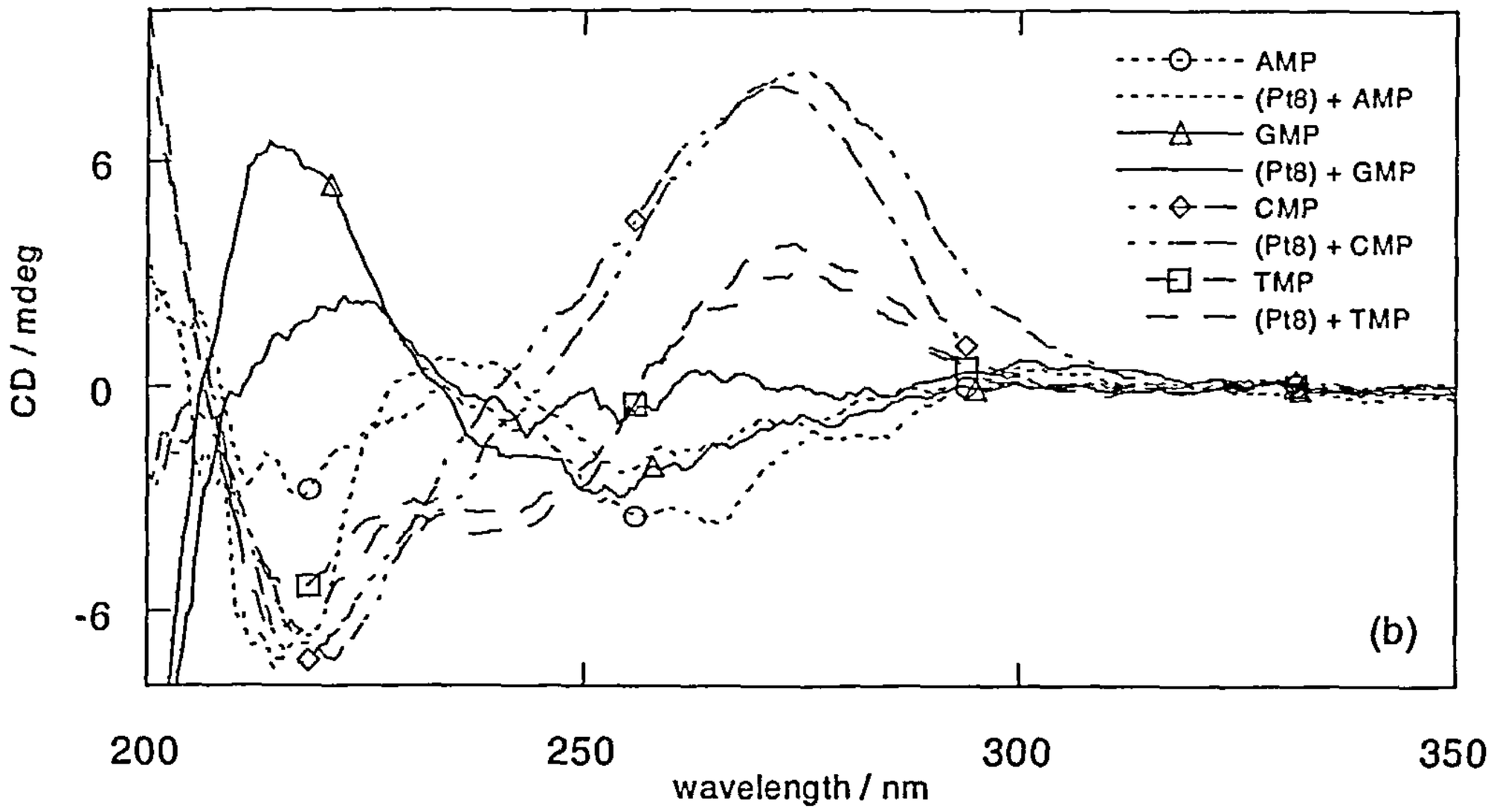

Figure 3.18 *CD* spectra of each nucleotide alone and on interaction with (Pt8).

Table 3.5 summarises all the nucleotide transition interactions with the (PtX) complexes. The (PtX) complexes show the largest (PtX) *ICDs* between 300 – 350 nm with GMP and AMP and also interact with CMP but show very little interaction with TMP. The common covalent bonding metal binding sites on the nucleotides are GN7, AN7 and CN3, but only GN7 and AN7 are accessible from solvent in double stranded DNA.[3]

Table 3.5 Summary of *CD* wavelength (λ) interactions of (Pt4 – Pt9) complexes with 5' -nucleotides

(PtX)	AMP		GMP		CMP		TMP	
	(+) /nm	(-)/nm	(+)/nm	(-)/nm	(+)/nm	(-)/nm	(+)/nm	(-)/nm
(Pt4)	300–310(s)	340–360	300–350	-	300–310 (sh)*	325	-	-
(Pt5)	300–340	-	295–340	-	300–310 (sh)*	-	-	-
(Pt6)	-	350–360	310–340	-	-	-	310 (s)	-
(Pt8)	295–310	330–360	290–340	-	300–310 (sh) *	-	-	-
(Pt7)	295–330	350–360 (s)	300–330	-	300–310 (sh)*	-		-
(Pt9)	295–330	330–370	300–330	-	300–310 (sh) *	-	-	-

(sh) = shoulder, (s) small, * = wavelength shift

3.3.4.2 Mass spectroscopic studies

Attempts were made to understand the nucleotide results using electrospray mass spectrometry. The aim of these mass spectroscopic studies was two-fold: (i) to determine what (PtX) adducts are formed/are to be found in solution, (ii) to look for evidence of which of the chloride or DMSO ligand is preferentially replaced on binding. The (PtX) complexes of the nitro subset, 5′-guanosine monophosphate (5GMP) and 9-methyl guanine (MG),[8] were used in these studies. Data were recorded on the ESI–MS Bruker BioTOF mass spectrometer in positive ion mode at the University of Warwick in collaboration with an ESI–MS operator, Dr. Karen Etherington. The nitro subset complexes were prepared using 50% MeCN and 2% formic acid solution. We anticipated that one or more of the following would take place: (1) DMSO or Cl loss or both, (2) addition of one or more GMP or MG (3) replacement of the labile chloride and DMSO with either MeCN or OH_2 or $^{\cdot}OH$, (4) no interaction. Mass spectra were recorded immediately on mixing unless stated otherwise.

Results

The mass spectra of each of the (PtX) complexes alone in solution show peaks corresponding to the presence of adducts that indicate the preferential loss of the chloride ion and replacement by the solvent, acetonitrile. If the DMSO group is lost preferentially, MeCN may also replace it, however, there was no evidence of this, as the complex must be charged to be observed, when a Cl is still attached it is neutral.

(Pt4),(Pt5)and (Pt6) showed major peaks corresponding to $PtL(MeCN)(DMSO)^+$ and $PtL(MeCN)_2^+$ adducts. Minor peaks common to all three complexes included: $PtL(MeCN)^+$; $PtL(DMSO)^+$ and $PtL(MeCN)(H_2O)^+$, (Pt6) also showed peaks

corresponding to PtL^+. This indicates that the nitro subset complexes can lose both their labile Cl and DMSO groups.[21]

These studies also show that after the loss of either the chloride ion or DMSO group or both, MeCN when used as solvent can and does coordinate to the (PtX) complexes, and lead to the formation of a number of additional adducts.

Initial studies on the interaction of guanosine monophosphate (GMP) with the (PtX) complexes of the nitro subset (Pt4 – Pt6) confirmed an interaction in the form of a peak corresponding to $[PtL(DMSO)(GMP)]^+$. However, the use of GMP led to the complications of additional adducts due to interactions with the sodium or the phosphate or the sugar of the nucleotide so the simpler guanine N7 binding model of methylguanine (MG) was used.

On addition of MG to (Pt4 – Pt6), a major peak corresponding to $[PtL(MG)DMSO]^+$ was observed with all three complexes, the major and minor adduct peaks observed in free solution decreasing in magnitude. After the mass spectra of the (Pt5):MG mixture was recorded on mixing, the remaining mixture was left to stand for a 40 minute period, before a second mass spectra was recorded. A five fold increase in the $[PtL(MG)DMSO]^+$ peak size was seen with significant decreases in the 'free' adduct peak sizes. Similar interactions were seen with (Pt4) and (Pt6).

Thus, it is clear that MG can displace Cl. Although there was no evidence of DMSO displacement, it should be noted that if MG displaces the DMSO, a neutral adduct would result which would not be seen in MS unless it acquired another cation.

3.3.5 Spectroscopic titration studies to investigate (PtX) interactions with DNA

On the basis of the preliminary results, the (PtX) complexes that make up the nitro and methoxy subsets *i.e.* (Pt4 – Pt6) and (Pt7 – Pt9) respectively were investigated

in depth. (Pt4/Pt8), (Pt5/Pt7) and (Pt6/Pt9) are identical pairs except for the nitro/methoxy groups.

The spectroscopic interactions of the (PtX) complexes were investigated with ct-DNA, AT and GC DNA using the spectroscopic techniques of absorbance, *CD* and flow *LD*. (Pt15) was also included in some parts to provide an intercalator for comparison. With ct-DNA, a constant 100 μM DNA concentration was used to investigate interactions over a mixing ratio, R, of [20:1–1:1] DNA base:(PtX). With GC and AT DNA, a constant 200 μM DNA concentration was used (unless otherwise stated) and interactions over R = [40:1–2:1] DNA base:(PtX) investigated. Where appropriate (see section 3.2.3 and 1.7), the salt concentrations used (with a constant 1 mM sodium cacodylate buffer) to maintain GC and AT DNA duplex structure are stated on the spectra.

Titrations were set up where the DNA concentration was kept constant (by adding increments of concentrated DNA at each step) as increasing amounts of (PtX) complex was added so that DNA perturbations on (PtX) addition as well as *ICDs* could be monitored. The binding constants for (PtX) with DNA are such that mixing ratio does not equal binding ratio.

For ease of comparison, each of the following figures have been laid out with the (PtX) complexes of the nitro subset in the left column and those of the methoxy subset in the right column with otherwise identical complexes side by side. This allows a direct comparison of the effect of the non-leaving groups (methoxy and nitro) attached to the aryl ring. The individual (PtX) complexes have been divided into three rows, a row for a complex from each subset containing the same amine substituent placed in descending order diethylamine, morpholine, diethanolamine thus allowing for comparisons between subsets.

Solubility

Platinum complexes (Pt6), (Pt8) and (Pt9) are more soluble in aqueous:MeCN solvent than (Pt4), (Pt5) and (Pt7). (Pt4) dissolves in 50% MeCN, (Pt5) dissolves in 59% MeCN, (Pt6) in 15% MeCN, (Pt7) in 30% MeCN, (Pt8) in 35% MeCN, (Pt9) in 40% MeCN and (Pt15) in 7.5 – 10 % MeCN. The % MeCN used for each experiment are indicated in the Figures.

3.3.5.1 UV-Visible absorbance titration spectra

The UV-Visible absorbance titrations for each complex, *i.e.* (Pt4 – Pt6) of the nitro subset and (P7 – Pt9) of the methoxy subset with ct-DNA (100 μM), GC DNA (200 μM) and AT DNA (200 μM) are shown in Figures 3.19, 3.20 and 3.21 respectively. The general trend of all eighteen absorption spectra is as expected: an increase in absorbance intensity as the metal complex concentration is increased.

The ct-DNA spectral data are entirely consistent with the snapshot spectra of the preliminary studies. The spectra are a combination of that due to free and bound (PtX). The effect of changing the DNA sequence is not really apparent in the absorbance spectra if one assumes the higher salt concentration of the AT and GC sets reduces the binding constants.

Within each of the nitro and methoxy series, the absorbance data look very similar, though the nitro (Pt4) and to a lesser extent the methoxy (Pt8) have significantly larger absorbances spectra in the DNA region. When one compares across the series, the 260 nm region of the nitro series is larger than the methoxy series giving a more distinctive maximum.

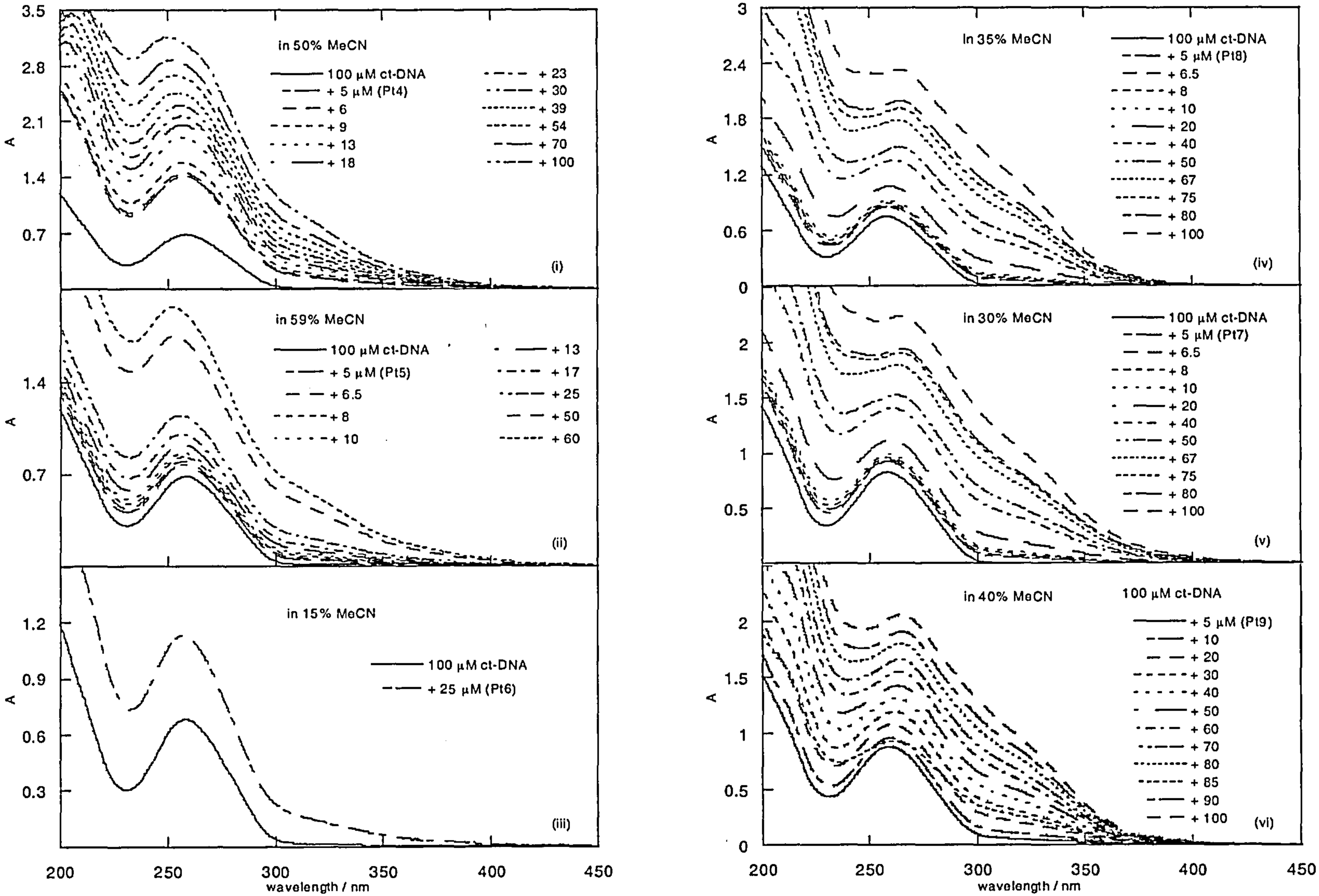

Figure 3.19 UV-Visible absorbance titration spectra of each (PtX) complex of the two subsets with ct-DNA. (i – iii) (Pt4 – Pt6) of the nitro subset and (iv – vi) (Pt8), (Pt7) and (Pt9) respectively of the methoxy subset. Working with a constant DNA concentration (100 µM) (solid line). Legend states µM (PtX) complex concentration added.

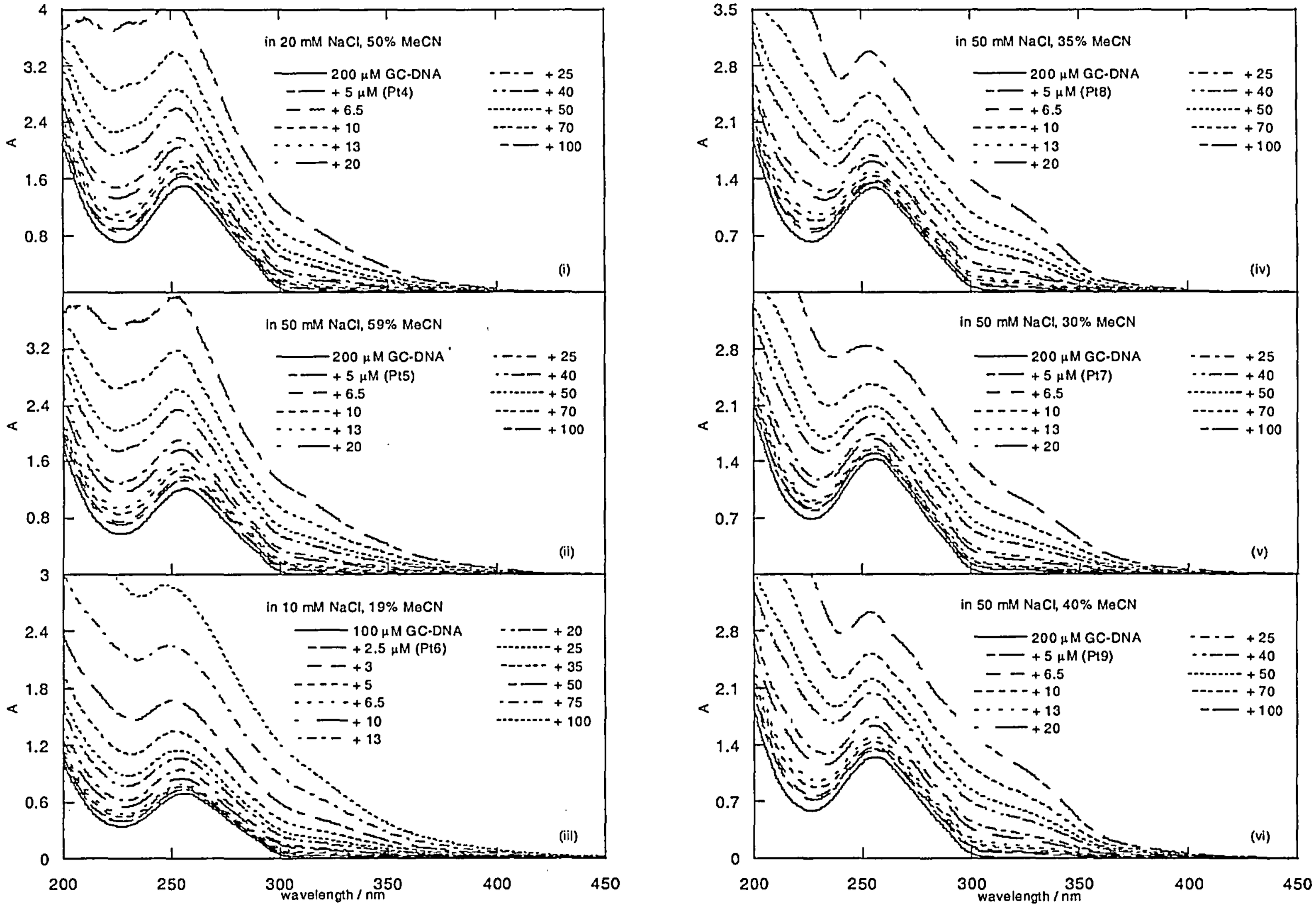

Figure 3.20 UV-Visible absorbance titration spectra of each (PtX) complex of the two subsets with GC DNA. (i – iii) (Pt4 – Pt6) of the nitro subset and (iv – vi) (Pt8), (Pt7) and (Pt9) respectively of the methoxy subset. The legend states the µM constant DNA concentration used (solid line) and the µM (PtX) complex concentration added. The salt concentration required to maintain duplex DNA is stated on each spectra.

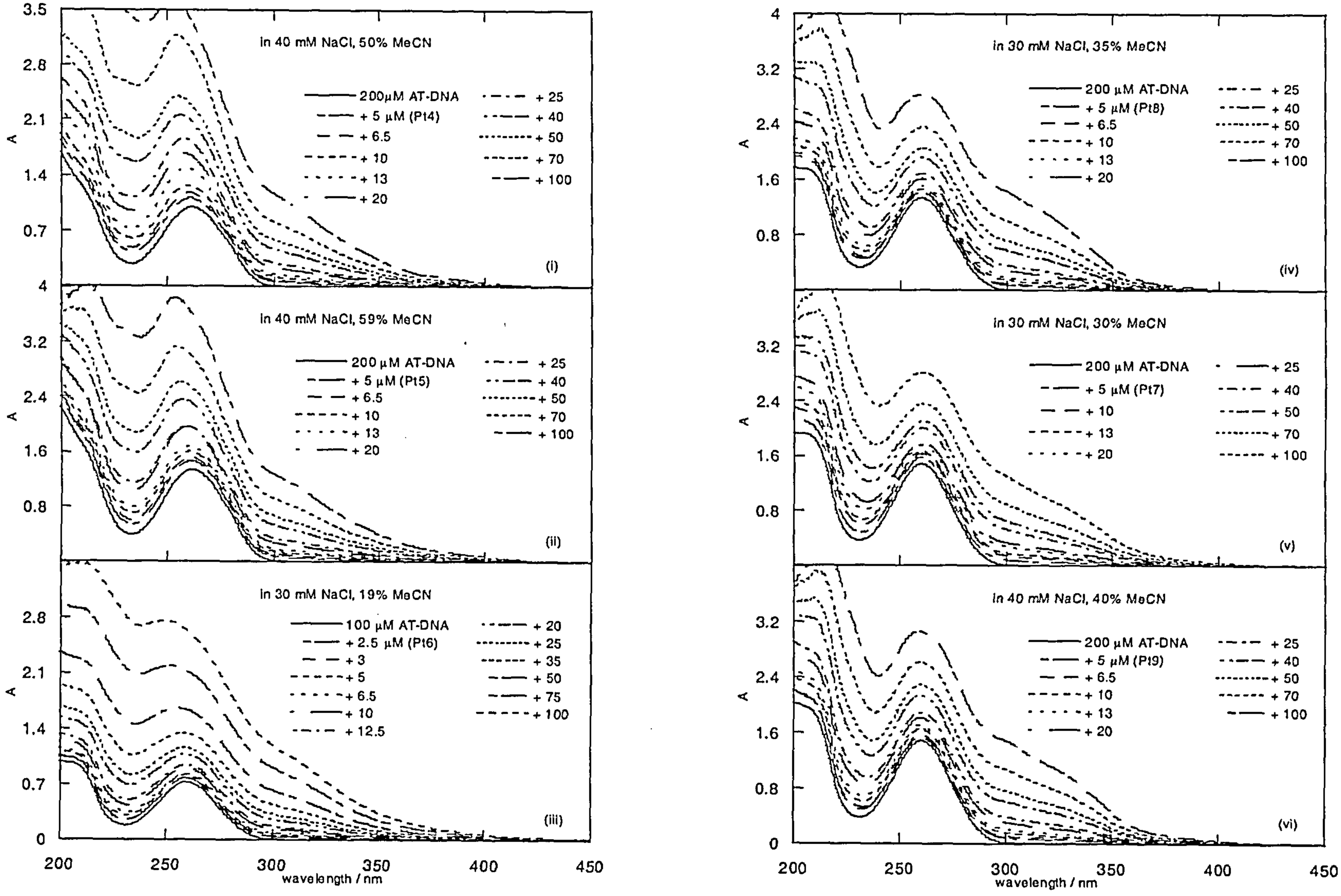

Figure 3.21 UV-Visible absorbance titration spectra of each (PtX) complex of the two subsets with AT DNA. (i – iii) (Pt4 – Pt6) of the nitro subset and (iv – vi) (Pt8), (Pt7) and (Pt9) respectively of the methoxy subset. The legend states the µM constant DNA concentration used (solid line) and the µM (PtX) complex concentration added. The salt concentration required to maintain duplex DNA is stated on each spectra.

3.3.5.2 Circular dichroism titration spectra

Figures 3.22, 3.23 and 3.24 show the *CD* data for the two subsets with ct-DNA, GC and AT DNA respectively. If we look at Figure 3.22 of the *CD* spectra of the interaction of each of the six complexes with ct-DNA, our arrangement of the (PtX) complex subsets in columns and their respective amine groups in rows, allows us to immediately note differences in the spectroscopy of each subset due to the nitro or methoxy susbstituent. Some immediate conclusions may be drawn.

(i) All six complexes interact with DNA as evidenced by their induced (PtX) chiral signature above 300 nm.

(ii) Each complex interacts with DNA producing a positively induced *CD* band (*ICD*) from 300 nm – 350 nm and a much smaller negative *ICD* band above 350 nm.

(iii) All six complexes exhibit an isosbestic point of zero *CD*. For the nitro subset the wavelengths are: (Pt4) (370 nm), (Pt5) (365 nm), (Pt6) (~365 nm). For the methoxy subset the wavelengths are: (Pt8) (~ 340 nm), (Pt7) (350 nm), (Pt9) (350 nm).

(iv) The spectra of the nitro subset (left hand column) exhibit a distinct positive band between 300 – 360 nm centred at ~330 nm for the short axis assigned Pt-Cl band and a small 380 – 400 nm negative band for the predominatly long axis polarised Pt-L MLCT bands. The 290 – 310 nm Pt-DMSO MLCT band at first sight appears to be absent but is more likely a negative band dominated by the positive DNA tail and the Pt-Cl band.

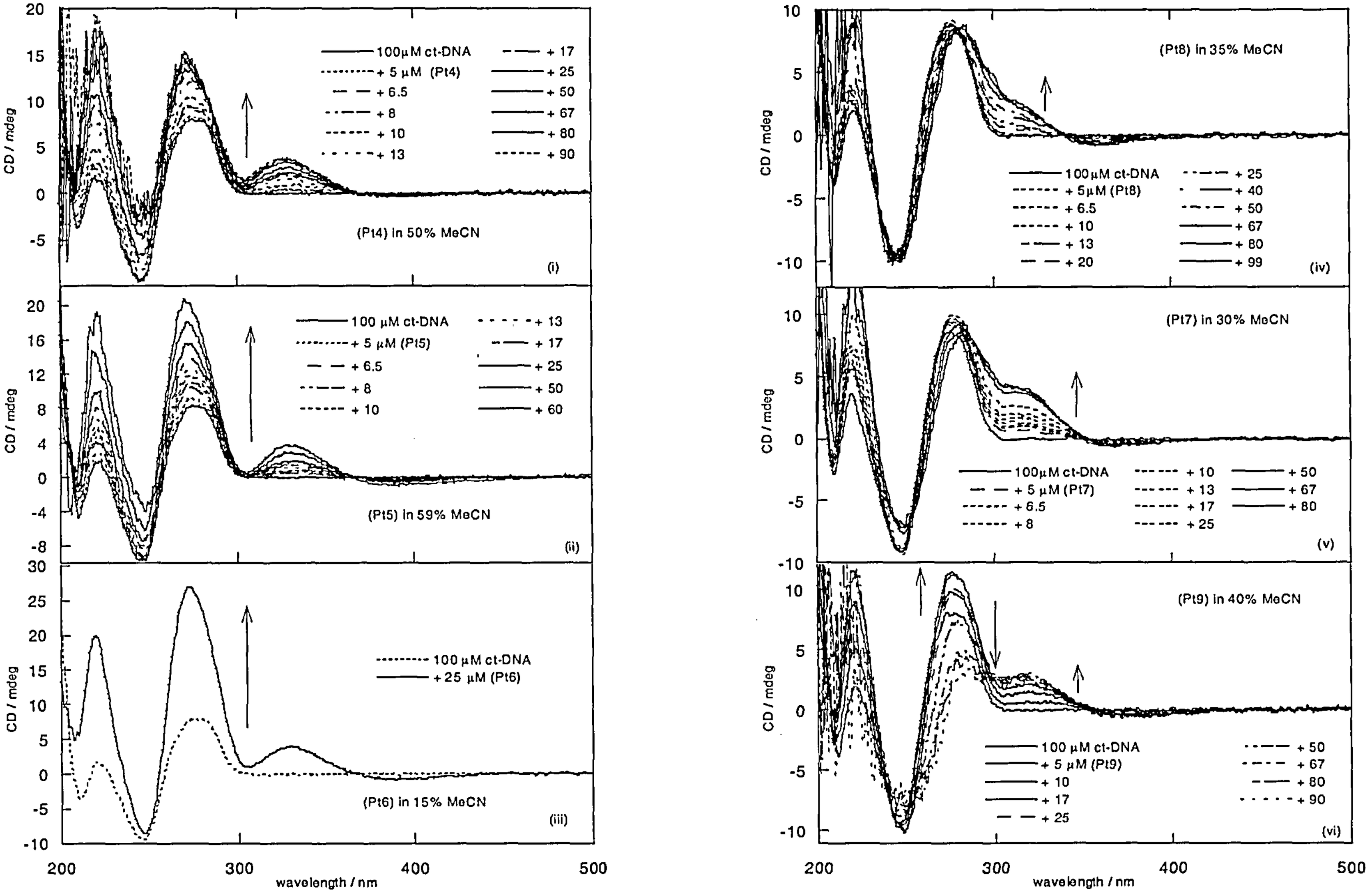

Figure 3.22 *CD* titration spectra of each (PtX) complex of the two subsets with ct-DNA. (i – iii) (Pt4 – Pt6) of the nitro subset and (iv – vi) (Pt8), (Pt7) and (Pt9) respectively of the methoxy subset. Working with a constant DNA concentration (*100 µM*). *Legend states µM (PtX) complex concentration added.*

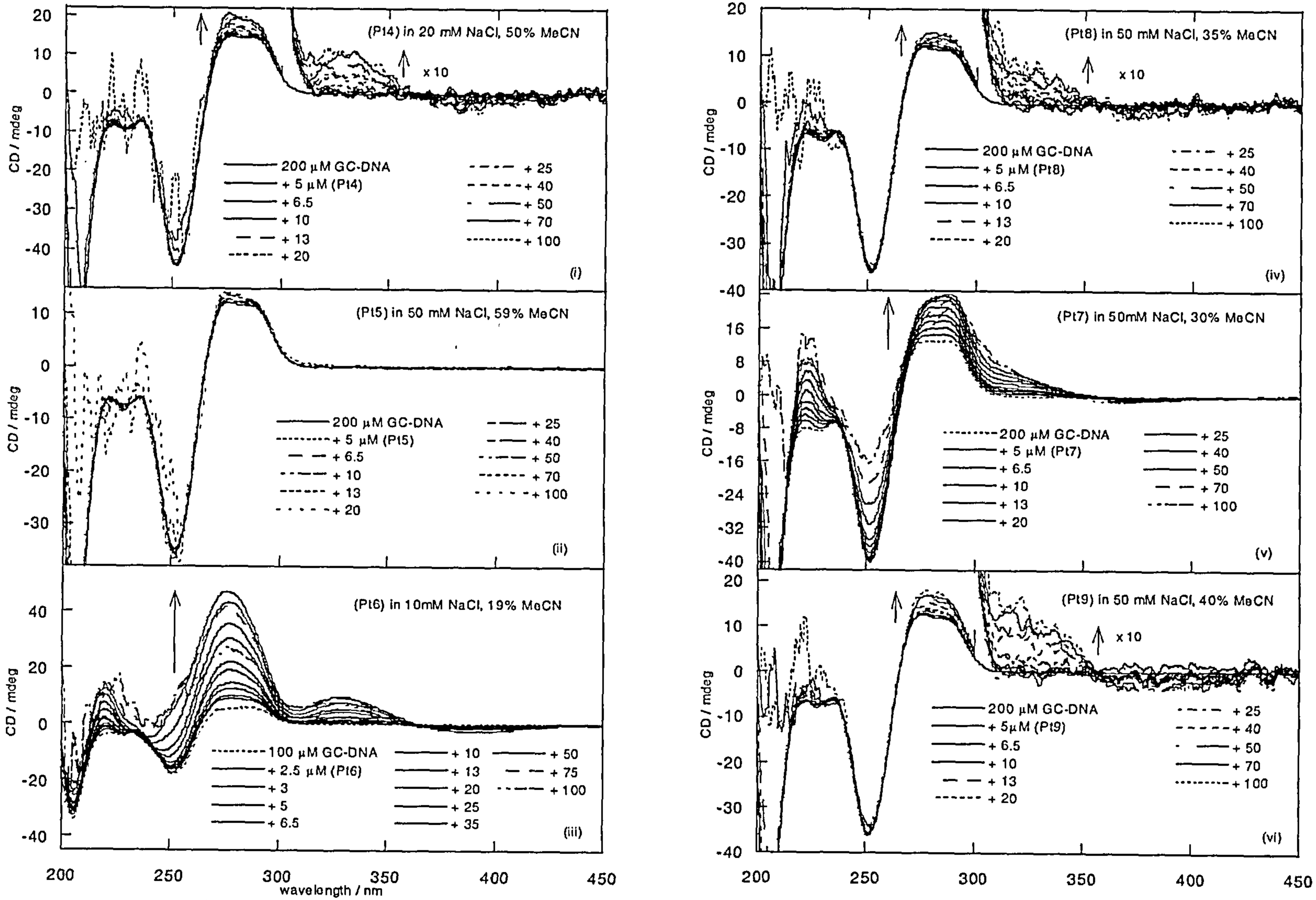

Figure 3.23 *CD* titration spectra of each (PtX) complex of the two subsets with GC DNA. (i – iii) (Pt4 – Pt6) of the nitro subset and (iv – vi) (Pt8), (Pt7) and (Pt9) respectively of the methoxy subset. The legend states the µM constant DNA concentration used and the µM (PtX) complex concentration added. The salt concentration required to maintain duplex DNA is stated on each spectra.

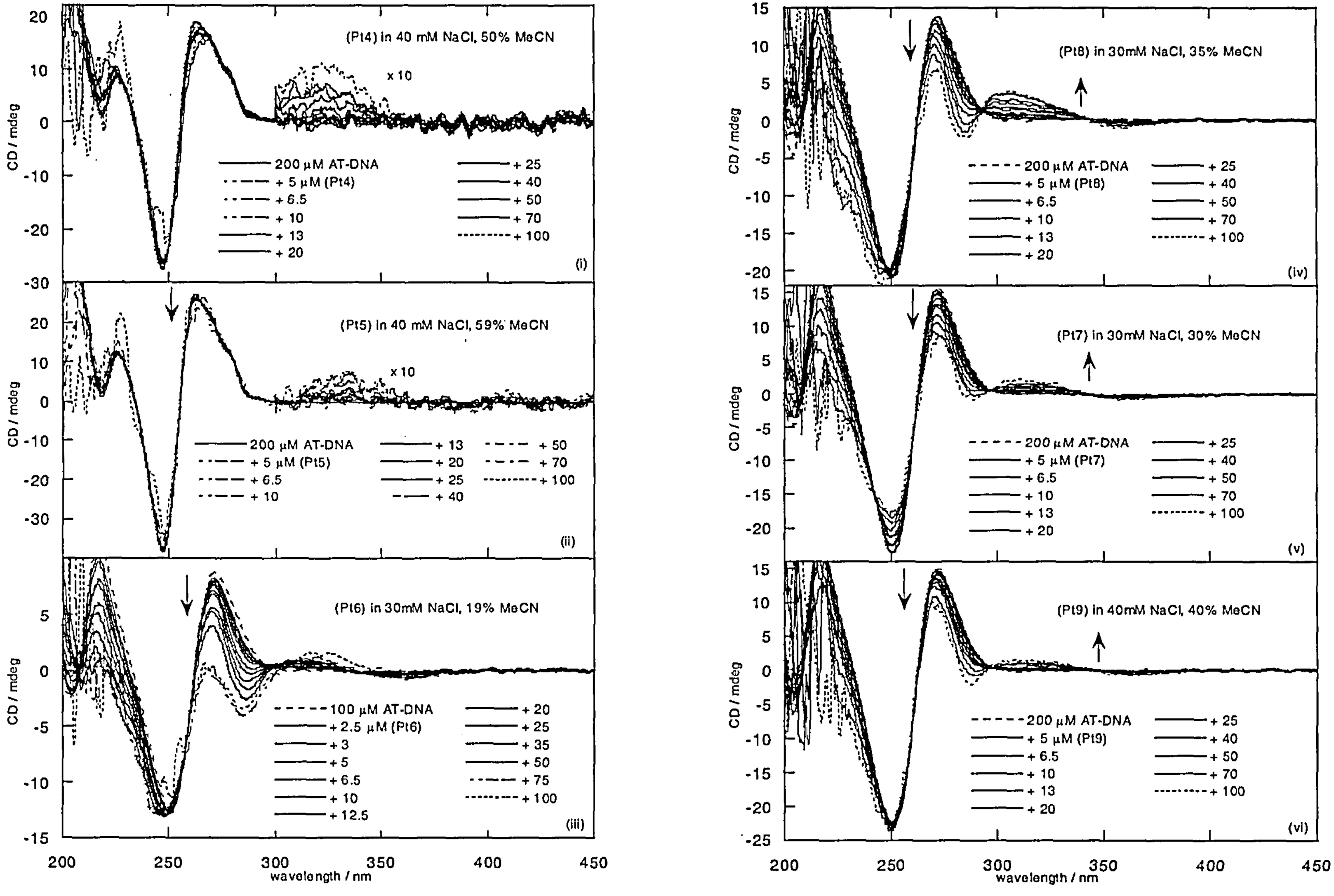

Figure 3.24 *CD* titration spectra of each (PtX) complex of the two subsets with AT DNA. (i – iii) (Pt4 – Pt6) of the nitro subset and (iv – vi) (Pt8), (Pt7) and (Pt9) respectively of the methoxy subset. The legend states the µM constant DNA concentration used and the µM (PtX) complex concentration added. The salt concentration required to maintain duplex DNA is stated on each spectra.

(v) In contrast, the methoxy subset (right hand column) does not exhibit a distinct band at 330 nm rather a broad positive shoulder extending from 300 – ~340 nm. They also have a long wavelength negative band at slightly shorter wavelengths. The distinctiveness of this band increases (Pt8) < (Pt7) < (Pt9).

(vi) Figures 3.23 and 3.24 with GC and AT DNA respectively also show a difference in spectroscopy for each subset. The GC DNA data in each case are probably analogous to that of ct-DNA. With AT DNA, (Pt4) and (Pt5) show little interaction. (Pt6), (Pt8), (Pt7) and (Pt9) show a different spectral form suggesting a different interaction with AT DNA from that observed with ct-DNA.

Thus the substituent on the aryl ring does seem to affect the binding mode, but the thiocarbonyl amine groups do not. They do, however, seem to alter the intensity of the *ICD* spectra, due presumably to the different hydrophobicities of these groups. In terms of magnitudes of transitions for the nitro series with ct-DNA, Pt-Cl transitions: (Pt6) > (Pt4) > (Pt5); Pt-L transitions: (Pt5) > (Pt6) > (Pt4); DNA transitions: (Pt6) > (Pt5) > (Pt4). Overall the order is (Pt6) > (Pt5) > (Pt4). This may in part be a solvent effect.

In light of the mass spectrometric results we might expect a binding mode where the Cl ion is displaced. If the Cl is displaced by the G bases but not so effectively by A bases then the AT versus 'the other differences' could be accounted for. Pt-GMP binding does result in a longer wavelength ~ 340 nm band than does Pt-AMP binding (refer to Table 3.5). However, the fact that the nitro and methoxy series differ in the 300 nm region suggests there are differences between these complexes. It could be that the nitro facilitates Cl ion displacement (as noted by Sacht and Datt)[12,13] and gives rise to a dominating negative Pt-DMSO *ICD*. This is certainly consistent with our MS

results and the nucleotide *CD* studies. A further factor to be considered with polymeric DNA is the steric effect of covalent binding via the chloride position. This brings the aryl group deeper into the groove than with the other binding modes (*e.g.* intercalation). The smaller nitro group with significant H-bonding acceptor capability compared with the methoxy would be preferred. In this context, the resemblence between the unsubstituted non-H-bonding (Pt1 – Pt3) and the methoxy series (see Figure 3.12) is probably relevant.

The methoxy series also differs from the nitro series above 300 nm both with polymeric DNA and with the nucleotides. There is generally a small shift in the 300 – 350 nm region to longer wavelength. This perhaps reflects a greater degree of DNA binding via DMSO displacement with (Pt8)>(Pt7)>(Pt9) which is consistent with no negative Pt-DMSO *CD* band obvious at ~ 300 nm.

3.3.5.3 Flow linear dichroism titration spectra

If (PtX) is oriented in solution it will have an *LD* signal for its transitions. As the (PtX) can only be flow oriented upon binding to DNA, the presence of an induced *LD* at wavelengths that correspond to platinum transitions confirm that an interaction has taken place between the unorientated platinum complex and ct-DNA.

Here the DNA concentration was kept constant as (PtX) complex was added in order to keep the solution viscosity constant.

Flow *LD* with organic solvents

As discussed in Chapter 1, organic solvent flow *LD* is less straight-forward than aqueous flow *LD*. When working with organic solvents in flow *LD* studies, the concentration of the DNA as well as evaporation, viscosity, turbulence effects all need to be taken into account and adjusted accordingly. The flow *LD* signal of ct-DNA is

large enough to compensate for the effects of using MeCN. The DNA signal of the shorter synthetic GC duplex and AT DNA is, however, much smaller and the experiments were more difficult or impossible. *LD* studies with AT DNA were not undertaken. Although the AT DNA does orientate the signal is very small. The more rigid GC DNA proved to give small but detectable signals.

The flow *LD* titration spectra of the two subsets (Pt4 – Pt9) with ct-DNA (100 μM) and GC DNA (200 μM) are shown in Figures 3.25 and 2.26 respectively. Each ct-DNA:(PtX) flow *LD* interaction was investigated over a mixing ratio, R, of [20:1–1:1] DNA base:(PtX) complex and GC DNA:(PtX) interaction over a [40:1–2:1] ratio. As a comparison, (Pt15) a DNA unwinder that has previously been concluded to intercalate between DNA base pairs was also studied (Figure 3.27). (Pt15) has a phenanthroline in the place of the chloride and DMSO groups that are found on (Pt4 – Pt9) (see Figure 3.9).

The flow *LD* spectra of the (PtX)-DNA complexes (Figure 3.25 and 3.26) are characterised by large negative bands due to DNA encompassing negative minima at 230 nm and negative maxima at 260 nm. All six complexes exhibit negative *LD* signals for (PtX) transitions with both ct-DNA and GC DNA indicating that each platinum complex transition is aligned more parallel to the DNA bases than to the helix axis. Since the film *LD* work showed that MLCT bands are almost certainly polarised in the plane of the molecule, this suggests the (PtX) complexes are oriented more parallel to the DNA bases than perpendicular.

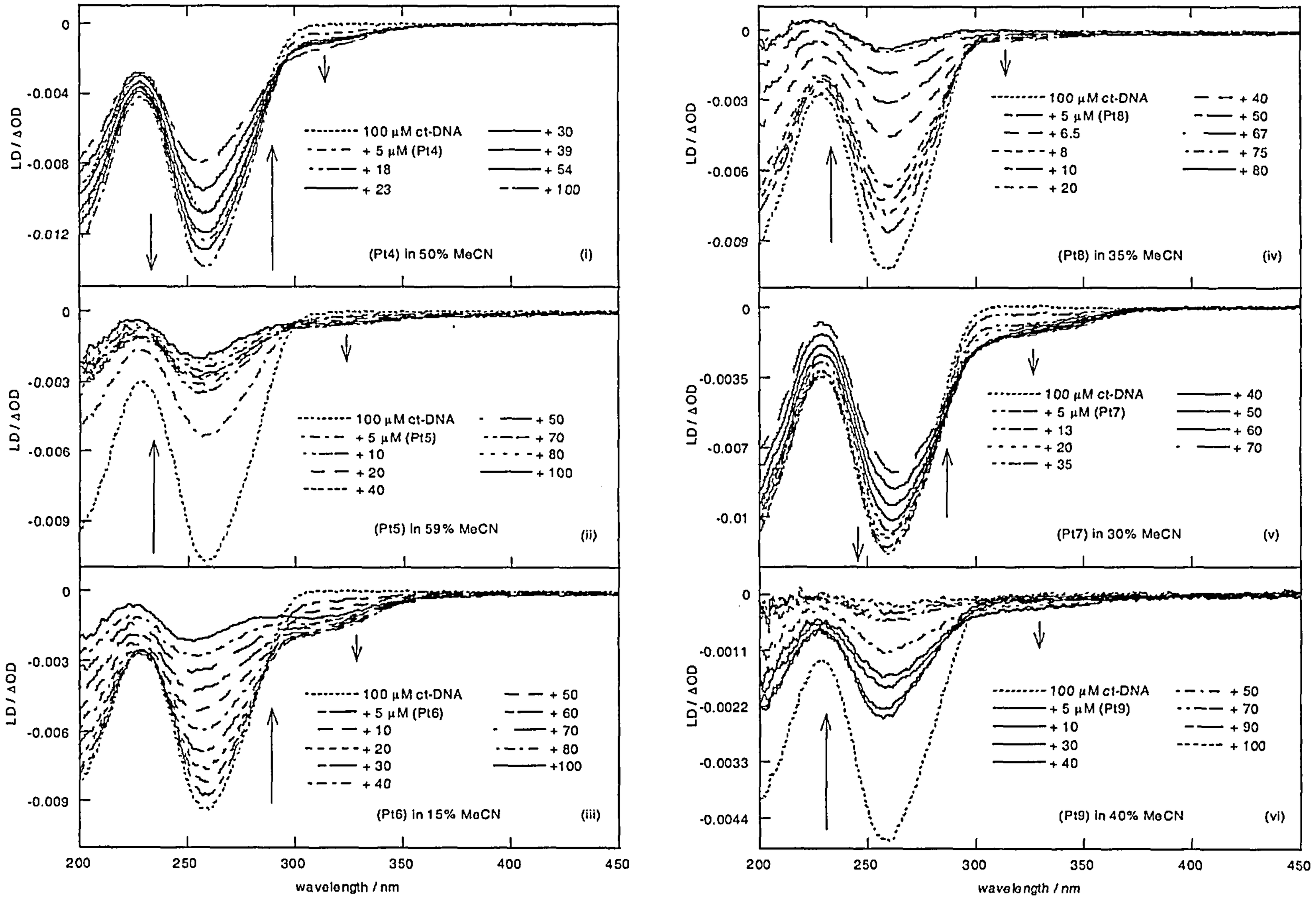

Figure 3.25 Flow *LD* titration spectra of each (PtX) complex of the two subsets with ct-DNA. (i – iii) (Pt4 – Pt6) of the nitro subset and (iv – vi) (Pt8), (Pt7) and (Pt9) respectively of the methoxy subset. Working with a constant DNA concentration (100 μM) (dotted line). Legend states μM (PtX) complex concentration added.

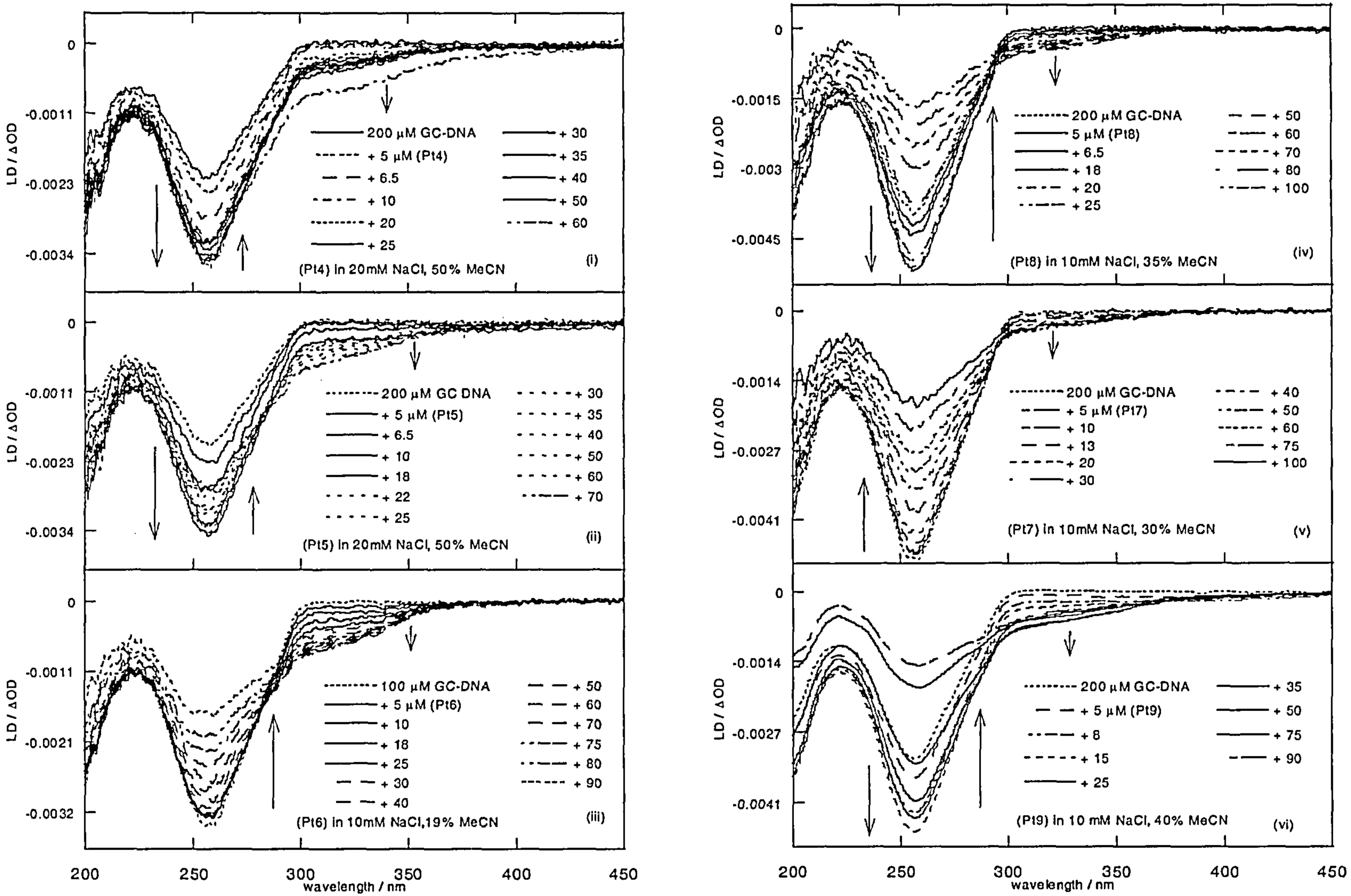

Figure 3.26 Flow *LD* spectra titration spectra of each (PtX) complex of the two subsets with GC DNA. (*i – iii*) (Pt4 – Pt6) of the nitro subset and (iv – vi) (Pt8), (Pt7) and (Pt9) respectively of the methoxy subset. The legend states the constant DNA concentration used and the μM (PtX) complex concentration added. The salt concentration required to maintain duplex DNA is stated on each spectra.

With ct-DNA (Figure 3.25), all six spectra exhibit non-zero isosbestic points, and in general similar spectra, but bend DNA by different amounts. In contrast, (Pt15) (Figure 3.27(a)) at low (PtX) load gives an increased DNA *LD* signal consistent with lengthening and stiffening of DNA due to intercalation. At high load the effect is reversed. Using selected flow *LD* and absorbance concentrations (absorbance data not shown), LD^r spectra (*i.e. LD* divided by A) were plotted (see Figure 3.27(b)) from which α (the angle between a transition polarisation and the orientation axis) $\geq 70°$ $\pm 10°$ was determined for (Pt15) relative to the DNA helix, (α is ~ 86° for DNA bases).[30] Section 1.3.3.2 contains an explanation, method and the equation (1.7) used to determine α. This data suggest that (Pt15) unwinds and lengthens ct-DNA by *intercalation* between the DNA bases.

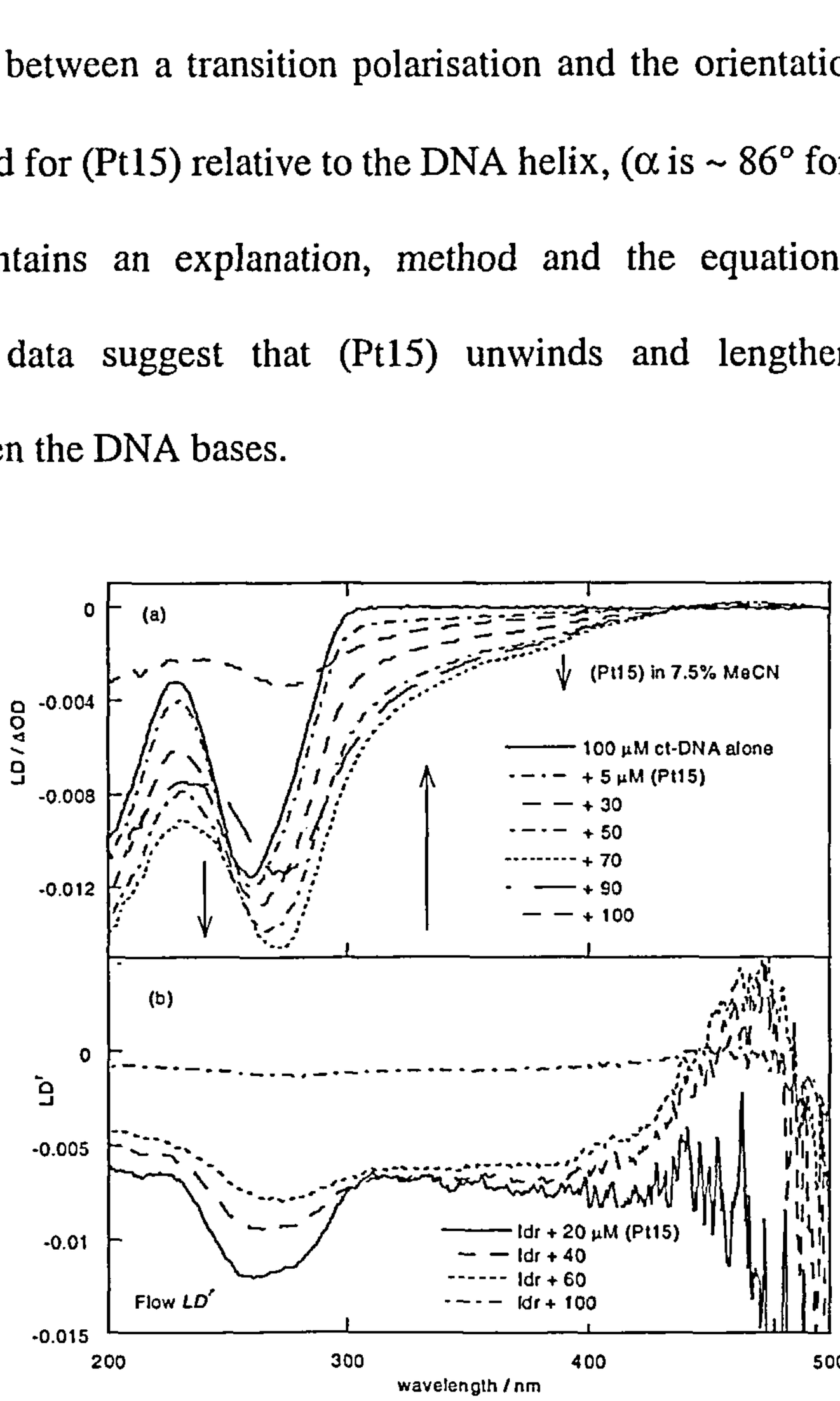

Figure 3.27 (a) The flow *LD* spectra of (Pt15) with ct-DNA, the legend states the μM (Pt15) concentration added to a constant ct-DNA concentration and (b) the LD^r spectra of (Pt15) with ct-DNA at selected concentrations.

(Pt4 – Pt9) differ in their effect on the degree of orientation of the DNA. At low R, metal complex loads, (Pt4) (0 – 18 μM) and (Pt7) (0 – 13 μM) both show an increase

in DNA *LD* magnitude (this is similar to the effect observed for (Pt15)); both complexes then gradually bend the DNA. The induced (PtX) transitions of (Pt4) and (Pt7) above 300 nm follow these trends also increasing in size as R is increased. Both (Pt4) and (Pt7) show an increase in magnitude at low R (0 – 23 μM) and (0 – 35 μM) respectively before decreasing at higher R. The 'stiffening' effect at low loads could indicate an intercalative interaction followed by another mode.

The flow oriented *LD* spectra of (Pt5), (Pt6), (Pt8) and (Pt9) show decreases in DNA *LD* magnitude as the (PtX) concentration is increased. (Pt5) and (Pt9) shows a large decrease even at low complex loads R [20:1]. Above 300 nm the flow *LD* spectra for all four complexes are characterised by a negative *LD* shoulder due to the (PtX) band between 300–400 nm. The signal increases with (PtX) concentration but decreases with the DNA bending. The latter eventually dominates. The *LD* spectra give no indication of big differences between the (Pt4 –Pt9) complexes upon binding to DNA except for the big orientation differences. Their spectral shape differences follow that of the normal absorbance. It is interesting to note that the orientation differences are less dramatic in the GC DNA titration series (Figure 3.26) where 10 – 20 mM NaCl was included. In any case it seems bending takes over before any intercalative binding mode might be saturated. Further, the (PtX) *LD* signal is significantly smaller compared with the DNA signal than is the case for (Pt15) (Figure 3.27), suggesting a sloped orientation of the plane of the molecule for (Pt4 – Pt9). Without significantly more data on the interplay of ionic strength and the organic solvents in *LD* spectroscopy it is difficult to make conclusions from this effect.

With the GC data, the nitro series has larger (PtX) *LD* signals relative to the DNA suggesting an orientation more parallel to the bases than is the case with the methoxy series. Given our previous hypothesis of a different preference for chloride or

DMSO displacement, this may be a steric factor of the binding mode that could be readily investigated by a molecular modelling study.

3.4 Conclusion

Under the conditions stated in this chapter the complexes exhibit concentration dependent interactions. We propose that complexes (Pt4), (Pt5), (Pt6), (Pt7), (Pt8) and (Pt9) covalently bind to DNA via the loss of the Cl or possibly the DMSO groups on the platinum. (Pt15) is an intercalator. Mass spectroscopic studies on the nitro subset have shown the preferential removal of the chloride ion and the formation of the major product of $[PtL(DMSO)(MG)]^+$.

Sacht *et al.* found that (Pt4), (Pt5) and (Pt7) exhibit biological activity[12,13] whereas the others do not. However, the spectroscopic studies reveal no significant differences in interaction with duplex DNA between those complexes that are biologically active and their structural analogues that are not. A possible conclusion may be that duplex DNA is not the primary target for these antitumour species, the complexes could target other DNA structures such as tetraplexes or *e.g.* proteins.

The major conclusion of this work therefore is that DNA binding does not equal biological activity. Molecular structure is related to biological activity, but all aspects of biological activity must be considered *i.e.* one must consider not only the activity of the complex when it gets to the target but also how it gets to the target and what else it may interact with. For example, organic solvent or ionic strength may affect (PtX) interactions. We propose therefore that the difference in activity for (Pt6), (Pt8) and (Pt9) (not biologically active) must be related to the delivery of the drug into the cell (this is consistent with the differences in solubility between the six complexes).

This novel class of (PtX) complexes, like cisplatin have a number of factors that can affect their interactions but they can bind to DNA and have the potential to be used as chemotherapeutic agents.

3.5 References

1. Z. Guo and P.J. Sadler, *Angew.Chem. Int. Ed.* 1999, **38**, 1512
2. Z. Guo and P. J. Sadler, *Med. Inorg. Chem.*, 2000, 49, 183
3. J. Reedijk, *Chem. Commun.*, 1996, 801
4. B. Lippert (ed.) *Cisplatin: Chemistry and biochemistry of a leading anticancer drug*, Wiley-VCH, 1999.
5. E. R. Jamieson and S. J. Lippard, *Chem. Rev.*, 1999, **99**, 2467
6. S. E. Sherman and S. J. Lippard, *Chem. Rev.*, 1987, **87**, 1553
7. M. N. Hughes, *The inorganic chemistry of biological processes,* John Wiley and Sons, 1990, 2nd Ed.
8. B. Lippert, *Coord. Chem. Rev.*, 1999,**182**, 263
9. P. Köpf-Maier and H. Köpf, *Chem Rev.*, 1987, **87**,1137
10. E. Wong and C. M. Gianomenico, *Chem. Rev.*, 1999, **99**, 2451
11. M. J. Clarke, F. Zhu and D. R. Frasca, *Chem. Rev.*, 1999, **99**, 2511
12. C. Sacht, M. S. Datt, S. Otto and A. Roodt, *J. Chem. Soc., Dalton Trans.*, 2000, 727
13. C. Sacht and M. S. Datt, *Polyhedron*, 2000, **19**, 1347
14. P. M. Takahara, A. C. Rosenzweig, C. A. Frederick and S. J. Lippard, *Nature*, 1995, **377**, 649
15. P. M. Takahara, C. A. Frederick and S. J. Lippard, *J. Am. Chem. Soc.*, 1996, **118**, 12309

16. U.-M. Ohndorf, M. A. Rould, Q. He, C. O. Pabo and S. J. Lippard, *Nature*, 1999, **399**, 708

17. J. Reedijk, *Chem Rev.*, 1999, **19**, 2499

18. Y. Chen, Z. Guo, S. Parsons and P. J. Sadler, *Chem. Eur. J.*, 1998, **4**, 672

19. T. W. Hambly, *Coord. Chem. Rev.*, 1997, **166**, 181

20. N. Farrell, D. M. Kiley, W. Schmidt and M. P. Hacker, *Inorg. Chem.*, 1990, **29**, 397

21. N. Farrell, *J. Chem. Soc., Chem. Commun.*, 1982, 331

22. D. H. Williams and I. Fleming, *Spectroscopic methods in Organic chemistry*, McGraw Hill, 1995, 5th Ed.

23. X. Y. Zhou and N. M. Kostic, *Polyhedron*, 1990, **9**, 1975

24. J. A. Bailey, M. G. Hill, R. E. Marsh, V. M. Miskowski, W. P. Schaefer and H. B. Gray, *Inorg. Chem.*, 1995, **34**, 4591

25. K. W. Jennette, J. T. Gill, J. A. Sadownick and S. J. Lippard, *J. Am. Chem. Soc.*, 1976, 6159

26. C. S. Peyratout, T. K. Aldridge, D. K. Crites and D. R. McMillin, *Inorg. Chem.*, 1995, **34**, 4484

27. T. K. Aldridge, E. M. Stacy and D. R. McMillin, *Inorg. Chem.*, 1994, **33**, 722

28. E. M. A. Ratilla, B. K. Scott, M. S. Moxness and N. M. Kostić, *Inorg. Chem.*, 1990, **29**, 918

29. E. M. A. Ratilla, H. M. Brothers II and N. M. Kostić, *J. Am. Chem. Soc.*, 1987, **109**, 4592

30. A. Rodger and B. Nordén, *Circular Dichroism and Linear Dichroism*, Oxford University Press, 1997.

4 Supramolecular metallo-cyclophanes and their interactions with small molecules in organic solvents

4.1 Introduction

The work in this chapter reports an investigation into the molecular sensor potential of novel self-assembling supramolecular metallo-cyclophanes formed using an inexpensive imine based approach.[1] A range of organic soluble supramolecular copper(I) and silver(I) metallo-cyclophanes were designed with their neurotransmitter binding being possible long term applications. In this thesis, the potential of these cyclophanes have been investigated in terms of their interactions with small neutral molecules *e.g.* aromatic di- and tri-methoxybenzenes (dmb, tmb) and chiral anionic compounds (sodium antimonyl-L-tartrate). The subsequent design and synthesis of a novel longer ligand capable of a facile one pot self-assembly into a supramolecular cyclophane structure with a larger cavity is also reported. Spectroscopic studies using UV-Visible absorbance and fluorescence as well as NMR studies and X-ray crystallography were used and are reported here.

Cyclophanes and their interactions in organic solvents

Molecules containing a bridged aromatic ring are termed 'cyclophanes'. [2–4] A variety of synthetic cavity containing cyclophane complexes (receptors/hosts) have been designed to bind organic molecules (substrates/guests) in aqueous and non-aqueous

media[2,4] and as such represent the main class of synthetic receptors in molecular recognition.[2]

The complexation of numerous synthetic cyclophane hosts[2] with a range of aromatic guests have been extensively studied in both water and organic solvents. A comprehensive review of these cyclophanes and their interactions with substrates has been compiled by Diederich.[2,4]

One of the first examples of neutral substrate complexation in organic solvent was reported by Siegel and Breslow in 1975. It involved the inclusion of neutral aromatics, toluene and anisole, by cyclodextrins in DMF and DMSO.[2,4] Many other similar investigations using other cyclophanes have been reported since and have been reviewed elsewhere.[2]

Connor states that the solvent itself is a molecular system rather than a continuous medium and the solvent molecules are subject to the same intermolecular forces as the interactants (solutes).[4,5] Solvents can therefore compete with the guest for the binding site. As solvent molecules are present in very large excess, their affinity for the cavity does not need to be very strong for them to displace the intended substrate or 'guest'. The extent to which a solvent molecule can act as an efficient competitor of the guest in the cavity binding site is also dependent on the affinity of the substrate for the solvent.

Organic solvent can affect binding interaction as reported by Diederich *et al.*[2,4] An investigation into the solvent's effect on binding interactions with a neutral macrobicyclic cyclophane host molecule [2,4] (Figure 4.1(a)) and its interactions with the arenes: pyrene and naphthalene was undertaken by Diederich *et al.* The cyclophane used was found to be soluble in most of a range of organic solvents from methanol to carbon disulfide.

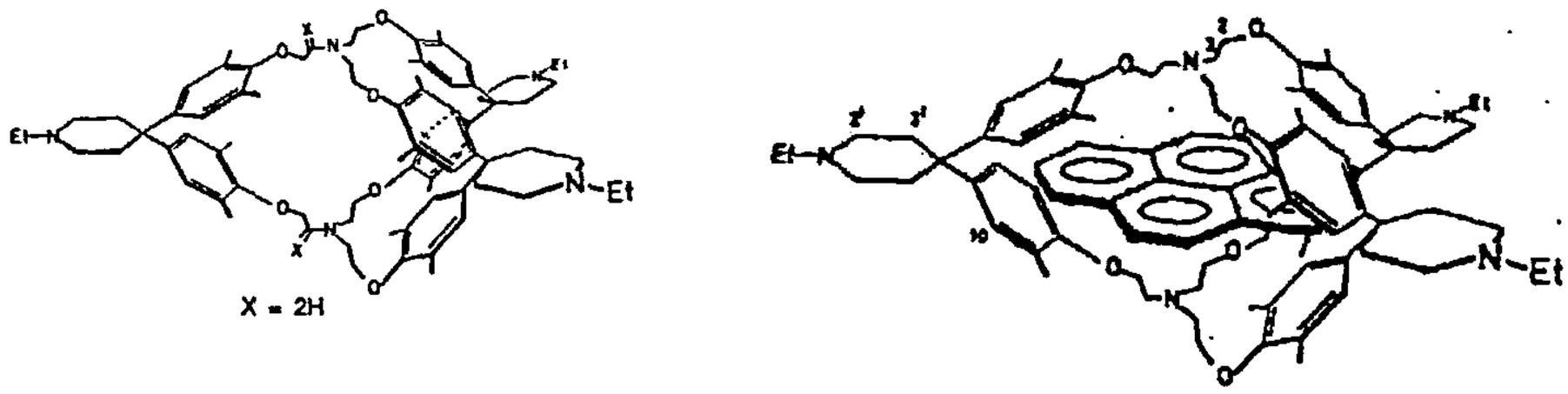

(a) (b)

Figure 4.1 (a) Macrobicyclic neutral molecule host (b) schematic of the geometry of the pyrene complex in methanol supported by ^{1}H NMR spectroscopy. (The diagrams were taken from p364 and p 370 of reference 4).

Proton NMR was used to show that similar geometric complexation of host molecule with pyrene (Figure 4.1(b)) occurred in a number of different solvents. The appropriate binding constant/association constants (K) values, however, were different. As the geometry of all the inclusion complexes is similar in all solvents, then the difference in the K values could not be due to any significant change in structural interactions, rather to the difference in non-covalent host-guest size or solvent-guest interaction, thus suggesting that any differences in K is due to a solvation effect. The binding constants for the pyrene inclusion complex were found to be strongest with polar solvents (the alcohols methanol and ethanol; $K \sim 10^4\,M^{-1}$) and then dipolar aprotic solvents acetone, DMSO, DMF, THF ($K \sim 10^3 - 10^2\,M^{-1}$) and weakest binding with chloroform, benzene and carbon disulfide ($K \sim 43$, 12 and 9 M^{-1} respectively). This led to the conclusion that the latter non-polar solvents can compete with the guest for the binding sites and also have a strong affinity for the pyrene itself.

This aptly demonstrates that solvent can effect the host-guest interactions, in turn effecting the magnitude of binding constants, K.[2] In general, for any type of complexation, geometrical complementarity between host and guest is crucial in determining the strength of complexation but the solvent plays a significant role too. Binding strengths for this type of host-guest complex decreases from water to polar protic solvents to dipolar aprotic and apolar solvents.

Electron donor–acceptor interactions have also been found to help stabilise the inclusion complexes of aromatic guests *e.g.* cyclobis (Figure 4.2) and Fujita's square (Figure 4.3).[6 – 15]

Binding constant determination

A comprehensive review of binding constant determination is provided by Connors.[5] A few of the methods that can be used to determine binding constants include UV-Visible spectroscopy,[16] fluorescence,[17] circular dichroism[18] and NMR.[4,19]

Table 4.1 Sensitivity of the various techniques in determining *K*

Technique	K / M^{-1}
NMR	$K < 10^4$
Absorbance	$10^2 < K < 10^6$
Fluorescence	$10^5 < K < 10^8$

The concentration ranges required for different experiments dictate the magnitude of the binding constants that can be measured. Table 4.1 summarises the sensitivity of the techniques mentioned. K values of $<10^4$ M^{-1} are measurable by NMR; UV-Visible absorbance is appropriate in the range 10^2–10^6 M^{-1}. As fluorescence is more sensitive than absorbance, binding constants in the region of 10^5 – 10^8 can be determined using this technique. Whether data from a particular technique will lead to a value for K rather than just an upper or lower limit can be seen by plotting signal change (chemical shift, change in absorbance *etc.*) versus added ligand or substrate concentration. If the plot is curved rather than linear, a binding constant value may be determined. If it is linear, then we are seeing all added substrates binding, rather than an equilibrium operating.

Several types of experimental methods are used to determine binding constants.[5] The main method that can be employed for both optical spectroscopy (UV-Visible absorbance and fluorescence) and ^{1}H-NMR, and which is used in this thesis, involves a titration of one analyte while keeping the concentration of the other constant.[4] Here a titration can be set up where the change of a guest property X is monitored as a function of increasing receptor concentration, while the total guest concentration is held constant. The property of X with UV-Visible absorbance is the intensity of an electronic absorption, or the fluorescence change of the guest. It can equally well be the chemical shift of a guest proton resonance. With absorbance (and fluorescence), a detection wavelength is usually chosen so as to give the largest possible values of ΔX, in order to provide the most accurate results. Ideally the detection wavelength is chosen to be in a region where the host property shows no effect under normal circumstances, so that changes in X as increasing amounts of host are added are a record of the interaction and not complicated by increasing host concentration. The plot of the change of the guest property (ΔX) as a function of increasing host concentration is termed a binding isotherm or more commonly a binding curve.

The presence of isosbestic points (points of constant absorbance) in the guest spectral region with constant guest concentration and varying host can be used to determine the number of species in a solution.[5] Generally, but not always consistently, one can establish whether the system includes one species (no complexes, just one species in solution with all spectra of exactly the same shape and magnitude), two states (two species, one bound and the other free with one isosbestic point), or more than two states (multiple equilibria indicated by changing spectral shapes and no isosbestic points.) This method is not entirely reliable and any other information regarding stoichiometry available must be taken into account.

NMR methods have an advantage over absorbance and fluorescence methods because NMR is not subject to misinterpretations caused by minor impurities *etc.* NMR data can also reveal more detailed structural information than UV-Vis data. Proton shifts for example, would be indicative of interaction. NMR or X-ray crystallography can be used to better define the binding interaction, provide proof of the actual shape, and the former to calculate binding constants. NMR observations of binding phenomena are usually in the so-called fast exchange limit ~ 10^{-2} seconds.[19]

The experimental methods that utilise NMR to calculate K and their binding isotherms are similar (as mentioned earlier) to spectrophotometric techniques, but there is a difference due to the different physical quantities being measured. In optical spectroscopy, an intensity — absorbance or fluorescence — is measured, and this is proportional to concentration, but in NMR spectroscopy a frequency (chemical shift, δ) is measured. Substrate concentration is therefore an experimental variable with which to manipulate the analytical signal in optical spectroscopy, but this is not viable in NMR, instead one determines relative percentages of each species present in the solution and calculates K directly.

In summary there are numerous methods that can be utilised to determine binding constants, and numerous effects that can affect the results. In the context of this chapter only the spectroscopic methods are of interest.

Receptor requirements

An understanding of the nature of non-covalent bonding interactions is necessary in the successful design, synthesis and stabilisation of self-assembling supramolecular synthetic structures. Modelling of biological interactions and processes represents an important target of supramolecular chemistry and as such most host-guest interactions have been investigated in water due to their specific and possible use in

biological interactions and reactions. The molecular interactions involved in host-guest molecular recognition (*i.e.* the forces that hold supramolecular complexes of cyclophanes together with neutral and charged molecules (substrates)) are covered in Chapter 1.

An effective receptor needs to meet certain criteria; three clear requirements have emerged for the design of an effective supramolecular receptor for a specific target molecule. These have been summarised by Hunter:[20] (i) the receptor should be polymacrocyclic and contain a cavity in which the interactions with bound substrate can be maximised; *i.e.* interactions are in the cavity rather than on the exterior of the cavity, (ii) the receptor should have the ability to establish non-covalent binding interactions with the substrate and to aid stability, this can be maximised by matching (complementing) substrate molecular size, shape and architecture, and (iii) the receptor should be relatively rigid, and binding/recognition should be favourable *i.e.* not involve the loss of shape. In order to achieve selectivity, a host molecule must be rigid so as to allow a pre-organised binding site which is complementary in size and polarity to a particular guest.[4,21]

Besides covalent pre-organised hosts, there are also hosts reported in the literature that do not form until guests are present, at which time the guests help to rigidify the cavity of the host,[22] or the host changes conformation and forms a rigid structure/cavity by encapsulating the guest.[23]

Synthesis of suitable rigid polymacrocyclic structures can be extremely difficult. The use of high dilution reactions is one way to encourage macrocyclisation and to reduce polymer formation but the yields can be low.[3] Template synthesis has also proved to be a very successful method, for generating macrocycles.[24] Other methods include cyclisation and normal covalent synthesis. A more promising (and more facile)

approach that has emerged in the last few years has been the application of self-assembly to generate compounds with large rigid molecular sized cavities.[23, 25, 26]

Two typical examples of cavity-containing cyclophane structures are the rectangular cyclobis formed by the template assisted assembly (Figure 4.2) and Fujita's square formed by self-assembly (Figure 4.4). The methods used in the formation of these cyclophane structures are briefly discussed below.

Template directed synthesis approach

The rigid cyclophane structure developed by Stoddart *et al.*[8–15] termed cyclobis (Figure. 4.2), is a good example of a macrocyclic box structure. It can be formed using template directed synthesis from a bis (pyridinium) salt, **A**, with 1,4 bis-bromomethyl benzene, **B,** in acetonitrile for a few hours.

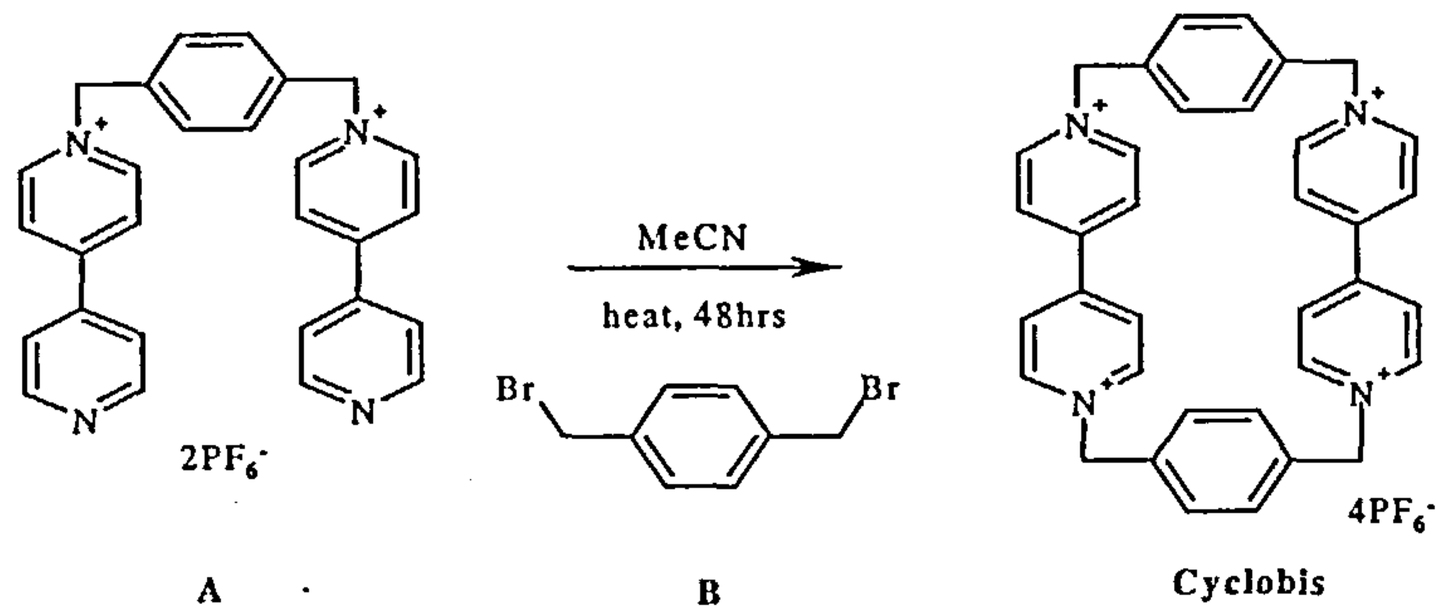

Figure. 4.2 *Schematic synthesis of the tetracationic rigid cyclophane box structure*

Cyclobis has a well-defined rigid cavity lined by two 1,4-dipyridinium acceptor units. These are electron deficient, and therefore make the cavity ideally designed for the inclusion of electron rich aromatic substrates, *e.g.* di-and tri-methoxybenzenes. The inclusion complex is also ideal for promotion of strong π-π stacking interactions between two electron deficient 2-dipyridinium units. The solubility of the tetracationic box can be controlled through the selection of appropriate counter ions. Cyclobis has been found to form stable complexes with a wide number of substrates including di-methoxybenzenes (dmb) and catecholamines.[2] These have been detected using UV-

Visible spectroscopy and ^{1}H NMR.[2] Cyclobis forms intensely coloured complexes with neutral electron rich benzene derivatives (*i.e.* isomers of di-methoxybenzene (dmb)) in acetonitrile. In solution, K values for 1,2-dimethoxybenzene (12dmb) and 1,3-dimethoxybenzene (13dmb) are $K \sim 8$ M^{-1} and 17 M^{-1} for 1,4-dimethoxybenzene (14dmb).[2,8]

Self-assembling approach

The alternative approach to the design of receptors is the self-assembly approach. Chemical self-assembly methods draw inspiration from natural self-assembly *e.g.* that of DNA (see section 1.6). Maverick *et al* [27] first described the preparation of inorganic self-assembled macrocyclic hosts[28] obtained in high yield by simply mixing suitable ligands and metal ions (Figure. 4.3). These offer advantages over the macrocyclic covalent analogues that require multistep synthesis and are generally produced in low yield. Since then a range of metals with various coordination geometries (*e.g.* linear, trigonal, square planar, tetrahedral and octahedral *etc.*) have been used for metal directed self-assembly of supramolecular host architectures.[20,29]

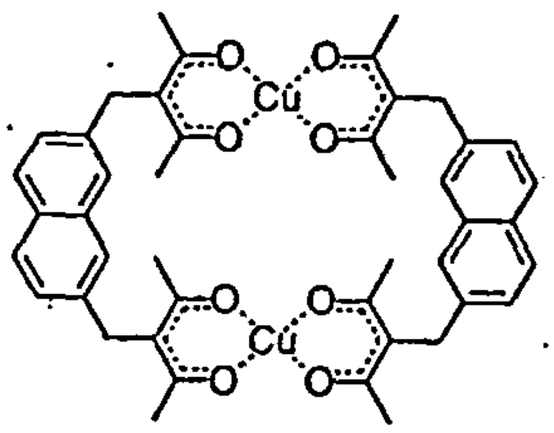

Figure. 4.3 Maverick's self-assembling macrocyclic host

Metal directed self-assembly

Metal ions that form four-coordinate square planar complexes are particularly well suited to act as the right-angled corners of square supramolecular structures. For

instance platinum(II) and palladium(II) complexes are known to form four coordinate, square planar species with approximately 90° bond angles at the metal centre.

The idea of supramolecular self assembly of square macrocycles (Figure 4.4(b)) using a protected, square planar transition metal (Figure 4.4(a)) in combination with a polydentate ligand was originally developed by Fujita *et al.*[29]

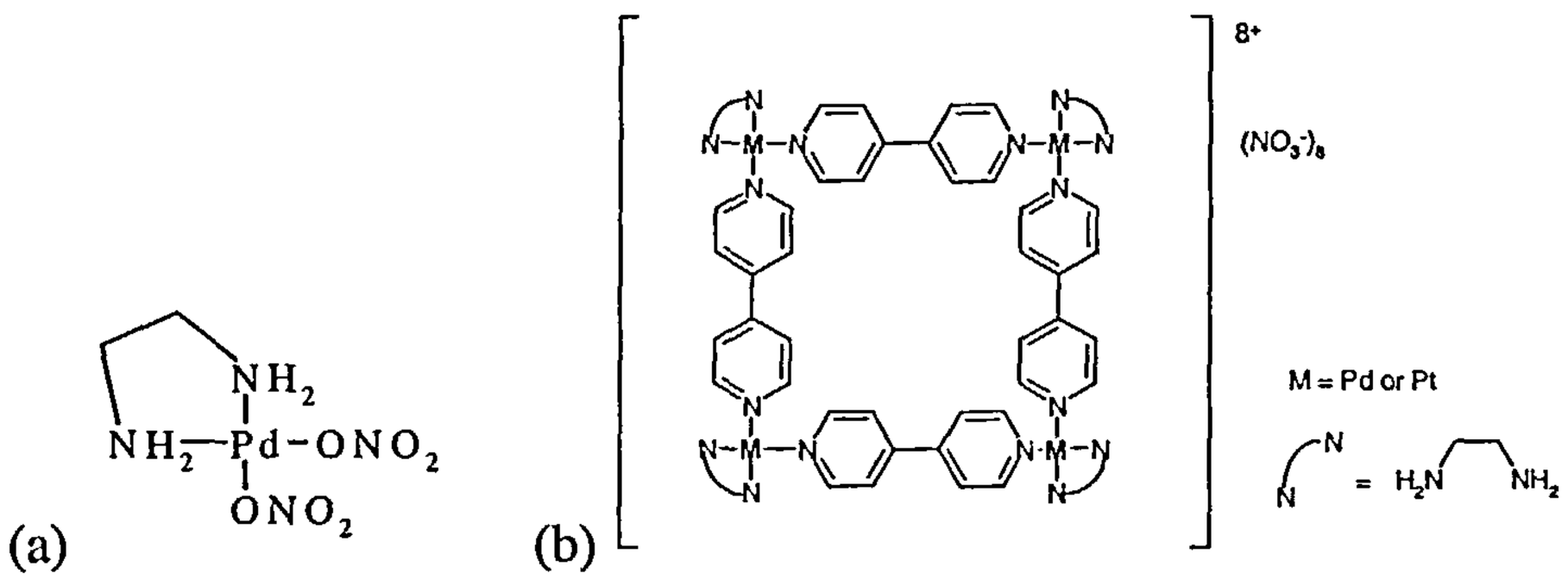

Figure 4.4 (a) cis-protected palladium(II) ethylenediamine, (b) Fujita's tetracationic box structure

Fujita and co-workers were the first to report on the spontaneous assembly of a tetranuclear palladium(II) square, using cis-protected palladium(II) ethylenediamine (where ethylenediamine is denoted 'en') (see Figure. 4.4) with one equivalent of 4,4′-bipyridine (4,4′-bipy) in water or water/methanol solution to form a tetranuclear palladium(II) complex, $[(en)Pd(4,4'\text{-bipy})]_4(NO_3)_8$, where the square planar palladium atoms were bridged by 4,4′-bipy. This unique tetranuclear structure in its solid state, was found to be a square, with 90° corners and an 8 Å cavity length. The central cavity is surrounded by 4,4′-dipyridinium units[2] and, like Stoddart's cyclobis, was found to be ideal for aromatic substrate (di-methoxybenzene) inclusion. In water, the hydrophobic cavity recognises small aromatic compounds. The binding of 1,3,5 tri-methoxybenzene, for example, was detected in deuterated water, (D_2O) using ^1H NMR. Complexation arises in part due to a charge transfer interaction, hydrophobic interactions between electron deficient pyridine ligands and the rich aromatic guests. π-stacking interactions

between aromatic portions of the substrates inside the box cavity was determined using proton NMR.[7]

Extension of the box cavity can be achieved simply by the incorporation of spacer groups *e.g.* C_6H_4, between the pyridine donor sites of the 4,4′-bipy walls of the cavity. Various difunctional ligands such as these have since been used to extend the box cavity.[30] Extensions of this type, can lead to the formation of mixtures of expanded molecular squares and triangles [30,31] and catenanes.[32]

For example, Fujita *et al.*[31] showed that not only are molecular squares formed by self assembly, but that their molecular square (Figure 4.4) was found to exist in equilibrium with another discrete structure, a molecular triangle as assigned in the solid state (see Figure 4.5).

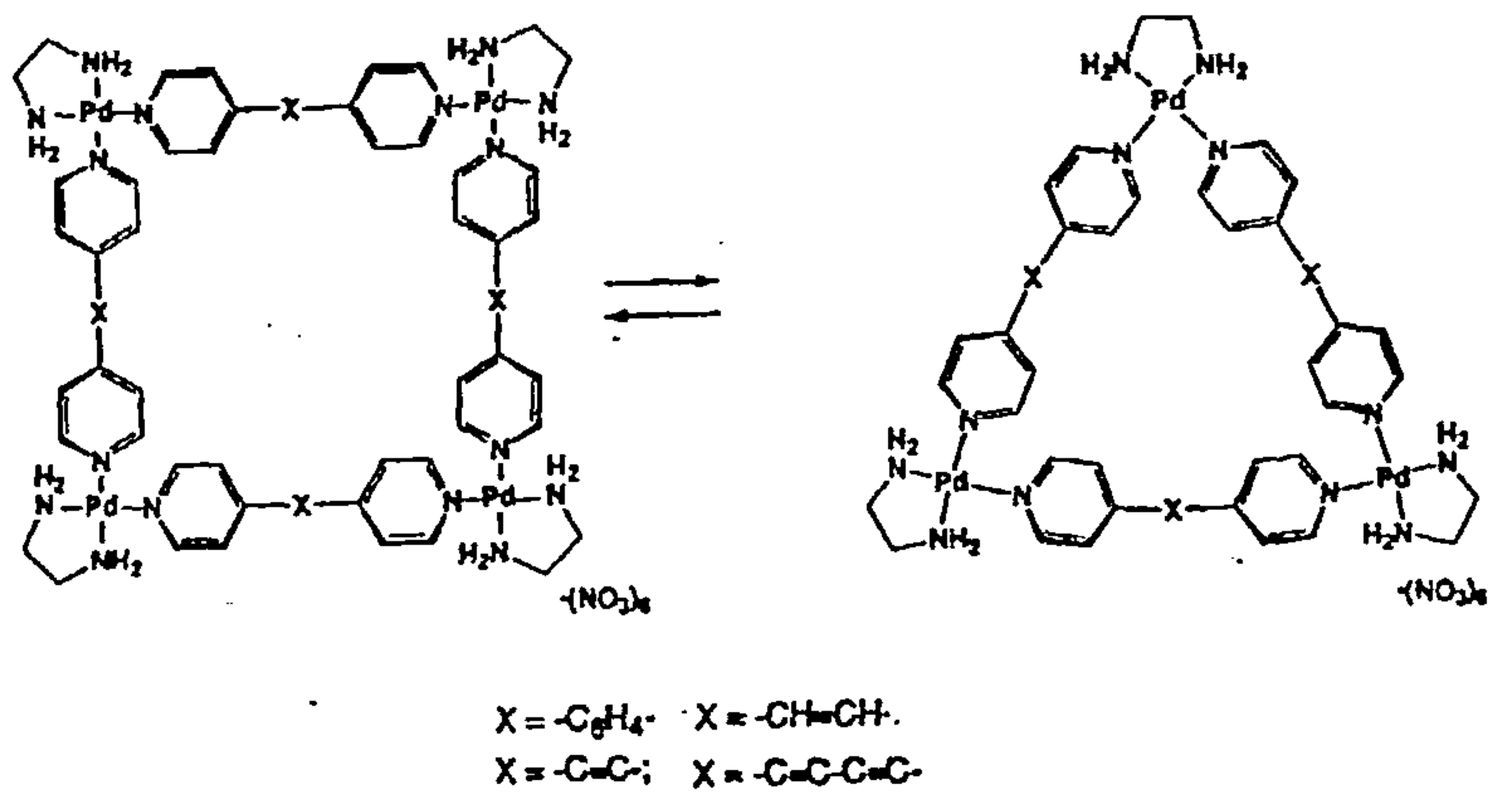

Figure 4.5 Fujita's molecular square and molecular triangle structures

When Fujita *et al.* [30] investigated replacing the ethylenediamine on the metal of the square (see Figure 4.4) with 2,2′ bipyridine (bipy), a mixture of squares and triangles were found to form in solution, this was thought to be due to steric repulsion of the bipy groups on the metal.

Interestingly, it has also been reported that when transition metals such as palladium(II) and certain organic ligands were combined in water in a 2:1:1

stoichiometry, they were found to bind so well that they self-assembled into a single product *i.e.*, rectangular molecular box catenanes (see Figure 4.6).[32]

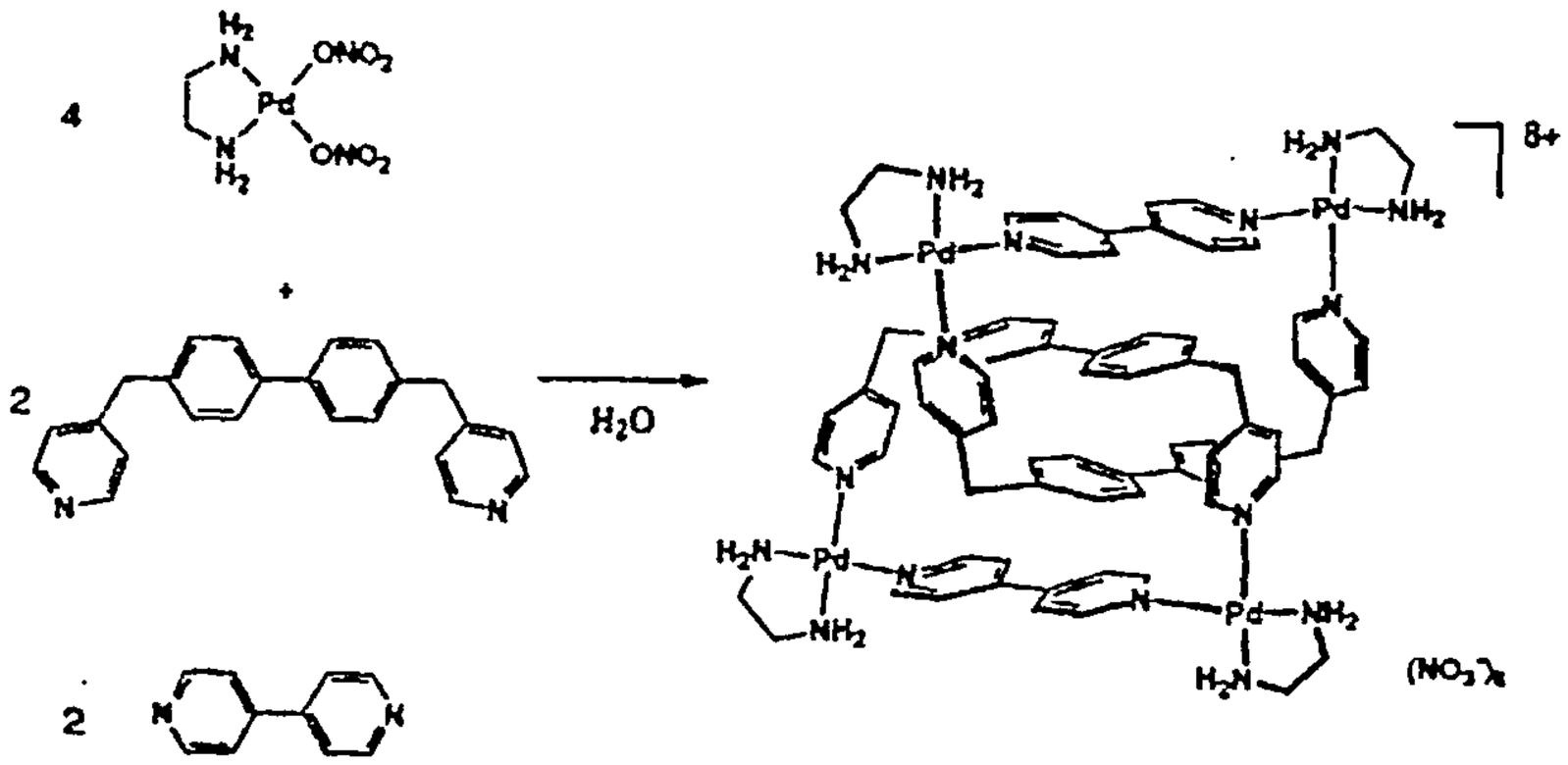

Figure 4.6 The ligands shown are combined in a 2:1:1 ratio to form catenanes

Stang *et al.* [33] have extended the approach, designing and characterising cationic and neutral homo and heterometallic Pt–Pt and Pt–Pd molecular squares with extremely high yields of 90–99%. Optically active chiral tetranuclear molecular squares, readily constructed by self assembly and coordination between the chiral square planar palladium(II) and platinum(II) bisphosphine triflate complexes and appropriate achiral building blocks have also been reported by this group (see Figure 4.7).[34 – 37]

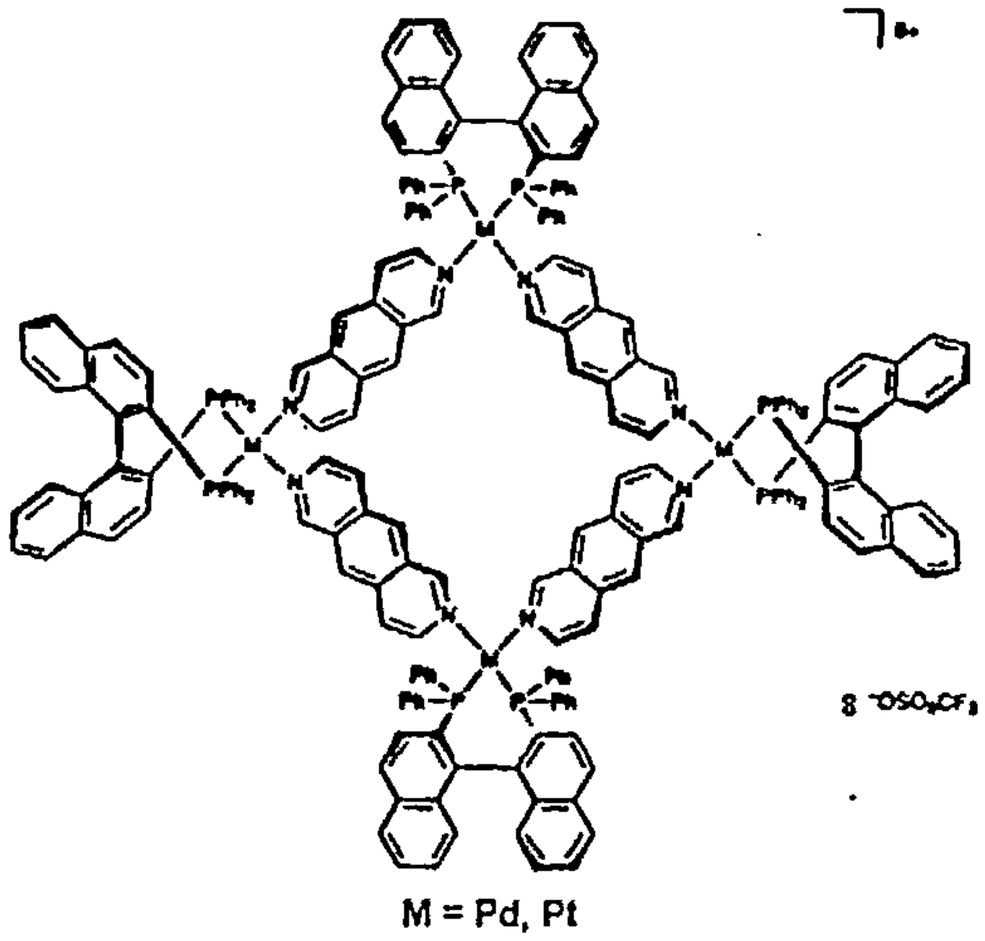

Figure 4.7 General structure of the chiral square planar palladium or platinum bisphosphine triflate complex

Hupp *et al.* extended this now growing area of self-assembling tetranuclear structures by incorporating octahedral metal centres such as rhenium into the structures (Figure 4.8).[37,38] Molecular squares derived from rhenium pentacarbonylchloride ($Re(CO)_5Cl$),[39] have been found to be fluorescent. The introduction of photo-luminescent characteristics is useful as an alternative to ^1H NMR spectroscopy for detection of guest binding. Hupp introduced heterobimetallic molecular squares, with $Re(CO)_5Cl$ incorporated in two opposite corners, and Pd(phosphane) at the other two within a square assembly [37] (see Figure 4.8(a)).

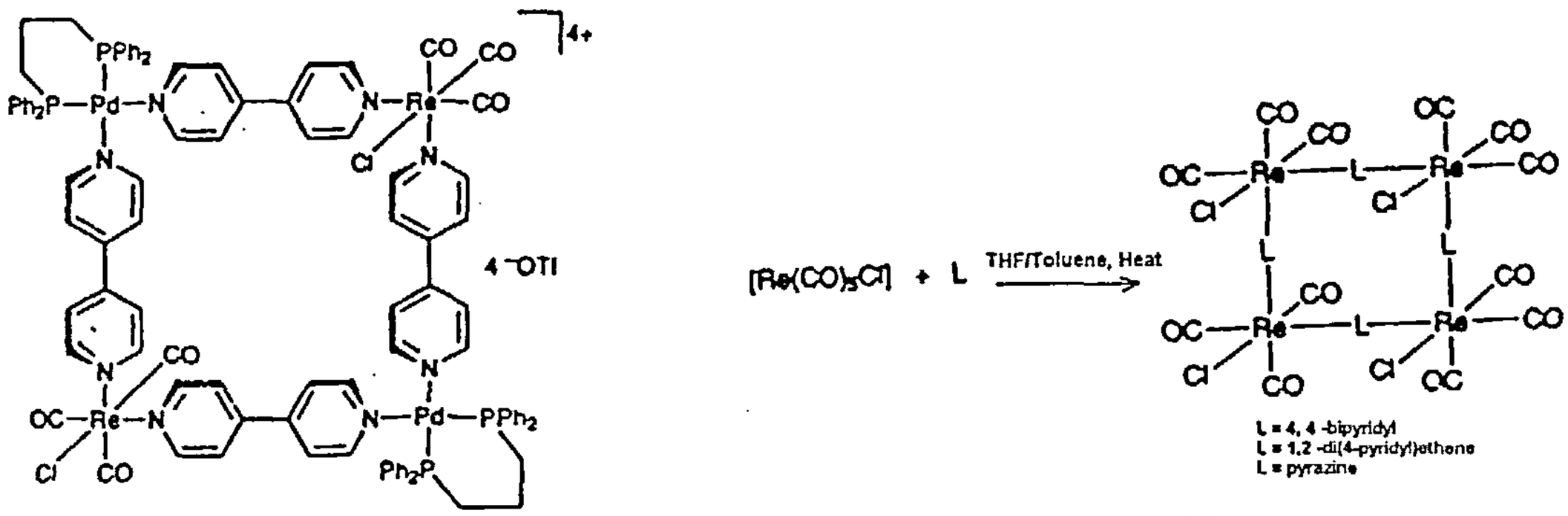

(a) (b)

Figure 4.8 Using octahedral metal centres (a) Hupp's heterobimetallic molecular square[37] (b) neutral molecular square with rhenium in all four corners.[38]

A large number of such homo- and hetero-metallic molecular squares which have been shown to recognise and encapsulate other molecules in their cavities, have now been reported incorporating metals such as platinum(II), palladium(II), cadmium(II),[28] rhenium(I),[38] osmium(VI), iron(II)[40] and colbalt(II).[41] Lippert *et al.*, have shown in principle that it is possible to reverse the situation where the metal unit provides the right-angled corner with four bifunctional ligands forming the sides, by placing the organic ligands at the corners and the metal units along the edges.[42] These structures can also be termed squares in the strict sense. Lippert and others have

reported on the formation of molecular boxes, rectangles and hexagons made up of nucleobases and other heterocycles.[43]

The concepts used to construct self assembling molecular boxes have been extended by Fujita [28] and others to include the construction of multimetallic arrays such as molecular networks, ladders and grids [44,45] cages,[46] grids[44] and channels.[47]

Having used pyridyl ligands with two coordination sites and square planar metals complexes as corner templates, two-dimensional squares have been synthesised. Three-dimensional architectures result when the ligands with higher numbers of coordination sites or metal ions with tetrahedral or octahedral coordination geometries are used in the self-assembly process. A nice example has been demonstrated by Jim Thomas and colleagues where in one step, eight octahedral metal corners and twelve 4,4′-bipy ligand edges, some twenty individual pieces, come together to form a supramolecular cube (Figure 4.9).[48,49]

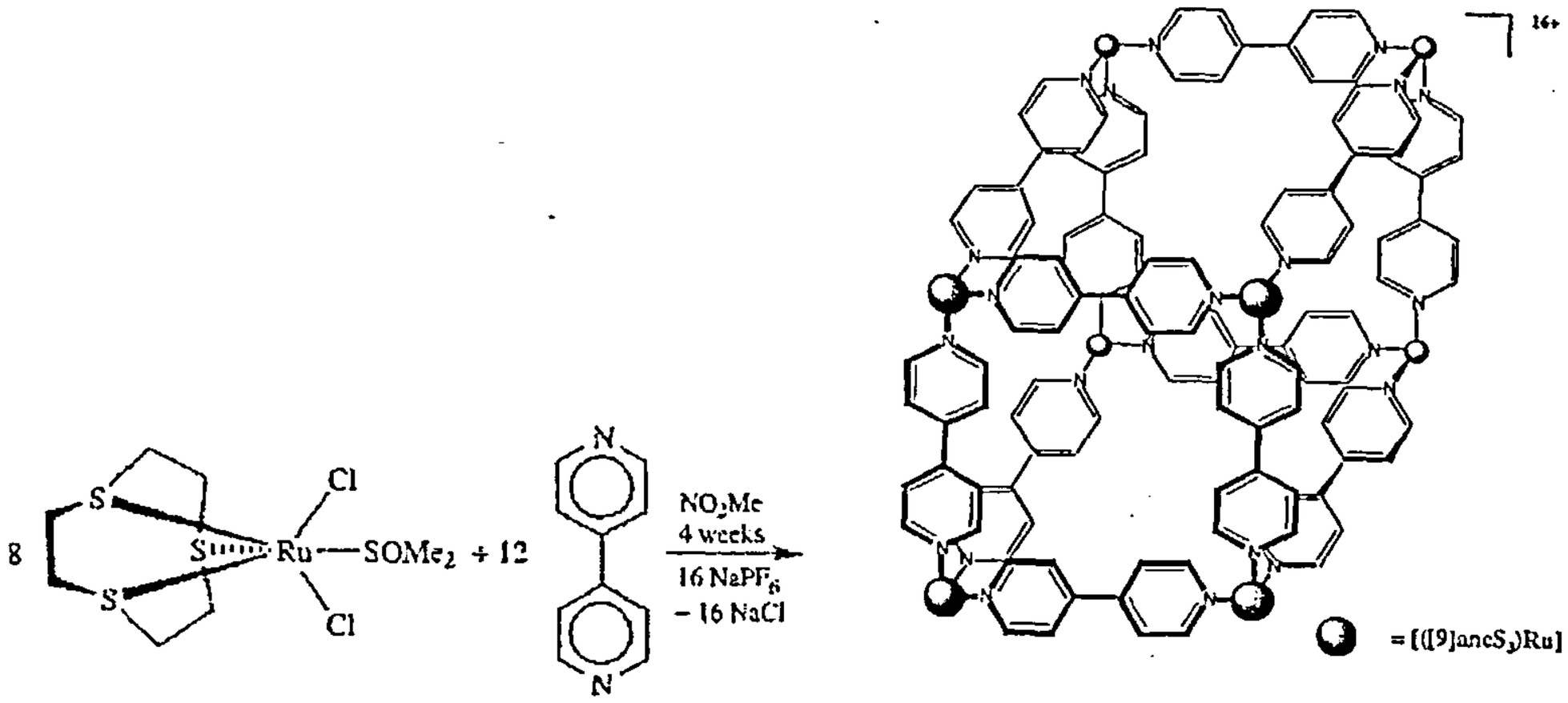

Figure 4.9 Twenty piece self-assembling supramolecular cube $[\{Ru([9]aneS_3)\}_8(4,4'\text{-bipy})_{12}](PF_6)_{16}$ (Diagram reproduced from reference 49)

Supramolecular self-assembling approach

Self-assembly (of polymacrocyclic structures) can be simply controlled by designing relatively rigid ligands, where the arrangement of ligand binding sites dictates the outcome, thus reducing the need for a protected metal. For example, Lehn and coworkers have explored the use of metal coordination for the construction of molecular racks, ladders and grids.[44,45] They recently reported on the synthesis and the structural characterisation of a self assembling symmetric [2×2] tetracopper grid box (see Figure 4.10), which was found to be electrochemically active and even more promisingly to exhibit guest inclusion in the solid state.[50,51] This approach is significantly different from that of metal directed self-assembly as it does not require the use of blocking ligands or metals.

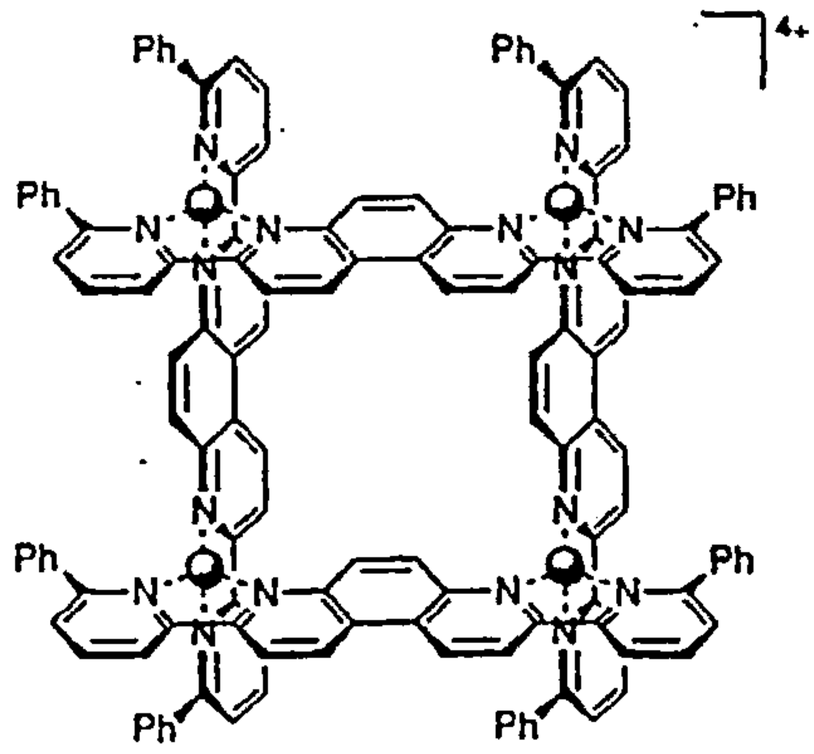

Figure. 4.10 Self-assembling tetracopper grid box

Hannon *et al.* have developed an inexpensive, simple self-assembling approach (where a protected metal is not needed) to the generation of self-assembling supramolecular architecture. This approach is based on imine ligands[1] and provides a facile one pot route to construction of supramolecular helical arrays,[52] cages[46] (see Figure 4.11) and grids, in high yield from inexpensive commercial reagents.

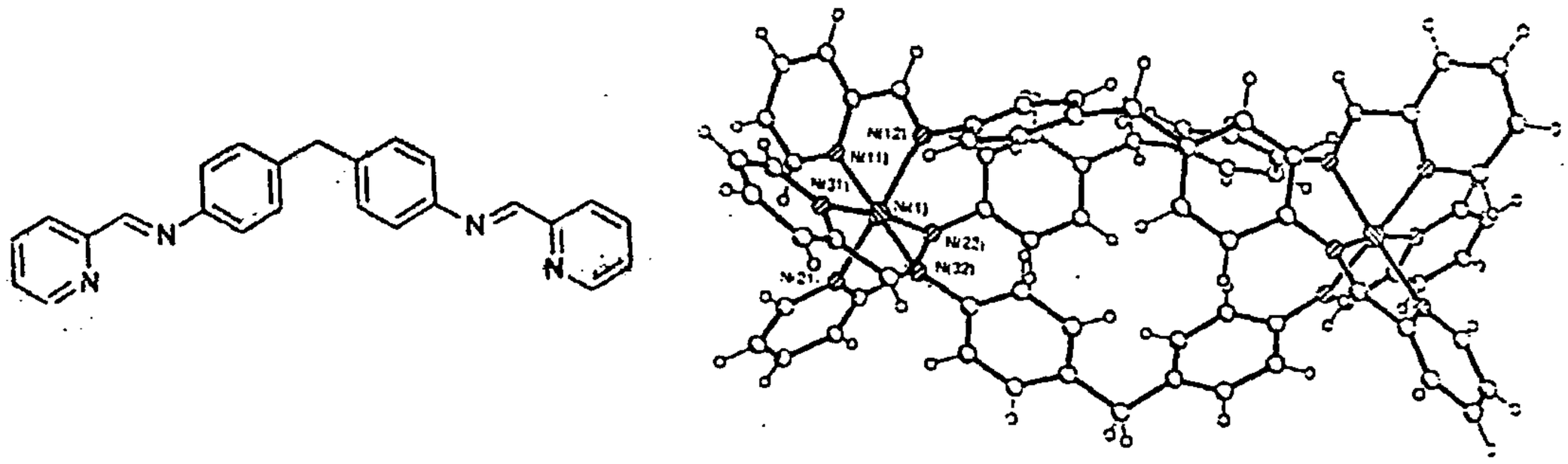

Figure 4.11 A ligand developed by Hannon *et al.* using an inexpensive approach. The triple helical structure is formed by simply warming a stoichiometric combination of 3 equiv. ligand and 2 equiv. nickel (II) salts in methanol.

Lehn *et al.*[53] have also reported on an equilibrating mixture of double helical (**1**), triangular (**2**) and square [2 × 2] grid (**3**) complexes that self assemble in solution in a 6:4:3 ratio respectively from a 1:1 ratio of ligand (L) and copper(I) salt in nitromethane (Figure 4.12) and convert to a single species (**1**) in the solid state.

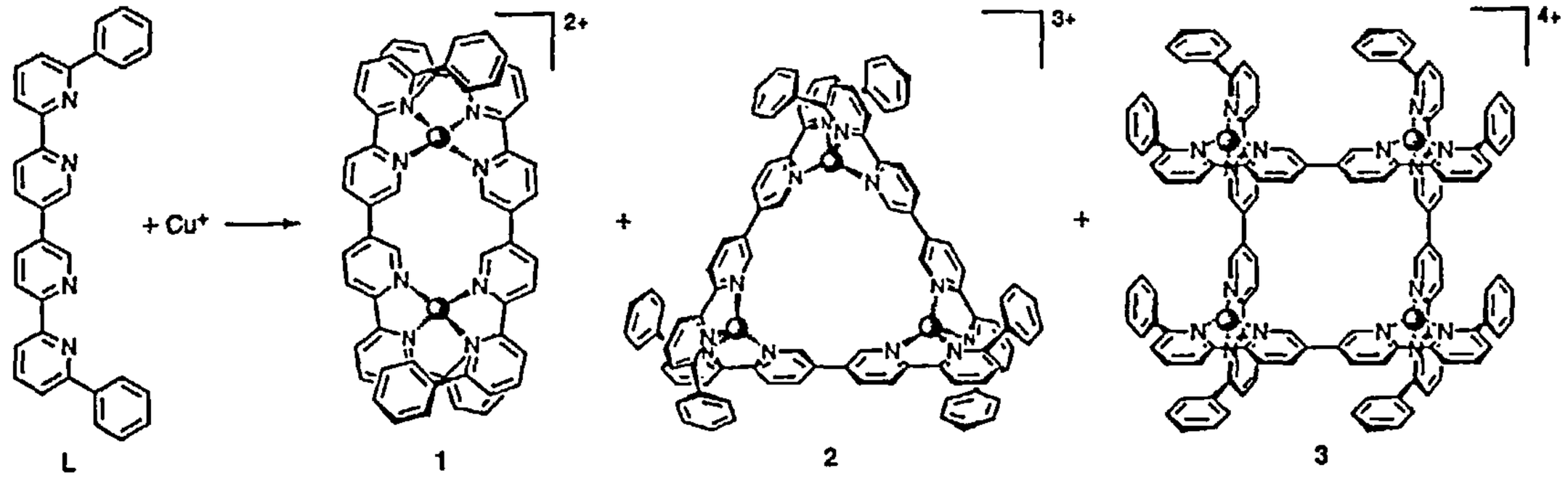

Figure 4.12 The double helical (**1**), triangular (2) and square (3) supramolecular structures form on reaction of ligand (L) with copper ions in a **1:1** ratio (taken from reference 53)

Using their inexpensive method, Hannon *et al.* have since reported using self-assembly to control the directionality of a supramolecular helical structure formed using an asymmetric ligand (L) (Figure 4.12).[54]

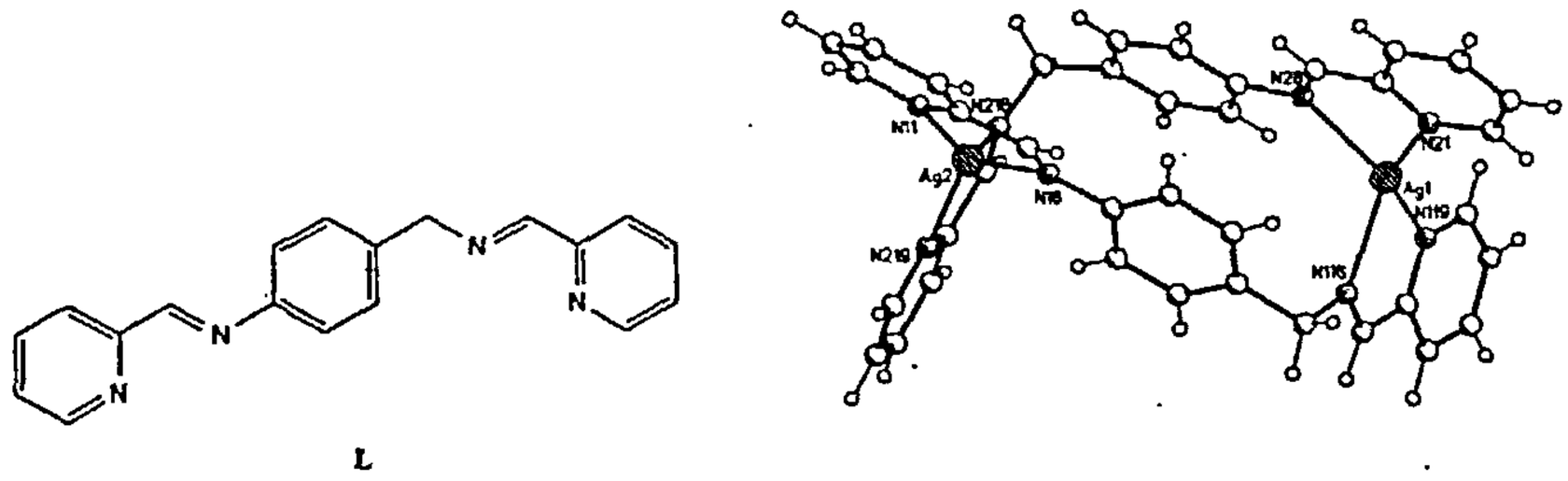

Figure 4.12 Asymmetric ligand (L) and the crystal structure of the cation $[Ag_2L_2]^{2+}$ (taken from reference 54)

As the design and synthesis of symmetric and asymmetric ligands for self-assembly of box structures can be controlled, so too can the aggregation of supramolecular boxes as reported by Hannon *et al.*[52] Firstly, by designing ligands[1] that incorporate nitrogen atoms as the metal binding sites (which can self assemble into cage-like structures) Hannon removed the need for the protected metal. Secondly, the deliberate incorporation of an additional ligating site (*e.g.* a thiomethyl substituent) on the outside of the structure, in such a position that would not be involved in the inital self assembly process of the box enabled aggregation of the boxes in a controlled fashion (see Figure. 4.13). This work has subsequently been extended to produce polymer arrays in a controlled fashion.

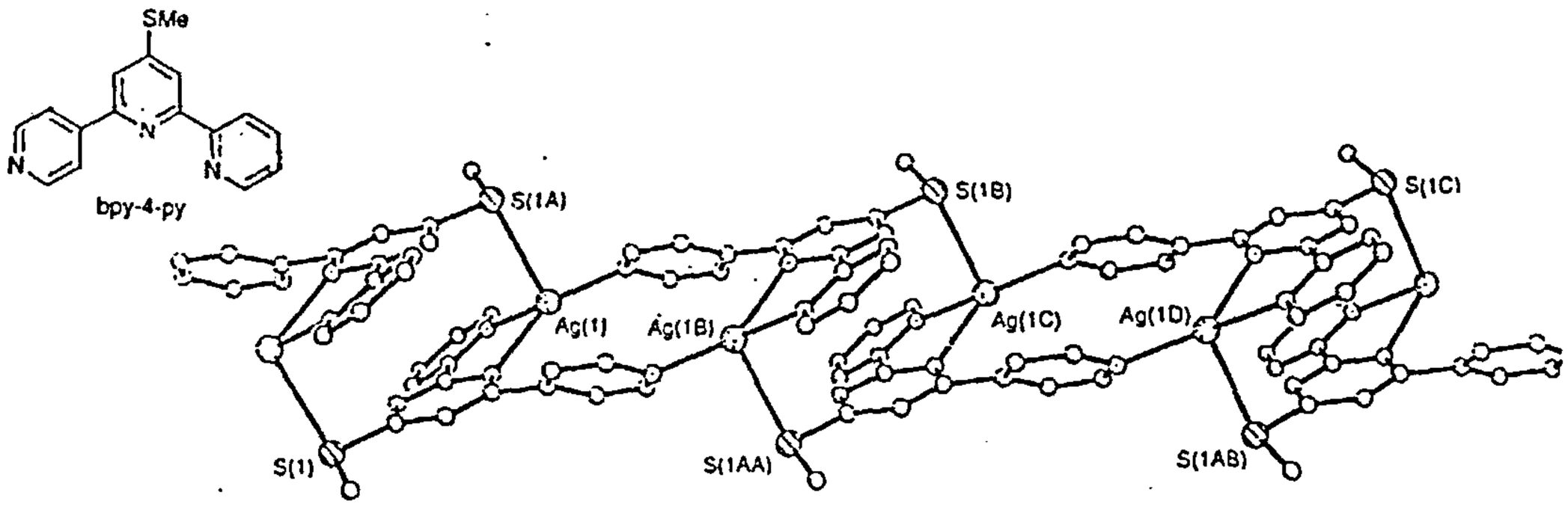

Figure 4.13 The ligand and the crystal structure of the agggregation of boxes

Hannon's development of supramolecular arrays in a few steps compared to multistep synthesis of polymacrocyclic structures is clearly an advantageous

development; it could lead to a significant increase in the potential usage of supramolecular self-assembling architecture in molecular sensing applications.

The development of new innovative, inexpensive approaches in the construction of large self-assembling cavities containing cyclophanes, together with (i) the ease with which such structures can be designed and synthesised to self assemble, (ii) the fact that cavity size, shape and properties can be altered by using different ligands and metals with different oxidation states has lead to metals now being a key feature in the formation of supramolecular structures and all seems to advocate the use of self assembling supramolecular structures in receptor-substrate chemistry. Thus, self-assembly is an extremely promising method for the construction of polymacrocyclic structures for use in molecular recognition.

4.2 The complexes of this study

The long-term aim of this research is to develop a solution sensor for dopamine and other neurotransmitters (Figure 4.14). To achieve this, suitable hosts need to be developed that can selectively bind these compounds. It is the molecular recognition properties of novel supramolecular metallo-cyclophanes formed following Hannon's inexpensive imine based approach[1] that have been investigated in this chapter, as a first step to a possible route to such a sensor.

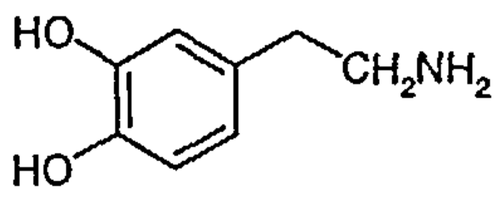

Dopamine

Figure 4.14 Structure of the neurotransmitter dopamine

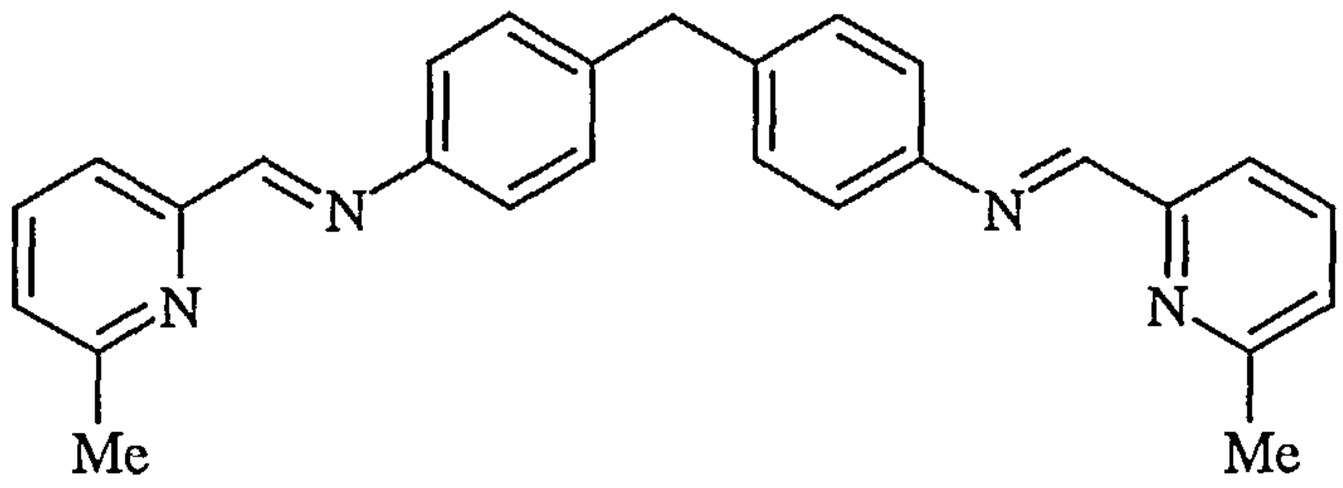

Figure 4.15 Ligand L^1

The imine ligand (L^1) (Figure 4.15) is formed by mixing two equivalents of 6-methylpyridine 2-carboxaldehyde with one equivalent of 4,4′-methylenedianiline in ethanol with stirring for 24 hrs. The yellow solid that precipitates out is isolated by filtration. The reaction of this ligand (L^1) with tetrahedral metal ions such as copper(I) and silver(I) leads to dimeric $[M_2L_2][X]_2$ supramolecular metallo-cyclophanes complexes[1] (where X = anion) (see Figure 4.16). The nitrogen atoms bind to the tetrahedral metal centres giving a supramolecular cyclophane structure.

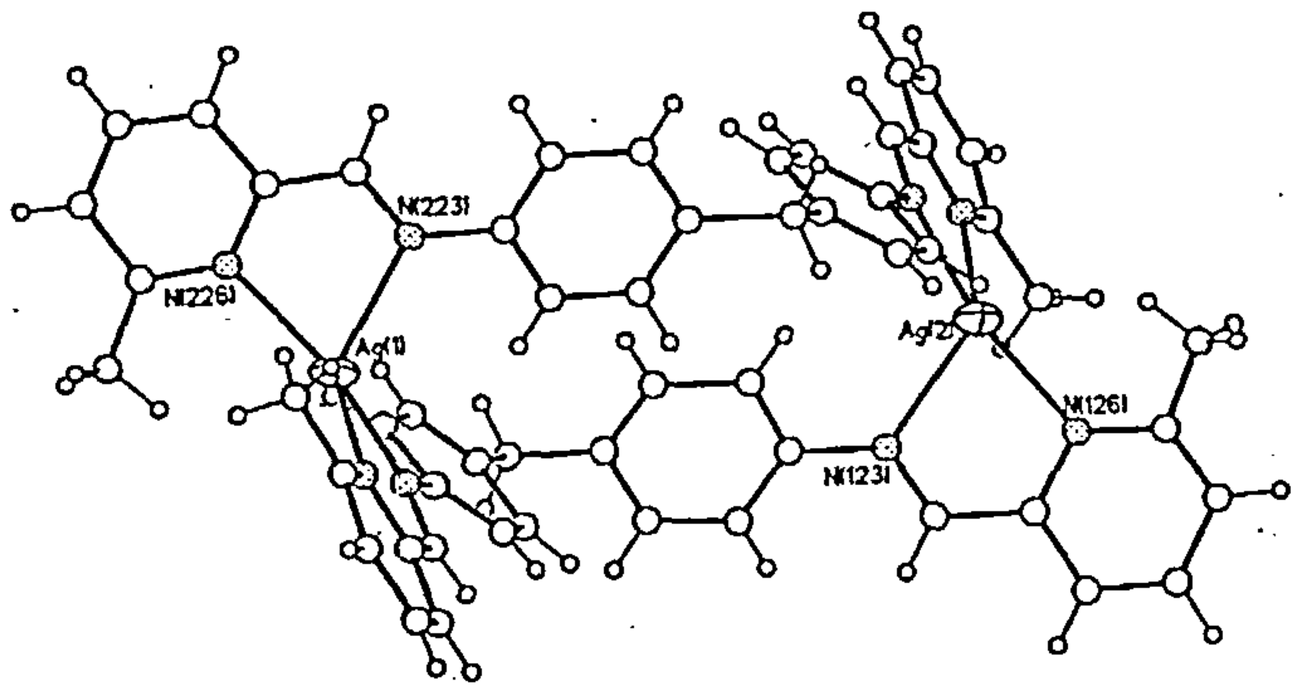

Figure 4.16 Crystal structure of $[Ag_2L^1_2]^{2+}$complex formed (BF_4 salt) (taken from C. L. Painting, PhD Thesis, University of Warwick,2000).

$[Cu_2L^1_2]^{2+}$, the copper cyclophane complex, was synthesised following the synthesis laid out by Hannon *et al.*[1]: simply mixing a $[Cu(MeCN)_4][X]$ salt (where X= tetrafluoroborate (BF_4) or hexafluorophosphate (PF_6)) with the imine ligand (L^1) in acetonitrile solution under N_2 for two hours. The red product that precipitated from

solution was left to cool in ice before being isolated by filtration. Recrystalisation was not necessary as ^{1}H NMR and CHN data indicated good complex purity.[1] This cyclophane complex is soluble in either acetonitrile or methanol. A range of similar organic soluble copper(I) and silver(I) metallo-cyclophanes using different salts were also prepared.[1]

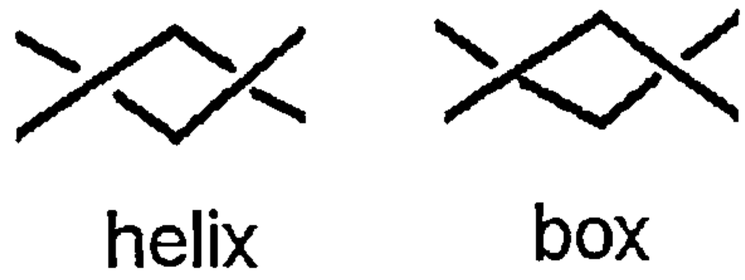

Figure 4.17 Schematic illustration of the conformations of $[Cu_2L_2][BF_4]_2$ cyclophane complex [1,54]

The $[Cu_2L^1{}_2]^{2+}[BF_4]_2$, copper(I) tetrafluoroborate cyclophane complex can adopt two conformations in solution: a helical (helix) structure or bridging non-helical (box) structure,[1,54] as shown in Figure 4.17. Similar conformations have been found with other dimeric metallo-cyclophanes.[55,56] The two conformations are attributed to the apparent flexibility of the ligand (L^1). Proton NMR of the complex in deuterated acetonitrile, CD_3CN, at low temperature confirms the presence of both species in a 2:1 ratio of helix:box.[1] The proton NMR of $[Cu_2L_2]^{2+}$ complex in deuterated methanol (d^3 MeOH) at room temperature shows the presence of two species in solution, whereas the proton NMR using deuterated acetonitrile (d^3 MeCN) indicates only one species[2] (see Figure 4.18) presumably due to fast exchange.

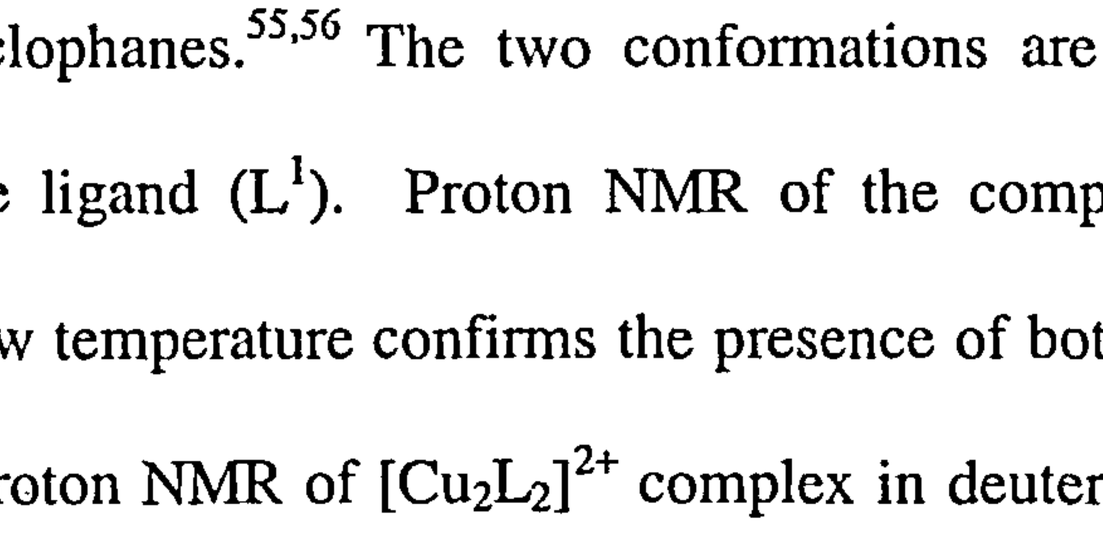

Figure 4.18 Room temperature proton NMR of the copper cyclophane in deuterated MeCN and MeOH (d^3 MeCN and d^3 MeOH)

Important features of these supramolecular metallo-cyclophane structures are (i) that they contain large enough cavities for small aromatic molecules to be bound and (ii) the metal centres (copper(I) or silver(I)) are incorporated into the cavity framework to hold the metallo-cyclophanes together.

If a binding event occurs in a host cavity, spectral changes in both the guest and host molecules may occur. For instance, metal-to-ligand charge transfer transitions may change upon substrate binding. The binding of a guest should also result in a change in the redox properties of the metal centre. It is these responses and others that can potentially be used to detect the presence of the aromatic substrate.

This chapter reports the investigation into the binding ability of these novel self-assembling cavity containing supramolecular metallo-cyclophane structures with a view to their possible eventual use as specific sensors. Here, investigations with a range of neutral molecules *e.g.* aromatic di- and tri-methoxybenzenes (dmb, tmb) and chiral anionic compounds (sodium antimonyl tartrate) are described. The synthesis of a new ligand capable of assembling into a larger metallo-cyclophane structure is also presented.

4.2.1 Electronic absorbance spectra of the ligand, L^1, and its metallo-complexes in methanol

The copper(I) complex ($[Cu_2L^1{}_2][BF_4]_2$) is a dark red coloured solid; in methanolic solution it is red-pink. Its silver(I) equivalent ($[Ag_2L^1{}_2][BF_4]_2$) is a bright yellow, light sensitive solid which is pale yellow in methanol solution. Methanol has a large spectroscopic window with a cut-off point at 210 nm. Absorbance spectra were therefore run from 210 nm – 750 nm. The absorbance spectra of both the copper and silver cyclophanes as well as that of the ligand used to form them are shown in Figure 4.19.

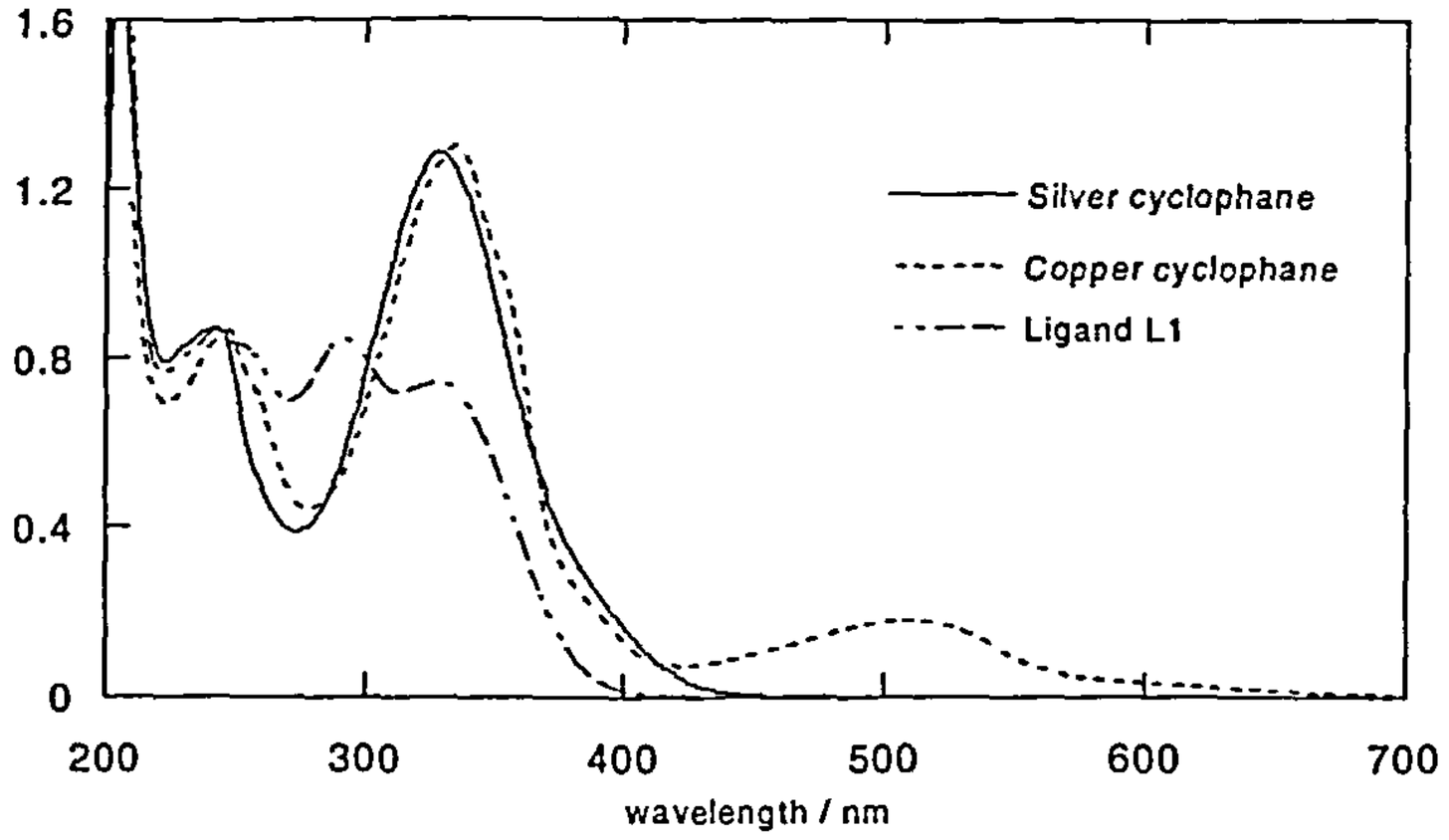

Figure 4.19 Absorbance spectra of copper cyclophane $[Cu_2L_2]^{2+}$ (20 μM), the equivalent silver complex (15 μM) $[M_2L_2][BF_4]_2$ and Ligand L^1 (39 μM) in methanol.

The spectra are characterised by a number of bands in the UV and visible region.

Table 4.2 summarises their absorption maxima and ε values.

Table 4.2 UV-visible absorbance assignments

Absorption maxima	λ_{max}/nm (ε = $mol^{-1}\ dm^3\ cm^{-1}$)
Ligand	210 (54,000), 240 (25,000), 255sh (24,500), 290 (26,000), 335 (24,500) tail up to 410 nm
Copper cyclophane	210 (62,500), 240 (40,000), 249 (45,000), 262 (37,500), 335 (65,000),as above with 386^{sh} (15,000), 510 (12,500), 560^{t} (5000)
Silver cyclophane	210 (93,300), 240 (57,000), 330 (83,000) with tail extending to ~450 nm

sh = shoulder, t=tail, IL= in-ligand, MLCT= metal-to-ligand charge transfer band.

To help interpret any interactions, the following assignment assumptions have been made. The ligand transitions centred at 210, 240, 290, 335 up to 410 nm, which have high ε values characteristic of π–π^* transitions are assumed to be almost unchanged upon complexation and are as assigned in-ligand (IL) transitions in the complexes. The copper cyclophane has additional bands at 249 nm, 262 nm and a shoulder at 386 nm. These are most likely charge transfer (CT) bands as they are quite intense. The band at 510 nm is assigned a metal (π_M) to ligand (π_L^*) charge transfer band (MLCT) with a long tail to ~560 nm. The silver cyclophane spectrum has bands at

240 and 330 nm assigned as IL, π–π^* transitions with a long shoulder extending to ~ 450 nm that is probably a metal-to-ligand CT, (MLCT) band.

4.3 Interactions with neutral molecules: Methoxybenzene metallo-cyclophane interactions

UV-Visible absorbance and fluorescene binding studies into the interactions of the host/receptor $[Cu_2L^1{}_2][BF_4]_2$, the copper cyclophane, with substrates neutral aromatic methoxybenzene molecules: 1,2-dimethoxybenzene (12dmb), 1,3-dimethoxybenzene (13dmb), 1,4-dimethoxybenzene (14dmb); 1,2,3-trimethoxybenzene (123tmb); and 1,3,5- trimethoxybenzene (135tmb) (Figure 4.19) were undertaken in dry methanol.

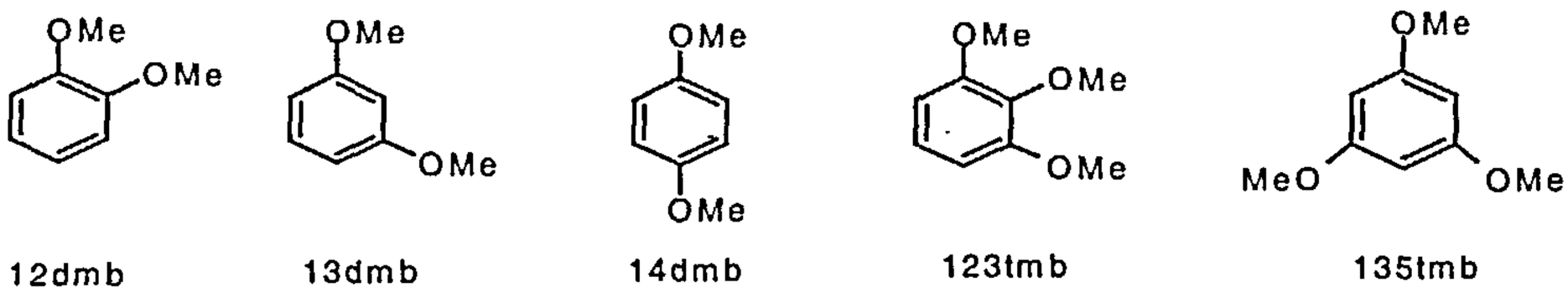

Figure 4.19 Di- and tri- methoxybenzenes used in this work

The di- and tri-methoxybenzenes were chosen for this study as they have been shown to bind well in organic solvent in other similar box structures such as Stoddarts' cyclobis and Fujita's tetranuclear square. These substrates may bind by (i) interactions in the cavity; (ii) electrostatic and charge transfer interactions; (iii) pi stacking. Aromatic compounds are held in box cavities by some combination of hydrophobic, electrostatic and charge transfer and π-stacking interactions. If substrates bind externally onto the supramolecular lattice they may self-aggregate in solution.

The di- and tri-methoxybenzene substrates are colourless in methanolic solution, absorbing in the UV region below 310 nm (Figure 4.20).

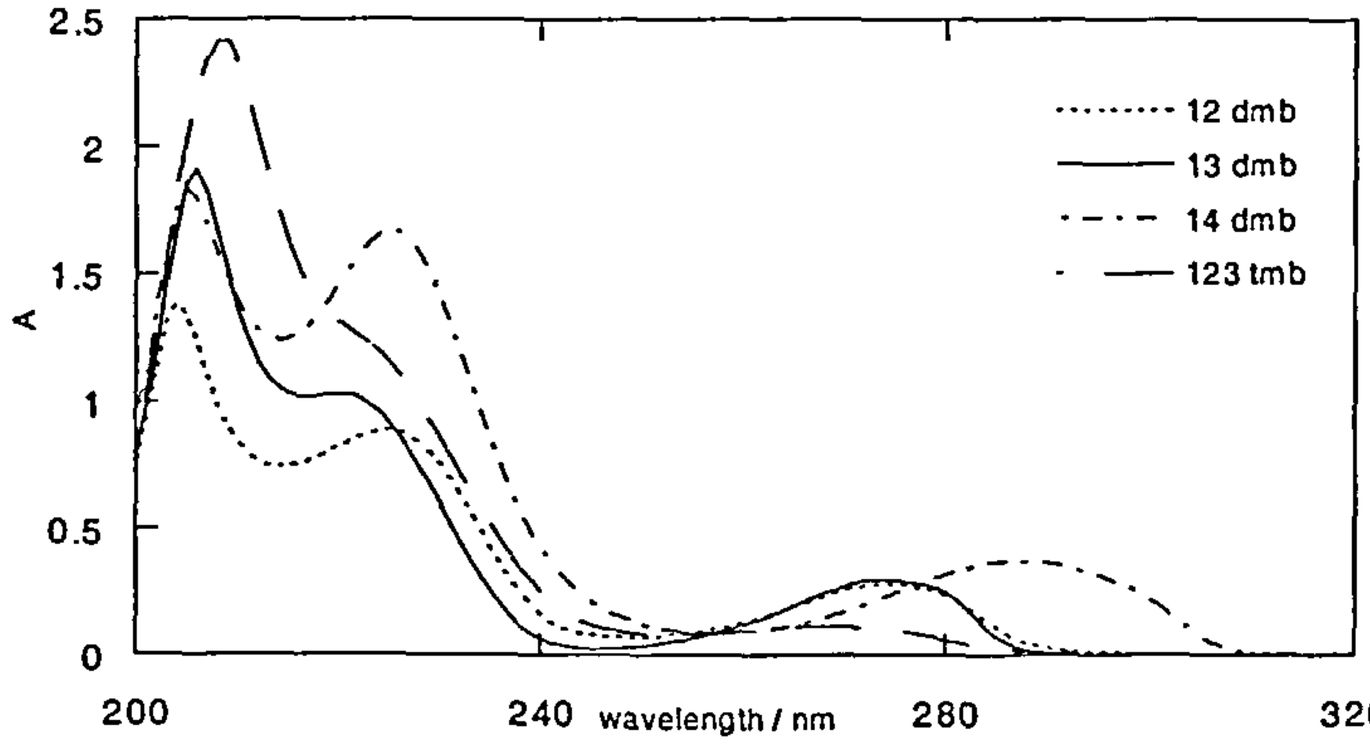

Figure 4.20 Absorbance spectra of substrates in methanol

4.3.1 Materials and Methods

1,3,5-tri-methoxybenzene was purchased from Aldrich, the other di- and tri-methoxybenzenes were purchased from Lancaster. Organic solvents were obtained as follows: Hi-dry MeOH (anhydrous solvent) from Romil; deuterated acetonitrile (CD_3CN) (99.8%), and methanol (CD_3OD) from GOSS. Molecular sieves (3Å, 1.66 mm pellets) used in the NMR experiments were obtained from Aldrich.

Titration experiments to determine binding constants were conducted using UV-Visible spectroscopy and fluorescence. Both experiments required that either the metallo-cyclophane or substrate concentrations be kept constant; titration sequences were set up to this effect. In general, methanolic stock solutions of the cyclophanes and substrates were made up in the following ranges: 300 – 500 μM substrates, 20 – 40 μM metallo-cyclophanes.

For UV-Visible absorbance studies, titration sequences were employed with the cyclophane concentration being kept constant as successive amounts of substrate concentration were added. The metallo-cyclophanes do not fluoresce whereas the substrates do. For fluorescence studies, therefore the substrate concentration was kept constant as the cyclophane concentration was varied.

Absorbance spectra were measured using a 1 cm pathlength quartz cuvette on a Jasco V550 UV-Visible spectropolarimeter. Fluorescence spectra were measured using a 1 cm pathlength, four-sided clear quartz cuvette on a Perkin Elmer LS50b. Each titration experiment was repeated three times or until consistent results were achieved. The error ranges quoted in the tables reflect the variation from experiment to experiment.

Stoichiometric ratios will be expressed in the order [substrate:receptor] where the receptor is the metal complex, or will be stated otherwise.

4.3.2 Equilibrium Binding Constant determination

Binding studies were undertaken using UV-Visible absorbance spectroscopy and fluorescence. The absorbance of the cyclophane in regions where the substrate has no spectroscopy and the fluorescence of the fluorescent substrate change upon mixing cyclophane and substrate solutions, so both have been used to probe the binding. In the absorbance experiments, the concentration of the cyclophane the receptor, was kept constant as the concentration of the methoxybenzene, the substrate was varied. Any change in absorbance signal of the metal complex would therefore be due to interactions with the substrate. Conversely, in the fluorescence experiments the substrate concentration was kept constant. This method can be used to determine the binding constant, *K*, of two species, if a single binding mode (or constant ratio of multiple binding modes) is in operation over a chosen concentration range.

Induced spectroscopy method (ISM) to determine *K*

ABSORBANCE BINDNG CONSTANT DETERMINATION: The induced spectroscopy method (ISM) as developed by Rodger[18] in combination with a Scatchard plot can be used to

determine the *K* value of the interaction of the copper cyclophane and di- and tri-methoxybenzenes. This method can be used when the higher limits of binding, *i.e.* the absorbance at full binding cannot be examined, if instead for example, a subsequent weaker binding mode begins to be occupied as the receptor sites are filled.

For comprehensive details on the ISM of determining binding constants please refer to reference 18.

The interaction between a receptor (R) and a substrate (S) with binding properties for the receptor can be described by the equation:

$$R + S \underset{k_2}{\overset{k_1}{\rightleftharpoons}} RS$$

(k_1, rate of association; k_2 rate of dissociation).

The simplest measure of the binding strength between two molecules, can be described by a binding association constant (K) where:

$$K = \frac{[RS]}{[R][S]} = \frac{k_1}{k_2} \qquad (4.1)$$

From above, in general terms:

$$R + S \rightleftharpoons RS$$

where R is the receptor (cyclophane), S is the substrate and RS is the bound species.

More specifically,

$$R_f + S_f \rightleftharpoons RS$$

i.e. free receptor + free substrate ⇌ bound species. As the total receptor concentration R_{tot} equals the free receptor concentration plus the concentration of the bound receptor,

$R_{tot} = R_f + R_b$ and, the total substrate concentration equals the free substrate concentration plus the concentration of the bound substrate $S_{tot} = S_f + S_b$. Therefore R_b is equivalent to RS which is equivalent to S_b. The equilibrium binding constant (equation 4.1) can therefore be defined as:

$$K = \frac{S_b}{S_f R_f} \tag{4.2}$$

The total receptor site concentration, (the total binding site concentration of the cyclophane) R_{tot} is equal to $\frac{C_m}{n}$, where C_m is the macromolecule concentration (the total constant cyclophane concentration) and, n is the number of cyclophane binding sites per substrate. If the experimental data show that the binding mode is constant, then, using spectroscopic data the starting point is equation 4.3:

$$S_b = \alpha\rho \tag{4.3}$$

where α (a function of wavelength) is a constant over the range of binding ratios being considered and ρ is the absorbance signal at a chosen wavelength, in this case ΔA (the change in absorbance due to the interactions of substrate with the box).

The induced spectroscopy method simply involves the rewrite of equation 4.2 to give an expression:

$$K = \frac{\alpha\rho}{(R_{tot} - \alpha\rho)(S_{tot} - \alpha\rho)} \tag{4.4}$$

which when rearranged to give S_{tot}, for two different substrate concentrations S^j_{tot} and S^k_{tot} at the same macromolecule concentration Cm, $R^j_{tot} = R^k_{tot}$ gives equation 4.5.

$$\frac{S^k{}_{tot} - S^j{}_{tot}}{\rho^k - \rho^j} = \frac{R_{tot}}{\alpha}\left[\frac{\frac{S^k{}_{tot} - S^j{}_{tot}}{\rho^k - \rho^j}}{\rho^k - \rho^j}\right] + \alpha \qquad (4.5)$$

A plot of y = $\frac{S^k{}_{tot} - S^j{}_{tot}}{\rho^k - \rho^j}$ versus x = $\left[\frac{\frac{S^k{}_{tot} - S^j{}_{tot}}{\rho^k - \rho^j}}{\rho^k - \rho^j}\right]$ should give a straight line plot with slope equal to $\frac{C_m}{n\alpha}$ and intercept α, from which R_{tot}/Cm (the amount of box that is binding box) and n can also be determined.

The α value calculated and the changes in signal value ρ can be used to determine S_f, which in turn can be used in a Scatchard plot of $\frac{r}{S_f}$ *vs* r, where $r = \frac{S_b}{C_m}$ is the ratio of bound substrate over the total constant box concentration and S_f the free substrate concentration. The plot should have a negative slope of K, with the intercept equal to K divided by n, the x intercept occurs where r equals n.

FLUORESCENCE BINDING CONSTANT DETERMINATION: A method to calculate K can be developed from the basic principles of fluorescence.

Fluorescence is made up of $F = F_b + F_f$ where F is the total fluorescence reading, F_b is the fluorescence reading of bound substrate and F_f is the fluorescence reading of free substrate. Similarly, if S_{tot} equals the total fluorescent substrate concentration (on the assumption that the substrate alone fluoresces), we can say that at any one time that, $S_{tot} = S_f + S_b$.. Both equations combined and rearranged give:

$$F = \frac{S_b}{S_{tot}} F_b + \frac{S_f}{S_{tot}} F_f \qquad (4.6)$$

If S_f is replaced in equation 4.6 and we can rearrange it to give

$$S_b = \frac{S_{tot}(F - F_f)}{F_b - F_f} \tag{4.7}$$

where S_b is the bound substrate concentration. A Scatchard plot of $\frac{r}{S_f} vs\ r$ where $r = \frac{S_b}{C_m}$ can be used to determine K. The binding curve should yield F_f and F_b, and the change in fluorescence ΔF *i.e.* $(F - F_f)$ on addition of cyclophane increments to substrate. S_b can be determined using the data available from equation 4.7. The negative slope of the Scatchard plot should yield K.

4.3.3 UV-Visible absorbance study

UV-Visible absorbance data was collected over a substrate:cyclophane concentration mixing ratio, R, of [0:1] – [6:1]. Figure 4.21 shows the absorbance spectra of the copper cyclophane complex and its spectroscopic interactions with 14dmb in methanolic solution. The absorbance spectral data of the complete titration sequences for all five methoxybenzene substrates with the copper cyclophane (working with a constant cyclophane concentration of 15 μM) are given in Appendix 4.1.

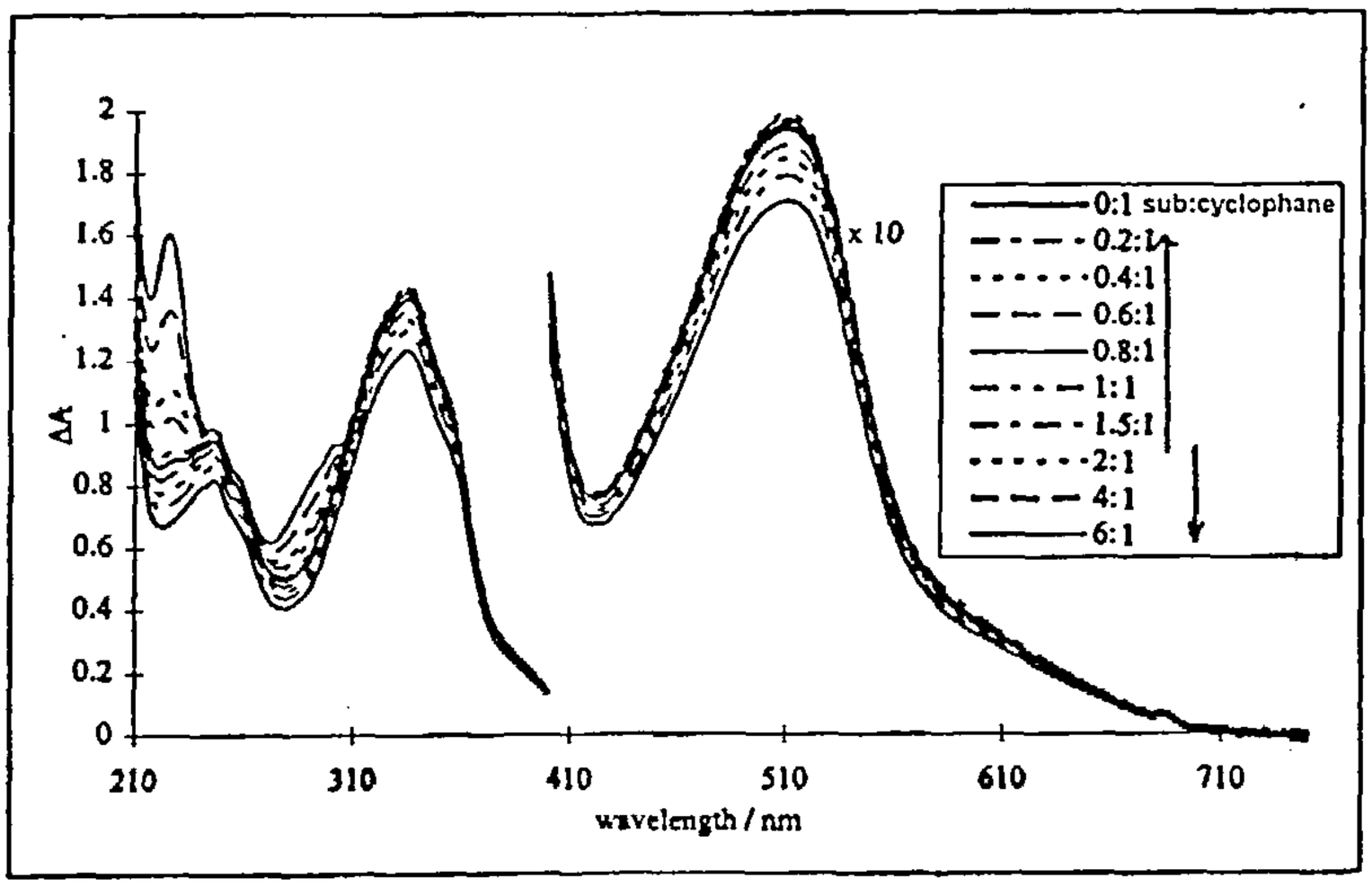

Figure. 4.21 Absorbance titration spectrum of copper cyclophane with 14dmb in methanol. Working with a constant cyclophane concentration of 15 μM. The arrows in the legend indicate whether the absorbance increases or decreases on addition of substrate.

In general, the absorbance intensity of the complex spectrum (Figure 4.21) initially increases on addition of substrate up to mixing ratios of ~1:1 – 2:1 with each substrate, after which two isosbestic points at 240 nm and 304 nm appear. Isosbestic points below 310 nm can be ignored, as they are manifestations of substrate additions. The absorbance intensity then gradually decreases at higher ratios. This decrease in absorbance intensity is termed a hypochromic shift and usually indicative of π-stacking.

The development of isosbestic points on successive additions from 2:1, and the decrease in absorbance intensity on successive additions from 2:1 to 6:1 (the last addition made) of substrate:cyclophane, seem to indicate that the system may possess more than two states, possibly one free, and two different bound species. The absorbance spectrum of the cyclophane with 14dmb shows isosbestic points at 240 nm and 304 nm after [2:1] substrate:cyclophane mixing ratio, indicating one binding mode; below ~[2:1] ratio there is an additional binding mode. Changes in absorbance intensity at 335 nm and at 509 nm (charge transfer band magnified ×10) are clearly distinguishable.

As the substrates all absorb below 310 nm, the change in absorbance (ΔA) at 335 nm (assigned to an IL π–π^* transition) and the MLCT band at $\lambda_{max} = 509$ nm over the length of each titration were followed (See Tables 1 and 2 in Appendix 4.1).

For each substrate, at 335 nm and ~510 nm, ΔA versus substrate:cyclophane concentration plots yielded smooth, positively increasing binding curves, up to ratios of approximately 1:1 or 2:1 substrate:cyclophane after which the absorbance intensity begins to decrease and the curve begins to slope downwards. Figure 4.22 illustrates the ΔA values for 14dmb in the form of a binding curve of ΔA as a function of substrate/cyclophane concentration.

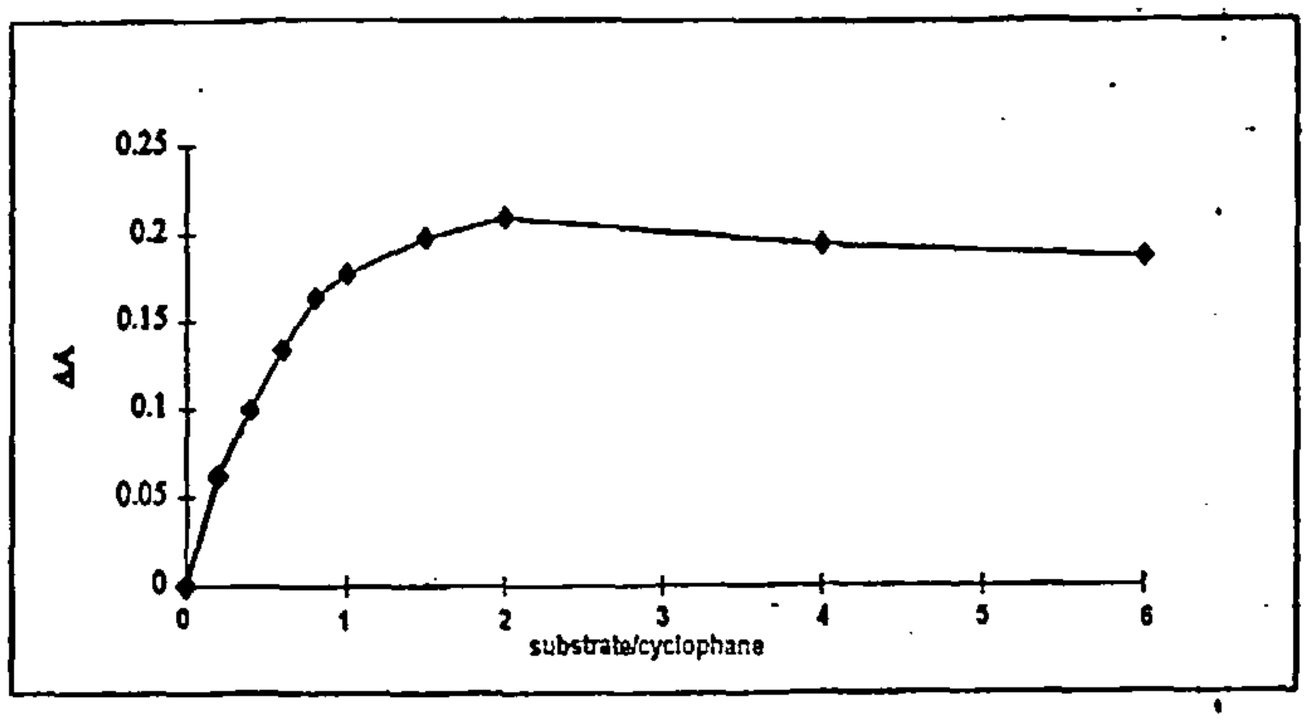

Figure 4.22 The binding curve of the interaction of the cyclophane with 14 dmb, a graphical version of its spectrum from Figure 4.21

As the early data points up to 2:1 probably correspond to a single binding regime, an induced spectroscopy method (ISM) analysis was attempted. The largest possible area on the binding curve was examined, in most cases [0.6:1]–[2:1]. (As *K* is constant in uniform binding modes, the same portion of each binding curve was examined for each substrate).

The appropriate spectra, and their *K* values deductions *i.e.* ISM and Scatchard plots for each substrate can be found in the Appendix 4.1. K values are summarised in Table 4.3.

12dmb, 13dmb, and 135tmb all have binding constants of ~ 10^6 M^{-1}, with 12dmb having the largest value of *K* suggesting its geometry is most suited to the binding site. The 14dmb substrate, which might have been expected to slot neatly through either the helix or box conformation of the cyclophane has a binding constant an order of magnitude weaker ~ 10^5 M^{-1} as does 123tmb.

4.3.4 Fluorescence study

Fluorescence experiments were set up to monitor the substrate fluorescence while the metal complex concentration was varied; here metal complex increments were added to constant substrate concentration in order to monitor quenching of substrate.

Fluorescence spectra were run from just before the excitation wavelength up to 700 nm (the presence of Rayleigh scattering was also noted). λex and λem refer to the excitation and emission wavelengths and ex/em refers to the size of the excitation and emission slits used on the fluorimeter. Once the excitation and emission slits were set to provide a reasonable intensity of substrate, they were not changed.

Preliminary investigations show that whilst the substrates were highly fluorescent, the cyclophane itself exhibited a fluorescence of less than 10 fluorescence units. When both were placed in solution the presence of the box seemed to produce a quenching effect on the fluorescent spectra of the substrate. Therefore fluorescence titration experiments were set up to monitor the substrate fluorescence while the cyclophane concentration was varied. The changes in fluorescence were a larger percentage of the total fluorescence signal than is the case with the absorbance experiments and so consistent data sets were easier to achieve. The [1:1 – 1:2.4] (substrate:cyclophane) binding region was examined in these experiments which corresponds to a similar portion of the UV-Visible titrations.

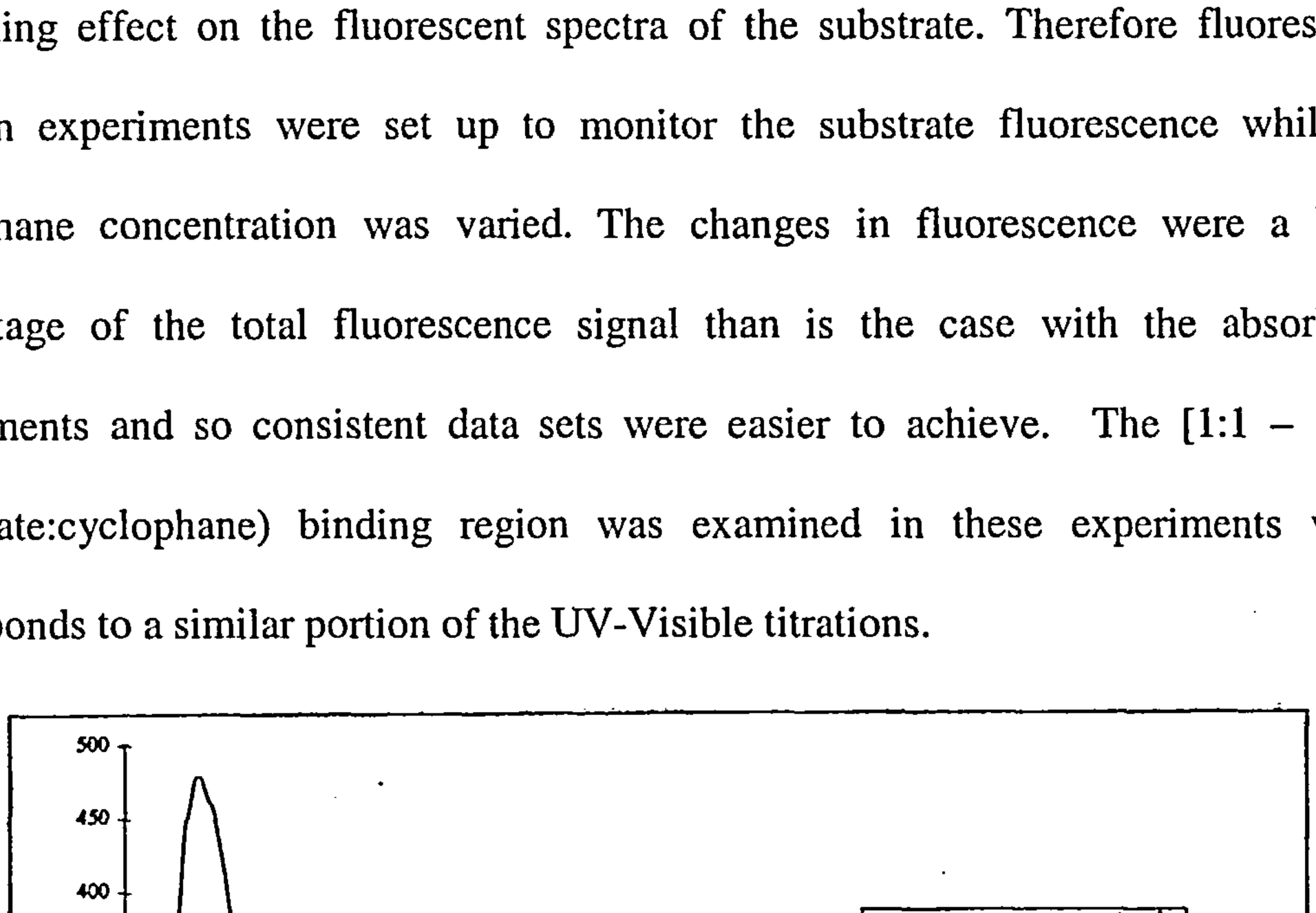

Figure 4.23 Fluorescence spectrum of the cyclophane with 13dmb. Working with a constant substrate concentration of 10 μM, ratios are indicated within the figure as are experimental parameters.

Figure 4.23 illustrates the fluorescence spectrum of a titration of the copper cyclophane with 13dmb. The substrate solution was excited at 273 nm (an IL substrate transition) and the change in emission recorded at 298 nm. A large quenching of the substrate (13dmb) fluorescence to a relatively small fluorescence intensity can be seen on the initial addition of cyclophane complex, this is followed by much smaller decreases in fluorescence on addition of cyclophane increments up to the [1:2] substrate:cyclophane mixing ratio. The fluorescence at λ_{max} for all the titration experiments is summarised in Table 1 Appendix 4.2 as are the ΔF values (where ΔF equals F the fluorescence of the box and substrate minus the free fluorescence F_f).

For each substrate, ΔF (the change in signal) versus box:substrate concentration plots were found to be smooth negatively decreasing binding curves (not shown). As the data produces a curve, these changes can be used to calculate the extent of binding. Appendix 4.2 holds the fluorescence spectra for all five substrates and their *K* values deductions.

The substrates were found upon ISM and Scatchard analysis to bind with binding constants of $10^5 - 10^6$ M^{-1}. *K* values were largest for 14dmb ($10^6 M^{-1}$), and weakest for 123 and 135 tmb ($10^5 M^{-1}$) as summarised in Table 4.3.

4.3.5 Summary of binding studies

The binding constants determined for the interactions of the copper cyclophane complex with di- and tri- methoxy benzenes are unusually high when compared to reported values for similar structures of this type (for 14dmb: *K* value of 1×10^4 M^{-1} with Fujita's square (Figure 4.5) in deuterated water,[7] $K= 340$ M^{-1} in deuterated methanol and water mix [2,7] and $K= 17M^{-1}$ with cyclobis (Figure 4.4) in acetonitrile solution).[2]

Table 4.3 Summary of binding constants determined using absorbance and fluorescence spectroscopy. The detailed *K* tables including error calculations for absorbance and fluorescence studies can be found in Appendix 4.1 and 4.2 respectively

Substrate	Absorbance *K* values / M^{-1}	Fluorescence *K* values / M^{-1}
12dmb	$4-5\times10^{6}$	$\sim 1\times10^{6}$
13dmb	$\sim 3\times10^{6}$	$\sim 1\times10^{6}$
14dmb	$2-8\times10^{5}$	$3-5\times10^{6}$
123tmb	$4\times10^{5}-1\times10^{6}$	$7\times10^{5}-1\times10^{6}$
135tmb	$1-2\times10^{6}$	$7\times10^{5}-1\times10^{6}$

Comparison of the binding constants determined using absorbance with those of fluorescence, do show agreement within acceptable limits of experimental error. The exception is the value for 14dmb. 14dmb's binding constant was found to be an order of magnitude weaker than other substrates when probed using UV ($\sim10^{5}M^{-1}$) and significantly larger when probed using fluorescence.

The absorbance studies seem to indicate the existence of at least two modes of binding to the metal complex, the first mode starts from [0:1–2:1] substrate:cyclophane, with the second switching on below R of [2:1]. The latter may perhaps involve substrates stacking in solution (as shown by the spectra and the binding curves). There was no indication of different binding modes from the fluorescence, but then a similar binding region to that for absorbance was not explored due to the non-fluorescence of the metal complex.

Absorbance experiments were set up to look at [0:1–6:1] substrate:cyclophane region of the binding curve by probing the box. *K* values were calculated in the [0.6:1–2:1] region, so the values reflect the earlier binding mode of the two exhibited by absorbance. The second mode can also be probed using absorbance, but calculations were only made on the first mode due to the overlay of signals. The fluorescence

experiments explored the [1:1–1:2.4] substrate:cyclophane binding region by probing the substrate.

4.3.6 Specific interaction investigations

Although the binding constant determinations gave real data and allow a determination of *K*, it remained possible that the process being probed was not the insertion of the dmb into the metallo-cyclophane cavity. In order to determine whether it is the inserted cyclophane complex associated with its ligand or the metal ion (copper(I) or silver(I)) or a salt effect (tetrafluoroborate) or a combination of these that we were observing, the interaction of each with 13dmb was investigated using fluorescence.

Ligand L^1 interactions

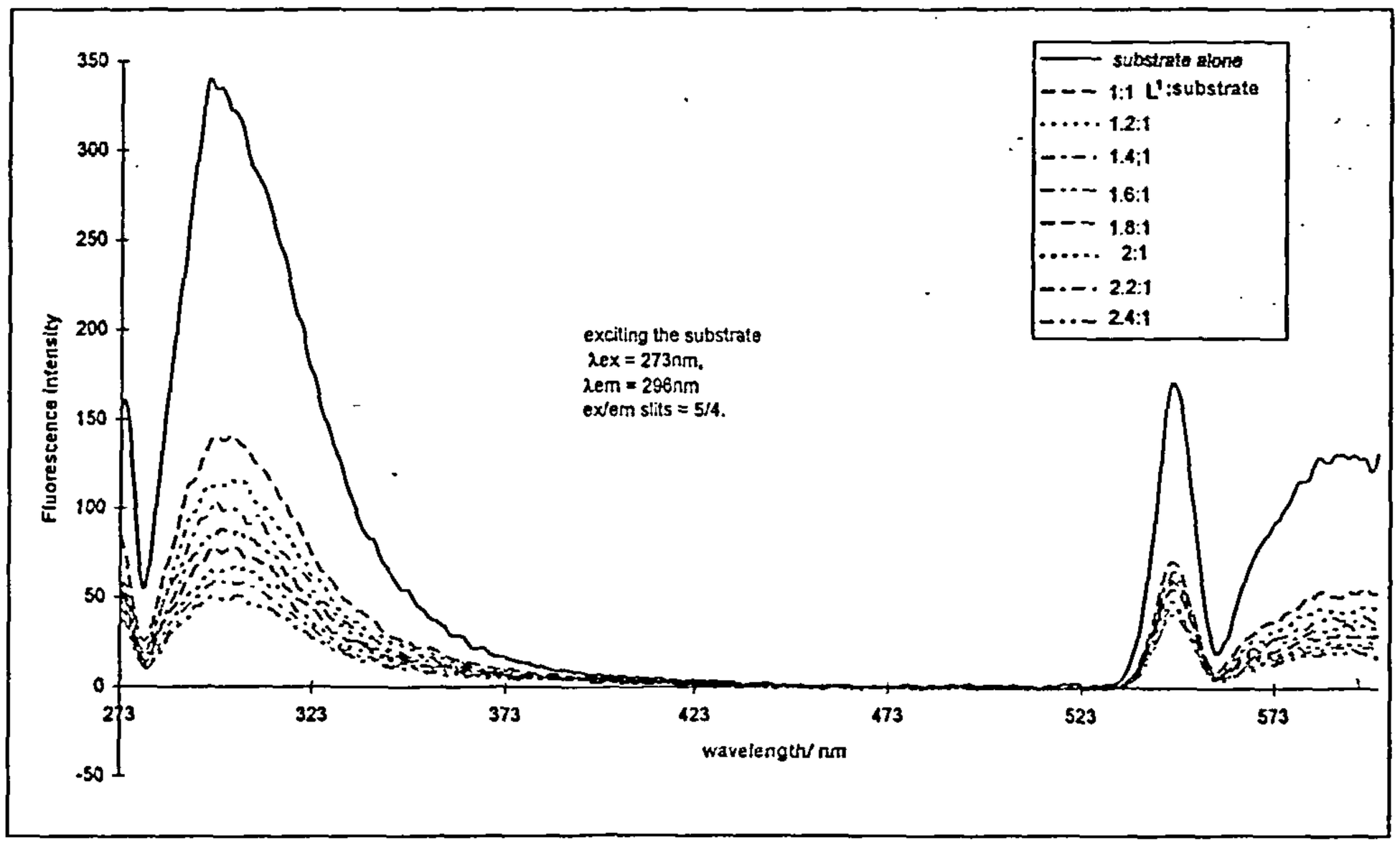

Figure 4.24 Fluorescence of ligand L^1 with 13dmb. Working with a constant substrate concentration of 10 μM, ratios are indicated within the figure as are experimental parameters.

The ligand itself does not fluoresce in these experiments. However, Figure 4.24 shows the fluorescence quenching of the substrate when ligand L^1 is added (see individual spectra for conditions, NB: ratios are [cyclophane:substrate] in contrast to the copper data). The quenching observed is similar to that observed when copper

cyclophane is added to substrate but not as large. A binding constant of $K=10^5\ M^{-1}$ — an order of magnitude weaker than that with the cyclophane complex was calculated. This is still a large binding constant, which suggests ligand-dmb interactions are a significant part of the cyclophane-dmb complexation. This result positively suggests the ligand takes part or has an effect on the substrate in some way, but also that the cyclophane structure enhances the binding interaction in some way. It is possible that the metal complex dissociates to metal plus ligand or metal plus ligands on substrate addition. This would account for the increase in absorbance as substrate concentration is increased up to a [2:1] substrate:cyclophane addition with the substrate reacting either with free ligand or a part of the metal complex.

Metal interactions

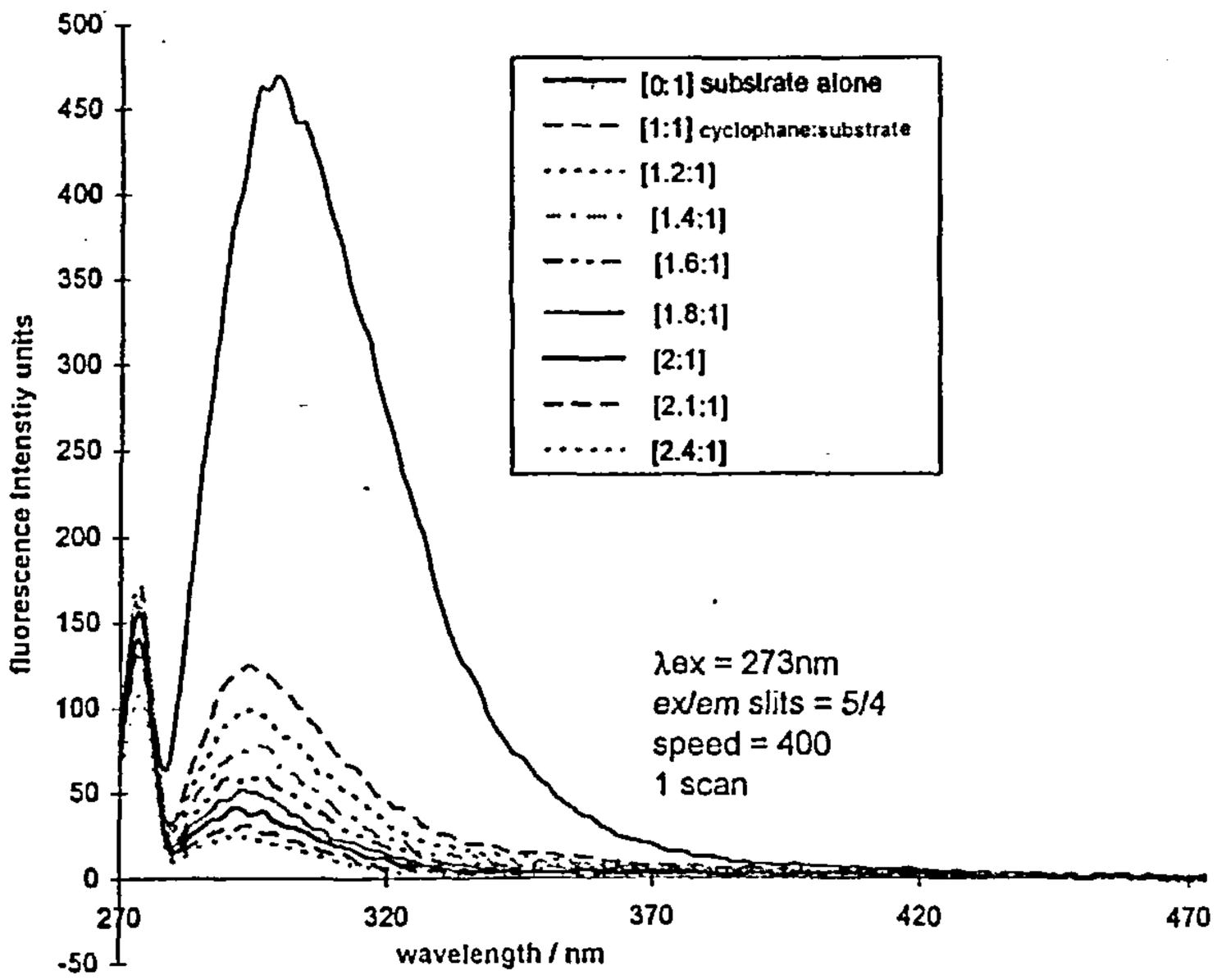

Figure 4.25 The fluorescence spectrum of 13dmb with the silver BF_4 cyclophane. Working with a constant substrate concentration of 10 μM, ratios are indicated within the figure as are experimental parameters.

To determine if the metal used in the complexation of the cyclophane affects the interaction between the substrate and the cyclophane, two experiments were set up. (i) The silver equivalent cyclophane and its interaction with 13dmb was investigated, (see

Figure 4.25). On comparison with Figure 4.23, changing the metal ion was found to have little or no effect on the interaction between the substrate and the cyclophane. (ii) The interaction of 13dmb with $[Cu(MeCN)_4][BF_4]$ was investigated. Figure 4.26 shows the fluorescence interactions of the substrate with the copper salt $[Cu(MeCN)_4][BF_4]$. Very little quenching of the substrate fluorescene is seen when the BF_4 salt is added to 13dmb. When the $[Cu(MeCN)_4][PF_6]$ salt was used (not shown) again only minor quenching was seen. Thus it was concluded that the metal centre itself was not playing a role in metallo-cyclophane/dmb interactions.

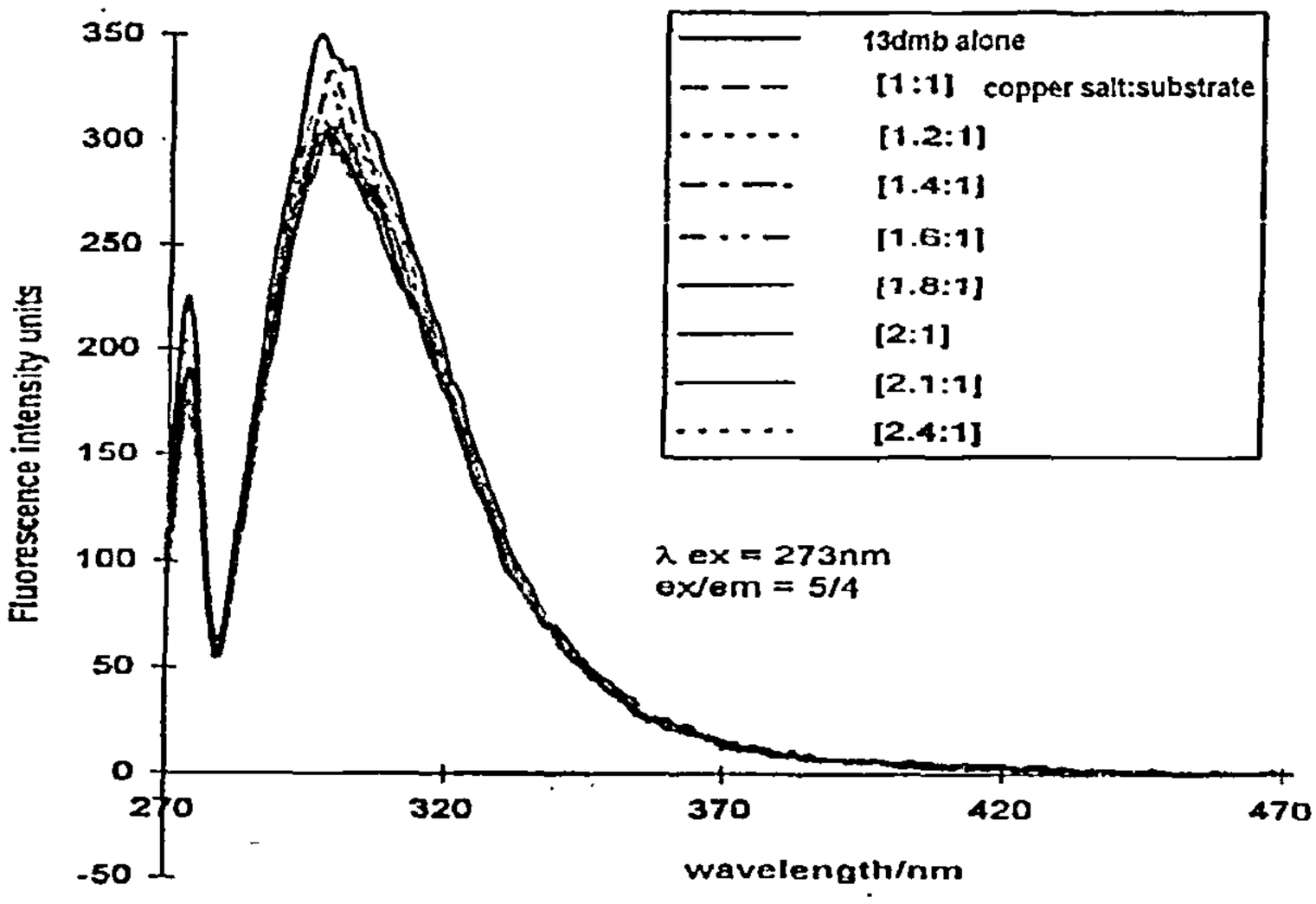

Figure 4.26 Fluorescence interactions of 13 dmb with $[Cu(MeCN)_4][BF_4]$ salt. Working with a constant substrate concentration of 10 μM

Stability Studies

Proton NMR, UV-Visible absorbance spectroscopy and mass spectrometry were used to investigate cyclophane stability over a range of concentrations 10^{-3}, 10^{-4}, 10^{-5} M and over time in methanolic solution. Proton NMR and absorbance studies show the same species to be present in solution at all of these concentrations. NMR and absorbance studies on comparable concentrations of the $[Cu_2L_2]^{2+}$ complex in CD_3OD

were undertaken. No evidence of aggregation at high concentration and/or of dissociation at lower concentrations was found (data not included).

Fourier transform – ion cyclotron resonance (FT-ICR) on the Bruker Apex II at Warwick (in collaboration with FT-ICR operators X. Feng and H. Fielding) and electrospray ionisation (ESI) mass spectrometry studies showed that the copper cyclophane of the formula $[M_2L_2][BF_4]_2$ has the same species in solution at 10^{-3}, 10^{-4} and 10^{-5} M. It also shows evidence of self association at higher concentrations *i.e.* a peak corresponding to $[M_4L_4][BF_4]_3^+$ was seen. When used to see if binding interaction is taking place, no peak corresponding to [cyclophane + substrate] was seen. However, this is not proof of lack of formation of such non-covalent complexes.

Interestingly, in absorbance studies, a defined increase in absorbance is seen as substrate concentration increases before decreasing at higher concentrations. A similar increase in the number and size of cyclophane peaks was also seen as substrate concentration was increased via mass spectrometry.

NMR studies to investigate interactions

NMR studies were conducted in deuterated methanol using dry molecular sieves (3Å 1.6 mm pellets). The NMR sample preparation and titration method employed was to weigh and mix directly in the NMR tube. Titrations similar to those employed for the spectroscopic methods were used. Concentrations were in the 1 mM concentration range as is necessary for NMR.

NMR studies were undertaken in order to confirm the spectroscopic data to provide reasonable explanations for the strength of binding and to determine if the ligand L^1 or the metallo-cyclophane complex affects interaction. The chemical shifts were compared and the formation of new species was sought. A comprehensive study

using low temperature ^{1}H NMR, ^{19}F and ^{11}B with 14dmb in deuterated methanol was undertaken.

Briefly, the following proton NMR were investigated at low temperature in deuterated methanol (CD_3OD): (i) ligand (L^1) alone; (ii) 1:1 ratio of L^1:14dmb; (iii) L^1+ $[Cu(MeCN)_4BF_4]$; (iv) 1:1:1 ratio of L^1 + 14dmb + $[Cu(MeCN)_4BF_4]$ salt; and (v)1:1 ratio of $[Cu_2L_2]^{2+}$ cyclophane complex:14dmb. ^{19}F and ^{11}B NMR of (iii) and (iv) at room temperature were also undertaken. The results are not included.

The results of (i) and (ii) suggested that the ligand has no interaction with the substrate alone. The results of (iii), (iv) and (v) were inconclusive in that no noticeable changes in NMR (>0.1 ppm shift) were observed. Initial studies had seemed to indicate that the substrate was interacting with the complex, with (a) the imine proton on the complex shifted upfield; (b) the CH_2 group in the middle of L^1 shifted upfield; and (c) the CH_3 groups at the tail end of the ligand exhibiting a downfield shift. These data initially suggested that 14dmb sits on the box but not in it. However, similar shifts were found to occur with L^1+$[Cu(MeCN)_4BF_4]$, L^1+$[Cu(MeCN)_4BF_4]$ + dmb over a temperature range so these results are inconclusive as any chemical shifts seen could be a result of temperature decrease.

Summary of methoxybenzene metallo-cyclophane interactions

Interactions between the metallo-cyclophane structure and neutral molecules (di- and trimethoxybenzenes) have resulted in unusually high binding constants of K ~10^5 – 10^6 M^{-1} being determined using both absorbance and fluorescence spectroscopy. Investigations into the specific interactions in solution, suggested that metallo-cyclophane binds unselectively but strongly with all the aromatic electron-rich substrates investigated. The copper and silver metal ions and their salts are not involved directly in complexation between the substrate and the metallo-cyclophane (studies

using a different metal centre (a silver cyclophane) showed similar interactions) but they do play a role since the presence of the metal gives a binding constant ×10 higher than with the ligand alone.

NMR studies were inconclusive, after preliminary results seemed to indicate that the substrate may interact/sit on the box rather than in it. NMR and absorbance studies indicate that the metallo-cyclophane does not dissociate in solution. Both the complex and the substrate are perturbed in some way but it is still unclear as to where the substrate is binding.

It may be that the metallo-cyclophanes are not large enough to accommodate the substrate in the cavity but the ligand or ligands and substrate interact in some way. This is addressed in section 4.6. Solvent molecules have been found inside the cyclophane cavity in the solid state,[1] but no larger molecules to date.

Further work

Although the cavity of the cyclophane should be large enough for single aromatic systems, this does not seem to be the binding mode adopted. Further work to design sensors for neurotransmitters will require the synthesis and analysis of a larger metallo-cyclophane. Molecular modelling studies on this and any new systems would aid in determining if and how the substrates sit in the box cavity, and to help account for the range of binding constants.

4.4 Interactions with anionic compounds

The interaction of the copper cyclophane with chiral anionic compounds was investigated and resulted in a method whereby the copper tetrafluorobarate cyclophane,

$[Cu_2L^1_2]^{2+}$ helix-box mixture (and other cyclophanes with similar ligands) can be resolved into its helical enantiomers.

4.4.1 Resolution of $[Cu_2L^1_2]^{2+}$ copper cyclophane helix-box mixture

Sodium antimonyl tartrate, NaSbtat, (Figure 4.27) is a member of a family of chiral molecules that are well known for their use in the resolution of racemic (rac) tris chelate complexes due to the different binding of NaSbtat to their Δ and Λ-enantiomers.[57,58] For example, $[Ru(1,10\text{-phen})_3]^{2+}$ where 1,10-phen = 1,10-phenanthroline, $[M(bipy)_3]^{2+}$ where bipy = 2,2′-bipyridine (see chapter 2) can be resolved by these compounds.[59] NaSbtat exists in a dianionic form, $(C_4O_6H_2Sb)_2{}^{2-}$, in solution (Figure 4.27).

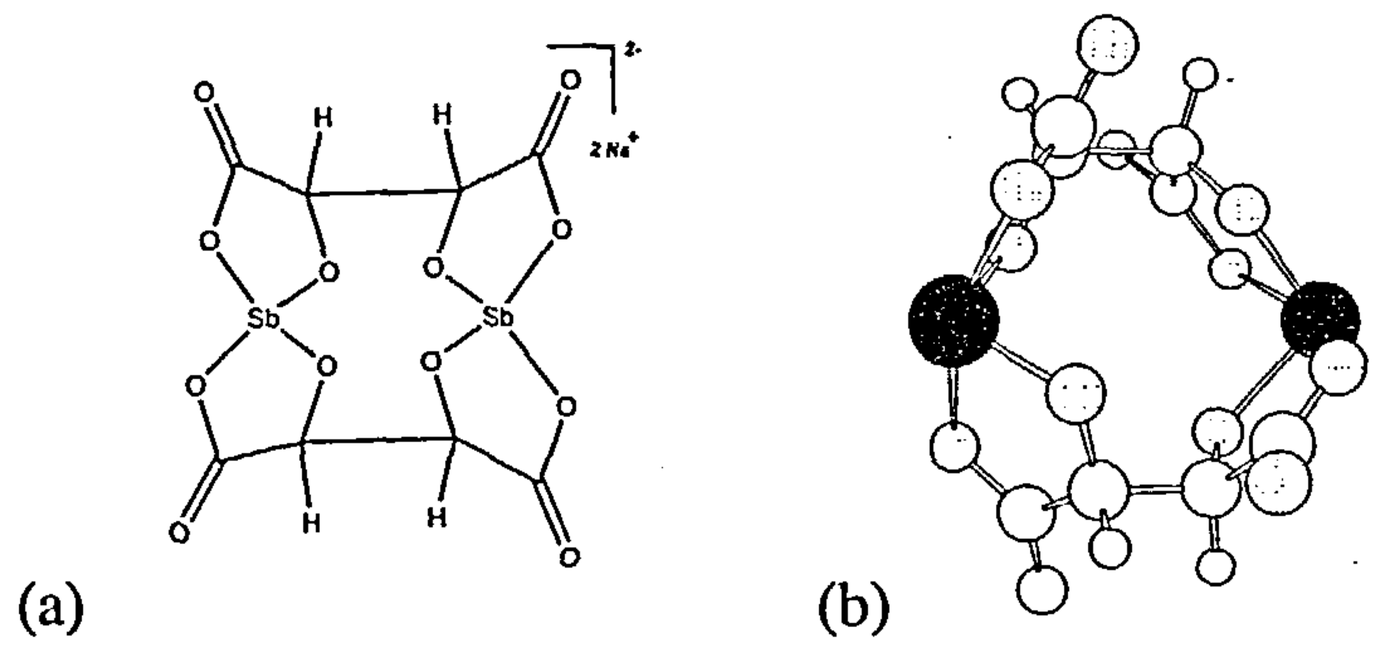

Figure 4.27 (a) The 2-D and (b) 3-D stick and ball structure of the chiral dianion, sodium antimonyl tartrate

Sodium antimonyl-L-tartrate (98%) was purchased from Avocado, the sodium antimonyl-D-tartrate is not commercially available and was synthesised using a modified version of the preparation described by Coggan *et al.* [59] An aqueous slurry of Sb_2O_3 + NaOH + D-tartaric acid (in a molar ratio 1:1:2) was heated under reflux for 2 – 3h. The white precipitate formed on cooling, NaSb-D-tat, was collected under vacuum, and used without further purification. The NaSb-D-tat is only sparingly soluble in water.

Spectroscopic investigation

The L isomer of NaSbtat, NaSb-L-tat, is chiral but colourless in solution, therefore exhibiting a *CD* signal in the far UV region only. A *CD* spectrum of the $[Cu_2L_2]^{2+}$ helix-box mixture exhibits no signal due to the racemic mix of the helices. On addition of NaSb-L-tat to a methanolic solution of the box:helix mixture, a *CD* signal is induced in the UV-visible region of spectra. The magnitude of the signal is reasonably large so it corresponds to a Pfeiffer effect shift (shift of Δ and Λ equilibrium) of the helix:box mixture to having an excess of one helical enantiomer (see Figure 4.28).

Both the D and L form of NaSbtat induce bands in copper cyclophane at 255 nm, 310 nm (IL transitions), 350 nm and 500 nm. The signals are equal in magnitude but opposite in sign.

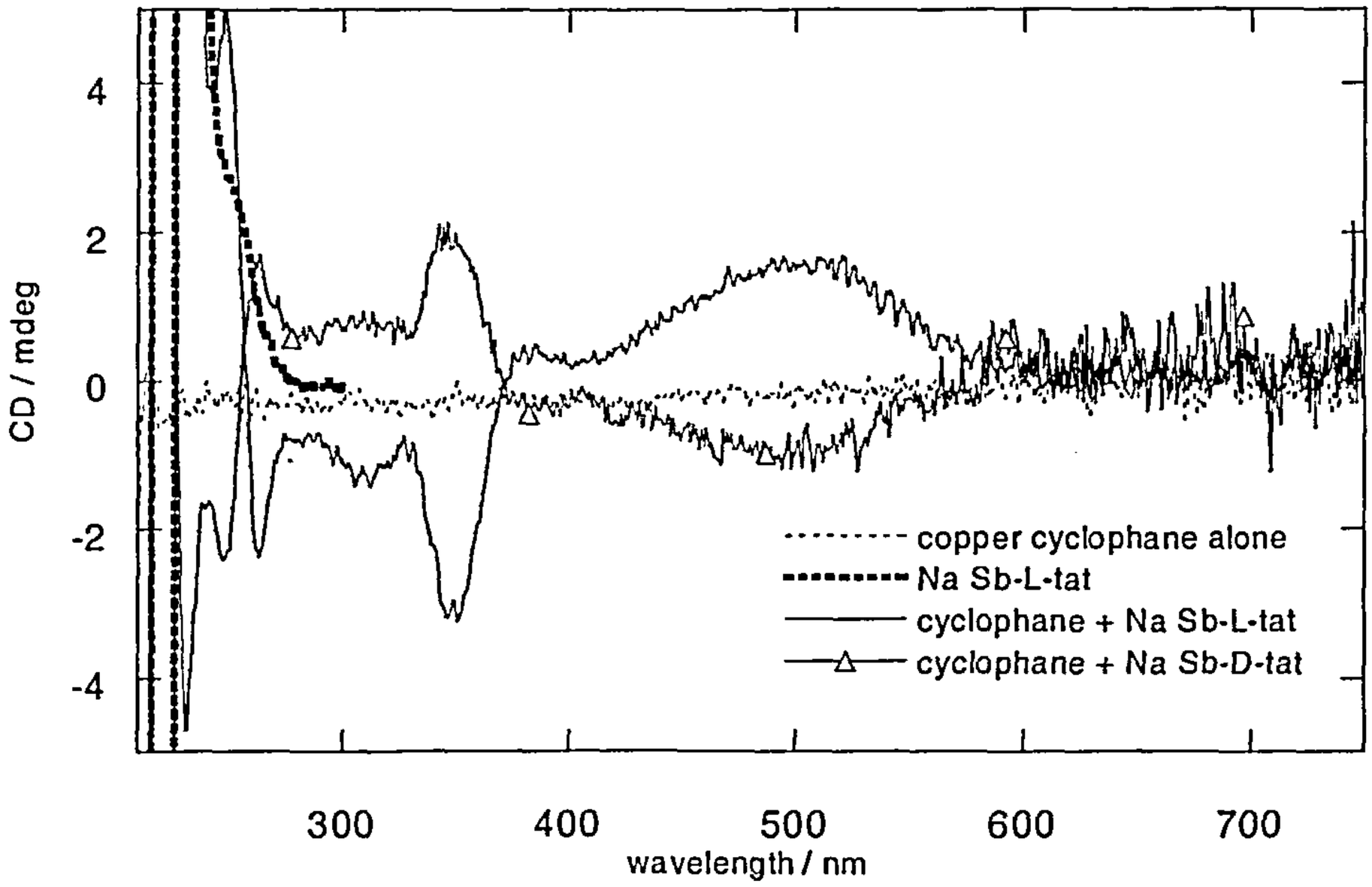

Figure. 4.28 *CD* spectra of the interaction of the D- and L- enantiomers of sodium antimonyl tartrate with a methanolic solution of the $[Cu_2L^1_2]^{2+}$ metal complex. The synthesised D-enantiomer[59] is not as soluble as the L-enantiomer in MeOH hence it exhibits a smaller signal.

Proton NMR investigations

Preliminary proton NMR studies confirmed that NaSb-L-tat interacts with the helix of the box:helix, through the splitting of its phenyl helix signals and an increase in the ratio of the helix:box.

A proton NMR study over [1:0–1:4] copper cyclophane:NaSb-L-tat mixing ratios was set up. A known concentration and volume of the copper cyclophane was placed in an NMR tube and its NMR run; additions of NaSb-L-tat were then added directly into the NMR tube to give [1:0.5]; [1:1]; [1:2]; [1:3] and [1:4] cyclophane:NaSb-L-tat mixing ratios. Figure 4.29 shows the proton NMR interactions that occur on increasing the anionic tartrate concentration. Figure 4.29(b) shows the aromatic portion of the NMR spectra of the copper metallo-cyclophane complex alone in deuterated methanol (CD_3OD). Figure 4.29(c) shows the effect of addition of the chiral NaSb-L-tat in a [1:1] cyclophane:NaSb-L-tat mixing ratio. Peak splittings suggest that the anion initially perturbs the helix of the box:helix mix. As the concentration of the anion is increased up to a [1:4] cyclophane:NaSb-L-tat ratio, an interaction with the box imine peaks is also seen (Figure 4.29(d)).

Thus, the helix:box metallo-cyclophane is in equilibrium between helix and box under normal circumstances and the Δ and Λ helices also exchange. Addition of the chiral anion shifts the equilibria to favour one enantiomer of the helix over the other enantiomer and the box. The integrals suggest that the equilibrium of the copper cyclophane, which is initially ~[2:1] helix:box is pushed to [3:1] in the presence of the tartrate.

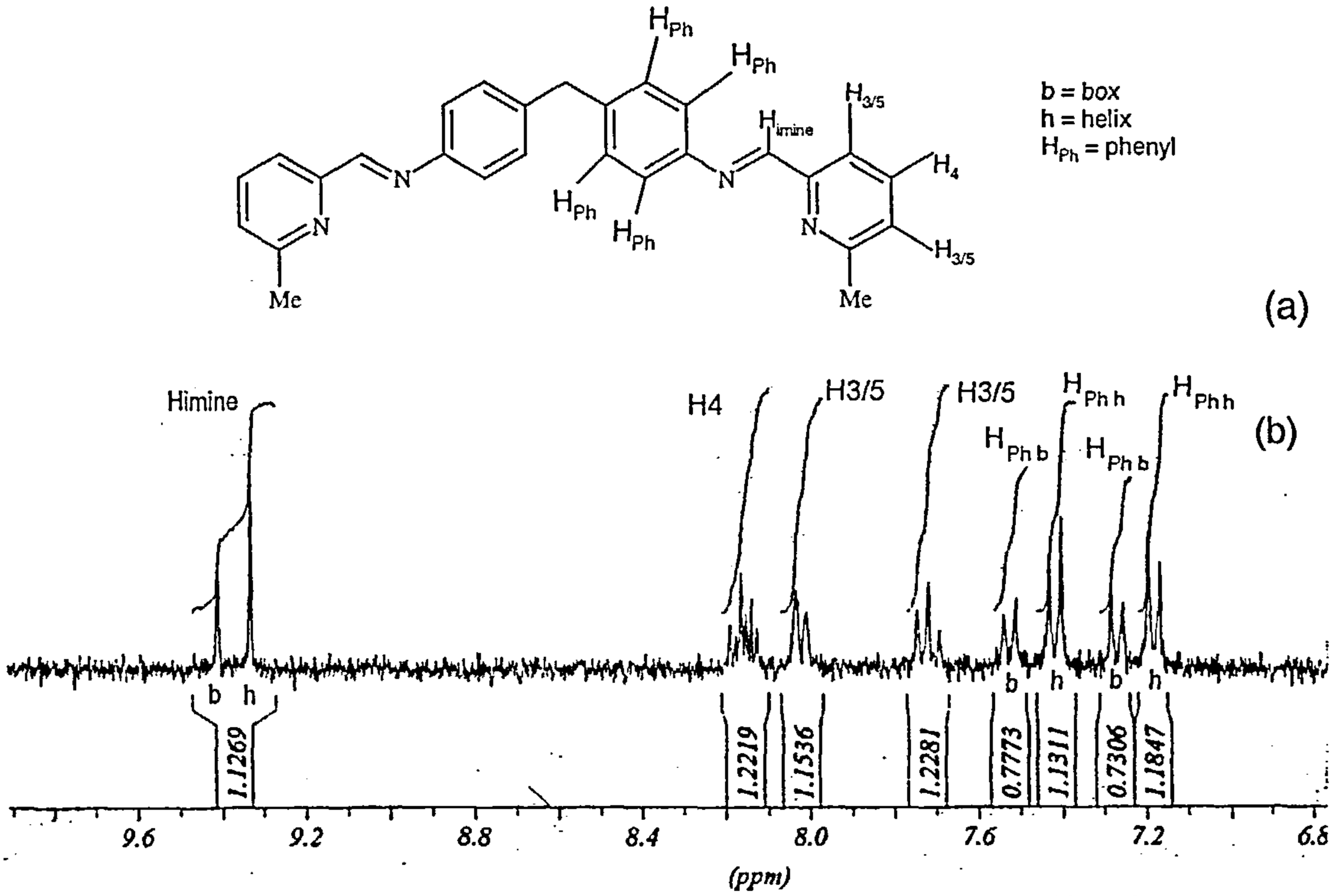

Figure 4.29. (a) NMR assignments of L^1 of the copper cyclophane; (b)The aromatic portion of the copper cyclophane (box-helix) spectra mix alone [1:0] in deuterated methanol (d^3 MeOH); (c) At [1:1] cyclophane: NaSb-L-tat, see splitting of the H phenyl helix assigned peaks and the H imine helix peak, (d) At [1:4] see the splitting of the Himine box and helix peaks, broad H4 and H3/5 and the separation of H phenyls of the *different helices and the box. NMR spectra were* recorded on a 300 MHz Bruker FT-NMR with 128 scans

The splittings observed are most dramatic for the phenyl and imine resonances, the CH_2 resonances are also perturbed (Figure 4.30) whereas the methyl group resonances are unchanged, implying that the chiral anion interacts with the metal complex in the perturbed region of the structure.

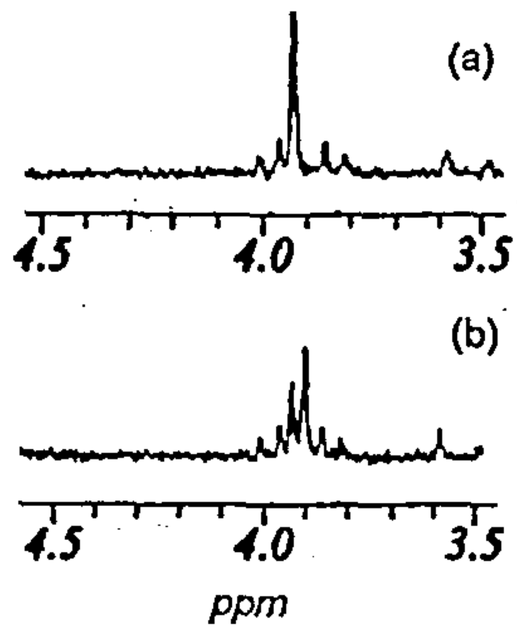

Figure 4.30 The CH_2 group resonances of the copper cyclophane box:helix mixture in d^3 MeOH (a) alone and (b) on interaction wih NaSb-L-tat, the CH_2 resonances also show splitting.

Proton NMR titration experiments set up to approximately determine the interactions of both enantiomers of antimonyl tartrate with the copper cyclophane over time in deuterated methanol, showed that the interactions are immediate with no big change over the space of 24 hours (data not shown). The solutions are a deep red in colour. Over the period of a week, however, the deep red solution containing the L anion eventually becomes colourless with the precipitation of a dark red crystalline solid.

Specific interaction investigation

To determine whether the interaction was due to the replacement of the tetrafluoroborate salt with the tartrate anion, interactions with other chiral tartrates such as sodium L-lactate, potassium L-tartrate, dibenzoyl-L-tartrate were examined. For each of these anions, no *CD* signal was seen, so the isolated tartrate portion plays no part in resolution rather it is the antimonyl complex that does. To investigate whether the Na^+

ions were interacting with the N atom binding sites, a proton NMR titration of sodium acetate CH_3COONa with the copper cyclophane in CD_3OD was examined. This showed no NMR interaction. KSb-D-tat is not very soluble in methanol but also provides a *CD* signal on mixing with the copper cyclophane. The cationic metallo-cyclophane must be sensitive to the shape of the sodium antimonyl tartrate dianion. This is analogous to the fact that unsaturated tris-chelate complexes can be resolved by antimonyl tartrate, whereas the saturated $[Co(ethylenediamine)_3]^{3+}$ can be resolved by barium tartrate, but not NaSb-tat.

4.4.2 Crystal structure

To try to examine the interaction in more detail, crystallisation was attempted. The copper cyclophane was mixed with NaSb-L-tat in acetonitrile and benzene diffused into the solution. Unfortunately the crystals obtained proved not to contain the chiral anion. The tetrafluoroborate salt that resulted (Figure 4.31) was similar to the previously characterised hexafluorophosphate salt (see Figure 4.16), although the crystal packing was quite different. A solvent molecule was present in the cavity. The X-ray crystal data can be found in Appendix 4.3.

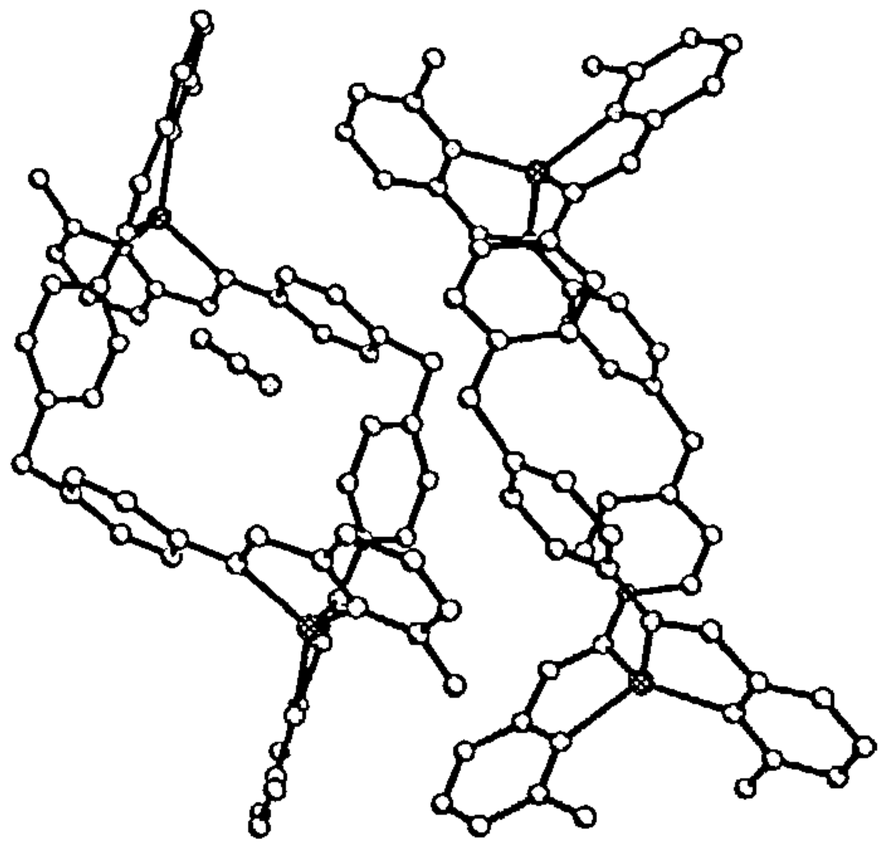

Figure 4.31 *Crystal structure* of the copper BF_4 cyclophane formed. Two non-identical but very similar boxes were found in the unit cell.

4.4.3 Summary

The cationic copper metallo-cyclophane has been shown to interact with chiral anionic sodium antimonyl tartrate showing its possible potential as a probe for certain types of chiral carbonyl compounds. The dianion antimonyl tartrate has been shown capable of resolving the box-helix mix of the cationic copper cyclophane by inducing helix formation.

4.5 Conclusion

The mechanism of action of the interaction of dmb with the copper(I) metallo-cyclophane complex is still not understood. Although binding occurs, the box does not bind dmbs in its cavity, it seems that the box cavity is not large enough to accommodate the substrates fully. This is addressed in section 4.6. The metallo-cyclophane, however, has been shown to interact with chiral anionic antimonyl tartrate leading to an excess of one helix over the other and the box.

4.6 Redesign

In this section, the design and synthesis of a novel longer asymmetric ligand (L^2) (Figure 4.32) capable of a facile one pot self-assembly into a supramolecular cyclophane structure is presented. L^2 has been designed such that one side is longer than the other; this change should produce a rectangular cyclophane structure with a larger cavity than that formed with L^1. The length of a benzene ring is 5.2 Å. The original copper and silver cyclophanes investigated were synthesised using L^1 having dimensions approximately 7 Å × 7 Å (length × width). With L^2 the metallo-cyclophane structure should have dimensions of approximately 11 Å × 7 Å. This metallo-

cyclophane should have the space to hold aromatic substrates comfortably inside its cavity. The asymmetry of the ligand may also disfavour helicate formation possibly resulting in one species in solution.

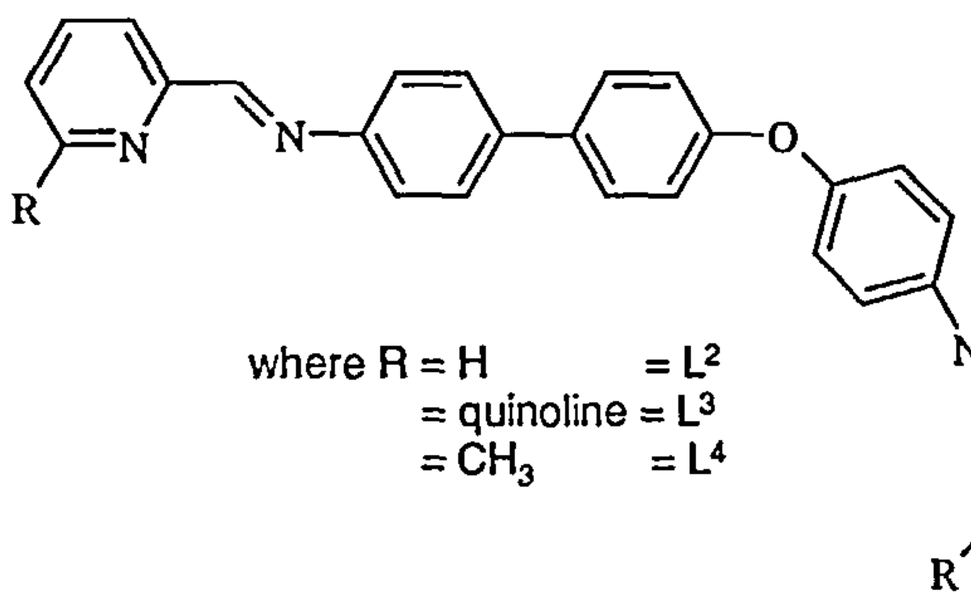

where R = H = L^2
= quinoline = L^3
= CH_3 = L^4

Figure. 4.32 The asymmetric Ligand 2, L^2, and its variations: Ligand 3 (L^3) and Ligand 4 (L^4)

The asymmetry of the ligand complicates the synthetic preparation of L^2 compared to that for L^1. The basic structure of L^2 is composed of a biphenylene group attached to a phenylene group via a bridging oxygen spacer. Variations using this basic structure are also presented as is the attempted extension of the ligand using a –(OCH_2)– spacer group in place of the oxygen.

4.6.1 Novel ligand synthesis

The asymmetry of L^2 and introduction of a bridging oxygen provide a challenge to ligand synthesis when compared to the simplistic synthesis of L^1. Scheme 4.1 outlines the synthetic route that has been developed to reach L^2. Using commercially inexpensive starting materials, the synthesis reported herein is a modification of numerous literature synthetic preparations.[60-69]

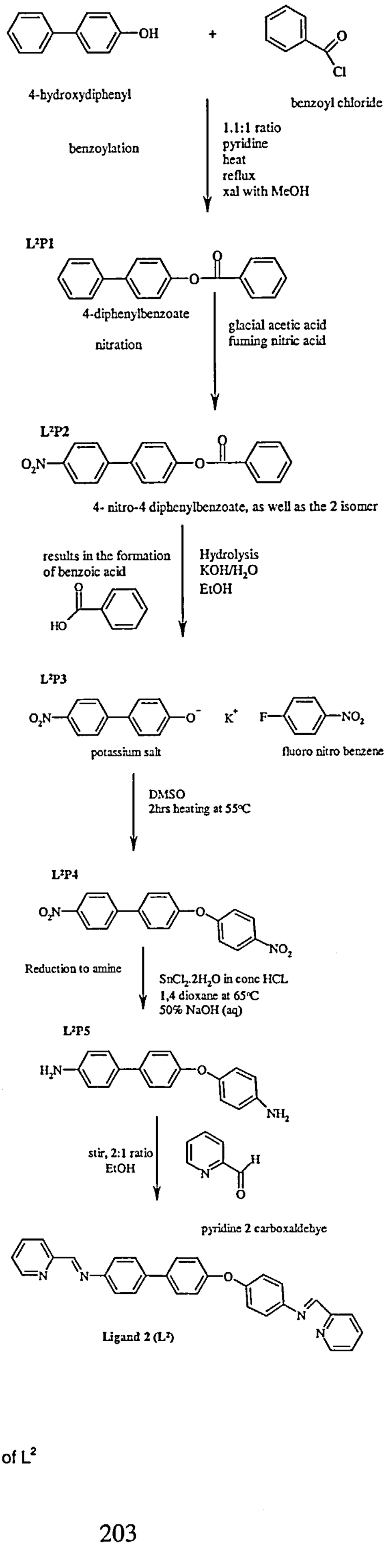

Scheme 4.1 Six synthetic preparation steps of L^2

Scheme 4.1 illustrates the five steps that are necessary (each step denoted precursor 1 (P1), step 2 precursor 2 (P2) *etc.*) in order to attain the diamino precusor ligand $H_2N–C_6H_4–C_6H_4–O–C_6H_4–NH_2$ (L^2P5). This is not commercially available but its synthesis is documented [60–64] as are those of L^2P3 and L^2P4 [65–66] *i.e.* $O_2N–C_6H_4C_6H_4–OH$. These are discussed in more detail in section 4.6.2.

L^2P5 can be used in the sixth step to synthesise the imine ligand L^2. Using Hannon's method,[1] mixing the commercially available 2-pyridine carboxaldehyde with L^2P5 results in the formation of L^2 in high yield. An advantage of this synthetic route is that other than recrystalisation, purification of the compound at each stage is not necessary. Thus time-consuming column chromatography can be avoided.

4.6.2 Ligand precursor synthesis

The synthesis of L^2 is outlined in the following sections:

Ligand 2, precursor 1 synthesis (L^2P1)

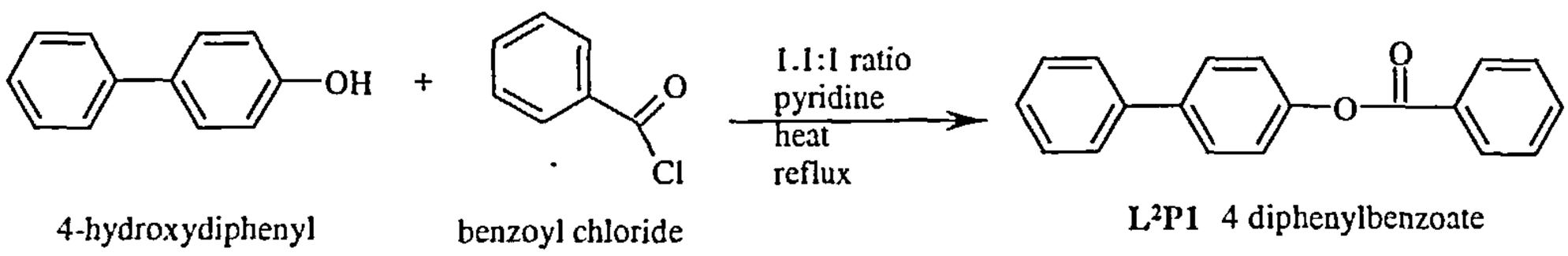

Scheme 4.2 Benzoylation of starting materials to form L^2P1

The first step is the formation of 4-diphenylbenzoate [61–63] through the nucleophilic substitution (*i.e.* the benzoylation) of the hydroxy group of 4-hydroxydiphenyl. Scheme 4.2 outlines L^2P1 synthesis using commercially available 4-hydroxydiphenyl. The proton NMR of L^2P1 in $CDCl_3$ was not easily assignable but the expected number and pattern of resonances were found.

Ligand 2, precursor 2 synthesis (L^2P2)

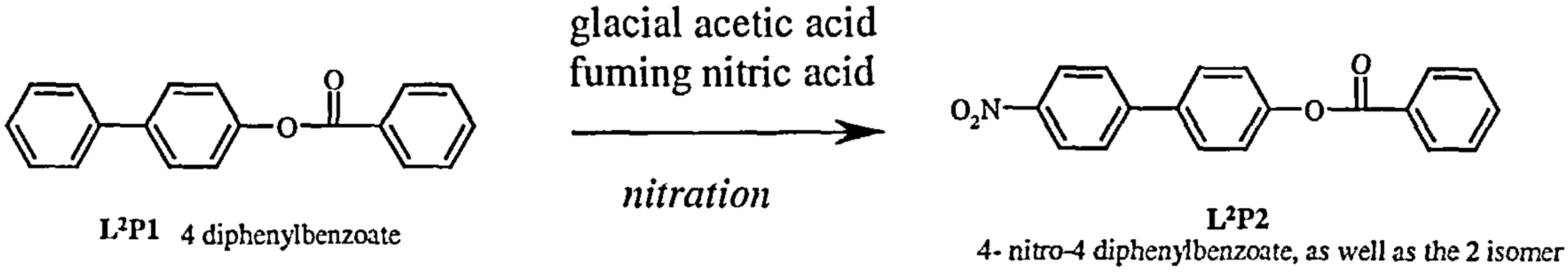

L^2P1 4 diphenylbenzoate

L^2P2
4- nitro-4 diphenylbenzoate, as well as the 2 isomer

Scheme 4.3 Nitration of L^2P1 to form L^2P2 using the Jones and Chapman preparation [64]

The second step involves the nitration of the 4-diphenylbenzoate in the 4′ position (see scheme 4.3). There are numerous preparations for the nitration of 4-phenylbenzoate.[63–64] Here the Jones and Chapman method using fuming nitric acid and glacial acetic acid was used.[64] The 4-diphenylbenzoate undergoes electrophilic substitution to form 4′-nitro-diphenyl benzoate and the 2- nitro compound with the 4′- the predominant species in a 4:1 ratio.

The benzoyl introduced in the previous step is a deactivating group, which reduces the activity of the OH group on the phenyl ring to which it is attached so that substitution does not occur on that phenyl ring. Due to the ortho/para directing effect of the phenyl ring containing the deactivating substituent (and its affect on the connecting ring), subsequent substitution takes place on the connecting phenyl ring in predominantly the 4′- position (as well as in the 2′ position).[64] The 4′-nitro-4-diphenylbenzoate is the least soluble of the isomers and it precipitates out (the 2′ nitro ester is more soluble and remains in solution).

An advantage of this reaction is that it does not require extensive purification or columning. However it was found that using larger quantities of starting material leads to a lower yield. The proton NMR in $CDCl_3$ was not easily assignable but the integrals do match the expected number and pattern of resonances.

Ligand 2, precursor 3 synthesis (L^2P3)

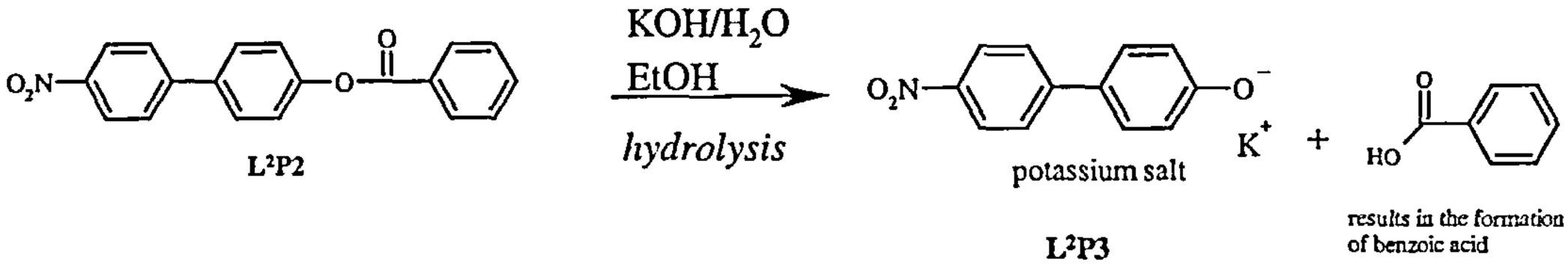

Scheme 4.4 Hydrolysis of L^2P2 to give the potassium salt of L^2P3 [64]

The third step involves the hydrolysis of 4-nitrodiphenylbenzoate to form L^2P3, [63,64] the potassium salt of ($HOC_6H_4C_6H_4N_2O$) (see scheme 4.4). Benzoic acid is a side product formed in the process, however there was no need to purify L^2P3. If needed the potassium salt of the complex can be dissolved in hot water and acidified, resulting in a yellow solid of $HOC_6H_4C_6H_4NO_2$. This ligand can also be formed using a range of different synthetic methods. [65,66]

Ligand 2, precursor 4 synthesis (L^2P4)

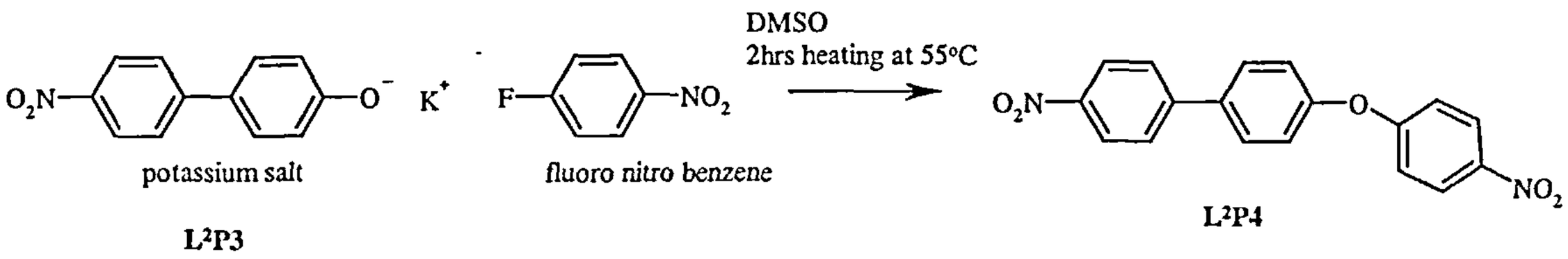

Scheme 4.5 Formation of the basic ligand L^2P4 structure using a modified version of Wilcox's synthesis [67]

The fourth step involves the reaction of L^2P3 with *para*-fluoronitrobenzene in DMSO leading to the formation of the dinitro compound, [67] via an SN_2 reaction. This step is a modified version of Wilcox's synthesis [67] where 4-cyanophenol was reacted with 4-fluoro-1-nitrobenzene (under the conditions outlined in Scheme 4.5, *i.e.* KOH, DMSO, 55°C) resulting in the p-nitrophenylether in a 98% yield.[67]

The Wilcox approach was chosen as it is synthetically simpler and results in a larger yield compared to a number of other methods.[60,68,69] For instance Steller *et al.* used a larger number of steps to achieve a 28% yield.[68] Rarick *et al.*[69] used similar materials (KOH, phenol and p-fluoronitrobenzene), but a different synthetic route whereby the solution was heated to 160°C for 30 minutes. The mixture was then poured into dilute NaOH and solid 4-nitrophenylether collected by filtration affording a 92% yield. Other similar methods include Acordia and Scarlatta who have suggested solid-state fusion, heating in an autoclave at 230°C.[60] The modified Wilcox approach results in a 95% yield of creamy white square-like crystals of L^2P4 ($O_2N–C_6H_4C_6H_4–O–C_6H_4–NO_2$).

Ligand 2, precursor 5 synthesis (L^2P5)

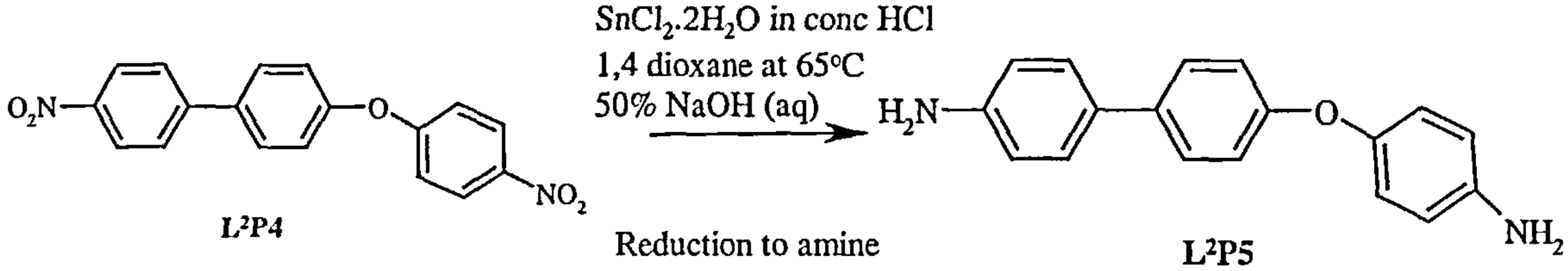

Scheme 4.6 Reduction of L^2P4 using the method set out by Arcordia and Scarlata[60,70]

The fifth step (L^2P5) involves the reduction of the nitro groups to form the di-amino L^2P5. Care has to be taken to ensure that the reduction is gentle enough to retain L^2P4 structure. Reduction of L^2P4 with stannous chloride leads to the L^2P5 [60,70] (see scheme 4.6) in 69% yield.

4.6.3 Ligand synthesis (L^2, L^3, L^4 and L^5)

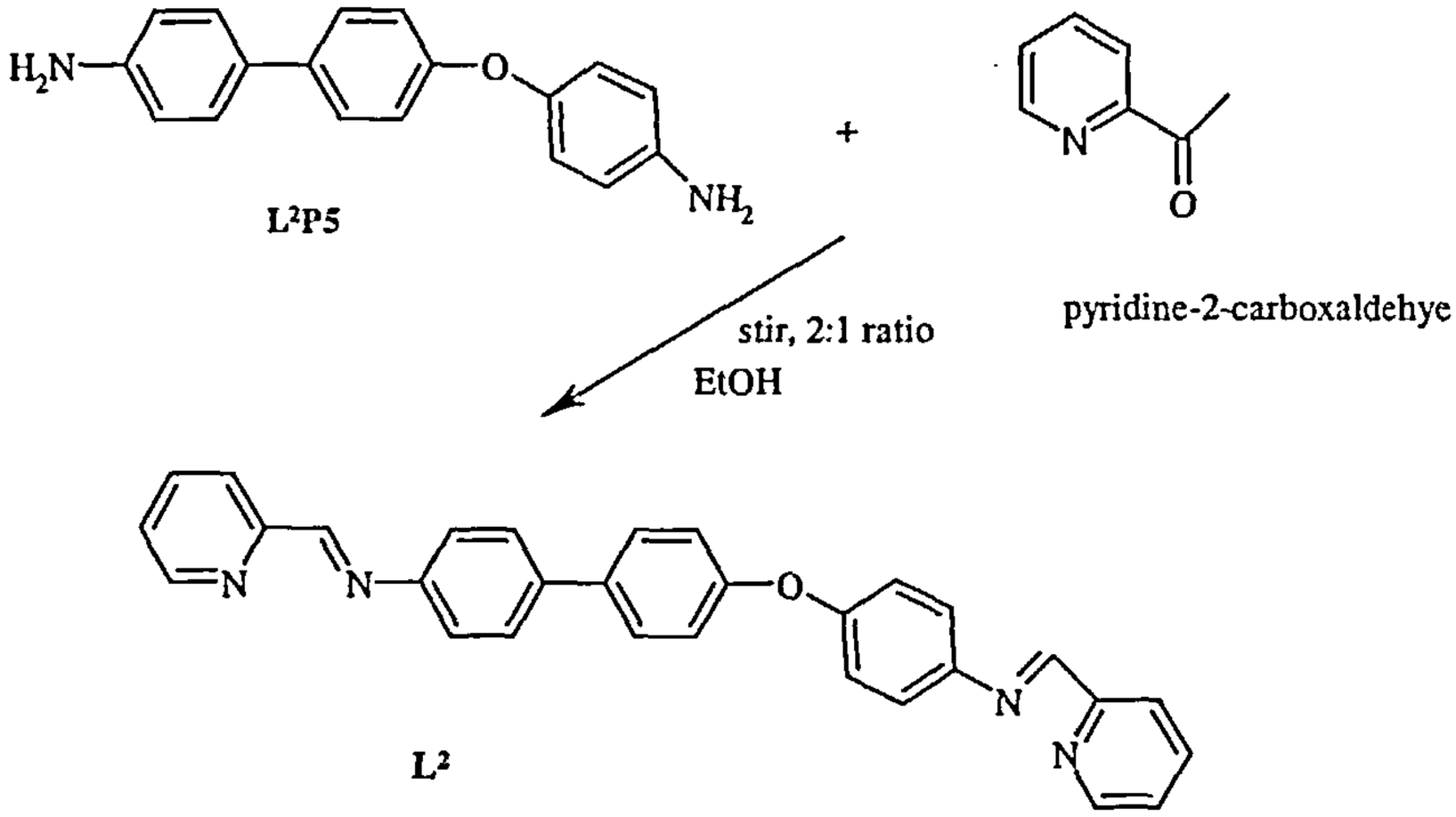

Scheme 4.7 Condensation reaction, the preparation of L^2 using Hannon's self assembling method [1]

The imine ligand L^2 can be formed by mixing two equivalents of pyridine-2-carboxaldehye with one equivalent of L^2P5 in ethanol and stirring under dintirogen for 24 hours. See Scheme 4.7. A bright yellow solid, L^2 was isolated by filtration under vacuum affording a 89% yield. The ligand is formed via a condensation reaction where the two molecules combine to form a third molecule with the loss of water.

Variations of L^2 can be synthesised by mixing L^2P5 with appropriate aldehydes. Quinoline-2-carboxaldehyde ligand has been used to form L^3 and 6-methylpyridine-2-carboxaldehye to form L^4 (see Figure 4.32)

The ^1H NMR of L^2 in deuterated chloroform was not easily assignable, its ^1H NMR in deuterated DMSO was also not easily assignable but the expected number and pattern of resonances were found. L^2, L^3 and L^4 were all found to contain traces of starting material (SM) of L^2P5 and the aldehyde used.

Extension of ligand L^2

The incorporation of a spacer –(CH_2)– group at the bridging oxygen site was also attempted, the new extended ligand denoted L^5.

L^2P3 can be used in the formation of L^5. In a similar fashion to the L^2P4 synthesis (scheme 4.8), L^2P3 was reacted with commercially available 4-nitrobenzylbromide to successfully form L^5P4, the nitro complex.

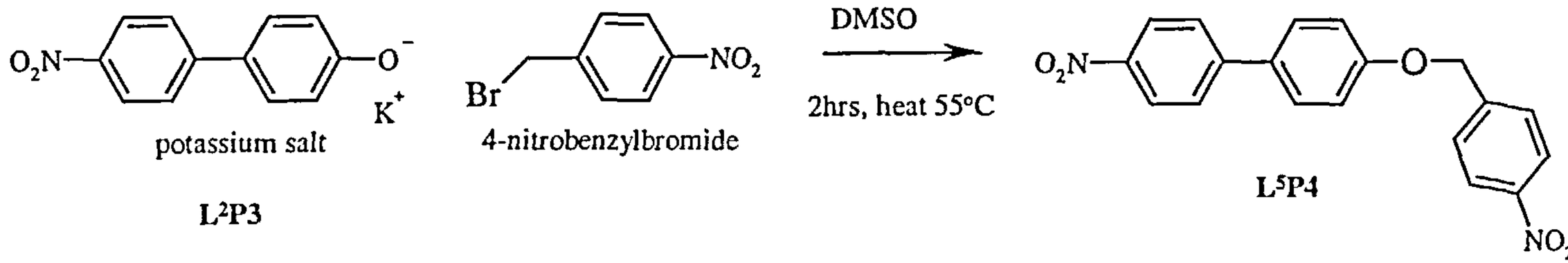

Scheme 4.8 Preparation of L^5 using L^2P3 to form L^2P4

However, using the reduction method outlined in Scheme 4.6, results in the break up of the ligand (see Scheme 4.9). The reduction method is too harsh for this compound so the synthesis was not pursued further (see section 4.6.5).

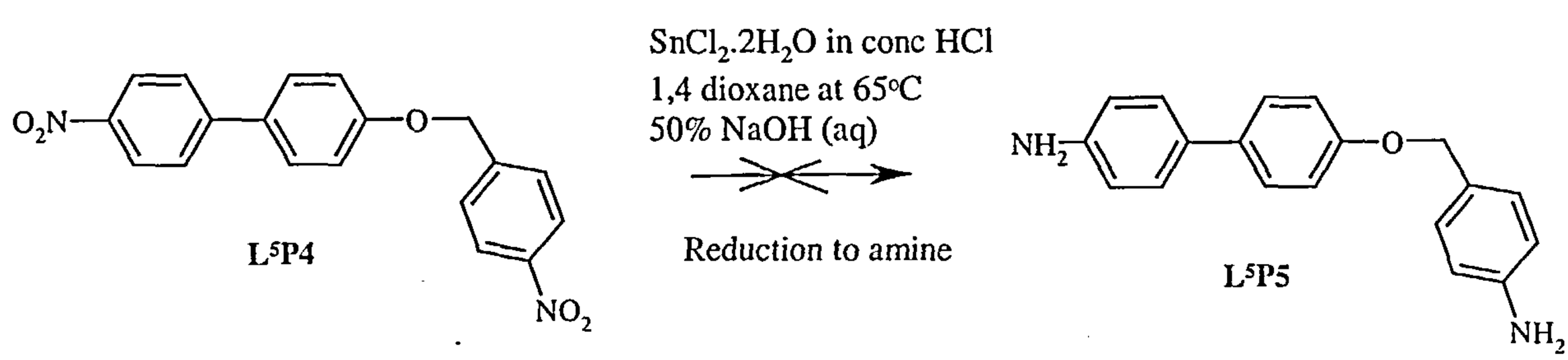

Scheme 4.9 Failed reduction step to the diamino complex

4.6.4 Metallo-cyclophane formation with L^2 and L^3

The reaction of L^2 and L^3 with tetrahedral metal ions, copper(I) and silver(I) as described[1] leads to the synthetically simple formation of novel dimeric supramolecular metallo-cyclophanes of the structure $M_2L_2[X]_2$ (where X = anion) (see experimental section).

The reactions of L^2 and L^3 with silver(I) acetate in methanol gave rise to dark yellow solutions, which on addition of methanolic hexafluorophosphate (PF_6) or

tetrafluoroborate (BF_4) salts precipitate dark yellow complexes. One of two methods can be used: refluxing for one hour, or stirring under N_2 for a few hours before addition of the methanolic salt. The latter method was found to result in larger and purer yields and was therefore used a majority of the time. Where reactions did not proceed then refluxing (a harsher method) or a combination of the two methods (refluxing followed by stirring) was then employed.

In order to remove impurities from the silver complexes, it was found that if the complex was dissolved in dichloromethane and filtered through a pasteur pipette packed with celite and then reduced to dryness under vacuum resulted in bright yellow silver(I) complexes containing little or no SM. Numerous salts of the complexes $[Ag_2L^2{}_2][X]_2$ of L^2 have been made including the BF_4 salt (formed by stirring), OTf (SO_3CF_3, trifluoromethanesulfonate) and CO_2CF_3 (trifluoracetate) (formed by stirring for 2h followed by refluxing for a further 2h). However, all contain traces of starting materials (by NMR) and were therefore not characterised.

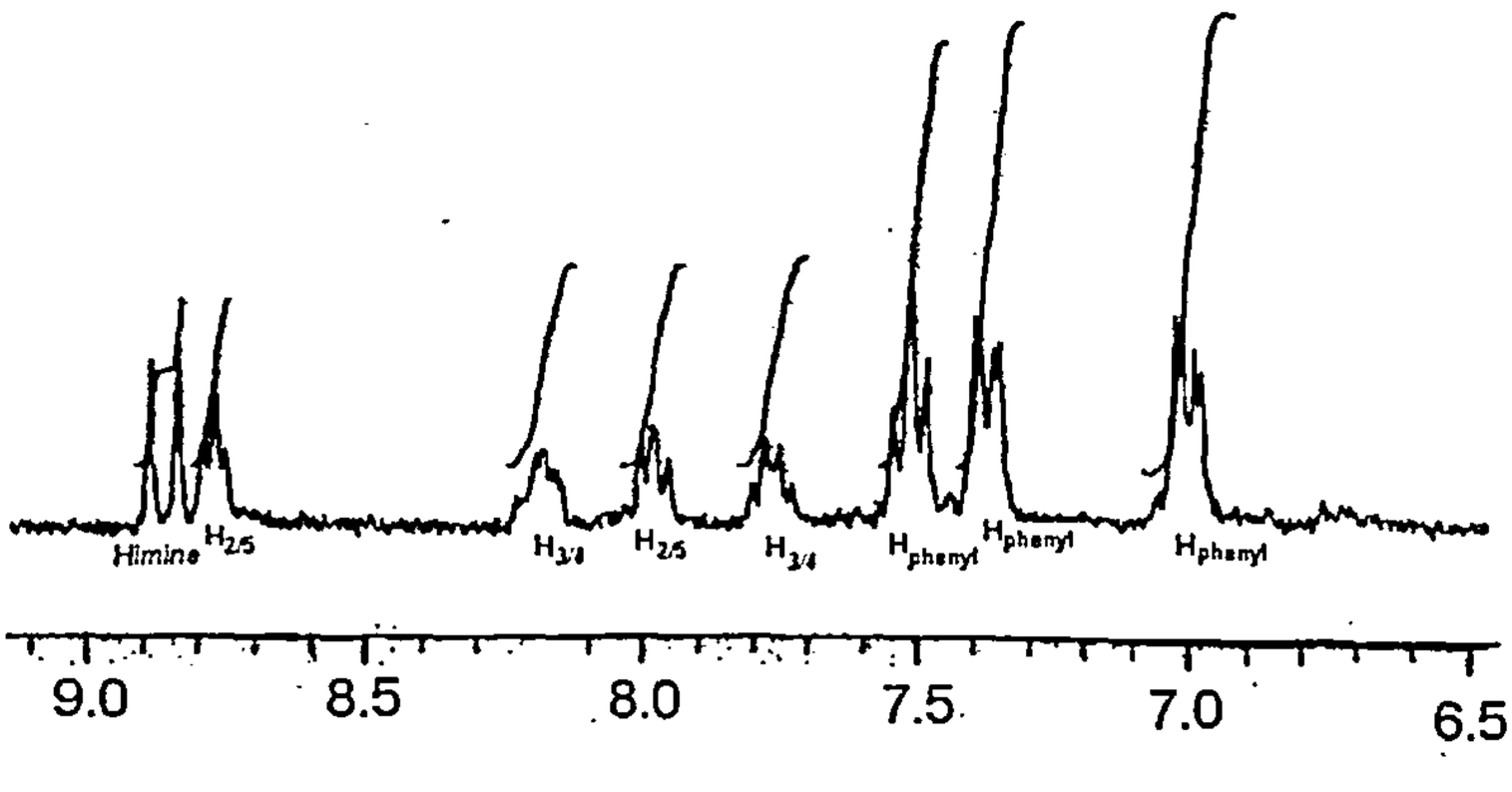

Figure 4.33 Proton NMR of $[Ag_2L^2{}_2][PF_6]_2$ in CD_2Cl_2 solution

The proton NMR of the silver cyclophane, $[Ag_2L^2{}_2][PF_6]_2$ in deuterated dichloromethane (CD_2Cl_2) at room temperature (Figure 4.33), however, was sufficiently pure enough to allow complex characterisation (see experimental section for assignments). At low temperature, broadening of the peaks in the proton NMR is seen,

(low temperature NMR were carried out by NMR operator Dr. Adam Clarke). Low temperature proton NMR of complexes in CD_3CN and CD_2Cl_2 that were synthesised using method 1 and not purified using dichloromethane show the presence of both starting materials and silver complex. Acetonitrile readily dissolves both complex and starting materials, hence its complicated NMR spectra. The characterisation data provides proof of L^2 formation and characterisation using proton NMR. The mass spectrum (+FAB) of $[Ag_2L^2{}_2][PF_6]_2$ confirms the presence of complex exhibiting peaks for $M_2L_2PF_6$ and M_2L_2 consistent with the formation of a dimeric species.

The proton NMR of the silver cyclophane, $[Ag_2L^3{}_2][PF_6]_2$ (the metallo-cyclophane complex formed using L^3), in CD_2Cl_2 at room temperature, was also pure enough to allow complex characterisation (see experimental section for assignments). The integrals indicate one species in solution at room temperature. The Himine (denoted H_a in the experimental section) proton resonances have a coupling constant (J) of 7.4 Hz corresponding to a Ag----Himine coupling interaction. Low temperature proton NMR shows that the size of the Ag----Himine coupling is unaffected by temperature. The proton NMR exhibits one species in solution, which shows broadening at low temperatures. This with a 2D ^1H-^1H COSY (correlated spectroscopy) NMR experiment (COSY assignments can be found in the experimental section) have been used to confirm the structure of the ligand (L^3) and hence the PF_6 salt complex. The data strongly suggests that there is only one complex species in solution. Synthesis of the equivalent BF_4 salt results in broad peaks that cannot be clearly assigned.

Reactions of L^2 and L^3 with $[Cu(MeCN)_4]^+$ salts in methanol result in red-brown solutions from which red-brown hexafluorophosphate or tetrafluoroborate salts may precipitate. The spectra of both L^2 salts exhibit broad complex peaks as well as starting

material; as a result the integrals are unreliable and the proton NMR spectra of both salts in CD_3CN or CD_2Cl_2 are not clearly assignable. Low temperature proton NMR in deuterated acetonitrile of both salt complexes (from 273 K to 193 K) shows the development of sharper peaks with the integrals eventually suggesting one species (*i.e.* 22H) as well as SM. The spectra of the L^3 salts are also broad and not readily assignable. The copper spectra have a tendency to be broad.

Complexation was not attempted using L^4 due to its low yield. The interaction of L^2 with octahedral iron(II) was also attempted, a dark purple complex of low solubility formed but was not investigated further.

Unfortunately, all attempts to obtain X-ray quality crystals of L^2, L^3 and their complexes proved unsuccessful.

4.6.5 Conclusion

Novel asymmetric ligands (L^2, L^3 and L^4) capable of a facile one pot self-assembly into supramolecular metallo-cyclophane box structures in solution have been synthesised and characterised. The silver PF_6 metallo-cyclophanes of L^2 and L^3 have also been synthesised and characterised

An advantage of this synthetic method is the ease of complex formation in relatively high yields as well as the use of cheap commercially available starting materials. A disadvantage of the ligand synthesis is that attempts to make larger amounts using larger quantities of reagents resulted in lower yields than if smaller amounts are used.

The main problem encountered is the presence of starting materials in some of the products. Although, relatively pure silver PF_6 complexes of L^2 and L^3 can be synthesised, it is obvious that a revised methodology is needed to provide consistently

pure complexes. As acetonitrile dissolves all complex and starting materials, perhaps complexation should be attempted in this solvent and not methanol.

Further work

Further work could involve the clean up of the ligands and complexes by: (i) the use of acetonitrile instead of methanol in complexation as acetonitrile seems to dissolve both starting material and ligand and complex as evidenced by proton NMR. (ii) the use of a modified version of Hannon's simple self-assembling method that involves the use of molecular sieves [71] to provide cleaner end products. (iii) Bellamy *et al.* have reported a mild, selective, inexpensive and general method for the reduction of nitro groups to amines using tin chloride in alcohol or ethyl acetate.[72] A part of further work could include an attempt at the reduction of L^5P4 using this milder reduction method.[72]

These suggestions were not attempted due to time constraints and also as the complexes could be purified as described here.

Further work in this area would also be to investigate the binding of guests to these species.

4.7 Experimental Section

^1H NMR spectra were recorded on 250 MHz, 300 MHz Bruker FT-NMR machines. Low temperature ^1H, and room and low temperature ^{19}F and ^{11}B NMR were conducted by NMR operator Dr. A. Clarke on the 400 MHz Bruker FT-NMR machine at the University of Warwick. Mass spectra were obtained from positive Fast Atom Bombardment (+ve FAB) conditions with 3-nitrobenzyl alcohol (NOBA) used as a matrix or Electrospray (ES) conditions using appropriate solvents. The Infra-Red (IR) spectra were recorded using KBr disks on a Perkin Elmer FT-IR Spectrometer (Paragon

1000), or alone on a Nicolet Avatar 320 FT-IR specac equipped with a Golden Gate accessory. Microanalyses (CHN) were conducted on a CHN CE440 Elemental Analyser by Warwick Analytical Services.

Ligand synthesis

L^2P1:

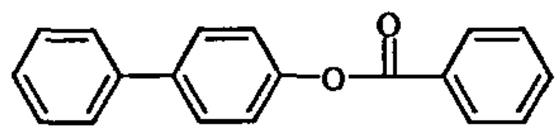

L^2P1 4 diphenylbenzoate

L^2P1 was prepared following the method of Hazlet *et al.*[61–63] 4-hydroxydiphenyl (5.136 g, 0.030 mol) was dissolved with stirring in a cooled solution of pyridine (100 cm^3) (in an ice water bath). The solution was held at this cooled temperature (~10°C) as benzoyl chloride (3.8 cm^3, 0.033 mol) was added in a 1:1.1 ratio with stirring. The mixture was then heated at 60°C for 30 minutes, refluxed gently for further 30 minutes, then was left to cool before treatment with water (in excess 100 cm^3) resulting in a white precipitate (water added with stirring until no more precipitate) and dilute HCl (20 cm^3). The white precipitate was then filtered under vacuum. Water was added to filtrate until no more precipitation was seen and that precipitate also collected. The white solid was then washed 5× with water, before being recrystallised from methanol (150 cm^3 per 2 g) and dried over P_2O_5 affording the fluffy white needle-like solid of 4-diphenylbenzoate (8.05 g, 93 %).

^1H NMR ($CDCl_3$): δ 8.23 (2H, d, J = 3.5 Hz); 7.63 (2H, d, J = 4.4 Hz); 7.59 (2H, d, J = 4.1 Hz); 7.54 (2H, d, J = 4 Hz); 7.48 (1H, dt, J = 1.7 Hz); 7.43 (2H, d, J = 2.9 Hz); 7.36 (1H, dt, J = 3.6 Hz); 7.29 (2H, d, J = 3.2 Hz); FAB +MS: *m/z* 275 [L^2P1+H]; IR (KBr)(cm^{-1}): 1732(s), 1280(s), 1234(m), 1194(m), 1169(m), 1087(m), 1064(m), 879(m);

818(w), 759(s), 704(s), 688(s); Found: C, 83.19; H, 5.18. Calc for L^2P1: $C_{19}H_{14}O_2$: C, 83.18; H, 5.15; mp: 149 – 150°C

L^2P2:

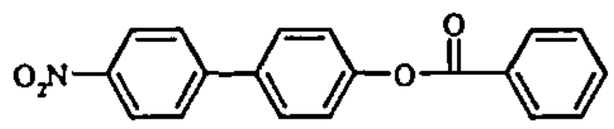

L^2P2

4- nitro-4 diphenylbenzoate

L^2P2 was prepared following the Jones and Chapman method. [64] L^2P1 (0.961 g, 3.5 mmol) was mixed with glacial acetic acid (8.5 cm^3). The suspension heated to 85°C – 95°C to ensure that all of L^2P1 dissolved to give a clear solution. If the solution is allowed to cool, the starting material will precipitate out. With the temperature maintained above 90°C, fuming nitric acid (2.4 cm^3) was added dropwise with stirring, the solution turned yellow and was left to cool, leading to the formation of a yellow precipitate. The precipitate was filtered by vacuum filtration, washed with water then methanol. The 2-nitro isomer could be isolated from the filtrate solution and the mother solutions.[64] The light yellow solid of 4-nitro-4-diphenylbenzoate (0.905 g, 81%) was dried over P_2O_5. Note: using larger quantities of starting material leads to less yield.

^1H NMR ($CDCl_3$):13H: δ8.27 (2H, d, J = 4.6 Hz); 8.22 (4H, m); 7.74 (2H, d, J = 4.4 Hz); 7.68 (2H, d, J = 4.4 Hz); 7.54 (1H, t); 7.36 (2H, d, J = 4.3 Hz); FAB +MS: *m/z* 320 [L^2P2 + H]; IR (KBr)(cm^{-1}): 1734(s), 1600(m), 1514(s); 1485(m); 1450(m), 1384(s), 1342(s), 1265(s), 1213(s), 1190(s), 1165(m), 1080(m), 1060(s), 1024(m), 1005(m), 858(m), 810(w), 790(w), 712(s)

L^2P3:

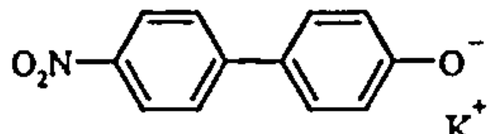

potassium salt

L^2P3

L^2P3 was prepared following the synthetic method laid out by Jones and Chapman.[64] L^2P2 (1.510 g, 4.7 mmol) was mixed with EtOH (40 cm^3), the yellow suspension then stirred to reflux before an aqueous solution of KOH (1.019 g in 7 cm^3) was added. The solution turning deep red immediately —showing rapid hydrolysis — and was left to reflux for a further 15 minutes to ensure hydrolysis was complete before being left to cool in ice overnight. Dark red blue-black crystals of L^2P3 formed were filtered under vacuum (0.828 g, 69%).

^1H NMR (CD_3CN): δ 8.23 (2H, d, J = 4.5 Hz); 7.79 (2H, d, J = 4.5 Hz); 7.59 (2H, d, J = 4.5 Hz); 6.89 (2H, d, J = 4.4 Hz); IR (KBr)(cm^{-1}): 1652(w), 1583(s), 1519(m), 1482(s), 1345(s), 1284(m), 1205(w), 1116(w), 836(m)

L^2P4:

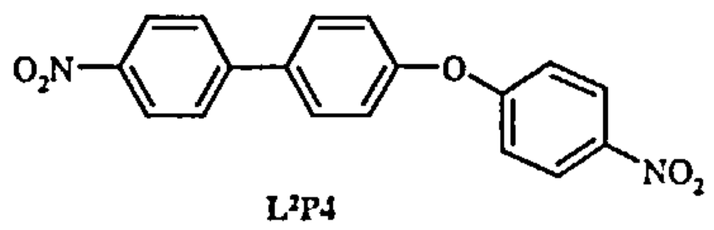

L^2P4

L^2 P4 was prepared following a modified version of Wilcox's synthetic approach.[67] The potassium salt L^2P3 (0.787 g, 3.1 mmol) was mixed in a 1:1 ratio with fluoronitrobenzene (0.436 g, 3.1 mmol) before DMSO (9 cm^3) was added. The dark red-purple solution was stirred with heating at 55°C for two hours. Over this time, the solution exhibited a colour change from dark purple to orange-red as a light yellow precipitate formed. The solution was then left to cool and crystallise out, filtered under vacuum to give cream coloured square-like crystals of L^2P4 (0.995 g, 95%), which

require no purification. (If the precipitate has a red/orange tinge, it is still wet with DMSO)

^{1}H NMR ($CDCl_3$): δ 8.30 (2H, d, J = 4.7 Hz); 8.24 (2H, d, J = 4.6 Hz); 7.73 (2H, d, J = 3.5 Hz); 7.68 (2H, d, J = 4.4 Hz); 7.21 (2H, d, J = 4.4 Hz); 7.09 (2H, d, J = 4.6 Hz); FAB +MS: m/z 336[L^2P4]; IR (KBr)(cm^{-1}): 1585(s); 1508(s); 1483(s); 1343(s), 1251(s); 1167(w); 1109(s); 1006(w); 881(m); 858(s); 840(s); 755(m)

L^2P5:

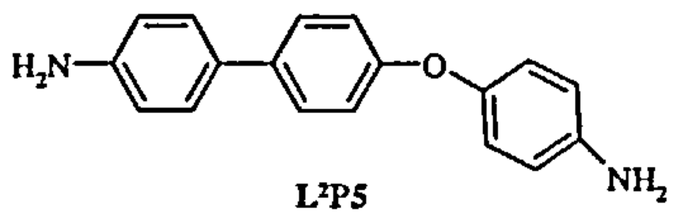

L^2P5

L^2P5 was prepared following the method of Acordia and Scarlatta. [60] L^2P4 (0.447 g, 3 mmol) was mixed with 1,4-dioxane (8.2 cm^3) and heated with stirring to 65°C. Once all L^2P4 was dissolved, (the solution turning yellow), a solution of tin chloride ($SnCl_2.2H_2O$) dissolved in concentrated HCl (2.213 g in 4.9 cm^3) (also known as stannous chloride) [60,70] was added dropwise over a 15 minute period, the solution was then left at 65°C for a further 2 hours.

On addition of concentrated HCl (in excess) to the solution, the white acidic protonated amine salt (NH_3^+) product was precipitated and collected by vacuum filtration. The salt was then dissolved in a little water before a chilled aqueous solution NaOH (50%) was added to make the solution strongly alkaline. The resulting white precipitate of L^2P5 that formed on cooling was filtered under vacuum and washed with water (can recrystallise from EtOH) (0.254 g, 69% yield).

^{1}H NMR (CD_3CN): δ 7.47 (2H, d, J = 3.3 Hz); 7.34 (2H, d, J = 4.4 Hz); 6.91 (2H, d, J = 4.5 Hz); 6.83 (2H, d, J = 4.5 Hz); 6.70 (2H, d, J = 3.3 Hz); 6.66 (2H, d, J = 3.5 Hz);

4.15 (4H, broad d); FAB +MS; *m/z* 276[L^2P5]; 552 [$L^2P5]_2$; IR (KBr) (cm^{-1}): 1612(m); 1508(s); 1494(s); 1244(s); 822(s)

Ligand 2 synthesis (L^2)

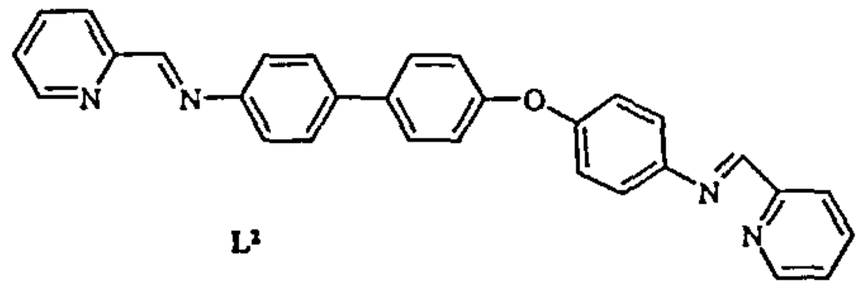

L^2

Pyridine 2-carboxaldehye (0.188 g, 1.75 mmol) was mixed with L^2P5 (0.243 g, 0.88 mmol) in ethanol (10 cm^3) with stirring under N_2 for 24 h. (L^2P5 sonicated to ensure dissolution). A bright yellow precipitate of L^2 formed which was filtered under vacuum and recrystallised from EtOH (0.330 g, 83%).

^{1}H NMR (DMSO): δ8.73 (m, 1H); 8.65 (t, 1H, J = 2.9 Hz, J = 1.8 Hz); 8.18 (2H, t, J = 3.5 Hz); 7.97 (2H, m); 7.74 (2H, dd, J = 1.2 Hz, J = 3 Hz), 7.55 (4H, m); 7.45 (4H, t, J = 3.5 Hz); 7.13 (2H, d, J = 4.4 Hz); 7.08 (2H, dd, J = 2.8 Hz, J = 2.59 Hz), 6.60 (2H, m); FAB +MS: *m/z* 455 [L^2H], 259 [$C_{18}H_4N_2$]; IR (solid)(cm^{-1}): 2358(m), 1576(m, broad), 1489(s), 1466(w), 1433(m), 1262(s, broad), 829(s), 775-600(w)

Ligand 3 synthesis (L^3)

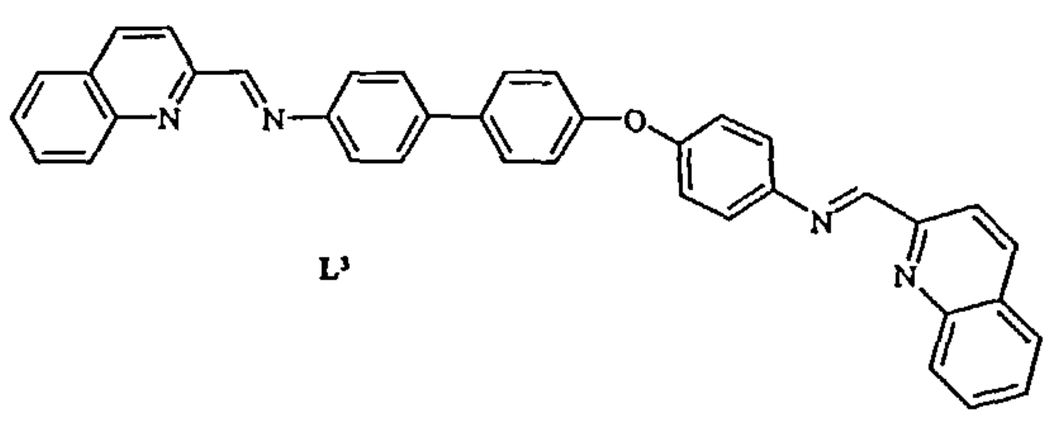

L^3

Quinoline 2-carboxaldehye (0.219 g, 1.39 mmol) was mixed with L^2P5 (0.133 g, 0.48 mmol) in EtOH (15 cm^3). The solution immediately turned bright yellow and was

left stirring under dinitrogen for 24h. The yellow precipitate of L^3 was filtered under vacuum (0.194 g, 73%).

^{1}H NMR ($CDCl_3$): not easily assignable, also contains starting materials (SM). FAB +MS: *m/z* 555 [L^3H]; IR (KBr) (cm^{-1}): 2359(s); 1623(m); 1594(m);1408(s); 1262(m); 834(s); 745(s)

Ligand 4 synthesis (L^4)

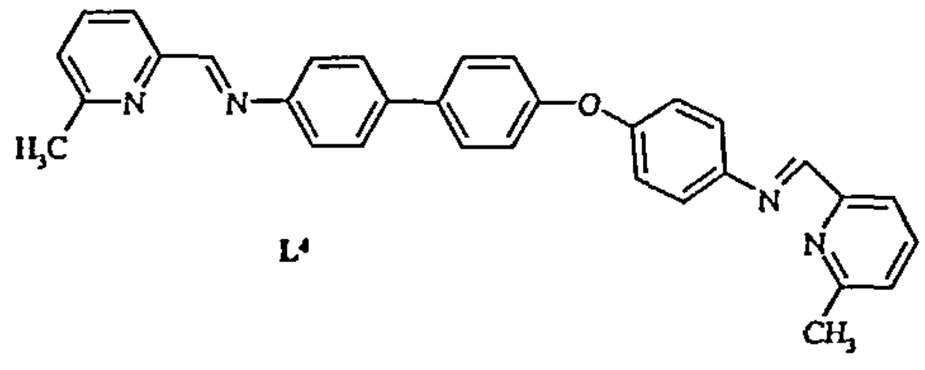

L^4

L^4 was prepared following Hannon's method.[1] 6-methyl pyridine 2-carboxaldehye (0.030 g, 0.24 mmol) was mixed with L^2P5 (0.032 g, 0.12 mmol) in ethanol (15 cm^3). This was left stirring under dinitrogen for 24h. The light yellow precipitate of L^4 was collected under vacuum filtration (0.015 g, 26%).

^{1}H NMR (CD_2Cl_2): H imine peak spliting, 2 species and SM (L^2P5 and aldehyde): δ8.62 (d, 2H, J = 1.3 Hz); (with secondary species at 8.62 (d)); 8.04 (t, 2H); 7.75 (td, 2H); 7.68 (mix, 4H); 7.39 (mix, 6H); 7.28 (dd,2H); 7.15 (q, 4H), 2.66 (s, 6H); FAB +MS: *m/z* 483 [L^4+ H].

Ligand L5 synthesis

L^5P4

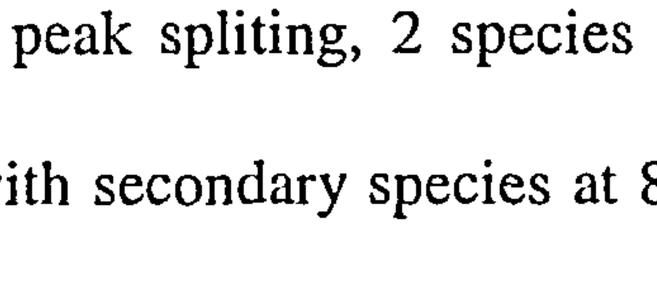

L^5P4

Using a modified version of Wilcox's approach.[67] L^2P3 (0.431 g, 1.7 mmol) was mixed with 1 equiv 4-nitrobenzylbromide (0.372 g, 1.7 mmol) to which DMSO (10

cm^3) was added. The resulting dark purple solution was then heated to 55°C. The solution gradually changed colour over a 15 minutes as a yellow precipitate formed, the solution was left stirring for a further 1.5h before it was left to cool in ice. A bright yellow crystalline solid of L^5P4 was filtered under vacuum (0.569 g, 95%), water was added to the filtrate to bring out more L^5P4.

^1H NMR ($CDCl_3$): δ 8.27 (4H, dd, J = 3.7 Hz); 7.68 (2H, d, J = 4.4 Hz); 7.63 (2H, d, J = 4.4 Hz); 7.59 (2H, d, J = 3.4 Hz); 7.07 (2H, d, J = 4.4 Hz); 5.24 (2H, s); FAB +MS: m/z 355 [L^5P3 + 5H]

Complexation synthesis using L^2

$[Ag_2L^2_2][PF_6]_2$.

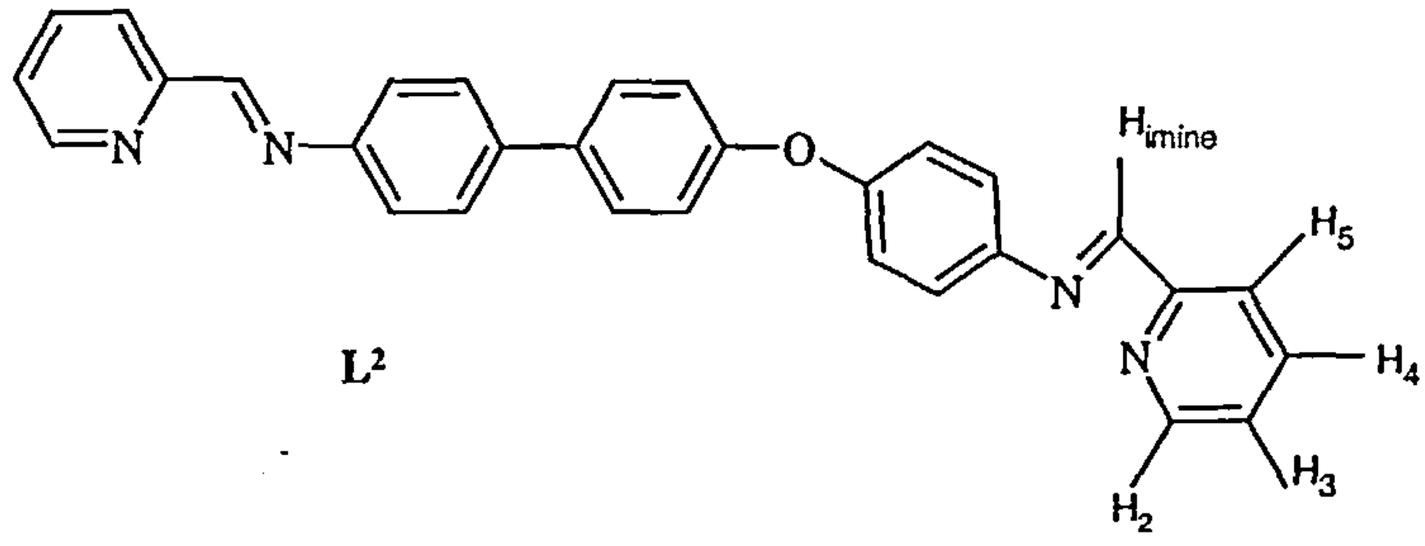

L^2

Method 1: The salt AgOAc (0.02 g, 0.043 mmol) and L^2 (0.007 g, 0.04 mmol) were heated to reflux in methanol (8 cm^3) for 1h. The reaction vessel covered in foil to exclude light. The solution was filtered through celite and treated with methanolic $[NH_4][PF_6]$ resulting in an immediate yellow precipitate, which was filtered under vacuum to yield the silver complex (0.031 g, 49%)

Method 2: The salt AgOAc (0.015 g, 0.088 mmol) and L^2 (0.030 g, 0.067 mmol) were stirred in methanol under dinitrogen for 3h. The dark orange solution was filtered through a pasteur pipette with cotton wool and celite, before treated with

methanolic $[NH_4][PF_6]$ resulting in a dark yellow precipitate of $[Ag_2L^2_2][PF_6]_2$ which was collected by filtration. (0.06 g, 67%)

^{1}H NMR (CD_2Cl_2) δ 8.87 (2H, d, H_{imine}, J = 6.4 Hz); 8.78 (2H, t, $H_{2/5}$, J = 2.6 Hz); 8.19 (2H, m, $H_{3/4}$); 7.99 (2H, t, $H_{2/5}$, J = 2.5 Hz, J = 3.9 Hz); 7.78 (2H, q, $H_{3/4}$, J = 2.9 Hz, J = 3.2 Hz); 7.52 (4H, t, H_{phenyl}, J = 3.5 Hz, , J = 4.4 Hz); 7.38 (4H, dd, H_{phenyl}, J = 3 Hz); 7.02 (4H, dd, H_{phenyl}, J = 2.8 Hz); FAB +MS: *m/z* 1272 [$M_2L_2PF_6$ + 3H]; 1126 [M_2L_2]

IR (solid) (cm^{-1}) 3380(w); 1684(w); 1590(w); 1489(m); 1242(m); 1170(w); 840(s); 774(w)

Other $[Ag_2L^2_2][X]_2$ complexes prepared include: BF_4 (67%) salt complex (using method 2). The AgOTf (56%) (OTf = SO_3CF_3, the trifluoromethanesulfonate salt) and the CO_2CF_3 (trifluoracetate salt) silver complexes were formed by stirring for 2h. followed by refluxing for a further 2h. But all of these contain traces of starting materials.

$[Cu_2L^2_2][BF_4]_2$

The salt $[Cu(MeCN)_4][BF_4]$ (0.025 g, 0.08 mmol) and L^2 (0.036 g, 0.08 mmol) was left stirring in methanol (10 cm^3) under N_2 for 24h. The resulting red solution was concentrated under vacuum; the resulting red precipitate was then filtered under vacuum (0.044 g, 47%).

FAB+MS: *m/z* 577 [M_2L_2-3H]; 603 [$MLBF_4$];870 [ML_2-2H]; IR (solid) 667-640(w);826(m); 1067(s); 1243(s); 1488(s); 1683-1593; 2388; ^{1}H NMR (CD_3CN) and (CD_2Cl_2) both unassignable, containing starting material and broad peaks, integrals unreliable. Low Temperature ^{1}H NMR (CD_3CN): as temperature decreases from 273K to 193K see the development of sharper peaks with the integrals eventually suggesting

one species (*i.e.* 22H) and SM. The proton NMR in CD_2Cl_2 exhibits broad peaks and does not yield much more information.

$[Cu_2L^2_2][PF_6]_2$.

The salt $[Cu(MeCN)_4][PF_6]$ (0.033 g, 0.089 mmol) and L^2 (0.037 g, 0.081 mmol) were stirred in MeOH (10 cm^3) under dinitrogen for 12h. The resulting red solution was concentrated and left to precipitate out before being filtered under vacuum. (0.03 g, 20%).

FAB +MS: *m/z* 577 $[M_2L\text{-}3H]$; 419 $[M_2(PF6)_2H]$; 663 $[MLPF_6]H$; IR(solid) (cm^{-1}): 2364(w); 1698-1592(w); 1489(m); 1244(m); 840(s); 649-600(w); Found C, 56.84; H, 3.78; N, 8.94; Calc for $[CuL^2PF_6]_2$: $(C_{30}H_{22}N_4O)_2Cu_2P_2F_{12}$: C, 54.37; H, 3.35; N,8.46; ^1H NMR (CD_3CN) and (CD_2Cl_2) both unassignable, containing starting material and broad peaks, integrals unreliable. Low Temperature ^1H NMR (CD_3CN): as temperature decreases from 273K to 193K see the development of sharper peaks with the integrals eventually suggesting one species (*i.e.* 22H) and starting material (SM) similarly for (CD_2Cl_2), broad peaks at 223K but the integrals match 22H, but still broad, indicates one species.

Complexation using L^3

$[Ag_2L^3_2][PF_6]_2$.

L^3

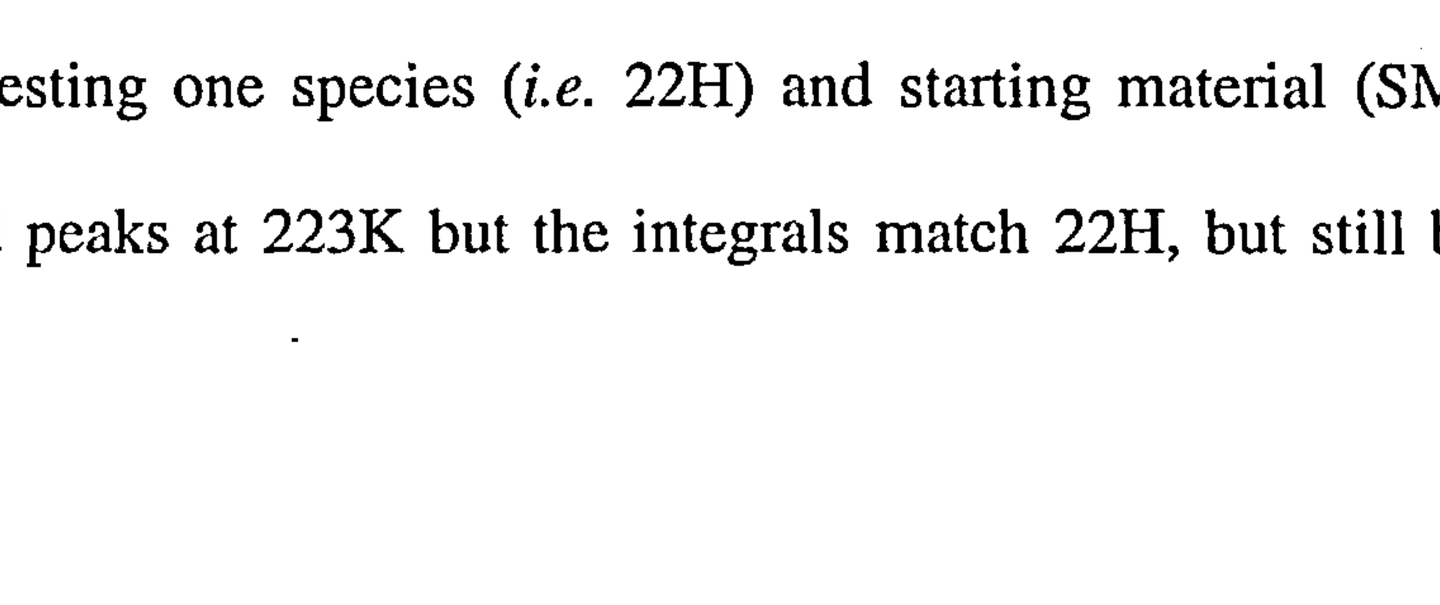

A suspension of the salt AgOAc (0.009 g, 0.054 mmol) and L^3 (0.029 g, 0.053 mmol) were stirred in methanol (15 cm^3) under N_2 for 2h. The resulting dark orange solution was filtered through a pasteur pipette with cotton wool and celite, before being treated with methanolic $[NH_4][BF_4]$. The bright yellow precipitate formed (0.063 g, 74%) was collected by vacuum filtration.

^{1}H NMR (CD_2Cl_2): δ9.20 (2H, d, J = 7.4 Hz, H_a); 8.76 (2H, dd, $H_{b/c}$, J = 2.2 Hz); 8.18 (2H,dd, $H_{c/b}$, J = 2.6 Hz); 8.09 (4H, td, $H_{d/e}$); 7.73 (4H, quintet, $H_{e/d}$), 7.53 (8H, m, f); 7.02 (4H, dd, g, J = 3.2 Hz). 2D COSY assignments: b is next to c, d is linked to e, f is next to g (where a – e refer to the quinoline portions of the complex, f refers to the biphenylene and g to the phenyl portion of the complex); FAB +MS: *m/z* 1470 $[M_2L_2PF_6 + 3H]$; 1324 $[M_2L_2]$; 1215 $[ML_2]$; 663 [ML]; 554[L]; IR (solid) (cm^{-1}): 1650(m); 1507(m); 844(s); 758(w).

$[Ag_2L^3{}_2][BF_4]_2$.

A suspension of the salt AgOAc (0.009 g, 0.056 mmol) and L^3 (0.026 g, 0.047 mmol) were stirred in methanol (15 cm^3) under N_2 for 2h. The solution changing from a bright yellow suspension to a dark orange clear solution. This dark orange solution was filtered through a pasteur pipette with cotton wool and celite, before treated with methanolic $[NH_4][BF_4]$ resulting in a bright yellow precipitate which was collected by vacuum filtration. (0.042 g, 60%)

^{1}H NMR (CD_2Cl_2): broad peaks but integrals do match the expected number and pattern of resonances (26H): δ 9.18 (2H, m); 8.78 (2H, m); 8.17 (6H, mix); 7.5 (12 H, broad mix); 7.02 (4H, m); FAB +MS: *m/z* 942 [$M_2L(BF_4)$]; IR (solid) (cm^{-1}): 1683(m); 1582(m); 1506(m); 1240(m); 1230(m); 1062(s); 833(w); 600(w).

$[Cu_2L^3{}_2][PF_6]_2$.

L^3 (0.028g, 0.054 mmol) was dissolved in methanol (15 cm^3) before the salt $[Cu(MeCN)_4][BF_4]$ (0.022 g, 0.06 mmol) was added. The mixture was stirred under dinitrogen for 48h. A dark red precipitate formed which was filtered under vacuum. (0.034 g, 42%)

^1H NMR (CD_3CN): is not readily assignable, all the peaks are broad and there is also very small amount of starting material present; 9.40 (d, 2H); 8.78 (d, 2H); 8.22 (s, 2H); 8.10 (s, 2H), 7.85 (s, 2H), 7.67 (m, 12H); 6.98 (s, 4H); ES +MS: *m/z* 618 $[M_2L_2]^{2+}$; IR (solid) (cm^{-1}): 1597(w); 1542(m); 1508(s); 1488(m); 1243(m); 841(s); 754(w).

$[Cu_2L^3{}_2][BF_4]_2$: The method used was the same as for the $[Cu_2L^3{}_2][PF_6]_2$. (71% yield) dark red black solid. ^1H NMR (CD_3CN): broad peaks and integrals do not match up; IR (solid)(cm^{-1}): 1630 (m); 1510–1488(s); 1244(s); 1057(s); 832 (m); 786(w); 750(w)

Low temperature proton NMR in CD_3CN and CD_2Cl_2 of both copper complexes show the presence of one complex species and SM. The PF_6 salt dissolves better in CD_2Cl_2 than in CD_3CN, whereas the BF_4 complex NMR spectrum looks much cleaner in CD_3CN than in CD_2Cl_2 where the complex exhibits broad peaks.

4.8 References

1. M. J. Hannon, C. L. Painting A. Jackson, J. Hamblin and W. Errington, *Chem Commun.*, 1997, 1807
2. F. Diederich, *Cyclophanes*, Cambridge: The Royal Society of Chemistry, 1991 and references therein

3. L. F. Lindoy, *The Chemistry of macrocyclic ligand complexes*, Cambridge University Press, 1989

4. F. Diederich, *Angew. Chem. Int. Ed. Engl.*, 1988, **27**, 362

5. K. A. Connors, *Binding constants: The Measurement of Molecular Complex Stability*, Wiley-Interscience, New York, 1987

6. M. Fujita and K. Orgura, *Bull. Chem. Soc. Jpn.*, 1996, **69**, 1471

7. M. Fujita, J. Yazaki and K. Ogura, *Tetrahedron letters*, 1991, **32**, 5589

8. A. Bernardo, J. F. Stoddart, A. E. Kaifer, *J. Am. Chem. Soc.*, 1992, **114**, 10624

9. B. Odell, M. V. Reddington, A. M. Slawin, N. Spencer, J. F. Stoddart and D. J. Williams, *Angew Chem. Int. Ed. Engl,* 1988, **27**, 1547

10. P. R. Ashton, B. Odell, M. V. Reddington, A. M. Z. Slawin, J. F. Stoddart and D. J. Williams, *Angew Chem. Int. Ed. Engl*, 1988, **27**, 1550

11. T. Goodnow, M. V. Reddington, J. F. Stoddart and A. E. Kaifer, *J. Am. Chem. Soc.*, 1991, **113**, 4335

12. A. Mirzolan and A. E. Kaifer, *J. Org. Chem.*, 1996, **60**, 8093

13. E. A. Smith, R. R. Lillenthal, R. J. Fonseca & D. K. Smith, *Anal. Chem.*, 1994, **66**, 3013

14. R. R. Lillenthal and D. K. Smith, *Anal. Chem.*, 1995, **67**, 3733

15. M. Asakawa, W. Dehaen, G. L'abbé, S. Menzer, J. Nouwen, F. M. Raymo, J. F. Stoddart and D.J. Williams, *J. Org. Chem.*, 1996, **61**, 9591

16. D. H. Williams and I. Fleming, *Spectroscopic Methods in Organic Chemistry*, McGraw-Hill, London, 1995

17. G. G. Guilbault, *Practical Fluorescence. Theory, Methods, and Techniques*; New York and Basel, 1973

18. A. Rodger and B. Nordén: *Circular Dichroism and Linear Dichroism*, Oxford University Press, 1997

19. J. K. M. Sanders and B. K. Hunter, *Modern NMR spectroscopy,* 1993, 2nd Ed.

20. C. A. Hunter, *Angew. Chem. Int. Engl.*, 1995, **34**, 1079.

21. Y. Aoyama in *Supramolecular Chemistry*, p17-30, eds., V. Balzani and L. De Cola, Kluwer Academic Publishers, 1992

22. M. Fujita, S. Nagao and K. Ogura, *J. Am. Chem. Soc.*, 1995, **117**, 1649.

23. M. M. Conn and J. Rebek Jr., *Chem Rev.,* 1997, **97**,1647.

24. B. Dietrich, P. Viout and J.-M. Lehn, *Macrocyclic chemistry*, VCH, 1993.

25. B. Linton and A. D. Hamilton, *Chem. Rev.*, 1997, **97**, 1669.

26. D. Philp and J. F. Stoddart, *Angew. Chem. Int. Ed. Engl.*, 1996, **35**, 1154.

27. A. W. Maverick, S.C. Buckingham, Q. Yao, J. R. Bradbury and G. G. Stanley, *J. Am. Chem. Soc.,* 1986, **108**, 7430.

28. M. Fujita, Y. J. Kwon, S. Washizu and K. Ogura, *J. Am. Chem. Soc.,* 1994, **116**, 1151

29. M. Fujita, J. Yazaki and K. Ogura, *J. Am. Chem. Soc.*, 1990, **112**, 5645

30. B. Olenyuk, A. Fechtėnkötter and P. J. Stang, *J. Chem. Soc., Dalton Trans.*, 1998, 1707

31. M. Fujita, O. Sasaki, T. Mitsuhashi, T. Fujita, J. Yazaki, K. Yamaguhi and K. Ogura, *Chem. Commun.*, 1996, 1535; M. Fujita, *Chem. Soc. Rev.,* 1998, **27**, 417

32. M. Fujita, M. Aoyagi, F. Ibukuro, K. Ogura and K. Yamaguchi, *J. Am. Chem. Soc.,* 1998, **120**, 611.

33. J. A. Whiteford, C. V. Lu and P. J. Stang, *J. Am. Chem. Soc.,* 1997, **119**, 2524

34. P. J. Stang and B. Olenyuk, *Angew. Chem. Int. Ed. Engl.*, 1996, **35**, 732.

35. B. Olenyuk, J. A. Whiteford and P. J. Stang, *J. Am. Chem. Soc.*, 1996, **118**, 8221.

36. P. J. Stang & K. Chen, *J. Am. Chem. Soc.*, 1995, **117**, 1667

37. R. V. Slone, D. I. Yoon, R. M. Calhoun and J. T. Hupp, *J. Am. Chem. Soc.*, 1995, **117**, 11813

38. R. V. Slone, J. T. Hupp, C. L. Stern and T. E. Albrecht-Schmitt, *Inorg. Chem.*, 1996, **35**, 4096

39. R. V. Slone and J. T. Hupp, *Inorg. Chem.*, 1997, **36**, 5422.

40. F. M. Romero, R. Ziessel, A. Dupont-Gervais and A. V. Dorsselaer, *Chem. Commun.*, 1996, 551.

41. J. Lu, T. Paliwala, S. C. Lim, C. Yu, T. Niu and A. J. Jacobson, *Inorg. Chem.*, 1997, **36**, 923.

42. H. Rauter, I. Mutikainen, M. Blomberg, C. J. L. Lock, P. Amo-Ochoa, E. Freisinger, L. Randaccio, E. Zangrando, E. Chiarparin and B. Lippert, *Angew. Chem. Int. Ed. Engl.*, 1997, **36**, 1296.

43. H. Rauter, E. C. Hillgeris, A. Erxleben, and B. Lippert, *J. Am. Chem. Soc.*, 1994, **116**, 616

44. P. N. W. Baxter, J.-M. Lehn, B.O. Kneisel and D. Fenske, *Angew. Chem. Int. Engl.*, 1997, **36**, 1979.

45. P. Baxter, J.-M Lehn, A. DeCian and J. Fischer, *Angew Chem. Int. Ed. Engl,* 1993, **32**, 69

46. M. J. Hannon, C. L. Painting and W Errington, *Chem Commun.*, 1997, 307

47. Y. Suenaga, S.G. Yan, L. P. Wu, I. Ono, T.Kuroda-Sowa, M. Maekawa and M. Munakata, *J. Chem. Soc., Dalton Trans.*, 1998, 1121.

48. S. Roche, C. Haslam, H. Adams, S. L. Heath and J. A. Thomas, *Chem. Commun.*, 1998, 1681

49. J. W. Steed and J.L.Atwood, *Supramolecular Chemistry*, 2000, John Wiley and Sons, 2000

50. P. N. W. Baxter, J.-M. Lehn, B. O. Kneisel and D. Fenske, *Chem. Commun.*, 1997, 2231.

51. P. N. W. Baxter, J.-M. Lehn, J. Fischer and M.-T. Youinou, *Angew. Chem. Int. Ed. Engl,.* 1994, **33**, 2284

52. M. J. Hannon, C. L. Painting and W. Errington, *Chem. Commun.*, 1997, 1805.

53. P. N. W. Baxter, J.-M. Lehn and K. Rissanen, *Chem. Commun.*, 1997,1323

54. M. J. Hannon, S. Bunce, A. J. Clarke and N.W. Alcock, *Angew Chem. Int. Ed. Engl.*, 1999, **38**,1277

55. C. O. Dietrich-Buchecker, J.-F. Nierengarten, J.-P. Sauvage, N. Annaroli, V. Balzani and L. De Cola, *J. Am. Chem. Soc.*, 1993, **115**, 11237

56. A. Bilyk, M. M. Harding, P. Turner and T. W. Hambley, *J. Chem. Soc. Dalton Trans.*, 1994, 2783

57. J. K. Barton, L.A. Basile, A. Danishefsky and A. Alexandrescu, *Proc. Natl. Acad. Sci. U.S.A.*, 1984, **81**, 1961

58. F. P. Dwyer and E. C. Gyarfas, *Proc. Roy. Soc. NSW*, 1951, **85**, 135

59. Z. Coggan, I. S. Haworth, P. J. Bates, A. Robinson and A. Rodger, *Inorg. Chem.*, 1999, **38**, 4486.

60. A. Arcordia and G. Scarlata, *Annali di Chimica (Rome)*, 1968, **58**, 32

61. S. E. Hazlet, *J. Am. Chem. Soc.*, 1937 Pt I, **59**, 287

62. S. E. Hazlet, G. Alliger and R. Tiede, *J. Am. Chem. Soc.*, 1939 Pt I, **61**, 1447

63. S. E. Hazlet and H. O. Van Orden, *J. Am. Chem. Soc.*, 1942 Pt II, **64**, 2505

64. B. Jones and F. Chapman, *J. Chem. Soc.*, 1952. Pt II, 1829

65. F. Bell and J. Kenyon, *J. Chem. Soc.*, 1926, **129**, 3048

66. J. H. Parish and M. C. Whiting, *J. Chem. Soc.*, 1964, 4713

67. C. S. Wilcox, *Tetrahedron Letters,* 1985, **26**, 5749

68. K. E. Steller and R. L. Letsinger, *J. Org. Chem.*, 1970, **35**, 308

69. M. J. Rarick, R. Q. Brewster and F. B. Dains, *J. Am. Chem. Soc.*, Pt I, 1933, **55**, 1289.

70. A. I. Vogel, *Vogel's textbook of quantitative inorganic analysis*, Longman, 1978, 4th Ed., p146; A. I. Vogel, *Textbook of Practical Organic Chemistry*, Longman, 3rd Ed., p559; F. G. Mann, *Practical organic chemistry*, p160

71. L. J. Childs, N. W. Alcock and M. J. Hannon, *Angew. Chem. Int. Ed.*, 2001, **40**, 1079

72. F. D. Bellamy and K. Ou, *Tetrahedron Letters,* 1984, **25**, 839

5 Conclusions and further work

This chapter contains the overall conclusions of the research presented in this thesis as well as suggesting further areas of work.

The DNA binding interactions of five novel ruthenium(II) bis-terpyridine complexes functionalised with an aryl tail group (i) biphenylene (biphen), (ii) β-napthyl (napth), (iii) phenanthrene (phen), (iv) anthracene (anth) and (v) pyrene (pyr) in the 4′ position on each terpyridine ligand were investigated with ct-DNA, AT DNA and GC DNA using the spectroscopic techniques of absorbance, *CD* and *LD*. Using qualitative spectroscopic assignments, all five ruthenium complexes have been found to bind non-covalently to DNA. At low complex concentrations, three of the complexes, the anth, phen and pyr complexes were found to intercalate their aryl tail groups between DNA bases. The napth complex was found to exhibit both an intercalative and a non-intercalative mode. The biphen complex was found to predominately exhibit groove binding with no significant tail intercalation. At high metal complex concentrations, the complexes exhibit a non-intercalative binding mode, *i.e.* π-π self-stacking interactions (aggregation) on the DNA is observed. Resonance light scattering studies indicate aggregates of low nuclearity along the groove.

The design of molecules with planar tails attached to the terpy groups has successfully led to intercalative binding in four out of five cases. These tails have the ability to act as low nuclearity aggregation agents, and can provide a useful platform from which to establish a basis for molecular designs. Further work on these complexes could take the form of *CD* and *LD* experiments with AT DNA to clarify any sequence

dependence, NMR investigations with small oligonucleotides and X-ray crystallography to confirm binding. Further mixed ligand complex synthesis using the substituted terpy tail groups may lead to novel complexes that can be finely tuned specific DNA binding agents or 'probes'.

The DNA binding interactions of a novel series of eighteen platinum(II) square planar complexes of the formula [Pt(L)Cl(DMSO)] where L = an acylthiourea ligand system R′C(O)NHC(S)NR_2, R′ = aryl and R = amine, (O) and (S) denote points of attachment of the ligand to platinum(II), and DMSO denotes dimethylsulfoxide or a derivative of it were investigated using absorbance, *CD*, *LD* and mass spectrometry. A preliminary screen of the eighteen platinum complexes with ct-DNA by absorbance and *CD* was followed by an in depth spectroscopic study on six complexes, structurally similar but with subtle ligand variations, with ct-DNA, poly $[d(A–T)]_2$, poly $[d(G–C)]_2$ DNA and 5′-mononucleotides. Ligand variation was found to affect DNA binding interaction. Mass spectrometric studies on three complexes of one particular subset with 9-methyl guanine and 5′-guanosine monophosphate indicate that these complexes bind covalently to DNA via the loss of the chloride or possibly the DMSO groups on the platinum. The spectroscopic studies suggest that duplex DNA may not be the primary target for these complexes and the use of organic solvent and ionic strength may affect interactions. This raising more questions that need answering.

Further work on the six (PtX) complexes in the form of AT DNA *LD* studies (if experimentally feasible) may help to clarify further any sequence dependence. Mass spectrometric studies (similar to those carried out with the nitro subset), with 9-methylguanine and the (PtX) complexes of the methoxy subset may show which of the chloride or DMSO groups leaves preferentially with the methoxy subset and help

explain further the different spectroscopy seen between both subsets. Further mass spectrometric studies on all six (PtX) complexes using dinucleotides and small oligonucleotides may also provide more information on the interactions. *CD* and mass spectrometry experiments on the effects of the chloride ion concentration and organic solvent effects may help make clearer the mechanism of action of these complexes and should help distinguish between the biologically active complexes and the others that are not. There is a very real possibility that once these questions have been answered, these (PtX) complexes could be systematically modified to provide optimum anti-tumour response. There are also twelve remaining (PtX) complexes, that have been examined briefly and been shown to interact with DNA, that, subject to compound availability could be investigated further.

The molecular sensor potential of a range of organic soluble supramolecular copper(I) and silver(I) metallo-cyclophanes and their interactions with small molecules *e.g.* the isomers of di- and tri-methoxybenzenes and chiral anionic compounds (sodium antimonyl-L-tartrate) were investigated using absorbance, fluorescence, NMR studies and X-ray crystallography. The metallo-cyclophanes can adopt two conformations, a helical (helix) and a bridging non-helical (box) structure. Using *CD* and proton NMR, the chiral dianion sodium antimonyl tartrate was found to be capable of resolving the metal complex box-helix mixture by inducing helix formation leading to an excess of one helix over the other and the box. Although the metallo-cyclophanes bind with the di- and tri methoxybenzenes, the mechanism of binding is still not understood. This has led to the subsequent design, synthesis and characterisation of novel longer asymmetric ligands capable of assembly into supramolecular cyclophane structures with larger cavities.

Further work, in the form of improving the purity of these novel complexes (as outlined in section 4.6.5), addressing the L^5 synthesis issue and complexation with octahedral metal ions could be investigated as well as the binding of 'guests' to these species.

The unifying theme of this thesis has been the biophysical investigations into novel metallo-systems and their interactions with DNA and small molecules. A variety of systems have been studied, the common features of which have been the spectral techniques used and the need to solubilise the systems in organic solvents, hence the development of methods to study the metallo-system biomolecular interactions spectroscopically in organic solvents.

The research presented in this thesis represents a variety of novel metallo-systems that have the potential to be adapted to have future biomedical applications

Appendices

Appendix 1 Absorbance and *CD* spectra of the organic solvent limits of MeCN, DMSO and DMF with ct-DNA

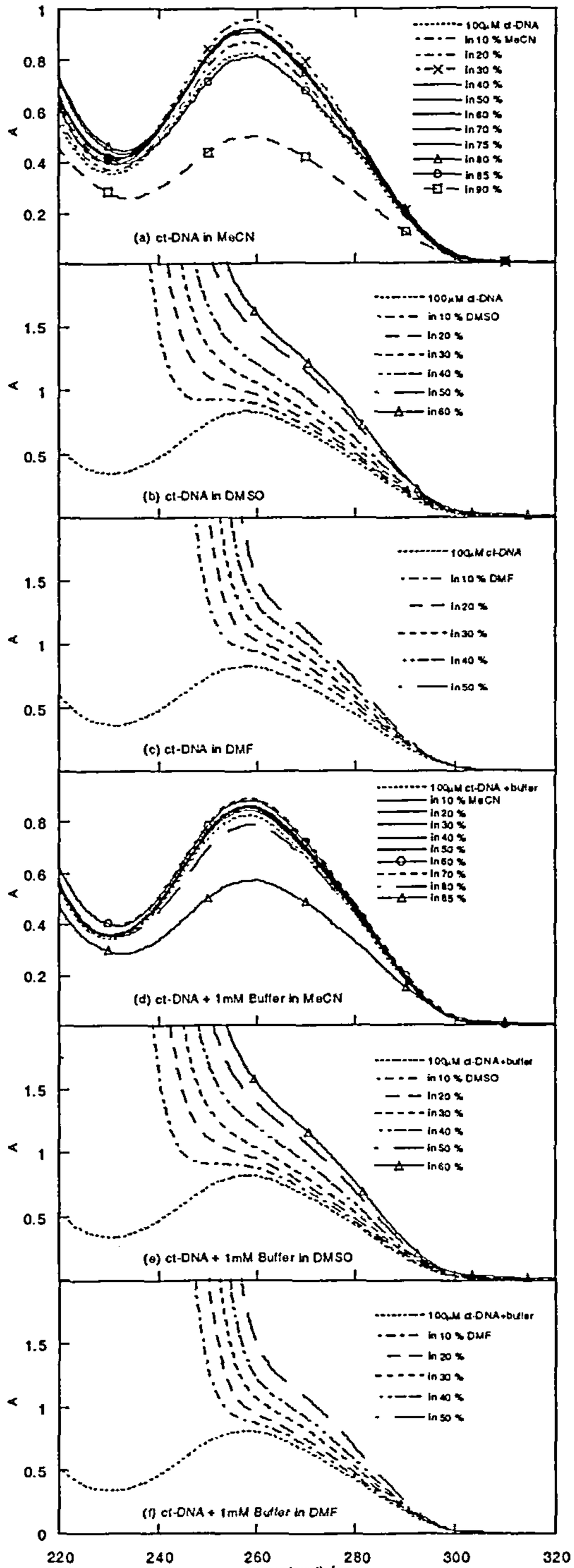

Appendix 1 The absorbance spectra of ct-DNA in MeCN, DMSO and DMF (a – c) and with 1mM sodium cacodylate buffer pH 6.92 (d – e)

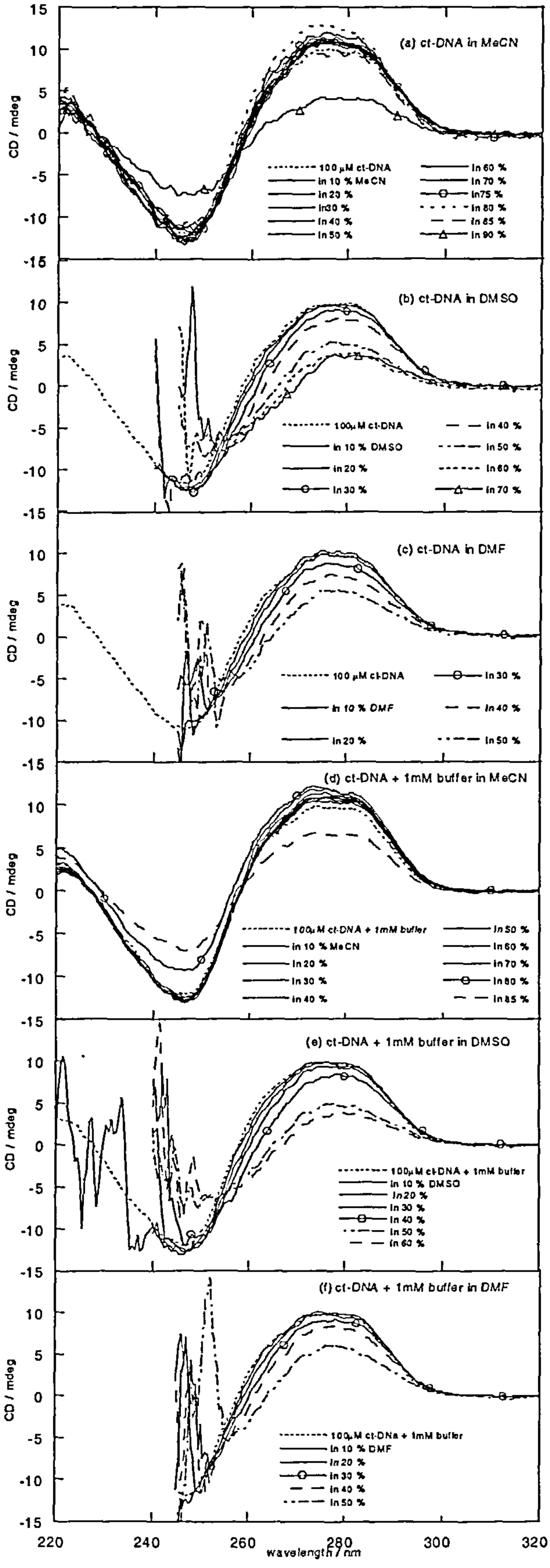

Appendix 1 The *CD* spectra of ct-DNA in MeCN, DMSO and DMF (a – c) and with 1mM sodium cacodylate buffer pH 6.92 (d – e)

Appendix 2.1 Flow *LD* and *LD*^{r} spectra for the ruthenium complexes with methylene blue and ct-DNA

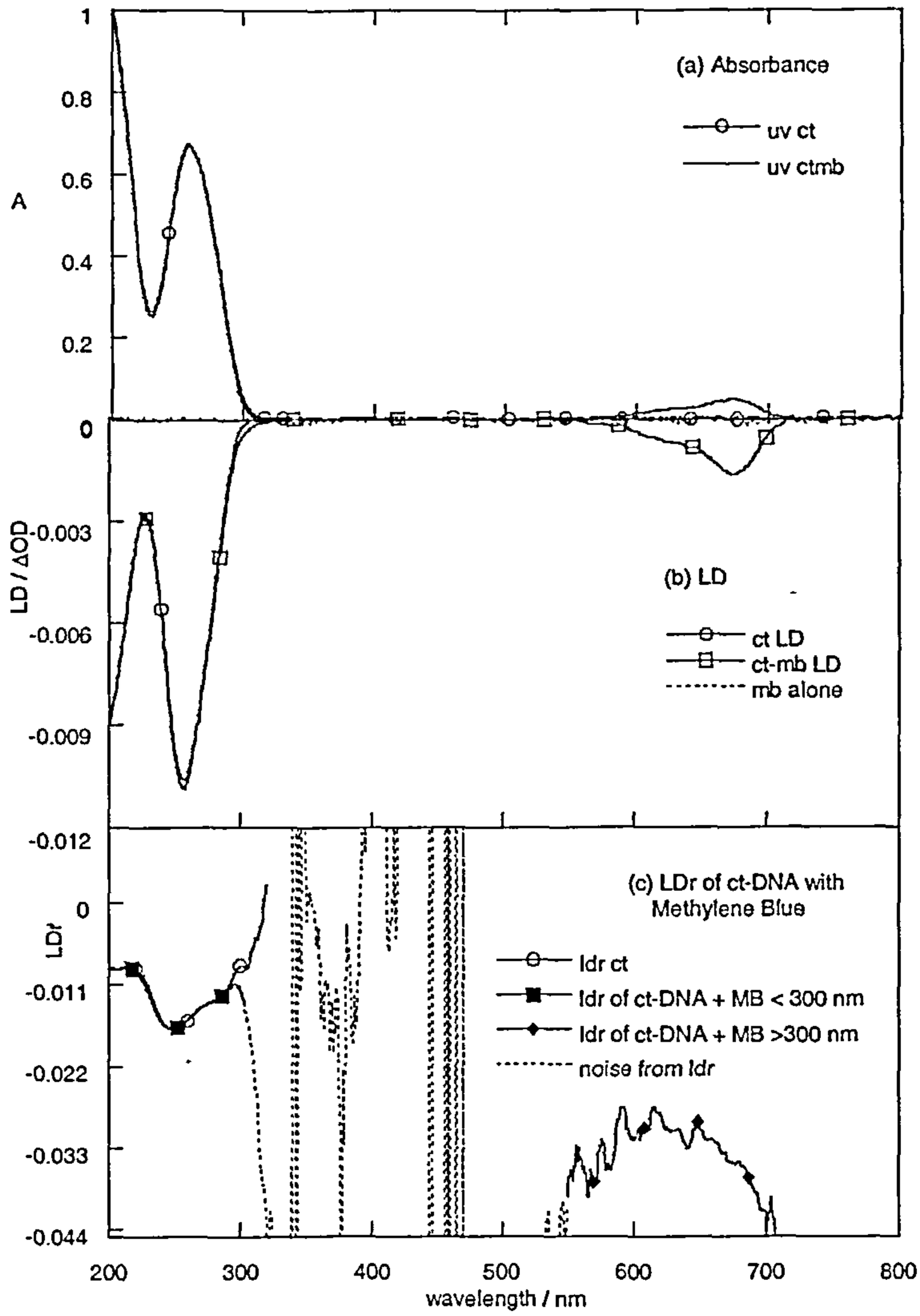

Figure A2.2.1 (a) *UV-Visible absorbance*, (b) flow *LD* and (c) *LD*^{r} of ct-DNA alone (100 μM), methylene blue alone (~ 1μM), and ct-DNA + methylene blue (100 μM :1 μM)

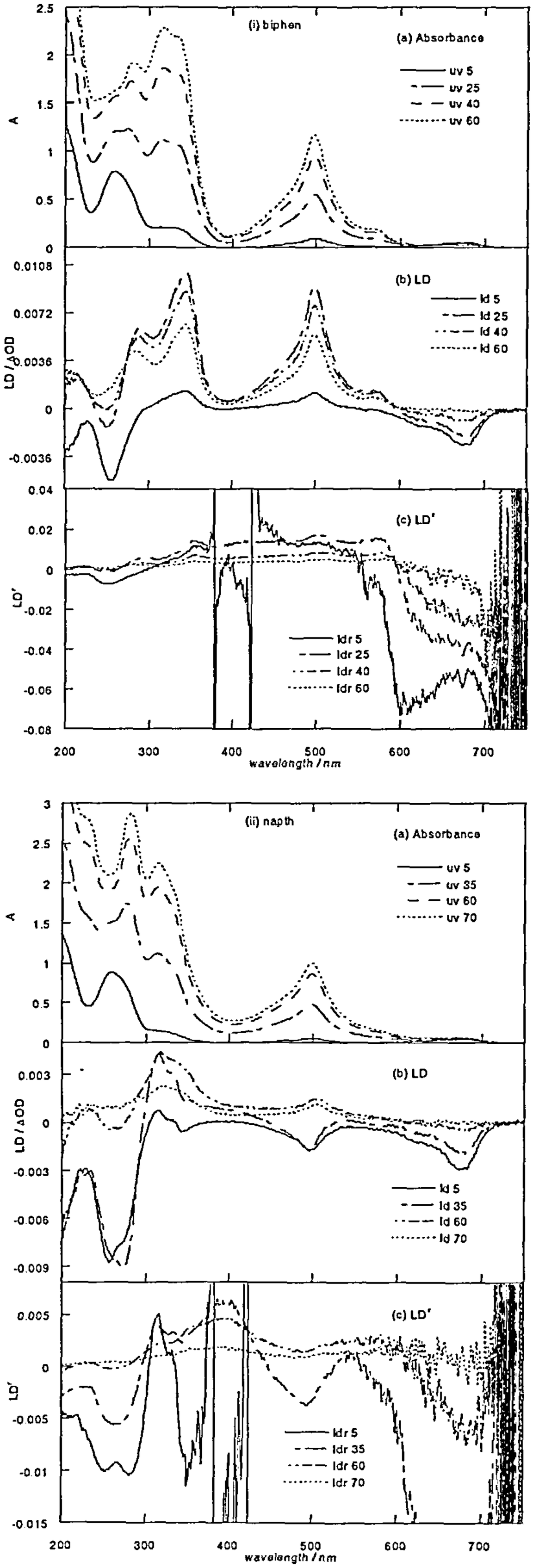

Figure A2.1.2 Flow *LD* and *LD'* spectra for the ruthenium complexes with ct-DNA and methylene blue. (a) absorbance, (b) flow *LD*, and (c) *LD'* of (i) biphen, (ii) napth, (iii)phen, (iv) anth, and (v) pyr. Working with ct-DNA (100 μM) + MB (1 μM) + ruthenium complex. Legend indicates μM ruthenium complex concentration, ct-DNA and MB concentrations are constant.

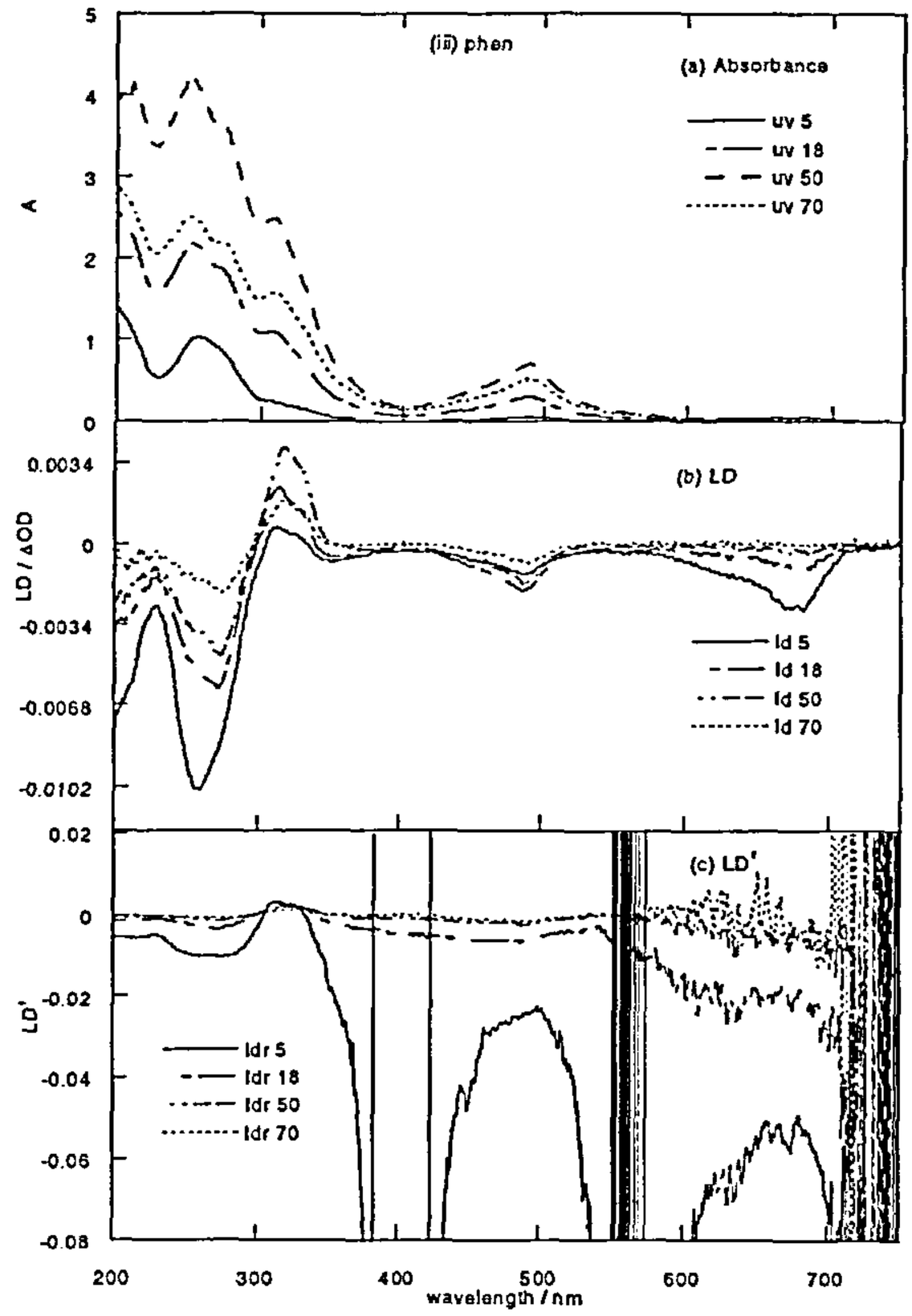

Figure A2.1.2 (iii)phen, (iv) anth

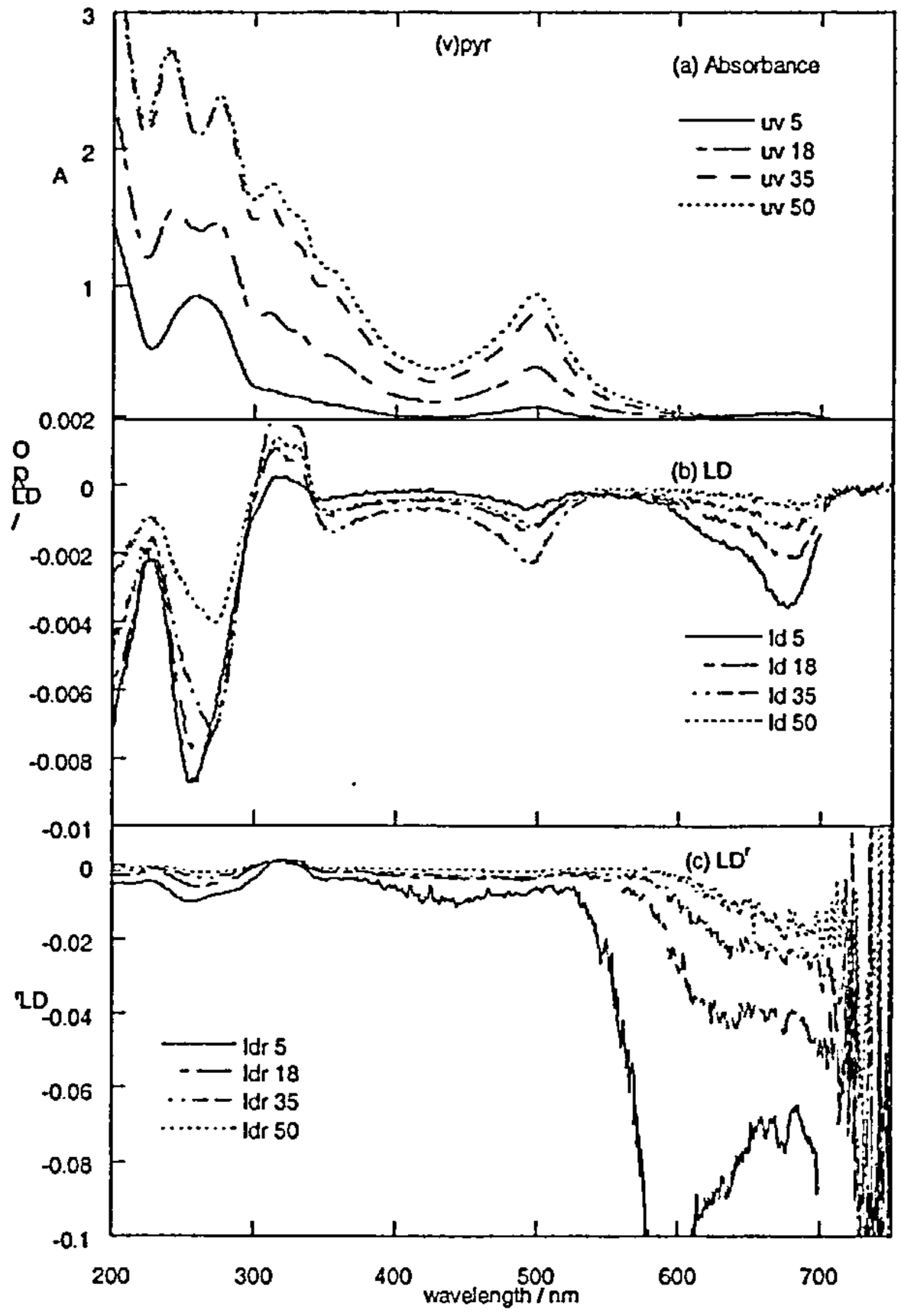

Figure A2.1.2 (v) pyr

Appendix 2.2 Absorbance titration spectra of biphen with (i) GC DNA and (ii) AT DNA, relating to Figure 2.19

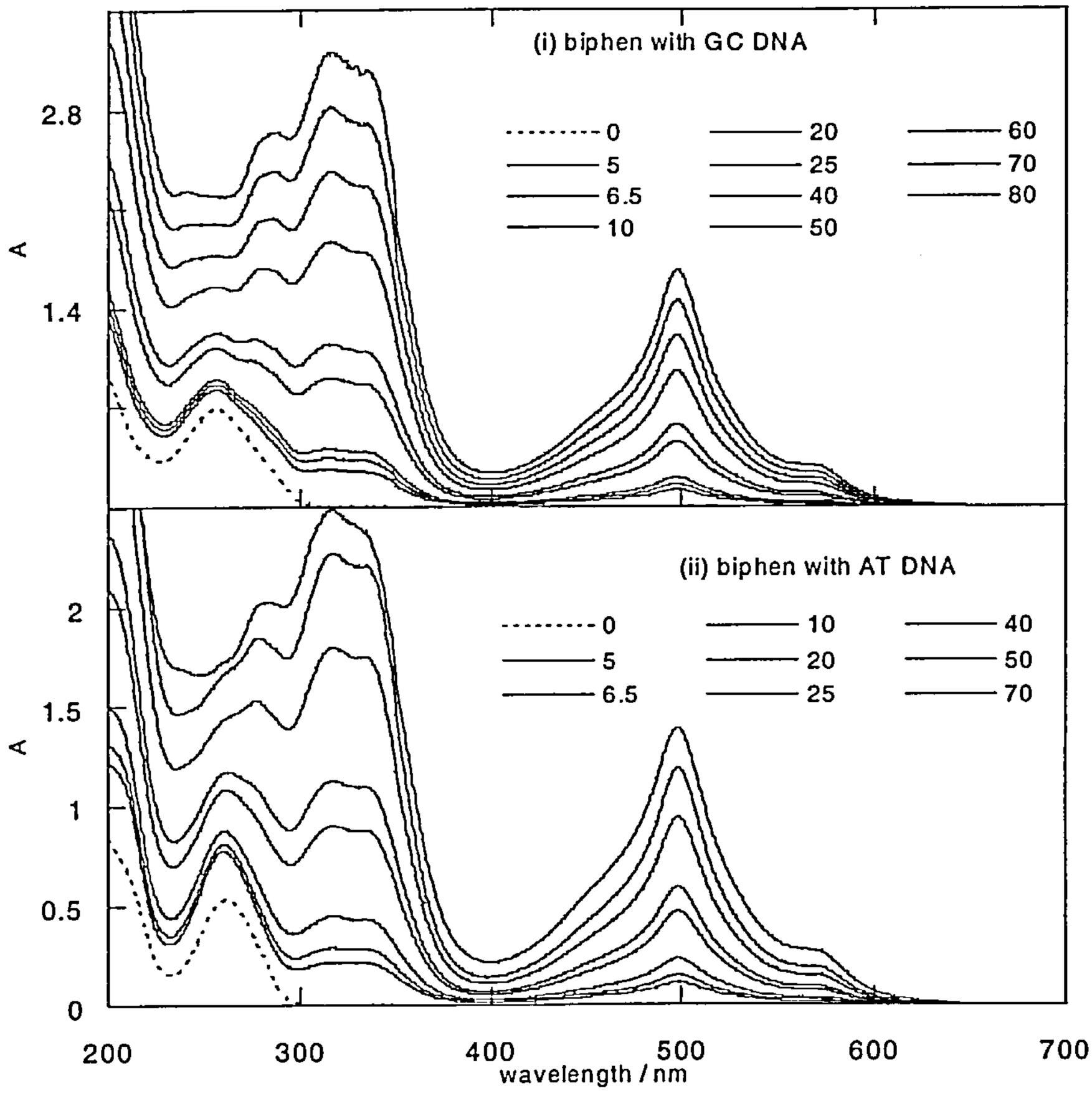

Appendix 4.1 Absorbance titration spectra, ISM and Scatchard plots.

ΔA absorbance value Tables 1 and 2

Binding constants table

The copper cyclophane is denoted 'box' in the legend of each spectra
Working with a constant cyclophane concentration of 15 μM

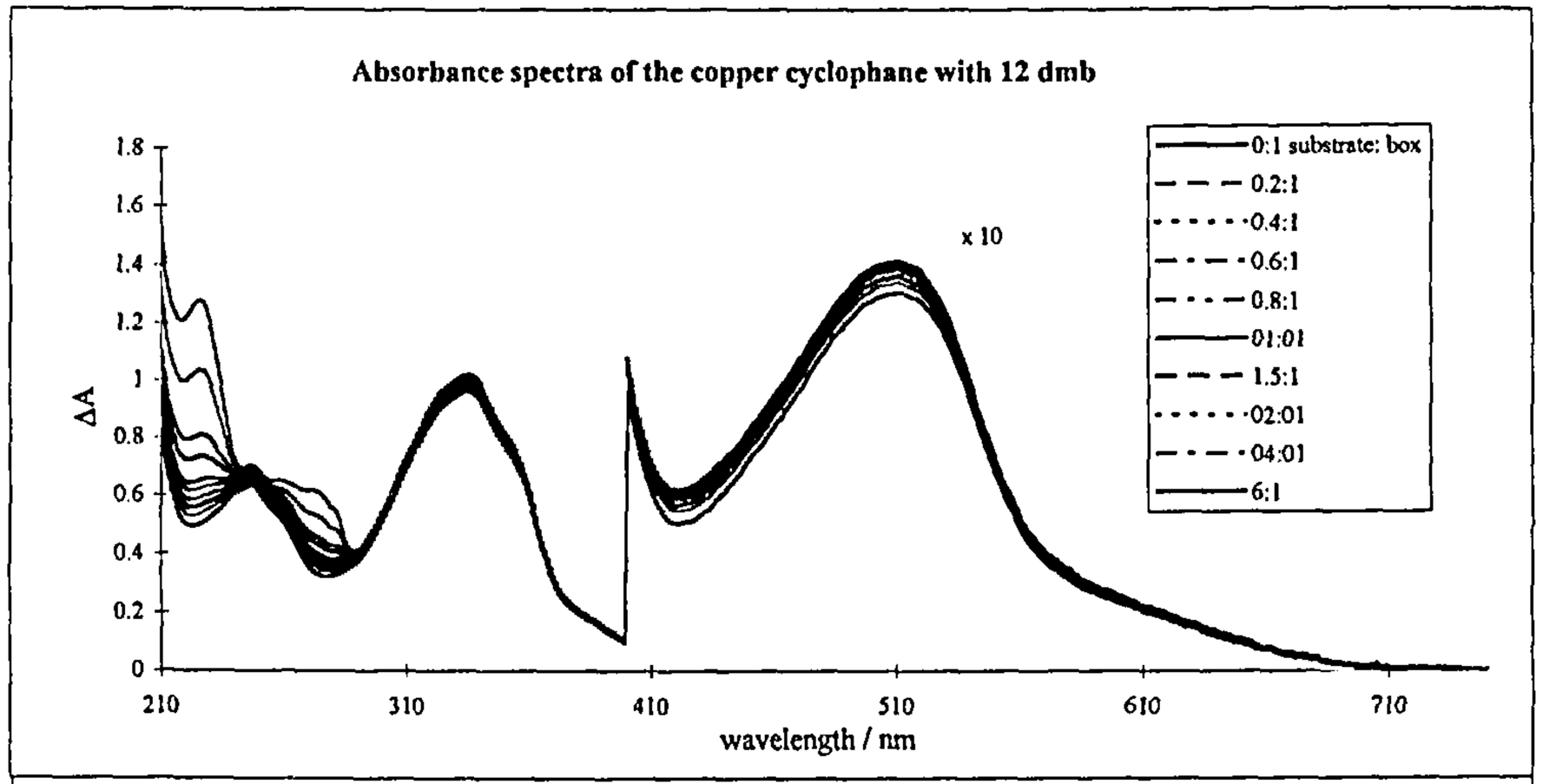
Absorbance spectra of the copper cyclophane with 12 dmb
ΔA
wavelength / nm
x 10
0:1 substrate: box
0.2:1
0.4:1
0.6:1
0.8:1
01:01
1.5:1
02:01
04:01
6:1

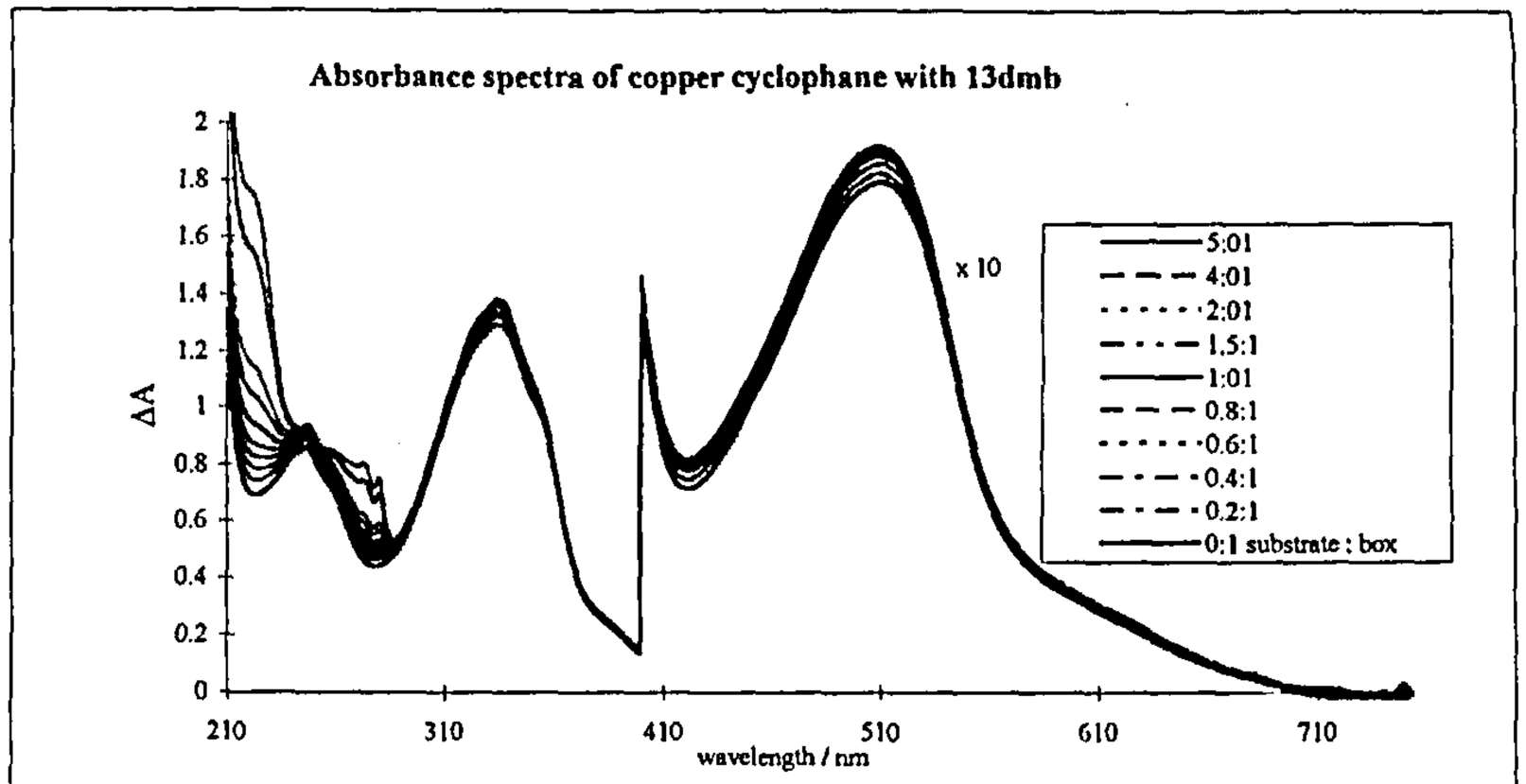
Absorbance spectra of copper cyclophane with 13dmb
ΔA
wavelength / nm
x 10
5:01
4:01
2:01
1.5:1
1:01
0.8:1
0.6:1
0.4:1
0.2:1
0:1 substrate : box

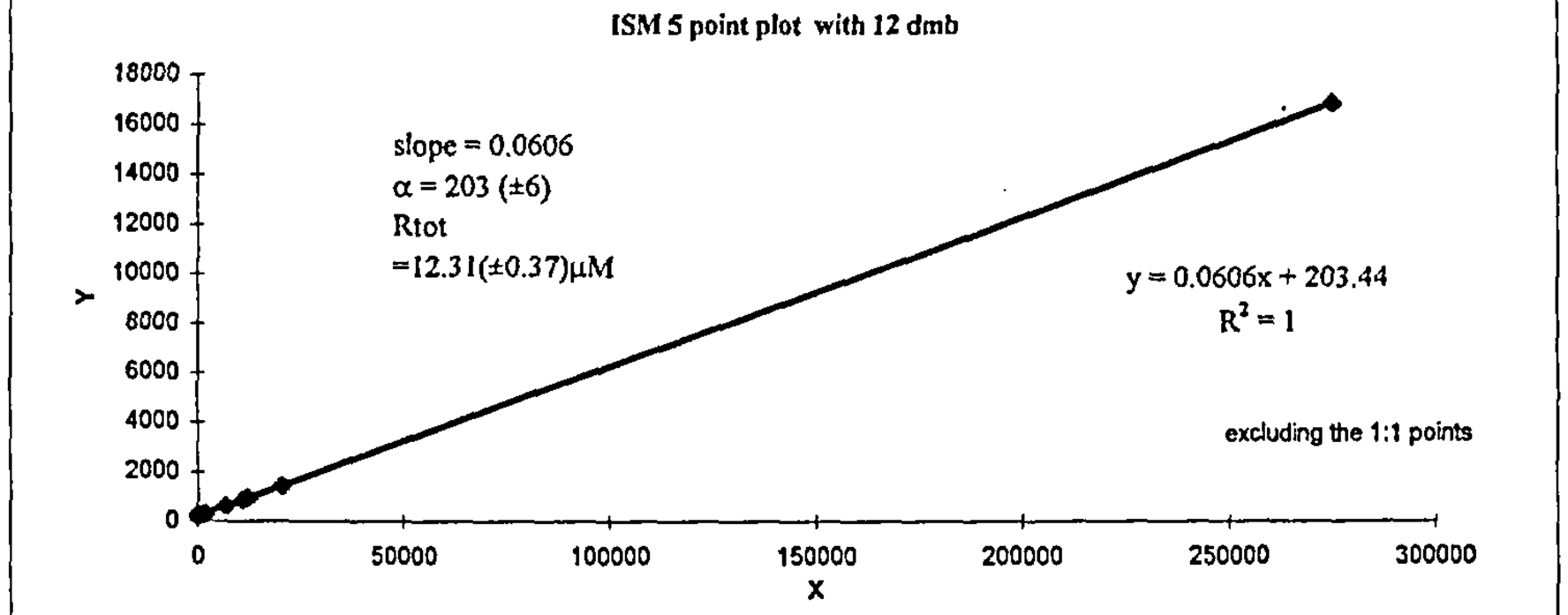
ISM 5 point plot with 12 dmb
slope = 0.0606
α = 203 (±6)
Rtot
=12.31(±0.37)μM
y = 0.0606x + 203.44
R² = 1
excluding the 1:1 points
Y
X

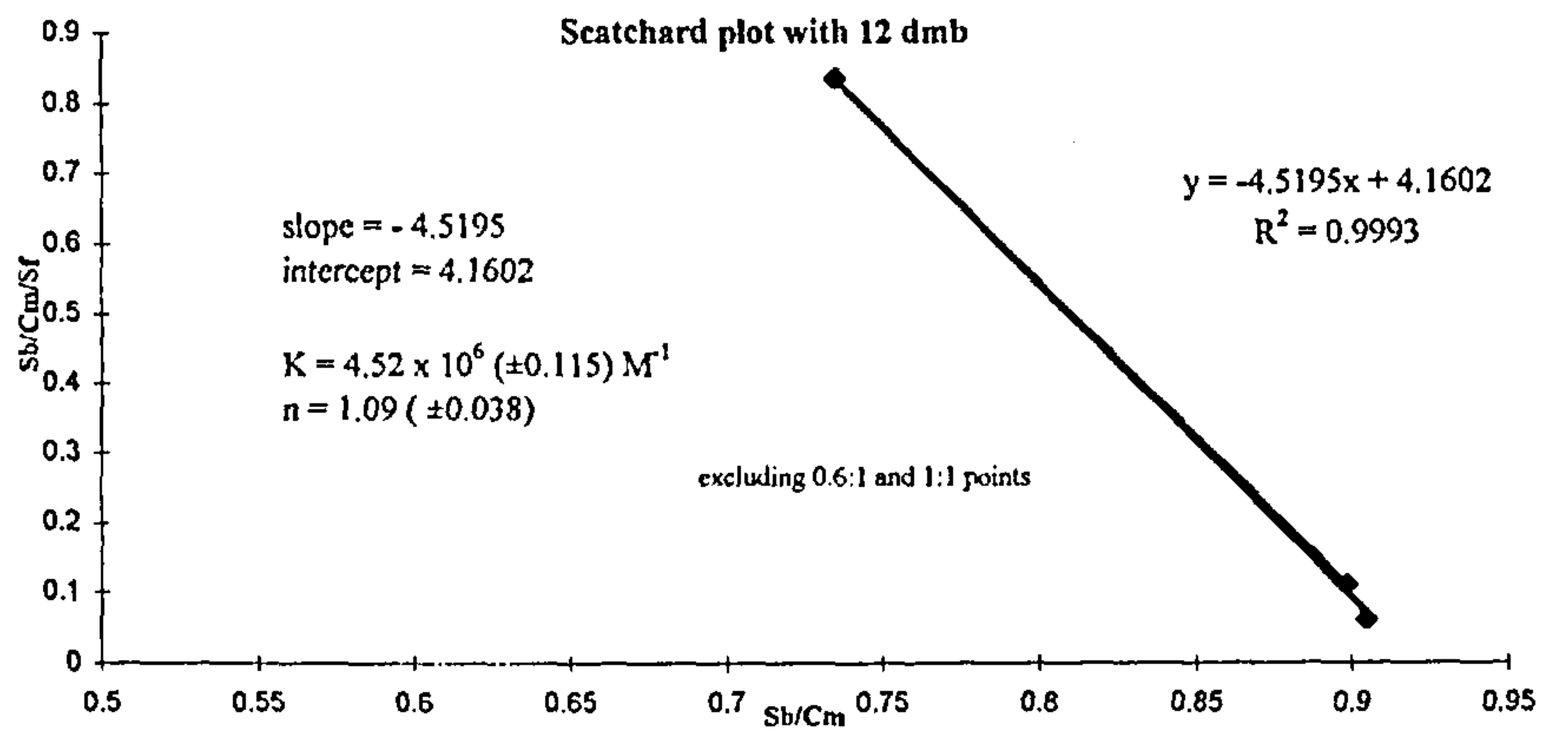
Scatchard plot with 12 dmb
slope = - 4.5195
intercept = 4.1602
K = 4.52 x 10⁶ (±0.115) M⁻¹
n = 1.09 (±0.038)
y = -4.5195x + 4.1602
R² = 0.9993
excluding 0.6:1 and 1:1 points
Sb/Cm/Sf
Sb/Cm

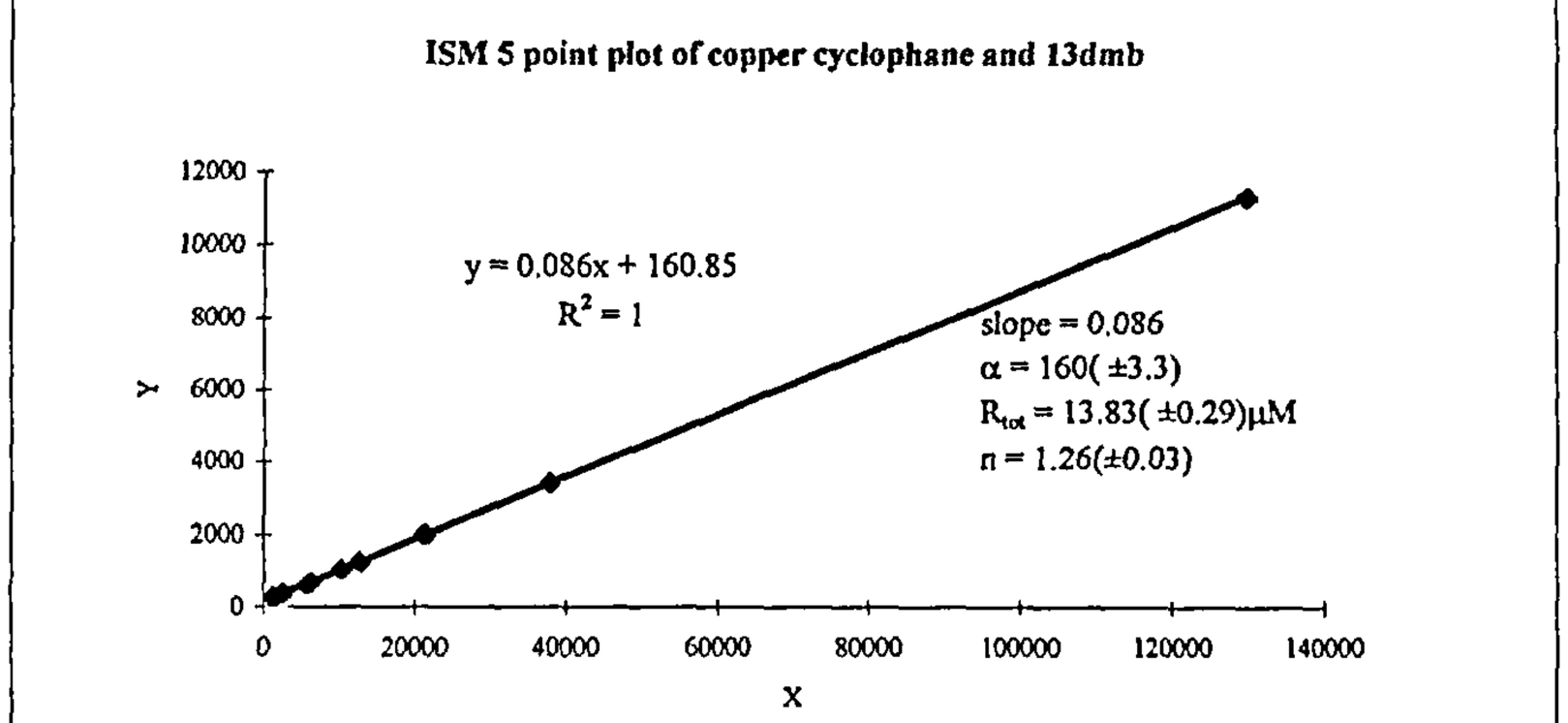
ISM 5 point plot of copper cyclophane and 13dmb
y = 0.086x + 160.85
R² = 1
slope = 0.086
α = 160(±3.3)
Rtot = 13.83(±0.29)μM
n = 1.26(±0.03)
Y
X

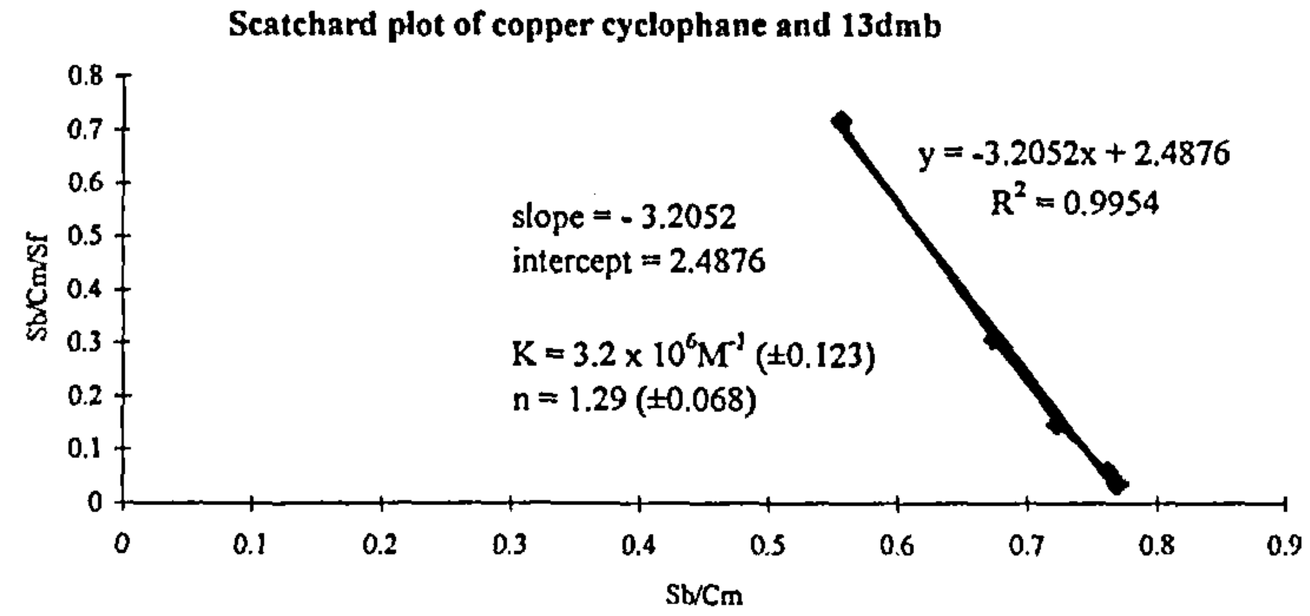
Scatchard plot of copper cyclophane and 13dmb
slope = - 3.2052
intercept = 2.4876
K = 3.2 x 10⁶M⁻¹ (±0.123)
n = 1.29 (±0.068)
y = -3.2052x + 2.4876
R² = 0.9954
Sb/Cm/Sf
Sb/Cm

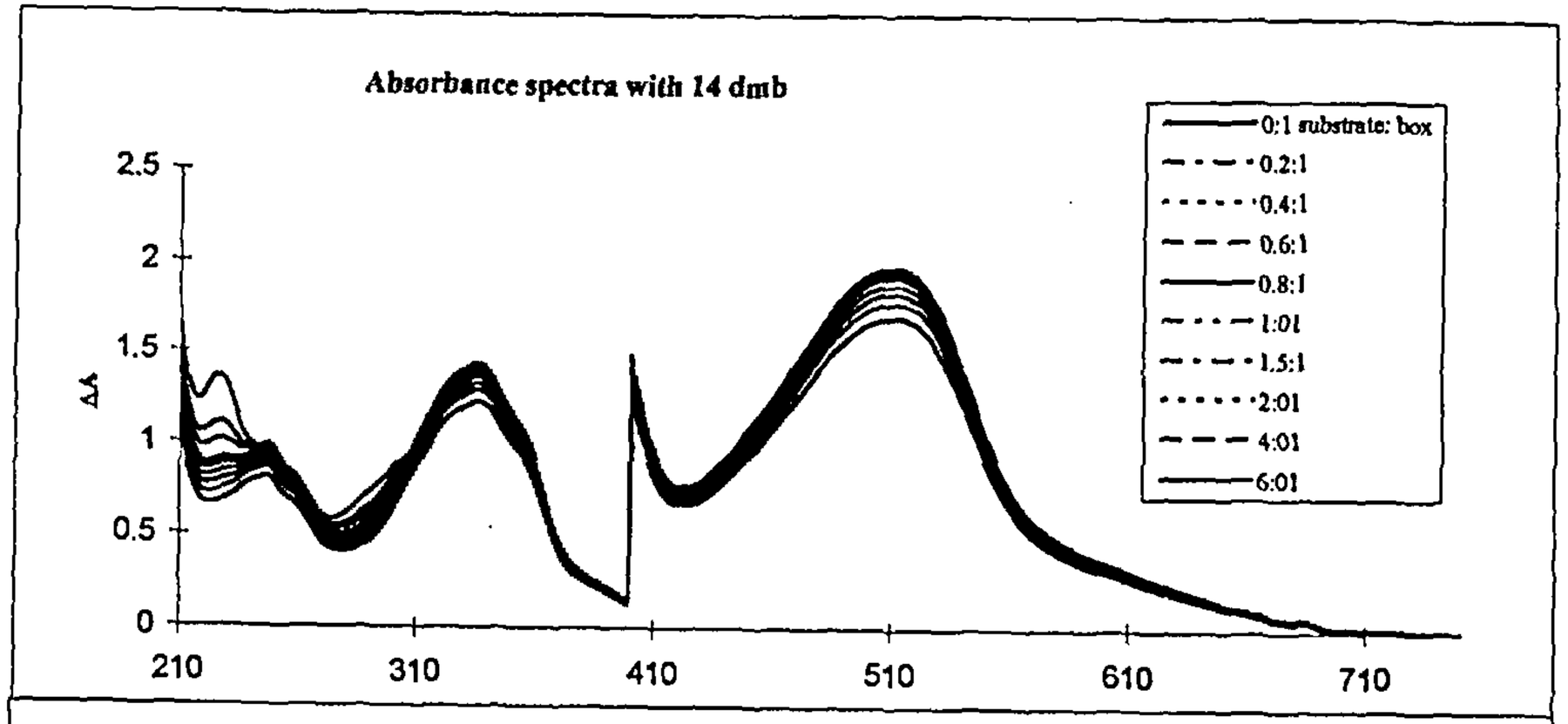
Absorbance spectra with 14 dmb
ΔA
0:1 substrate: box
0.2:1
0.4:1
0.6:1
0.8:1
1:01
1.5:1
2:01
4:01
6:01
2.5
2
1.5
1
0.5
0
210
310
410
510
610
710

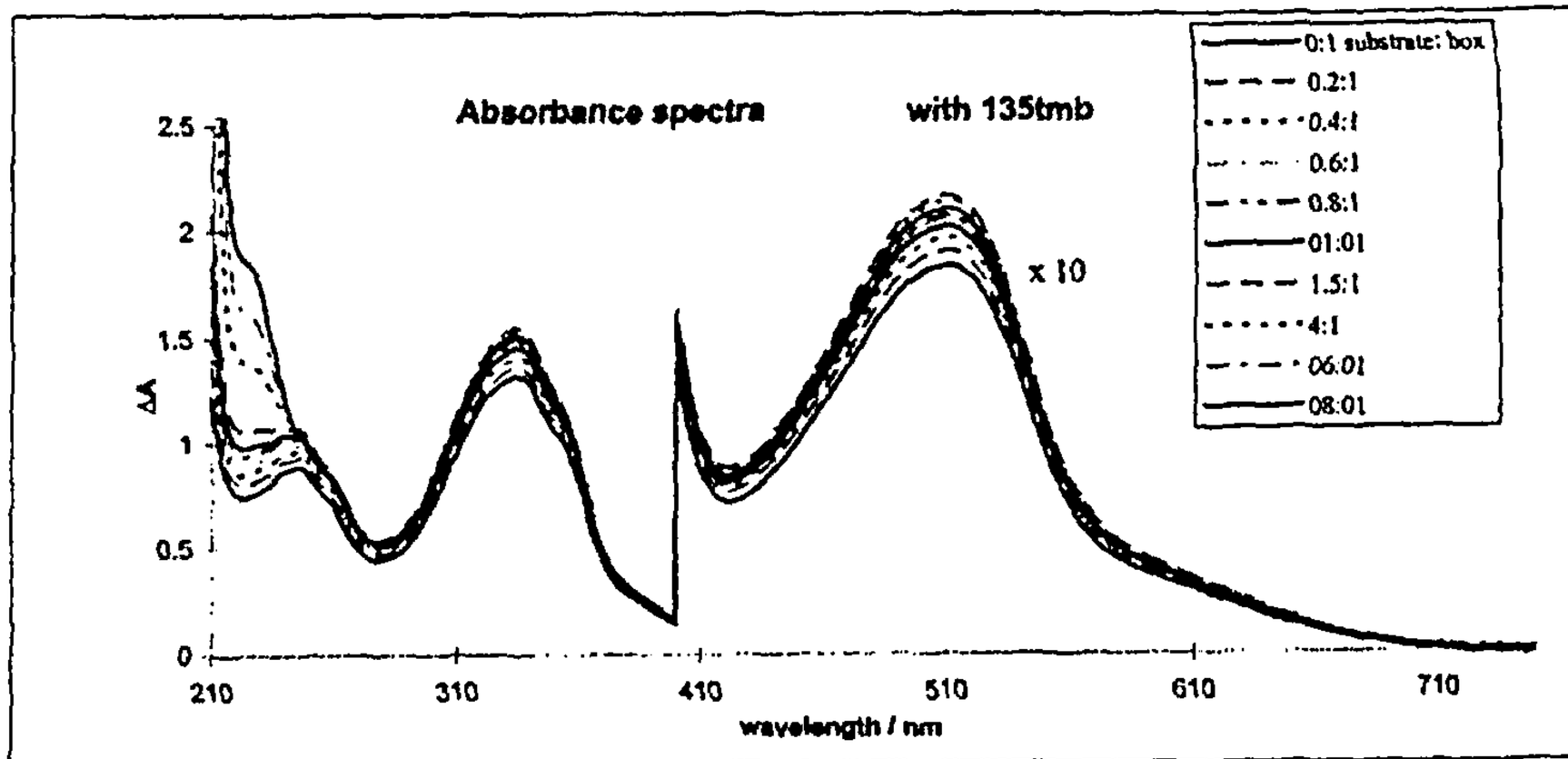
Absorbance spectra with 135tmb
ΔA
x 10
0:1 substrate: box
0.2:1
0.4:1
0.6:1
0.8:1
01:01
1.5:1
4:1
06:01
08:01
2.5
2
1.5
1
0.5
0
210
310
410
510
610
710
wavelength / nm

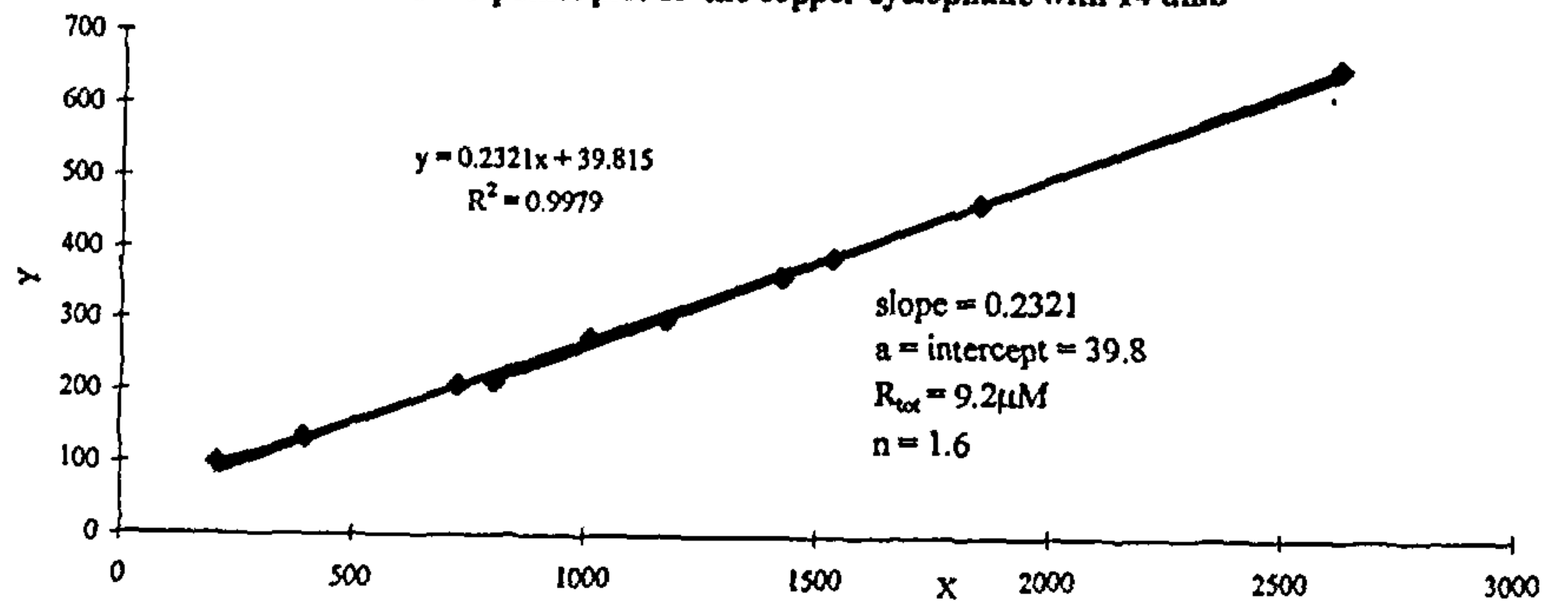
Ism 5 points plot of the copper cyclophane with 14 dmb
y = 0.2321x + 39.815
R² = 0.9979
slope = 0.2321
a = intercept = 39.8
R_tot = 9.2μM
n = 1.6
Y
X
700
600
500
400
300
200
100
0
0
500
1000
1500
2000
2500
3000

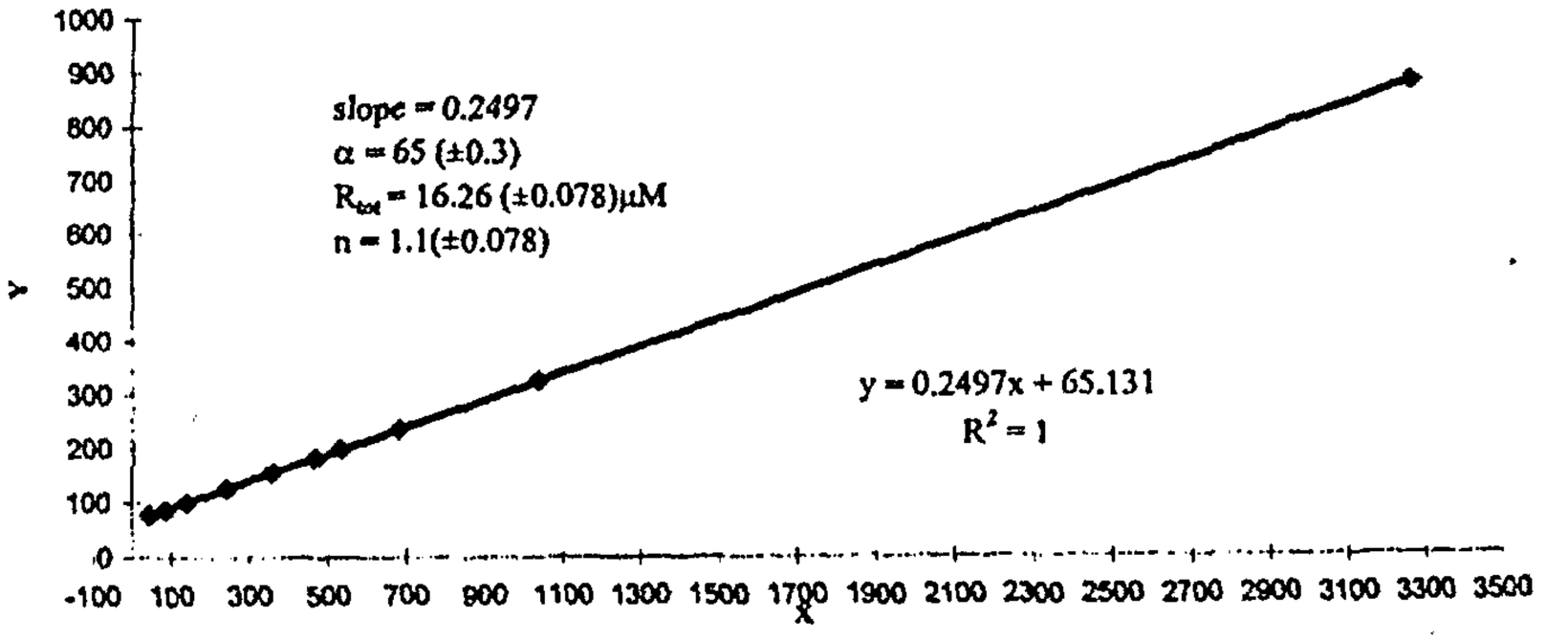
ISM 5 point plot with 135 tmb
slope = 0.2497
α = 65 (±0.3)
R_tot = 16.26 (±0.078)μM
n = 1.1(±0.078)
y = 0.2497x + 65.131
R² = 1
Y
X
1000
900
800
700
600
500
400
300
200
100
0
-100
100
300
500
700
900
1100
1300
1500
1700
1900
2100
2300
2500
2700
2900
3100
3300
3500

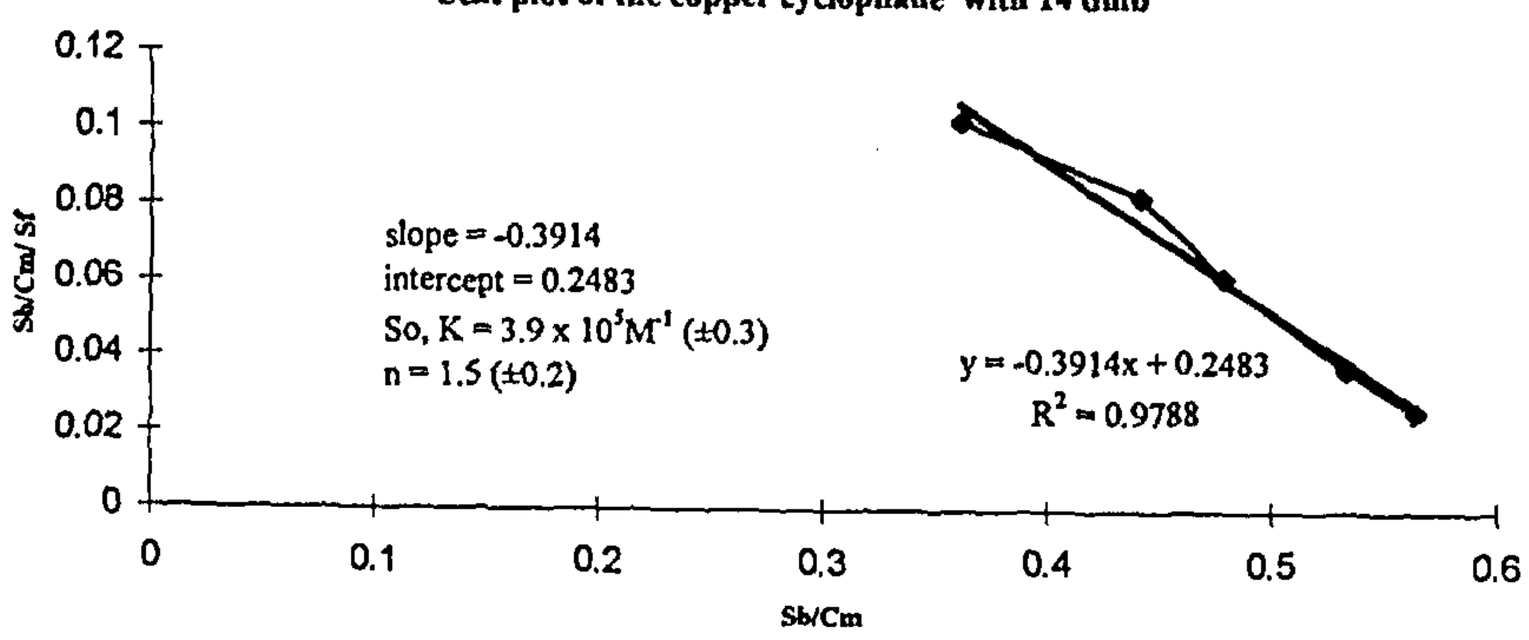
Scat plot of the copper cyclophane with 14 dmb
slope = -0.3914
intercept = 0.2483
So, K = 3.9 x 10⁵M⁻¹ (±0.3)
n = 1.5 (±0.2)
y = -0.3914x + 0.2483
R² = 0.9788
Sb/Cm/ Sf
Sb/Cm
0.12
0.1
0.08
0.06
0.04
0.02
0
0
0.1
0.2
0.3
0.4
0.5
0.6

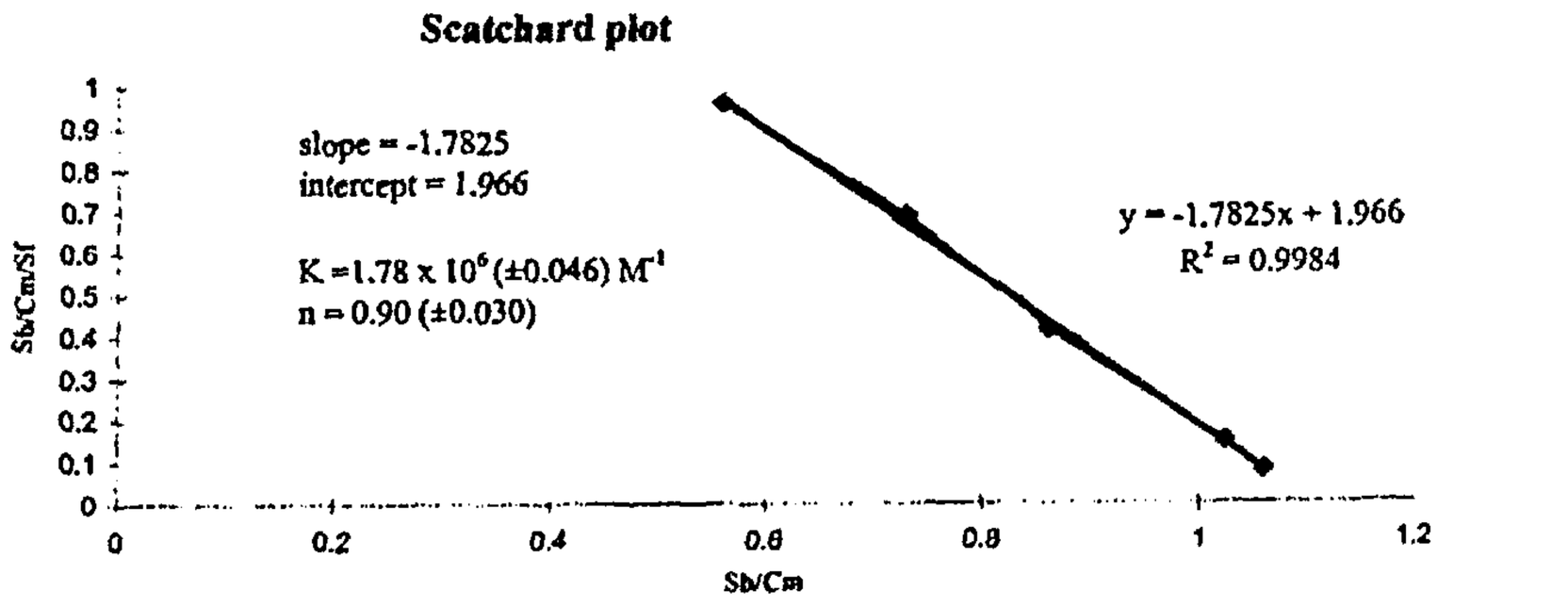
Scatchard plot
slope = -1.7825
intercept = 1.966
K =1.78 x 10⁶ (±0.046) M⁻¹
n = 0.90 (±0.030)
y = -1.7825x + 1.966
R² = 0.9984
Sb/Cm/Sf
Sb/Cm
1
0.9
0.8
0.7
0.6
0.5
0.4
0.3
0.2
0.1
0
0
0.2
0.4
0.6
0.8
1
1.2

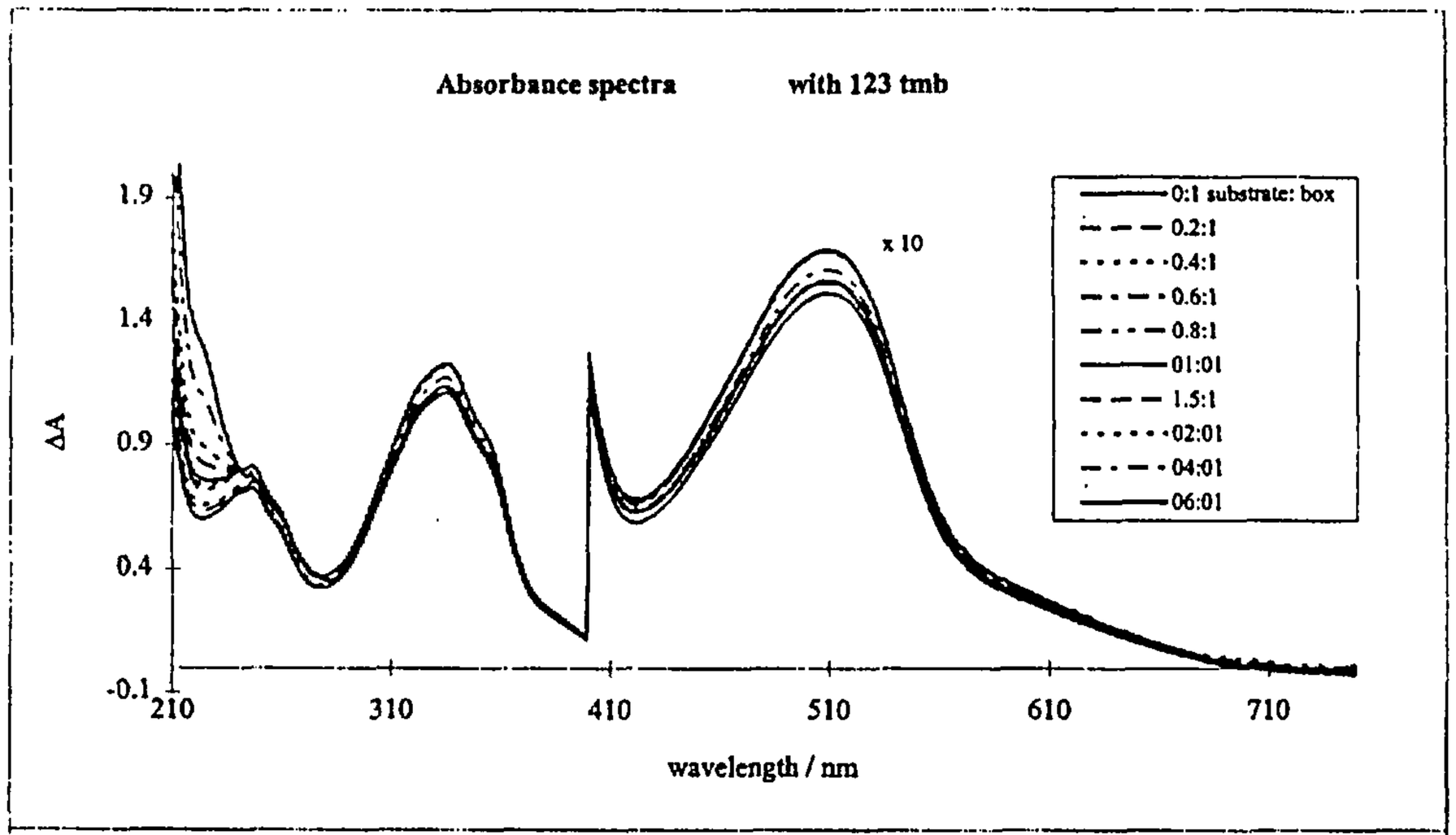
Absorbance spectra with 123 tmb
ΔA
1.9
1.4
0.9
0.4
-0.1
210
310
410
510
610
710
x 10
wavelength / nm
0:1 substrate: box
0.2:1
0.4:1
0.6:1
0.8:1
01:01
1.5:1
02:01
04:01
06:01

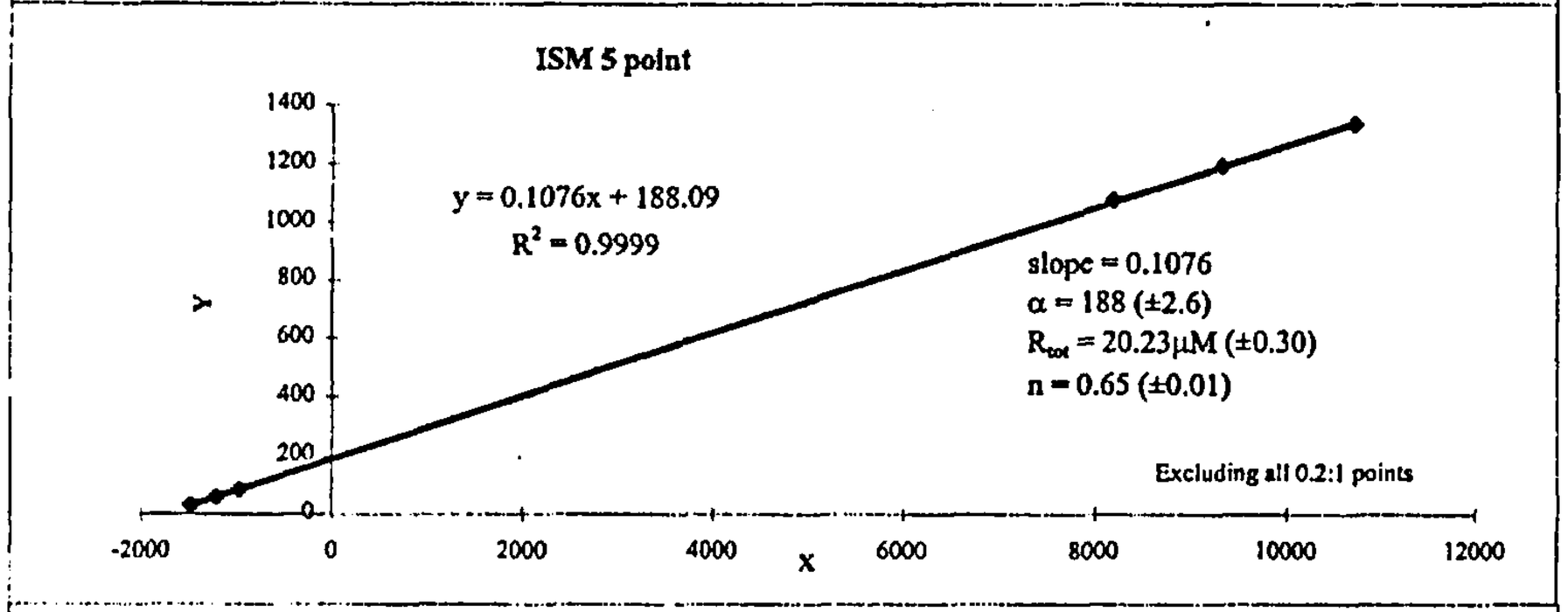
ISM 5 point
y = 0.1076x + 188.09
R² = 0.9999
slope = 0.1076
α = 188 (±2.6)
R_tot = 20.23μM (±0.30)
n = 0.65 (±0.01)
Excluding all 0.2:1 points
Y
X
1400
1200
1000
800
600
400
200
0
-2000
0
2000
4000
6000
8000
10000
12000

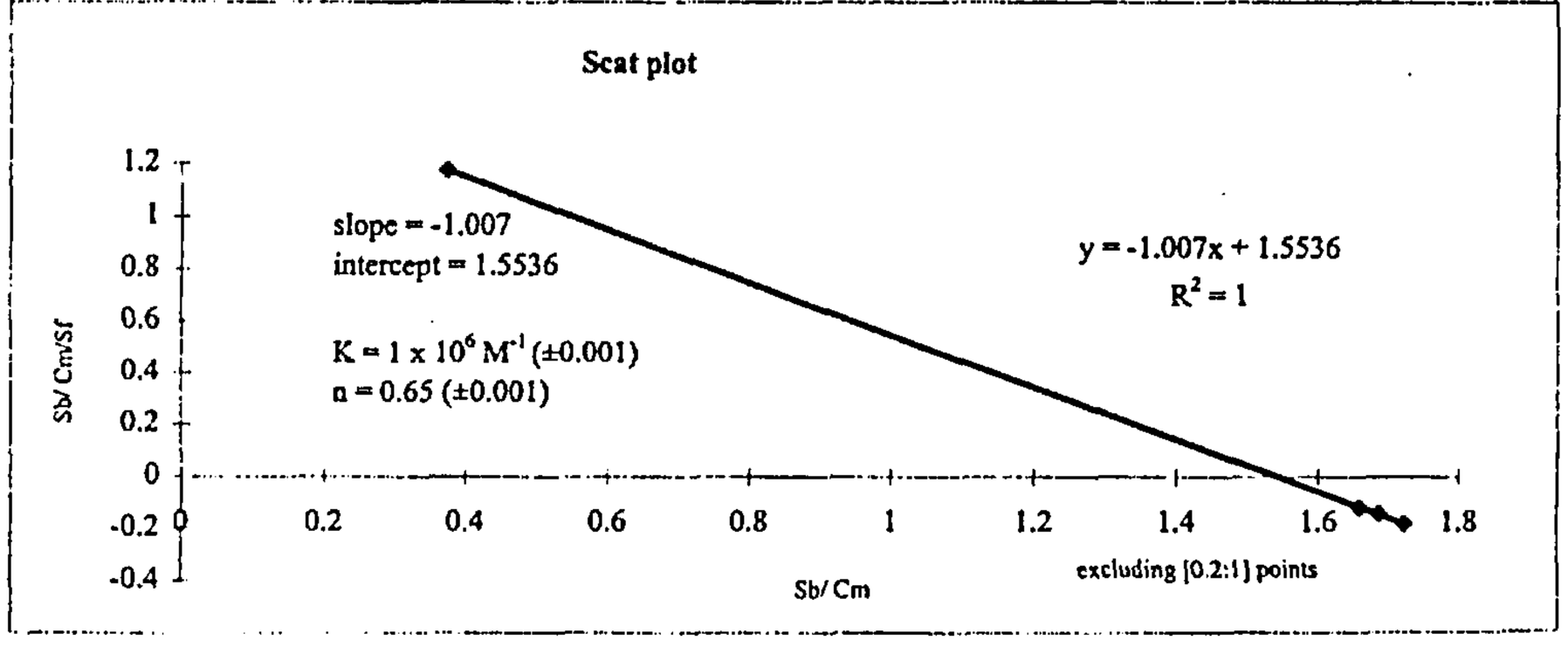
Scat plot
slope = -1.007
intercept = 1.5536
K = 1 x 10⁶ M⁻¹ (±0.001)
n = 0.65 (±0.001)
y = -1.007x + 1.5536
R² = 1
excluding [0.2:1] points
Sb/ Cm/Sf
Sb/ Cm
1.2
1
0.8
0.6
0.4
0.2
0
-0.2
-0.4
0
0.2
0.4
0.6
0.8
1
1.2
1.4
1.6
1.8

Table 1: Absorbance value tables of the copper cyclophane with di- and tri- methoxybenzenes at 335 nm.

with 14dmb		
[substrate: box]	absorbance A	ΔA
00:01	1.233	0.000
0.2:1	1.294	0.062
0.4:1	1.332	0.099
0.6:1	1.366	0.134
0.8:1	1.396	0.163
01:01	1.410	0.177
1.5:1	1.430	0.197
02:01	1.441	0.208
04:01	1.426	0.193
06:01	1.419	0.186

with 13dmb		
[substrate: box]	A	ΔA
00:01	1.301	0.000
0.2:1	1.323	0.022
0.4:1	1.342	0.041
0.6:1	1.362	0.061
0.8:1	1.375	0.074
01:01	1.381	0.080
1.5:1	1.385	0.084
02:01	1.386	0.085
04:01	1.366	0.065
05:01	1.364	0.063

with 12dmb		
[substrate: box]	A	ΔA
00:01	0.961	0.000
0.2:1	0.975	0.013
0.4:1	0.989	0.028
0.6:1	1.001	0.040
0.8:1	1.010	0.049
01:01	1.022	0.061
1.5:1	1.021	0.060
02:01	1.021	0.060
04:01	1.013	0.052
06:01	1.010	0.049

135tmb		
[substrate: box]	A	ΔA
00:01	1.320	0.000
0.2:1	1.364	0.045
0.4:1	1.410	0.090
0.6:1	1.447	0.127
0.8:1	1.485	0.165
01:01	1.515	0.195
1.5:1	1.552	0.232
02:01	1.560	0.240
04:01	1.532	0.212
06:01	1.493	0.174
08:01	1.455	0.135

123tmb		
[substrate: box]	A	ΔA
00:01	1.110	0.000
0.2:1	1.127	0.017
0.4:1	1.136	0.026
0.6:1	1.226	0.116
0.8:1	1.228	0.118
01:01	1.230	0.121
1.5:1	1.226	0.116
02:01	1.217	0.107
04:01	1.173	0.063
06:01	1.137	0.027

Table 2: Absorbance value tables at λ_{max} of the charge transfer regions

14dmb	λmax = 509 nm	
substrate: box	absorbance A	ΔA
00:01	0.170	0.000
0.2:1	0.178	0.008
0.4:1	0.184	0.014
0.6:1	0.188	0.018
0.8:1	0.193	0.023
01:01	0.194	0.024
1.5:1	0.197	0.027
02:01	0.198	0.028
04:01	0.197	0.026
06:01	0.195	0.025

13dmb	λmax = 510 nm	
[substrate: box]	A	ΔA
00:01	0.180	0.000
0.2:1	0.183	0.003
0.4:1	0.186	0.006
0.6:1	0.189	0.010
0.8:1	0.188	0.009
01:01	0.191	0.012
1.5:1	0.192	0.012
02:01	0.192	0.012
04:01	0.189	0.010
05:01	0.189	0.009

12dmb	λmax = 510 nm	
[substrate: box]	A	ΔA
00:01	0.131	0.000
0.2:1	0.134	0.003
0.4:1	0.136	0.005
0.6:1	0.139	0.008
0.8:1	0.140	0.009
01:01	0.141	0.010
1.5:1	0.141	0.011
02:01	0.141	0.011
04:01	0.140	0.010
06:01	0.140	0.009

135tmb	λmax = 510 nm	
[substrate: box]	A	ΔA
00:01	0.183	0.000
0.2:1	0.190	0.007
0.4:1	0.196	0.013
0.6:1	0.201	0.018
0.8:1	0.206	0.023
01:01	0.210	0.027
1.5:1	0.216	0.033
02:01	missing	-
04:01	0.213	0.030
06:01	0.205	0.022
08:01	0.201	0.019

123tmb	λmax = 510 nm	
[substrate: box]	A	ΔA
00:01	0.151	0.000
0.2:1	0.156	0.005
0.4:1	0.157	0.005
0.6:1	0.169	0.017
0.8:1	0.169	0.017
01:01	0.169	0.018
1.5:1	0.169	0.018
02:01	0.168	0.017
04:01	0.161	0.009
06:01	0.156	0.005

Table 3: Binding constants using UV-Visible absorbance spectroscopy

substrate	binding range	α	R_{tot}/C_m	n	K / M^{-1}	n
12dmb	[0.6:1]–[2:1] and [0.4:1]–[1.5:1]	173(±4) – 203(±6)	0.88(±0.03) – 0.91(±0.03)	1.13 – 1.09(±0.03)	$4.34x10^6$(±2.39) – $5.37x10^6$(±0.92)	1.14(±0.24) – 1.09(±0.04)
13dmb	[0.6:1]–[2:1] and [0.4:1]–[1.5:1]	60(±3.3) – 217(±10.5	0.79 (±0.02) – 0.92(±0.045	.26(±0.03) – 1.09(±0.05	$3.2x10^6$(±0.12) – $3.04x10^6$(±0.22) (up to 2.:1)	1.29(±0.07) –1.05(±0.1)
14dmb	[0.6:1]–[2:1]	35(±15) – 85(±11)	0.57 – 1.14	0.79 – 1.7(±0.73)	$1.97x10^5$(±0.63) – $8.5x10^5$	0.81 – 1.69
123tmb*	[0.6:1]–[2:1]	76 – 82, 156* large diff	1.14 – 1.38	0.73 – 0.87	$4.2x10^5$ – $1.15x10^6$	0.67 –1.05
135tmb	[0.6:1]–[2:1]	59(±11) – 73(±1)	0.99(±0.2) – 1.1(±0.02)	0.9(±0.012) – 1.1(±0.2)	$1.30x10^6$(±0.23) –$1.78x10^6$	0.89(±0.02) – 1.05(±0.28)

* = unsure about the data, not very consistent,both the [0.2:1]-[1:1] and [0.6:1]-[2:1] were examined

Appendix 4.2 Fluorescence titration spectra and Scatchard plots.

ΔF fluorescence value table

Binding constants table

Working with á constant substrate concentration of 10 μM

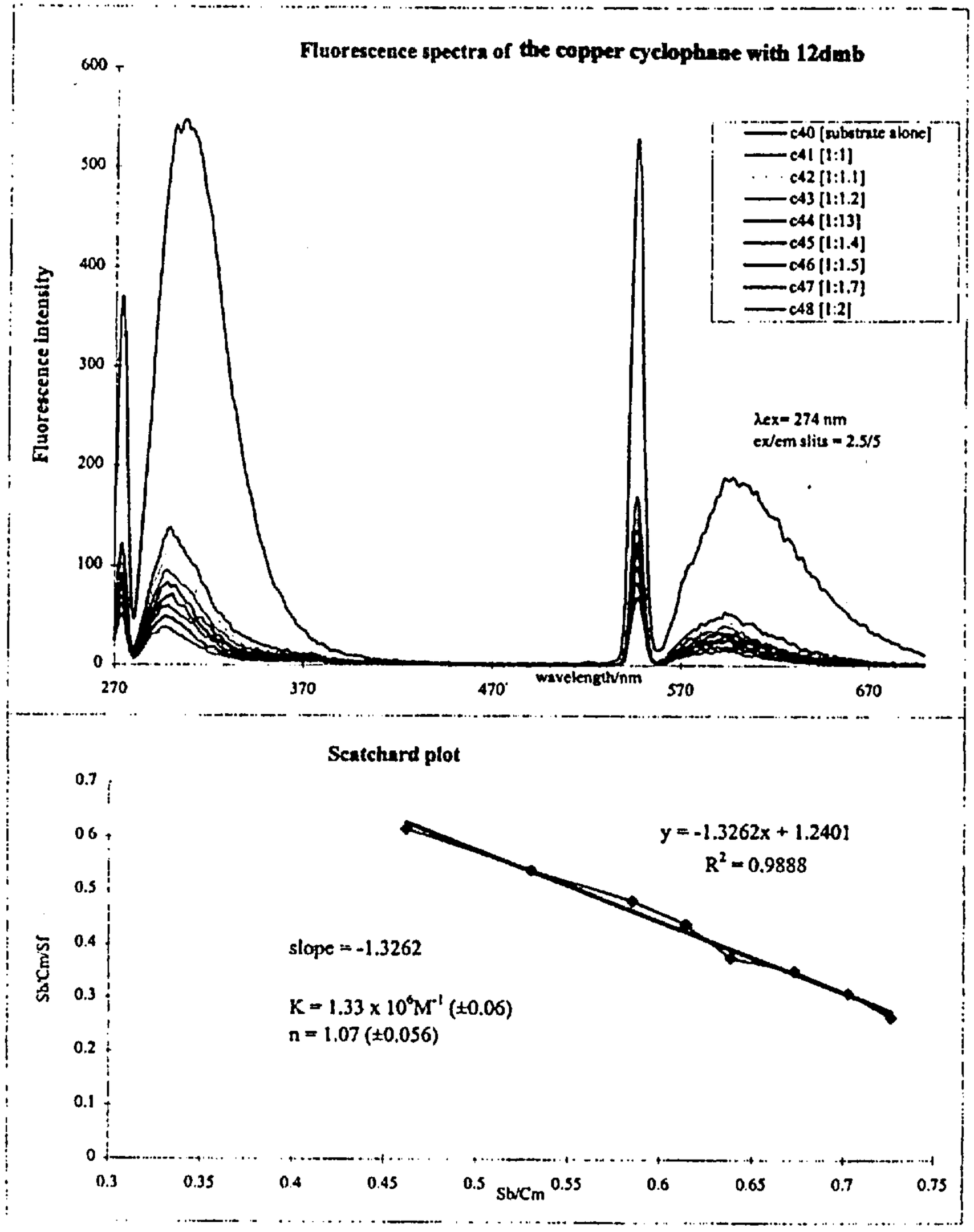
Fluorescence spectra of the copper cyclophane with 12dmb
Fluorescence Intensity
wavelength/nm
c40 [substrate alone]
c41 [1:1]
c42 [1:1.1]
c43 [1:1.2]
c44 [1:13]
c45 [1:1.4]
c46 [1:1.5]
c47 [1:1.7]
c48 [1:2]
λex= 274 nm
ex/em slits = 2.5/5
Scatchard plot
Sb/Cm/Sf
Sb/Cm
y = -1.3262x + 1.2401
R² = 0.9888
slope = -1.3262
K = 1.33 x 10⁶M⁻¹ (±0.06)
n = 1.07 (±0.056)

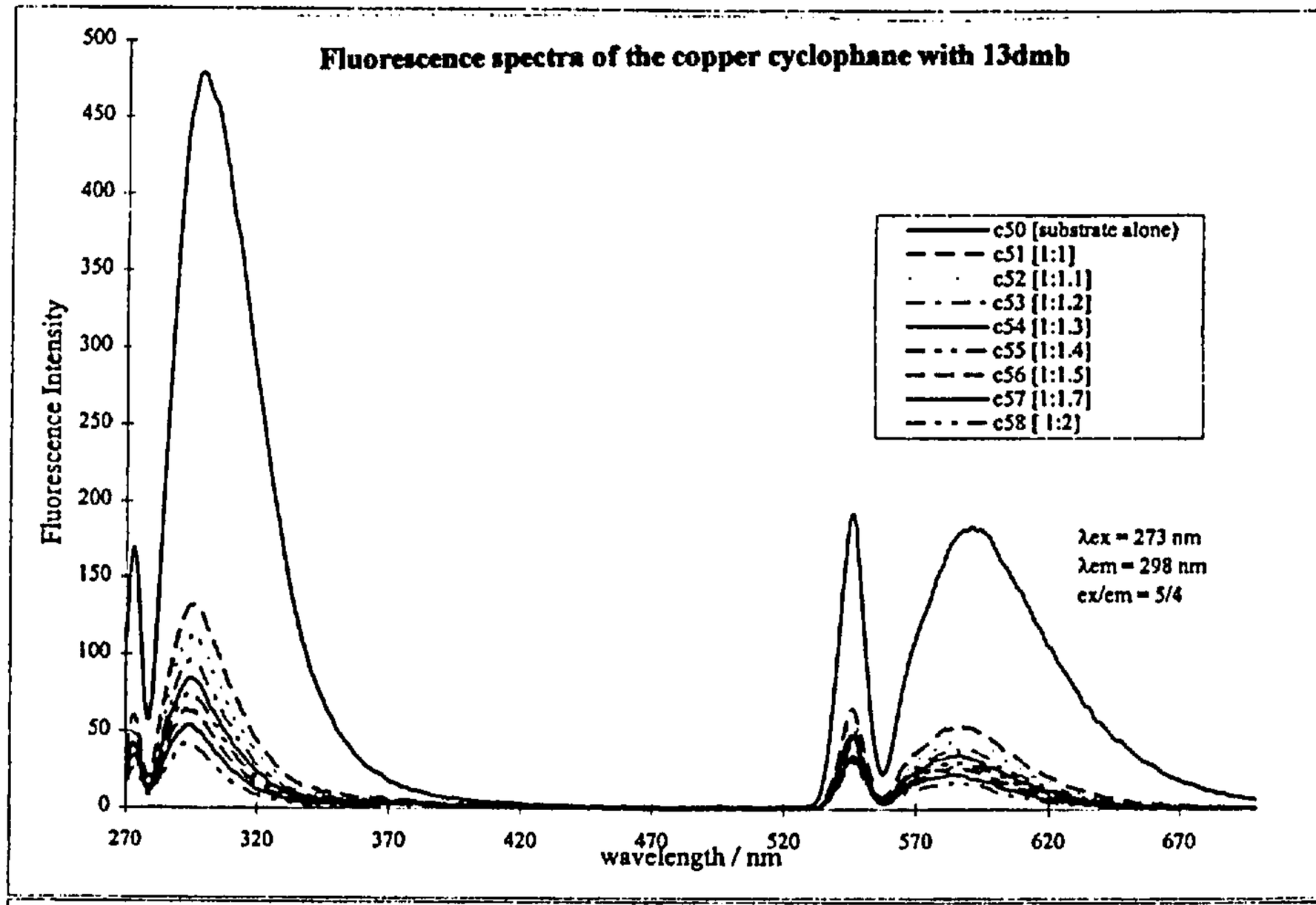
Fluorescence spectra of the copper cyclophane with 13dmb
Fluorescence Intensity
wavelength / nm
c50 [substrate alone)
c51 [1:1]
c52 [1:1.1]
c53 [1:1.2]
c54 [1:1.3]
c55 [1:1.4]
c56 [1:1.5]
c57 [1:1.7]
c58 [1:2]
λex = 273 nm
λem = 298 nm
ex/em = 5/4

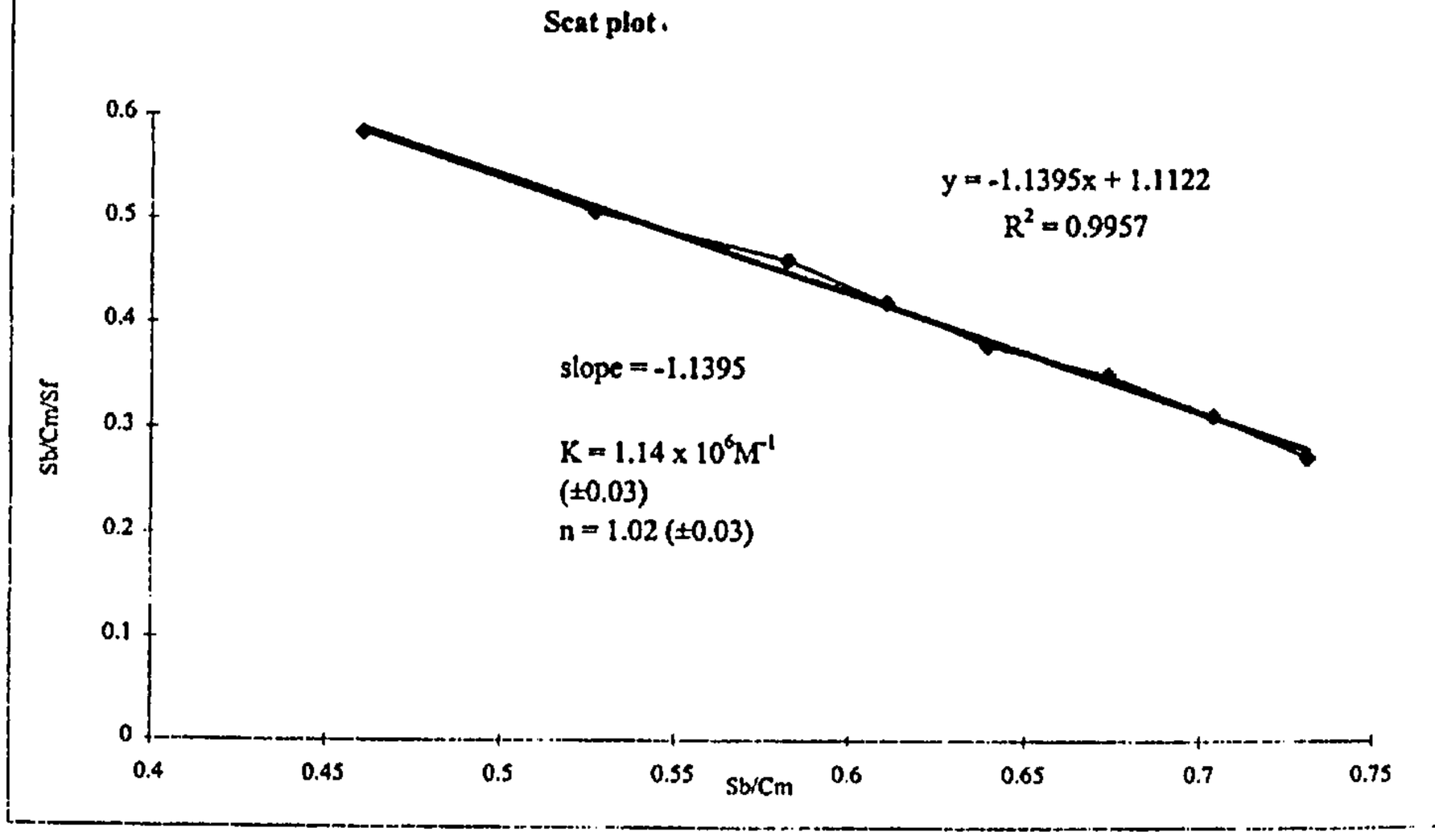
Scat plot .
Sb/Cm/Sf
Sb/Cm
y = -1.1395x + 1.1122
R² = 0.9957
slope = -1.1395
K = 1.14 x 10⁶M⁻¹
(±0.03)
n = 1.02 (±0.03)

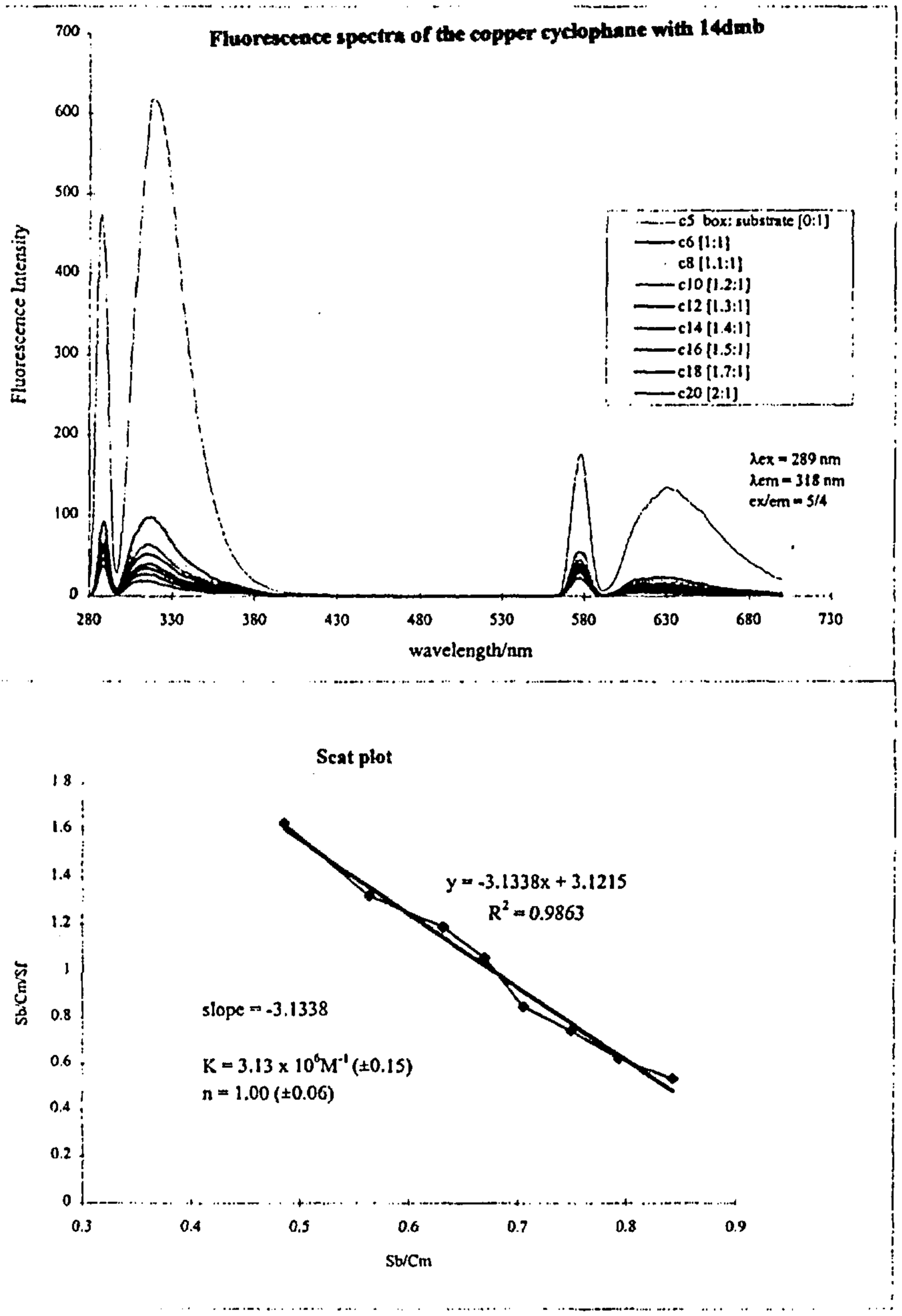
Fluorescence spectra of the copper cyclophane with 14dmb
Fluorescence Intensity
wavelength/nm
c5 box: substrate [0:1]
c6 [1:1]
c8 [1.1:1]
c10 [1.2:1]
c12 [1.3:1]
c14 [1.4:1]
c16 [1.5:1]
c18 [1.7:1]
c20 [2:1]
λex = 289 nm
λem = 318 nm
ex/em = 5/4

Scat plot
Sb/Cm/Sf
Sb/Cm
y = -3.1338x + 3.1215
R² = 0.9863
slope = -3.1338
K = 3.13 x 10⁶M⁻¹ (±0.15)
n = 1.00 (±0.06)

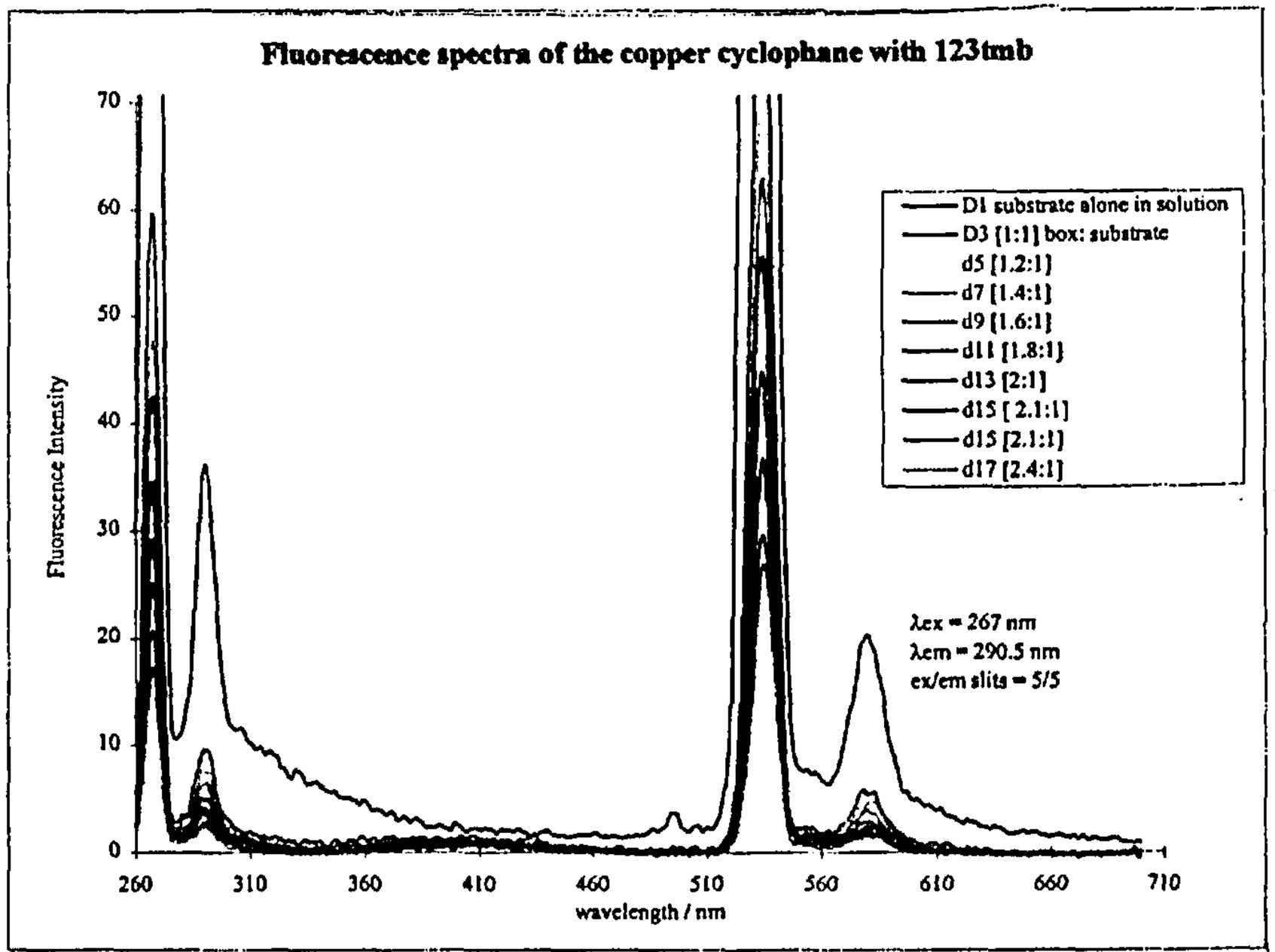
Fluorescence spectra of the copper cyclophane with 123tmb
Fluorescence Intensity
wavelength / nm
D1 substrate alone in solution
D3 [1:1] box: substrate
d5 [1.2:1]
d7 [1.4:1]
d9 [1.6:1]
d11 [1.8:1]
d13 [2:1]
d15 [2.1:1]
d15 [2.1:1]
d17 [2.4:1]
λex = 267 nm
λem = 290.5 nm
ex/em slits = 5/5

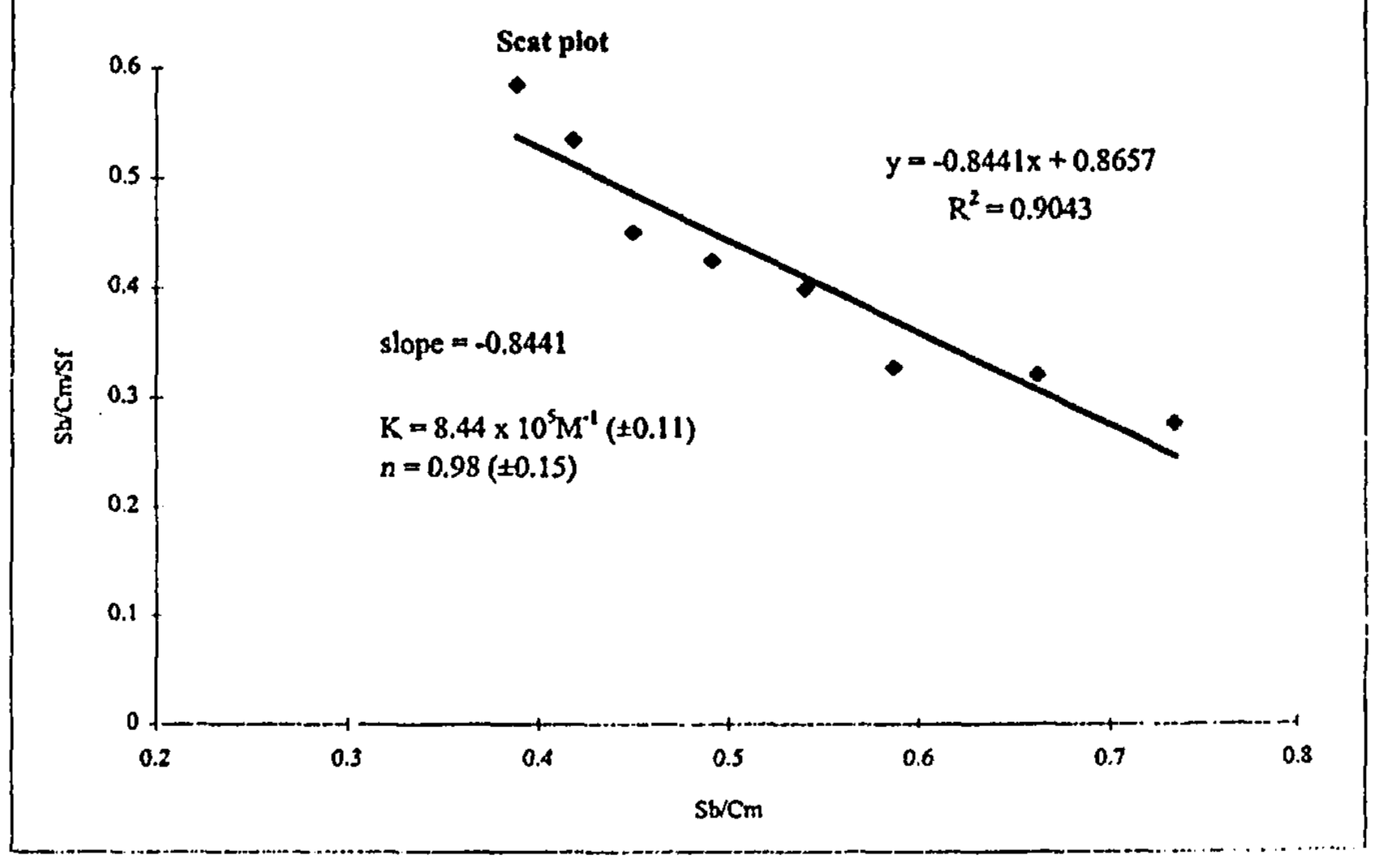
Scat plot
Sb/Cm/Sf
Sb/Cm
y = -0.8441x + 0.8657
R² = 0.9043
slope = -0.8441
K = 8.44 x 10⁵M⁻¹ (±0.11)
n = 0.98 (±0.15)

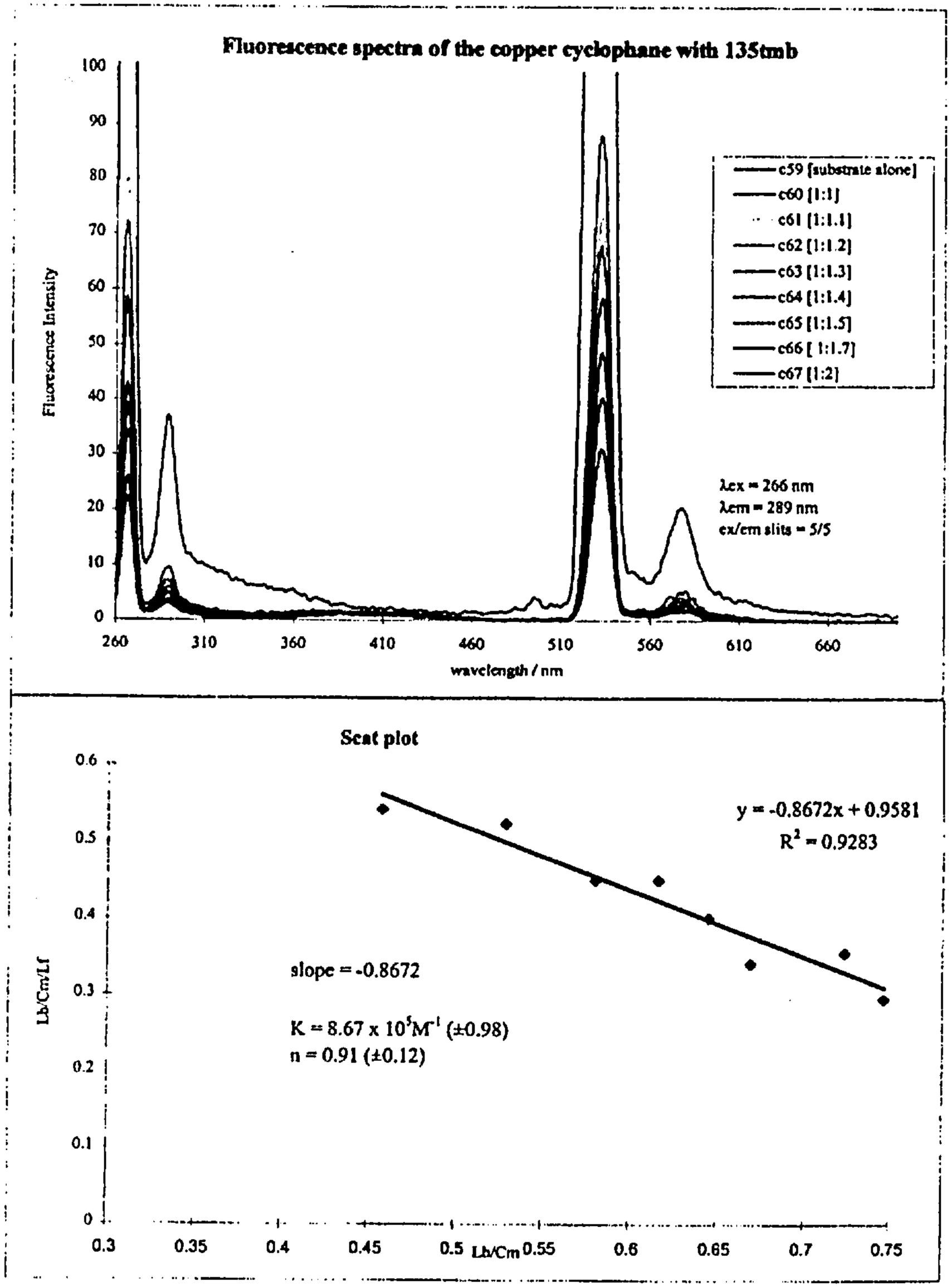
Fluorescence spectra of the copper cyclophane with 135tmb
Fluorescence Intensity
wavelength / nm
c59 [substrate alone]
c60 [1:1]
c61 [1:1.1]
c62 [1:1.2]
c63 [1:1.3]
c64 [1:1.4]
c65 [1:1.5]
c66 [1:1.7]
c67 [1:2]
λex = 266 nm
λem = 289 nm
ex/em slits = 5/5
Scat plot
Lb/Cm/Lf
Lb/Cm
y = -0.8672x + 0.9581
R² = 0.9283
slope = -0.8672
K = 8.67 x 10⁵M⁻¹ (±0.98)
n = 0.91 (±0.12)

Table 1: Fluorescence value tables of the copper cyclophane with di and tri- methoxy benzenes

	with 13 dmb		
	[box:substrate]	Fluorescence F	ΔF
F_f	00:01	479	0
	01:01	129	-350
	1.2:1	108	-371
	1.4:1	92	-387
	1.6:1	81	-398
	1.8:1	70	-409
	2.0:1	61	-418
	2.2:1	50	-429
F_b	2.4:1	38	-441

	with 12 dmb		
	[box:substrate]	F	ΔF
F_f	00:01	494	0
	01:01	135	-359
	1.1:1	112	-382
	1.2:1	95	-399
	1.3:1	84	-410
	1.4:1	69	-424
	1.5:1	60	-434
	1.7:1	49	-445
F_b	02:01	37	-456

	with 14 dmb		
	[box:substrate]	F	ΔF
F_f	00:01	619.4	0.0
	01:01	97.7	-521.7
	1.1:1	79.0	-540.4
	1.2:1	62.6	-556.8
	1.3:1	51.7	-567.7
	1.4:1	39.2	-580.1
	1.5:1	32.9	-586.4
	1.7:1	26.5	-592.9
F_b	02:01	18.5	-600.9

	with 135 tmb		
	[box:substrate]	F	ΔF
F_f	00:01	37.17	0.00
	01:01	9.41	-27.76
	1.1:1	7.57	-29.60
	1.2:1	7.30	-29.87
	1.3:1	5.99	-31.19
	1.4:1	5.10	-32.08
	1.5:1	4.80	-32.37
	1.7:1	3.76	-33.42
F_b	02:01	3.14	-34.03

	with 123 tmb		
	[box:substrate]	F	ΔF
F_f	00:01	36.1	0.0
	01:01	9.6	-26.5
	1.2:1	7.4	-28.7
	1.4:1	6.5	-29.7
	1.6:1	4.9	-31.2
	1.8:1	4.2	-31.9
	2.0:1	3.6	-32.5
	2.2:1	2.8	-33.3
F_b	2.4:1	2.4	-33.7

Table 2: Binding constants using fluorescence

substrate	K / M^{-1}	n
12dmb	$1.33 \times 10^6(\pm 0.06) - 1.56 \times 10^6(\pm 0.21)$	$1.07(\pm 0.05) - 1.08(\pm 0.17)$
13dmb	$1.14 \times 10^6(\pm 0.003) - 1.56 \times 10^6(\pm 0.03)$	$1.02(\pm 0.03) - 0.99(\pm 0.17)$
14dmb	$3.13 \times 10^6(\pm 0.65) - 5.22 \times 10^6(\pm 0.99)$	$1.00(\pm 0.60) - 1.06(\pm 0.24)$
123tmb	$7.47 \times 10^5(\pm 0.11) - 1.06 \times 10^6(\pm 0.11)$	$0.98(\pm 0.15) - 1.14(\pm 0.13)$
135tmb	$7.55 \times 10^5(\pm 1.48) - 1.18 \times 10^6(\pm 0.10)$	$0.91(\pm 0.12) - 1.27(\pm 0.14)$

Appendix 4.3 X-ray crystal data

Table 1. Crystal data and structure refinement for jnat.

Identification code	jnat
Empirical formula	C56 H51 B2 Cu2 F8 N9
Formula weight	1150.76
Temperature	293(2) K
Wavelength	0.71073 A
Crystal system, space group	Triclinic, P-1
Unit cell dimensions	a = 11.6049(2) A alpha = 87.9650(10) b = 14.8366(3) A beta = 73.5870(10) c = 16.37190(10) A gamma = 79.6210(1
Volume	2659.40(7) A^3
Z, Calculated density	2, 1.437 Mg/m^3
Absorption coefficient	0.875 mm^-1
F(000)	1180
Crystal size	0.50 x 0.40 x 0.04 mm
Theta range for data collection	1.89 to 28.97 deg.
Limiting indices	-15<=h<=15, -18<=k<=19, -20<=l<=21
Reflections collected / unique	17626 / 12215 [R(int) = 0.0310]
Completeness to theta = 28.97	86.6 %
Absorption correction	Semi-empirical from equivalents
Max. and min. transmission	0.928 and 0.670
Refinement method	Full-matrix least-squares on F^2
Data / restraints / parameters	12215 / 94 / 694
Goodness-of-fit on F^2	1.017
Final R indices [I>2sigma(I)]	R1 = 0.0636, wR2 = 0.1264
R indices (all data)	R1 = 0.1221, wR2 = 0.1561
Largest diff. peak and hole	0.930 and -0.714 e.A^-3

Table 1. Selected bond lengths [A] and angles [deg] for jnat.

Cu(1)-N(30)#1	2.007(3)
Cu(1)-N(7)	2.025(3)
Cu(1)-N(9)	2.042(3)
Cu(1)-N(23)#1	2.084(3)
N(38)-C(33)	1.347(6)
N(38)-C(37)	1.358(6)
N(38)-Cu(2)	2.010(3)
N(40)-C(39)	1.281(5)
N(40)-C(41)	1.433(5)
N(40)-Cu(2)	2.073(3)
N(54)-C(55)	1.288(5)
N(54)-C(51)	1.426(5)
N(54)-Cu(2)	2.029(3)
N(61)-C(60)	1.339(5)
N(61)-C(56)	1.360(5)
N(61)-Cu(2)	2.053(3)
N(7)-C(2)	1.343(5)
N(7)-C(6)	1.368(5)
N(9)-C(8)	1.283(5)
N(9)-C(10)	1.426(5)
N(23)-C(24)	1.285(5)
N(23)-C(20)	1.424(5)
N(23)-Cu(1)#1	2.084(3)
N(30)-C(29)	1.336(6)
N(30)-C(25)	1.356(6)
N(30)-Cu(1)#1	2.007(3)
N(30)#1-Cu(1)-N(7)	130.17(14)
N(30)#1-Cu(1)-N(9)	128.17(14)
N(7)-Cu(1)-N(9)	82.04(14)
N(30)#1-Cu(1)-N(23)#1	81.78(14)
N(7)-Cu(1)-N(23)#1	127.31(14)
N(9)-Cu(1)-N(23)#1	111.96(13)
C(33)-N(38)-C(37)	119.0(4)
C(33)-N(38)-Cu(2)	128.5(3)
C(37)-N(38)-Cu(2)	112.4(3)
C(39)-N(40)-C(41)	120.4(4)
C(39)-N(40)-Cu(2)	111.4(3)
C(41)-N(40)-Cu(2)	128.1(3)
C(55)-N(54)-C(51)	118.6(4)
C(55)-N(54)-Cu(2)	112.5(3)
C(51)-N(54)-Cu(2)	128.2(3)
C(60)-N(61)-C(56)	118.5(4)
C(60)-N(61)-Cu(2)	130.2(3)
C(56)-N(61)-Cu(2)	111.2(3)
N(38)-Cu(2)-N(54)	134.98(14)
N(38)-Cu(2)-N(61)	123.76(14)
N(54)-Cu(2)-N(61)	81.46(14)
N(38)-Cu(2)-N(40)	81.58(14)
N(54)-Cu(2)-N(40)	120.42(13)
N(61)-Cu(2)-N(40)	119.78(14)
C(2)-N(7)-C(6)	118.1(4)
C(2)-N(7)-Cu(1)	131.2(3)
C(6)-N(7)-Cu(1)	110.4(3)
C(8)-N(9)-C(10)	119.4(4)
C(8)-N(9)-Cu(1)	111.4(3)
C(10)-N(9)-Cu(1)	128.9(3)
C(24)-N(23)-C(20)	120.8(4)
C(24)-N(23)-Cu(1)#1	110.1(3)
C(20)-N(23)-Cu(1)#1	128.1(3)
C(29)-N(30)-C(25)	119.1(4)
C(29)-N(30)-Cu(1)#1	128.3(3)
C(25)-N(30)-Cu(1)#1	112.6(3)

Symmetry transformations used to generate equivalent atoms:
#1 -x,-y,-z

Table 2. Atomic coordinates (x 10^4) and equivalent isotropic displacement parameters (A^2 x 10^3) for jnat.
U(eq) is defined as one third of the trace of the orthogonalized Uij tensor.

	x	y	z	U(eq)
Cu(1)	-808(1)	-1183(1)	-2975(1)	31(1)
N(38)	2443(3)	6593(2)	2878(2)	30(1)
N(40)	667(3)	5715(2)	2789(2)	27(1)
N(54)	3358(3)	4783(2)	1178(2)	27(1)
N(61)	3427(3)	4158(2)	2712(2)	27(1)
C(32)	4625(5)	6553(4)	2506(4)	56(2)
C(33)	3358(5)	7016(3)	2923(3)	39(1)
C(34)	3094(5)	7862(3)	3343(3)	47(1)
C(35)	1920(6)	8267(3)	3713(4)	52(1)
C(36)	975(5)	7830(3)	3676(3)	39(1)
C(37)	1272(4)	6995(3)	3257(3)	29(1)
C(39)	338(4)	6498(3)	3171(3)	28(1)
C(41)	-228(4)	5222(3)	2669(3)	26(1)
C(42)	-1460(4)	5403(3)	3114(3)	35(1)
C(43)	633(4)	5952(3)	-1871(3)	37(1)
C(45)	-2257(4)	4914(3)	2920(3)	37(1)
C(44)	1864(4)	5765(3)	-2296(3)	32(1)
C(46)	174(4)	4527(3)	2060(3)	38(1)
C(47)	2758(4)	6225(3)	-2012(3)	35(1)
C(48)	2936(4)	5847(3)	-1175(3)	30(1)
C(49)	2954(5)	4923(3)	-1000(3)	46(1)
C(50)	3124(5)	4564(3)	-245(3)	47(1)
C(51)	3241(4)	5126(3)	375(3)	27(1)
C(52)	3221(4)	6052(3)	212(3)	30(1)
C(53)	3076(4)	6405(3)	-554(3)	32(1)
C(55)	3915(4)	3955(3)	1212(3)	28(1)
C(56)	3975(4)	3578(3)	2033(3)	26(1)
C(57)	4582(4)	2702(3)	2110(3)	31(1)
C(58)	4630(4)	2406(3)	2910(3)	39(1)
C(59)	4089(4)	2992(3)	3598(3)	38(1)
C(60)	3492(4)	3871(3)	3484(3)	31(1)
C(62)	2893(5)	4532(4)	4211(3)	49(1)
Cu(2)	2551(1)	5367(1)	2349(1)	31(1)
N(7)	-2486(3)	-711(2)	-3122(2)	28(1)
N(9)	-1806(3)	-1337(2)	-1749(2)	26(1)
N(23)	-569(3)	433(2)	3039(2)	27(1)
N(30)	-598(3)	2066(2)	3698(2)	29(1)
C(1)	-1899(5)	-651(4)	-4662(3)	47(1)
C(2)	-2844(4)	-454(3)	-3819(3)	34(1)
C(3)	-4036(5)	-19(3)	-3754(4)	43(1)
C(4)	-4872(5)	153(3)	-2975(4)	45(1)
C(5)	-4527(4)	-131(3)	-2250(3)	37(1)
C(6)	-3339(4)	-573(3)	-2345(3)	30(1)
C(8)	-2920(4)	-935(3)	-1619(3)	30(1)
C(10)	-1400(4)	-1734(3)	-1051(3)	27(1)
C(11)	-2133(4)	-2176(3)	-396(3)	34(1)
C(12)	-1693(4)	-2539(3)	269(3)	33(1)
C(13)	-535(4)	-2473(3)	311(3)	28(1)
C(14)	201(4)	-2046(3)	-361(3)	29(1)
C(15)	-225(4)	-1687(3)	-1036(3)	29(1)
C(16)	-91(4)	-2803(3)	1073(3)	32(1)
C(17)	-191(4)	-2004(3)	1649(3)	27(1)
C(18)	-1281(4)	-1687(3)	2267(3)	32(1)
C(19)	-1426(4)	-912(3)	2749(3)	31(1)
C(20)	-482(4)	-407(3)	2611(3)	28(1)
C(21)	627(4)	-747(3)	2020(3)	31(1)
C(22)	771(4)	-1527(3)	1543(3)	32(1)
C(24)	-1614(4)	909(3)	3416(3)	30(1)
C(25)	-1682(4)	1788(3)	3814(3)	32(1)
C(26)	-2780(4)	2299(3)	4275(3)	40(1)
C(27)	-2768(5)	3128(4)	4622(3)	50(1)
C(28)	-1665(5)	3409(3)	4508(3)	45(1)
C(29)	-578(4)	2864(3)	4042(3)	34(1)
C(31)	630(5)	3152(3)	3915(3)	46(1)
B(1)	-3784(5)	7650(4)	4191(3)	39(1)
F(1)	-3800(3)	7882(2)	3372(2)	59(1)
F(2)	-2608(2)	7468(2)	4255(2)	50(1)
F(3)	-4448(3)	8362(2)	4747(2)	69(1)
F(4)	-4311(3)	6881(2)	4416(2)	63(1)
B(2)	-4451(5)	1562(4)	-501(4)	49(2)
F(5)	-5261(4)	993(3)	-463(3)	142(2)
F(6)	-3478(3)	1249(4)	-1112(3)	143(2)
F(7)	-5003(5)	2432(3)	-574(3)	121(2)
F(8)	-4257(8)	1571(5)	260(4)	220(4)
N(1S)	-2711(4)	1145(3)	1825(3)	49(1)
C(1S)	-2465(4)	641(3)	1273(3)	40(1)
C(2S)	-2143(6)	-2(4)	564(4)	70(2)

Table 3. Selected bond lengths [A] and angles [deg] for jnat.

Symmetry transformations used to generate equivalent atoms:

C(10)-C(15)	1.384(6)
C(10)-C(11)	1.392(6)
C(11)-C(12)	1.383(6)
C(12)-C(13)	1.385(6)
C(13)-C(14)	1.398(6)
C(13)-C(16)	1.514(6)
C(14)-C(15)	1.387(6)
C(16)-C(17)	1.509(6)
C(17)-C(18)	1.393(6)
C(17)-C(22)	1.394(6)
C(18)-C(19)	1.376(6)
C(19)-C(20)	1.399(6)
C(20)-C(21)	1.395(6)
C(21)-C(22)	1.376(6)
C(24)-C(25)	1.458(6)
C(25)-C(26)	1.385(6)
C(26)-C(27)	1.376(7)
C(27)-C(28)	1.379(7)
C(28)-C(29)	1.399(6)
C(29)-C(31)	1.495(7)
B(1)-F(2)	1.376(6)
B(1)-F(1)	1.376(6)
B(1)-F(4)	1.381(6)
B(1)-F(3)	1.385(6)
B(2)-F(6)	1.303(6)
B(2)-F(8)	1.329(7)
B(2)-F(7)	1.351(6)
B(2)-F(5)	1.359(7)
N(1S)-C(1S)	1.132(6)
C(1S)-C(2S)	1.450(8)
N(30)#1-Cu(1)-N(7)	130.17(14)
N(30)#1-Cu(1)-N(9)	128.17(14)
N(7)-Cu(1)-N(9)	82.04(14)
N(30)#1-Cu(1)-N(23)#1	81.78(14)
N(7)-Cu(1)-N(23)#1	127.31(14)
N(9)-Cu(1)-N(23)#1	111.96(13)
C(33)-N(38)-C(37)	119.0(4)
C(33)-N(38)-Cu(2)	128.5(3)
C(37)-N(38)-Cu(2)	112.4(3)
C(39)-N(40)-C(41)	120.4(4)
C(39)-N(40)-Cu(2)	111.4(3)
C(41)-N(40)-Cu(2)	128.1(3)
C(55)-N(54)-C(51)	118.6(4)
C(55)-N(54)-Cu(2)	112.5(3)
C(51)-N(54)-Cu(2)	128.2(3)
C(60)-N(61)-C(56)	118.5(4)
C(60)-N(61)-Cu(2)	130.2(3)
C(56)-N(61)-Cu(2)	111.2(3)
N(38)-C(33)-C(34)	119.9(5)
N(38)-C(33)-C(32)	117.5(4)
C(34)-C(33)-C(32)	122.5(5)
C(35)-C(34)-C(33)	120.8(5)
C(34)-C(35)-C(36)	119.5(5)
C(37)-C(36)-C(35)	118.0(5)
N(38)-C(37)-C(36)	122.8(4)
N(38)-C(37)-C(39)	115.5(4)
C(36)-C(37)-C(39)	121.7(4)
N(40)-C(39)-C(37)	119.0(4)
C(46)-C(41)-C(42)	118.6(4)
C(46)-C(41)-N(40)	116.9(4)
C(42)-C(41)-N(40)	124.5(4)
C(45)-C(42)-C(41)	119.8(4)
C(46)#2-C(43)-C(44)	121.0(4)

C(42)-C(45)-C(44)#2	121.7(4)
C(43)-C(44)-C(45)#2	117.9(4)
C(43)-C(44)-C(47)	120.1(4)
C(45)#2-C(44)-C(47)	121.6(4)
C(43)#2-C(46)-C(41)	120.9(4)
C(48)-C(47)-C(44)	111.5(4)
C(49)-C(48)-C(53)	117.8(4)
C(49)-C(48)-C(47)	120.4(4)
C(53)-C(48)-C(47)	121.9(4)
C(50)-C(49)-C(48)	121.3(4)
C(49)-C(50)-C(51)	120.7(4)
C(50)-C(51)-C(52)	118.7(4)
C(50)-C(51)-N(54)	122.0(4)
C(52)-C(51)-N(54)	119.3(4)
C(53)-C(52)-C(51)	120.4(4)
C(52)-C(53)-C(48)	121.1(4)
N(54)-C(55)-C(56)	119.2(4)
N(61)-C(56)-C(57)	122.8(4)
N(61)-C(56)-C(55)	115.2(4)
C(57)-C(56)-C(55)	122.0(4)
C(58)-C(57)-C(56)	118.4(4)
C(59)-C(58)-C(57)	119.1(4)
C(58)-C(59)-C(60)	120.2(4)
N(61)-C(60)-C(59)	121.0(4)
N(61)-C(60)-C(62)	116.9(4)
C(59)-C(60)-C(62)	122.1(4)
N(38)-Cu(2)-N(54)	134.98(14)
N(38)-Cu(2)-N(61)	123.76(14)
N(54)-Cu(2)-N(61)	81.46(14)
N(38)-Cu(2)-N(40)	81.58(14)
N(54)-Cu(2)-N(40)	120.42(13)
N(61)-Cu(2)-N(40)	119.78(14)
C(2)-N(7)-C(6)	118.1(4)
C(2)-N(7)-Cu(1)	131.2(3)
C(6)-N(7)-Cu(1)	110.4(3)
C(8)-N(9)-C(10)	119.4(4)
C(8)-N(9)-Cu(1)	111.4(3)
C(10)-N(9)-Cu(1)	128.9(3)
C(24)-N(23)-C(20)	120.8(4)
C(24)-N(23)-Cu(1)#1	110.1(3)
C(20)-N(23)-Cu(1)#1	128.1(3)
C(29)-N(30)-C(25)	119.1(4)
C(29)-N(30)-Cu(1)#1	128.3(3)
C(25)-N(30)-Cu(1)#1	112.6(3)
N(7)-C(2)-C(3)	121.0(4)
N(7)-C(2)-C(1)	116.7(4)
C(3)-C(2)-C(1)	122.2(4)
C(4)-C(3)-C(2)	120.6(5)
C(3)-C(4)-C(5)	119.1(4)
C(6)-C(5)-C(4)	118.3(5)
N(7)-C(6)-C(5)	122.7(4)
N(7)-C(6)-C(8)	115.5(4)
C(5)-C(6)-C(8)	121.8(4)
N(9)-C(8)-C(6)	118.8(4)
C(15)-C(10)-C(11)	119.3(4)
C(15)-C(10)-N(9)	118.3(4)
C(11)-C(10)-N(9)	122.4(4)
C(12)-C(11)-C(10)	119.7(4)
C(11)-C(12)-C(13)	121.9(4)
C(12)-C(13)-C(14)	117.7(4)
C(12)-C(13)-C(16)	121.8(4)
C(14)-C(13)-C(16)	120.4(4)
C(15)-C(14)-C(13)	121.0(4)
C(10)-C(15)-C(14)	120.3(4)
C(17)-C(16)-C(13)	110.2(3)
C(18)-C(17)-C(22)	118.2(4)
C(18)-C(17)-C(16)	120.5(4)
C(22)-C(17)-C(16)	121.2(4)
C(19)-C(18)-C(17)	121.4(4)
C(18)-C(19)-C(20)	120.3(4)
C(21)-C(20)-C(19)	118.1(4)
C(21)-C(20)-N(23)	117.3(4)
C(19)-C(20)-N(23)	124.5(4)
C(22)-C(21)-C(20)	121.2(4)
C(21)-C(22)-C(17)	120.6(4)
N(23)-C(24)-C(25)	119.9(4)
N(30)-C(25)-C(26)	122.7(4)
N(30)-C(25)-C(24)	115.2(4)
C(26)-C(25)-C(24)	122.1(4)
C(27)-C(26)-C(25)	118.5(5)
C(26)-C(27)-C(28)	118.8(5)
C(27)-C(28)-C(29)	120.5(5)
N(30)-C(29)-C(28)	120.4(4)
N(30)-C(29)-C(31)	118.2(4)
C(28)-C(29)-C(31)	121.5(4)
F(2)-B(1)-F(1)	111.0(4)
F(2)-B(1)-F(4)	109.1(4)
F(1)-B(1)-F(4)	109.1(4)
F(2)-B(1)-F(3)	109.0(4)
F(1)-B(1)-F(3)	109.8(4)
F(4)-B(1)-F(3)	108.8(4)
F(6)-B(2)-F(8)	113.9(6)
F(6)-B(2)-F(7)	116.6(6)
F(8)-B(2)-F(7)	102.9(5)
F(6)-B(2)-F(5)	106.8(5)
F(8)-B(2)-F(5)	107.6(6)
F(7)-B(2)-F(5)	108.7(5)
N(1S)-C(1S)-C(2S)	179.6(6)

Symmetry transformations used to generate equivalent atoms:
#1 -x,-y,-z #2 -x,-y+1,-z

Table 5. Anisotropic displacement parameters (A^2 x 10^3) for jnat.
The anisotropic displacement factor exponent takes the form:
-2 pi^2 [h^2 a*^2 U11 + ... + 2 h k a* b* U12]

	U11	U22	U33	U23	U13	U12
Cu(1)	24(1)	38(1)	29(1)	-3(1)	-4(1)	-4(1)
N(38)	38(2)	23(2)	34(2)	0(2)	-17(2)	-7(2)
N(40)	29(2)	24(2)	28(2)	-1(2)	-11(2)	-3(2)
N(54)	27(2)	30(2)	24(2)	0(2)	-9(2)	-6(2)
N(61)	26(2)	26(2)	28(2)	-6(2)	-6(2)	-1(1)
C(32)	40(3)	61(4)	71(4)	-8(3)	-18(3)	-18(3)
C(33)	46(3)	39(3)	39(3)	7(2)	-17(2)	-16(2)
C(34)	61(4)	40(3)	55(3)	0(2)	-27(3)	-26(3)
C(35)	77(4)	27(3)	58(4)	-8(2)	-27(3)	-13(3)
C(36)	55(3)	26(2)	39(3)	-4(2)	-20(2)	0(2)
C(37)	41(3)	22(2)	28(2)	1(2)	-16(2)	-5(2)
C(39)	30(2)	25(2)	28(2)	0(2)	-10(2)	2(2)
C(41)	28(2)	28(2)	25(2)	2(2)	-11(2)	-3(2)
C(42)	38(3)	38(3)	26(2)	-5(2)	-7(2)	-4(2)
C(43)	34(3)	31(2)	46(3)	-11(2)	-13(2)	-3(2)
C(45)	28(2)	51(3)	28(2)	1(2)	-3(2)	-6(2)
C(44)	36(3)	37(3)	28(2)	9(2)	-15(2)	-12(2)
C(46)	25(2)	35(3)	52(3)	-12(2)	-11(2)	0(2)
C(47)	35(3)	40(3)	35(3)	9(2)	-13(2)	-15(2)
C(48)	26(2)	33(2)	32(2)	4(2)	-9(2)	-9(2)
C(49)	69(4)	42(3)	38(3)	0(2)	-30(3)	-19(3)
C(50)	80(4)	29(3)	47(3)	6(2)	-37(3)	-20(3)
C(51)	23(2)	34(2)	26(2)	1(2)	-8(2)	-7(2)
C(52)	27(2)	33(2)	33(2)	-8(2)	-12(2)	-3(2)
C(53)	30(2)	29(2)	38(3)	4(2)	-10(2)	-4(2)
C(55)	21(2)	37(2)	26(2)	-5(2)	-7(2)	-3(2)
C(56)	24(2)	25(2)	28(2)	-4(2)	-7(2)	-4(2)
C(57)	30(2)	29(2)	31(2)	-7(2)	-6(2)	0(2)
C(58)	40(3)	30(2)	42(3)	-1(2)	-10(2)	0(2)
C(59)	47(3)	35(3)	29(2)	4(2)	-9(2)	-1(2)
C(60)	34(2)	30(2)	28(2)	-2(2)	-8(2)	-3(2)
C(62)	68(4)	43(3)	30(3)	-9(2)	-10(3)	4(3)
Cu(2)	30(1)	27(1)	35(1)	-8(1)	-10(1)	0(1)
N(7)	29(2)	28(2)	29(2)	1(2)	-13(2)	-6(2)
N(9)	23(2)	29(2)	26(2)	-2(2)	-6(1)	-8(2)
N(23)	25(2)	34(2)	21(2)	0(2)	-4(1)	-6(2)
N(30)	27(2)	31(2)	26(2)	-2(2)	-7(2)	0(2)
C(1)	61(3)	51(3)	31(3)	5(2)	-19(2)	-10(3)
C(2)	45(3)	25(2)	39(3)	4(2)	-22(2)	-11(2)
C(3)	50(3)	33(3)	57(3)	11(2)	-33(3)	-10(2)
C(4)	33(3)	39(3)	69(4)	-2(3)	-27(3)	0(2)
C(5)	27(2)	34(3)	50(3)	-8(2)	-11(2)	-5(2)
C(6)	25(2)	28(2)	38(3)	-6(2)	-10(2)	-7(2)
C(8)	25(2)	32(2)	31(2)	-1(2)	-5(2)	-6(2)
C(10)	30(2)	26(2)	24(2)	-6(2)	-7(2)	-3(2)
C(11)	29(2)	41(3)	33(3)	3(2)	-8(2)	-14(2)
C(12)	36(3)	35(2)	30(2)	6(2)	-7(2)	-16(2)
C(13)	35(2)	23(2)	27(2)	-5(2)	-10(2)	-4(2)
C(14)	24(2)	29(2)	32(2)	-1(2)	-7(2)	-5(2)
C(15)	25(2)	30(2)	28(2)	0(2)	-2(2)	-6(2)
C(16)	34(2)	29(2)	34(3)	4(2)	-11(2)	-8(2)
C(17)	30(2)	27(2)	27(2)	6(2)	-15(2)	-4(2)
C(18)	31(2)	39(3)	31(2)	6(2)	-11(2)	-16(2)
C(19)	22(2)	39(3)	30(2)	2(2)	-4(2)	-8(2)

Table 6. Hydrogen coordinates (x 10^4) and isotropic displacement parameters (A^2 x 10^3) for jnat.

	x	y	z	U(eq)
H(32A)	4608	5982	2256	84
H(32B)	5072	6440	2922	84
H(32C)	5014	6938	2070	84
H(34A)	3729	8153	3369	57
H(35A)	1752	8832	3990	62
H(36A)	165	8094	3925	47
H(39A)	-485	6745	3389	34
H(42A)	-1746	5853	3540	41
H(43A)	346	6407	-1449	44
H(45A)	-3081	5046	3217	44
H(46A)	1001	4380	1775	45
H(47A)	3537	6130	-2446	42
H(47B)	2455	6879	-1948	42
H(49A)	2850	4539	-1400	55
H(50A)	3159	3939	-152	56
H(52A)	3304	6437	619	36
H(53A)	3072	7026	-657	39
H(55A)	4273	3602	716	34
H(57A)	4949	2322	1634	37
H(58A)	5024	1817	2983	46
H(59A)	4121	2802	4139	45
H(62A)	2541	5097	4004	74
H(62B)	3490	4644	4481	74
H(62C)	2264	4278	4617	74
H(1A)	-1140	-950	-4571	70
H(1B)	-1787	-87	-4954	70
H(1C)	-2163	-1043	-5000	70
H(3A)	-4265	156	-4245	51
H(4A)	-5661	457	-2933	54
H(5A)	-5080	-27	-1712	44
H(8A)	-3450	-877	-1071	35
H(11A)	-2916	-2226	-406	40
H(12A)	-2189	-2836	702	39
H(14A)	987	-2001	-354	34
H(15A)	281	-1413	-1482	34
H(16A)	-576	-3238	1386	38
H(16B)	752	-3112	881	38
H(18A)	-1924	-2007	2356	38
H(19A)	-2155	-723	3168	37
H(21A)	1282	-442	1946	37
H(22A)	1516	-1737	1148	39
H(24A)	-2326	694	3434	36
H(26A)	-3509	2087	4349	48
H(27A)	-3492	3492	4927	60
H(28A)	-1642	3965	4742	53
H(31A)	1264	2696	3577	70
H(31B)	771	3215	4459	70
H(31C)	630	3727	3629	70
H(2S1)	-1630	243	72	105
H(2S2)	-2872	-103	441	105
H(2S3)	-1714	-573	709	105